Chem Soc Rev

REVIEW ARTICLE

Cite this: *Chem. Soc. Rev.*, 2018, **47**, 2065

Towards flexible solid-state supercapacitors for smart and wearable electronics†

Deepak P. Dubal,*[ab] Nilesh R. Chodankar,[c] Do-Heyoung Kim[c] and Pedro Gomez-Romero*[b]

Received 9th July 2017

DOI: 10.1039/c7cs00505a

rsc.li/chem-soc-rev

Flexible solid-state supercapacitors (FSSCs) are frontrunners in energy storage device technology and have attracted extensive attention owing to recent significant breakthroughs in modern wearable electronics. In this study, we review the state-of-the-art advancements in FSSCs to provide new insights on mechanisms, emerging electrode materials, flexible gel electrolytes and novel cell designs. The review begins with a brief introduction on the fundamental understanding of charge storage mechanisms based on the structural properties of electrode materials. The next sections briefly summarise the latest progress in flexible electrodes (*i.e.*, freestanding and substrate-supported, including textile, paper, metal foil/wire and polymer-based substrates) and flexible gel electrolytes (*i.e.*, aqueous, organic, ionic liquids and redox-active gels). Subsequently, a comprehensive summary of FSSC cell designs introduces some emerging electrode materials, including MXenes, metal nitrides, metal–organic frameworks (MOFs), polyoxometalates (POMs) and black phosphorus. Some potential practical applications, such as the development of piezoelectric, photo-, shape-memory, self-healing, electrochromic and integrated sensor-supercapacitors are also discussed. The final section highlights current challenges and future perspectives on research in this thriving field.

1. Introduction

In the 21st century, no one can even imagine a world without portable/wearable electronic devices including mobile phones, laptops, cameras, smartwatch, activity trackers and many more, which has greatly changed our lifestyles and brought significant convenience to us. Yet, the increased energy consumption of these smart electronics requires improved energy storage devices. Indeed, in the sustainable post-fossil-fuels era that we are constructing, electrochemical energy storage (EES) is playing an increasingly important role. Among different EES systems, supercapacitors (SCs) and batteries are the most successful players on the Ragone chessboard and widely investigated in both academia and industries.[1–3] The basic differences between SCs and batteries lie in their different charge storage mechanisms and their materials/structures. Typically batteries are designed to provide high energy density by storing charge in bulk electrodes through faradaic reactions while SCs can provide high power density due to the surface charge storing mechanisms.[1–5]

Over the past decade, with the continuous emergence of applications in various sectors (mobility, biomedical, consumer electronics, sports, clean energy and environmental), flexible and wearable microelectronic devices and systems have gained significant importance.[1,2] Thus, the commercialisation of flexible electronics poses new challenges to well-established energy storage systems.[3] For instance, new energy storage devices need to maintain high-quality performance under continuous mechanical deformation, such as bending, folding, twisting and stretching, for long cycles. Moreover, recent progress in implantable/wearable healthcare devices (*e.g.*, spirometers, sphygmomanometers and wristbands) has led to new self-sustainable energy storage devices being developed, which can harvest/store body energy (generated through actions such as breathing, arm pressing and chest compression) and power smart electronics.[4,5] The key challenge is to design and assemble flexible electrode materials with high energy and power densities and excellent long-cycle stability with compatible electrolytes and separators in a flexible assembly. Safety and cost should also be considered, especially for wearable and implantable devices. Thus, we believe that the demand for flexible energy storage systems for next-generation implantable/wearable electronics will increase significantly.

[a] *School of Chemical Engineering, The University of Adelaide, Adelaide, South Australia 5005, Australia. E-mail: dubaldeepak2@gmail.com, pedro.gomez@cin2.es; Fax: +61883134373; Tel: +6183131535*

[b] *Catalan Institute of Nanoscience and Nanotechnology (ICN2), CSIC and The Barcelona Institute of Science and Technology, Campus UAB, Bellaterra, 08193 Barcelona, Spain*

[c] *School of Chemical Engineering, Chonnam National University, Gwangju 500-757, South Korea*

† Electronic supplementary information (ESI) available. See DOI: 10.1039/c7cs00505a

Supercapacitors (SCs) are promising electrochemical energy storage devices that have attracted significant interest in both academia and industry during the past several decades because of their superior energy density (compared with conventional

Deepak P. Dubal

Dr Deepak Dubal is currently working as Vice Chancellor's Research Fellow at University of Adelaide, Australia. He received his PhD in 2011 from Shivaji University Kolhapur, India, in Solid State Physics and joined as a Post-doctoral Fellow at Gwangju Institute of Science and Technology (GIST), South Korea. In 2012, he was awarded "Alexander von Humboldt" fellowship to work at Chemnitz University of Technology, Germany. He is also a recipient of "Marie-Curie" fellowship in 2014 to join Catalan Institute of Nanoscience and Nanotechnology ICN2 (CSIC-BIST), Spain. His research expertise is in design and development of multifunctional hybrid materials for clean energy conversion and storage technologies with special focus on supercapacitors, lithium-ion batteries, Li-ion capacitors and electrochemical flow cells. With Prof. Gomez-Romero, he has participated as founding partner of Earthdas graphene mobility spin-off Company. He is scientific editor of the book "Metal Oxides in Supercapacitors" D. P. Dubal, P. Gomez-Romero (Eds.) (Elsevier-2017) and member of Editorial board Scientific Reports (Nature Publishing Group). He was selected as Young Scientist to attend the 63rd Lindau Nobel Laureate Meeting (2013), Germany and recently nominated in top four young scientists for USERN Prize-2017.

Nilesh R. Chodankar

Dr Nilesh R. Chodankar is currently working as Postdoctoral Researcher at the School of Chemical Engineering, Chonnam National University, South Korea. Dr Nilesh received his PhD from the Shivaji University, Kolhapur, India, in 2016 in Physics. His current research interests include the synthesis and characterization of atomically thin nanomaterials by atomic layer deposition and their applications in flexible energy storage devices particularly for the supercapacitors.

Do-Heyoung Kim

Do-Heyoung Kim is a full professor in the school of chemical engineering at Chonnam National University in South Korea and also working as an Editor-in-Chief of Korean Journal of Chemical Engineering. He obtained his PhD in the department of chemical engineering at Rensselaer Polytechnic Institute (Troy, USA) in 1993. Before joining Chonnam National University, he worked as a senior researcher at the central research center of LG Semicon after postdoctoral research at North Carolina State University. His research interests are applications of atomic layer deposition for IC devices, supercapacitors, batteries, solar cells, and sensors.

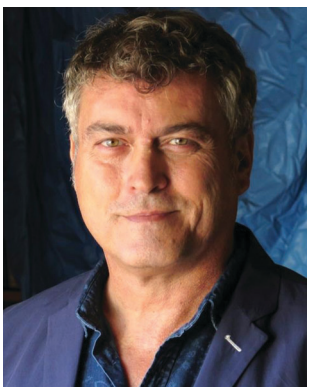

Pedro Gomez-Romero

Prof. Pedro Gomez-Romero, FRSC (BSc and MSc Universidad de Valencia, Spain. PhD in Chemistry, Georgetown University, USA, 1987, with Distinction) is Full Professor of the Spanish National Research Council (CSIC) since 2006. He is the Head of the NEO-Energy Group at the Catalan Institute of Nanoscience and Nanotechnology, ICN2 (CSIC-BIST) since 2007. Sabbatical Fellow at the National Renewable Energy Laboratory, USA (1998–99). Director of projects on energy materials, hybrid organic–inorganic nanostructures, graphene, nanocomposite materials for energy storage and conversion (lithium batteries, supercapacitors, flow batteries, solar-thermal energy, nanofluids). Cofounder of Earthdas graphene mobility spin-off Company. Author of more than 200 publications. Scientific editor of the books "Functional Hybrid Materials" P. Gómez-Romero, C. Sanchez (Eds.) (Wiley-VCH 2004) and "Metal Oxides in Supercapacitors" (Elsevier, 2017, D. P. Dubal, P. Gomez-Romero) and author of four award-winning popular science books. Winner of the CIDETEC Award for Research on Electrochemistry 2017.

capacitors), good power density (compared with batteries), fast charge–discharge rates and long cycle life.[6,7] Currently, SCs are used extensively in many applications, such as consumer electronics, transportation, military and aerospace, grid balancing and power backup, to protect, enhance and/or replace batteries.[8–10] The history and origin of SCs has been discussed extensively in the literature.[9,10] In brief, the first SC patent was granted in 1957, when Becker from General Electric Corp. developed a high-surface-area carbon-coated metallic current collector in H_2SO_4 solution. Sohio was the first to commercialise SCs in 1969.[7–10] Between 1975 and 1981, Conway[10] proposed a new concept of energy storage in SCs using a RuO_2 film in aqueous H_2SO_4 electrolyte. The charge storage mechanism was referred to as a 'pseudocapacitor' and was based on a faradaic process derived from surface redox reactions. In the 1990s, SCs became prominent when they began to be used, along with rechargeable batteries, to provide additional power in electric vehicles (EVs) and hybrid electric vehicles (HEVs). These SCs captured and stored energy from regenerative braking and supplied vehicle acceleration power.

Traditional SCs exhibit clumsy bulk shapes (*i.e.*, a separator sandwiched between two electrodes sealed in a liquid electrolyte), which presents some major drawbacks for their use in practical wearable applications. For example, the toxic liquid electrolyte requires high-standard safety encapsulation materials and technology to prevent its leakage. Moreover, because SC components can only be assembled in a few shapes/sizes, such as button and spiral wound cylinders, it is difficult to integrate them with other functional systems on the electronic motherboard. Thus, to overcome these limitations, flexible solid-state SCs (FSSCs) have emerged as a new class of energy storage devices and have attracted considerable attention in recent years.[11,12] FSSC devices comprise flexible electrodes, a solid-state gel electrolyte, a separator and flexible packaging material similar to those of conventional SCs. The main advantage of FSSCs over conventional SCs is the use of a solid-state gel electrolyte and flexible electrodes that can be assembled in thin, light and smart designs of any shape and size, thereby increasing their potential for application in flexible and wearable electronics.

Research on solid-state SCs began with the study of carbon and conducting polymer- (CP) based materials after 1990,[13] and the beginning of the 21st century witnessed some major contributions.[14] In these studies, the solid-state SCs were typically assembled by sandwiching a polymer gel electrolyte between two electrode pellets or films (active materials deposited on substrates, such as stainless steel (SS)) and pressed together into one device. This approach of first fabricating the electrodes and polymer electrolyte separately and subsequently assembling them together poses two major shortcomings: first, the reduction in device thickness is limited because thick solid-state gel electrolytes (the thinnest membrane prepared in a petri dish was 0.15 mm) and metallic current collectors are used. Thus, the middle polymer gel electrolyte needs to be as thin as possible but thick enough to separate the two electrodes. Second, because the solid electrodes are in contact with the solid-state electrolyte under pressure, only the electrode part near the geometric electrode/electrolyte interface can be utilised effectively. However, the past few years have witnessed several innovative strategies to address previous challenges and excellent breakthrough investigations have been reported.[15,16] The graphs shown in Fig. 1(a and b) depict the number of articles published thus far and the corresponding number of citations (source: Scopus). The remarkable increasing trend in the number of articles published per year together with the outstanding number of citations suggests the prominence of next-generation FSSC technology.

Currently, although many excellent reviews on FSSCs are available,[1,15–18] few give a complete picture on the nature of the substrates, electrolytes and cell design together[16] and instead focus on these features separately.[18,19] In addition, the past few years have witnessed many new materials emerging for FSSC application, including two-dimensional (2D) materials, polyoxometalates (POMs), metal–organic frameworks (MOFs), which are yet to be reviewed. Thus, a systematic summary of the latest innovations in FSSCs, which would cover a fundamental understanding,

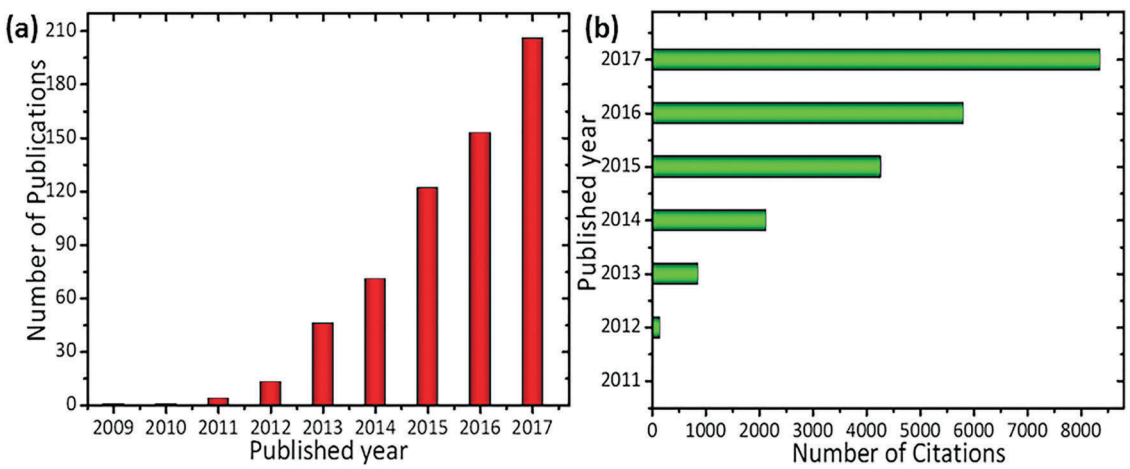

Fig. 1 Bibliometric data on the number of papers published and number of citations per year. The results obtained for "Flexible solid-state supercapacitors" from scoups.

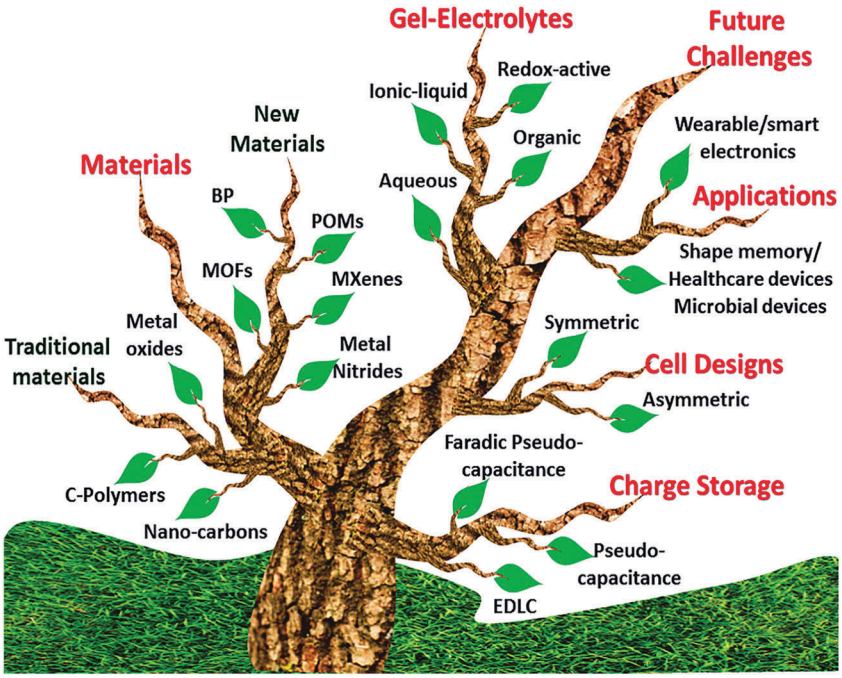

Fig. 2 An overview of the latest advancement in the field of flexible solid-state supercapacitors (FSSCs) as a green energy storage technology.

new emerging materials and novel cell designs, is highly required. Accordingly, as shown in Fig. 2, this review briefly describes the latest scientific progress in FSSCs, which is divided into the following sections. First, we highlight the latest findings on ionic charge storage mechanisms and transport pathways. Second, we present a summary of recent progress in developing flexible substrates based on a variety of materials, including metallic foil/mesh/wire, conventional and carbon paper, carbon fabric, yarn or polyme substrates. In the third section, a discussion on the mechanical flexibility of electrodes and devices is presented. The fourth section is focused on recent advancements in polymer gel electrolyte synthesis and the corresponding effect on electrochemical performance. Various gel electrolytes, such as aqueous, organic, ionic liquid and redox-active gels, are briefly discussed. In the fifth section, we review symmetric and asymmetric configurations with the introduction of novel materials, such as MXenes, metal nitrides, black phosphorus (BP) and MOF-derived materials. A brief description on the various negative electrode materials used in all solid-state asymmetric SCs is also provided. The sixth section presents a review of innovations in cell designs. The seventh and last section details state-of-the-art research in device innovation for next-generation SCs, including piezoelectric, photo-, shape-memory, electrochromic, self-healing SCs. To facilitate further research and development, some future research trends and directions are discussed in the conclusions.

2. Novel insights on charge storage mechanisms

Several reviews provide brief descriptions about SC charge storage mechanisms and basic electrochemistry.[7,20] However, this is not the scope of this review, we only discuss recently reported insights. According to previous studies, SCs are generally classified into two broad categories,[20,21] namely electrical double-layer capacitors (EDLCs) and pseudocapacitors. In EDLCs, the electrical charge is stored at the electrode–electrolyte interface. Charge separation is a physical process without any faradaic reactions on the electrode surface. Thus, EDL capacitance strongly depends on the surface properties of the electrodes, such as pore size distribution and specific surface area (SSA).[5,20,21] It was recommended that the pore size in porous EDLCs should be approximately twice the size of the electrolyte ions to allow full access into the pore walls. Moreover, the solvated ions do not enter the pores if the size exceeds the pore dimensions. However, some studies have invalidated this assumption through experiments and reported record-breaking specific capacitance values by decreasing the pore width for pores smaller than double the size of the bare ions.[22,23] Ultimately, no clear correlation has been found between the SSA and specific capacitance, implying that the capacitance cannot be increased by increasing the SSA and average pore size.[24] As presented in Fig. 3(a), the specific capacitance normalised by SSA, suggests that the effect of pore size is unrelated to surface area. Notably, volumetric capacitance increased $\sim$1.5-fold (from 55 to 80 F cm^{-3}) when microporous carbon with pores $<$1 nm were employed.[22] According to Monte Carlo simulation results, the anomalous increase in capacitance with decreasing pore width can be ascribed to the exponential screening of the electrostatic interactions of the ions inside the pore as well as the image-charge ionic attraction to the pore surface.[25] Thus, it was recently reported that the pore size and carbon nanostructure (rather than the SSA) play an important role in increasing the specific capacitance.[26] Recent developments in various advanced *in situ* spectroscopic and simulation

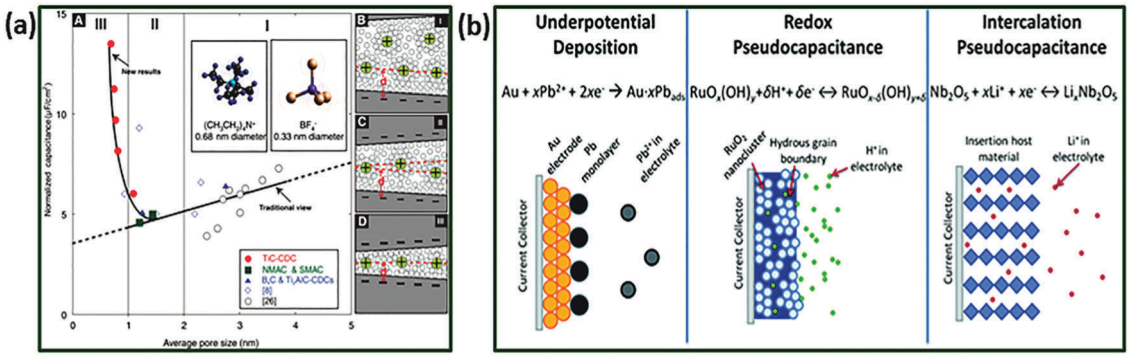

Fig. 3 (a) Plot of capacitance normalized by BET surface area *vs.* average pore size suggesting decrease in capacitance with pore size until critical value. Reprinted with the permission from ref. 23*a*, Copyright 2006, The American Association for the Advancement of Science. (b) Different types of reversible redox mechanisms that give rise to pseudocapacitance: (left) underpotential deposition, (center) redox pseudocapacitance, (right) intercalation pseudocapacitance. Reproduced with Permission from ref. 21*a*, Copyright 2014, Royal Society of Chemistry.

techniques allow close examination of the physical processes and origin of the charge storage mechanisms in carbon-based materials.

Conway's work suggests that various faradaic reactions can result in capacitive electrochemical features as shown in Fig. 3(b),[10] such as (1) underpotential deposition, (2) redox pseudocapacitance (normally observed in $RuO_2{\cdot}nH_2O$) and (3) intercalation pseudocapacitance (observed in V_2O_5, TiO_2 and Nb_2O_5). A brief description on 'pseudocapacitance in metal oxides' can be found in the recent literature.[27] Underpotential deposition usually occurs when metal ions form an adsorbed monolayer at a different metal's surface well above their redox potential.[21,28] In redox pseudocapacitance, the charge is stored through surface or near-surface charge transfer reactions. An intercalation pseudocapacitance mechanism was recently proposed whereby electrolyte ion intercalation in the tunnels or layers of a redox-active material is accompanied by a faradaic charge transfer without changing the original crystal structure. In some recent investigations, unfortunately, some electrode materials are described as "pseudocapacitive" materials despite the fact that their electrochemical features such as cyclic voltammetry and charge/discharge curves are similar to that of a "battery" materials (for example $Ni(OH)_2$ and cobalt oxides in KOH electrolyte). Conversely, true pseudocapacitive electrode materials show electrochemical signature similar to the carbon-based electrode (*e.g.* MnO_2, RuO_2 *etc.*).[27] Thus, it is recommended that the term "pseudocapacitive" must be only used to describe electrode materials such as MnO_2 in mild aqueous electrolyte and not for materials such as $Ni(OH)_2$ or cobalt oxides in KOH electrolytes.

The charge kinetics of pseudocapacitive materials can be characterised by estimating the capacitive and diffusion-controlled charge contributions to the total charge stored by the electrode using cyclic voltammetric data at various scan rates. Generally, the charge storage mechanism can be determined from the dependence of the current (i) on the scan rate (ν):[29]

$$i = a\nu^b \quad (1)$$

where a and b are adjustable parameters and b is determined from the slope of the plot of $\log(i)$ *vs.* $\log(\nu)$. Typically, $b = 0.5$ and corresponds to the diffusion-controlled faradaic intercalation process, suggesting typical battery behaviour where the current is proportional to the square root of the sweep rate ($\nu^{1/2}$) according to the following equation:

$$i = nFAC^*D^{1/2}\nu^{1/2}(\alpha nF/RT)^{1/2}\pi^{1/2}\chi(bt) \quad (2)$$

where C^* is the surface concentration of the electrode material, α is the transfer coefficient, D is the chemical diffusion coefficient, n is the number of electrons involved in the electrode reaction, A is the electrode material surface area, F is the Faraday constant, R is the molar gas constant and T is the temperature; function (bt) represents the normalised current. Conversely, for the capacitive process, the current response is directly proportional to the scan rate ($b = 1$). Generally, the total charge stored in the electrode is the sum of the currents resulting from capacitive ($k_1\nu$) and diffusion-controlled ($k_2\nu^{1/2}$) faradaic processes. Thus, eqn (1) can be modified as follows:

$$i = k_1\nu + k_2\nu^{1/2} \quad (3)$$

The current at a fixed potential is therefore equal to the sum of the capacitive ($k_1\nu$) and diffusion-controlled ($k_2\nu^{1/2}$) contributions.[6a] Constants k_1 and k_2 can be determined by plotting $i/\nu^{1/2}$ *versus* $\nu^{1/2}$ and measuring the slope and the y-axis intercept point of the straight line, respectively.

Notably, standardised methods are yet to be formulated to evaluate the capacitive performance of SC electrode materials used in different techniques (three-electrode *vs.* two-electrode configurations, different electrode thickness, CC discharge *vs.* CV curves, discharge current intensity and voltage scan rate) that yield widely varying results. Many excellent reviews explain these issues in great detail.[30] Moreover, macroscale SC performance is usually evaluated by SC gravimetric capacitance, energy and power densities.[31] Conversely, for microscale SCs (MSCs) or thin film based SCs, the mass of active materials is often very small and the limited space is a key constraint. Thus, volumetric/areal capacitance and energy and power densities

based on volume/area are more meaningful evaluating parameters. Further, for portable and wearable device applications, FSSC performance stability under different mechanical bending, twisting, compressing, stretching and extreme environmental conditions (high or low temperature and moisture) is also an important performance metric. These conditions depend mainly on the substrates and polymer gel electrolytes. Thus, third section briefly describes advances in fabricating flexible substrates for FSSCs.

3. Current advances and challenges in flexible electrodes

The most crucial factor in fabricating flexible SCs is using flexible electrodes (flexible substrate) with high electrical conductivity to ensure fast charge–discharge. Considering recent developments, flexible electrode fabrication can be divided into two main categories: (i) flexible freestanding films of active materials and (ii) supporting/depositing active materials on flexible substrates. In this section, we highlight recent developments in flexible electrodes for all-solid-state SCs.

3.1 Freestanding flexible electrodes

An emerging approach for fabricating flexible electrodes is to develop freestanding or self-standing films of active materials. This approach avoids using current collectors, conductive additives and binders, considerably reducing the final device weight. Thus, the complete volume is used, leading to excellent volumetric capacitance and energy density of SC devices. From a volumetric perspective, manufacturing solid-state SC devices with freestanding electrodes has been demonstrated as an excellent strategy for best material utilisation.[32] Numerous solution-processing methods have been presented to fabricate freestanding SC electrodes based on carbon materials,[33] especially carbon nanoparticles, graphene[34] and carbon nanotubes (CNTs).[35] Compared with other carbon materials, CNTs are excellent electrode materials, especially for FSSCs, owing to their high SSA (1240–2200 $m^2 g^{-1}$), high electrical conductivity (10^4–10^5 S cm^{-1}) and controllable regular pore structure.[36] Moreover, CNTs possess a high aspect ratio, which provides long continuous conductive paths and ensures high flexibility. Vacuum filtration is among the most widely used methods in CNT film preparation and can be easily achieved in a laboratory with simple equipment. However, the area of CNT films prepared thus is limited by the filter size. The resultant flexible CNT film, also known as buckypaper, presented desirable conductivity and specific areas and can be directly used as both the current collector and the active material for the FSSC.[35] Thus, Kang *et al.*[37] deposited CNTs onto a bacterial nanocellulose substrate through a vacuum filtering process to afford paper with high flexibility, a large SSA (460 $m^2 g^{-1}$) and superior chemical stability (Fig. 4(a and b)). The assembled FSSC exhibited a high specific capacitance of 46.9 F g^{-1} at a scan rate of 0.1 V s^{-1} and excellent stability with $<0.5\%$ capacitance loss after 5000 charge–discharge cycles at a high current density of 10 A g^{-1} as shown in Fig. 4(c).

Owing to its many similarities to CNTs, including a large SSA, superior electronic and mechanical properties and chemical stability,[38] graphene has also been investigated for its potential as an electrode in SCs.[39] As a consequence, Weng *et al.*[40] prepared graphene-cellulose paper (GCP) membranes by vacuum filtration of graphene suspension, which exhibited great advantages for use as freestanding and binder-free electrodes for flexible SCs. These GCP-based SCs exhibited a high areal capacitance of 46 mF cm^{-2} for the complete device under highly bent conditions. Freestanding, flexible and transparent graphene

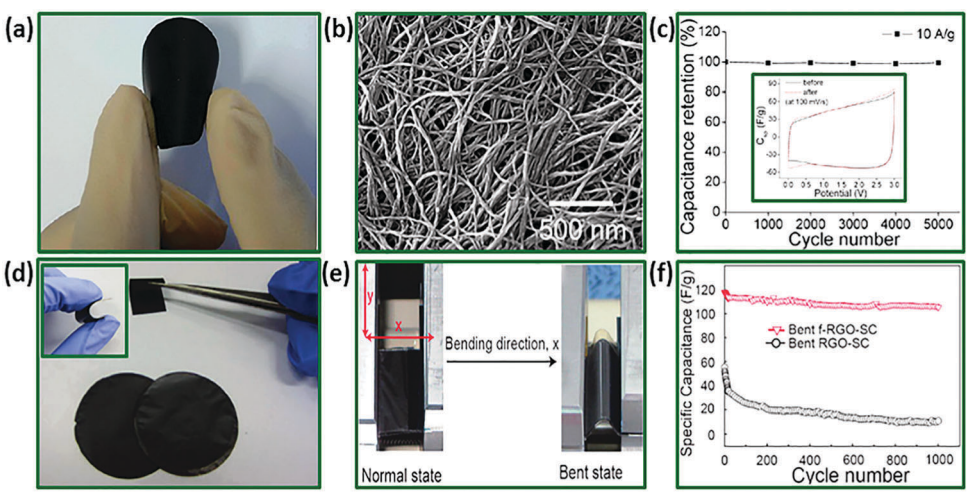

Fig. 4 (a) Flexible CNT-coated bacterial nanocellulose (BNC) paper, (b) SEM image of CNTs coated on a BNC paper (c) capacitance retention over 5000 cycles of charge/discharge at a current density of 10 A g^{-1}, inset shows CV curves measured before and after 200 bending cycles, reprinted with permission from ref. 30*d*, Copyright 2012 American Chemical Society. (d) Photograph of free-standing f-RGO films, inset shows the photograph of all solid-state flexible thin f-RGO-SC (e) photographs of SC prior to the bent experiments, (f) stability test of RGO-SC and f-RGO-SC by measuring 1000 charge–discharge cycles with a constant current density of 1 A g^{-1} at the bent state. Reprinted with permission from ref. 45, Copyright 2012 American Chemical Society.

paper was also prepared from a microwave plasma-enhanced chemical vapor deposition (CVD) process for optoelectronic application.[41] SCs based on flexible transparent graphene exhibited excellent electrochemical performance with high specific capacitance (3.3 mF cm^{-2}), volumetric energy (430 μW h cm^{-3}) and power density (190 mW cm^{-3}). This remarkable electrochemical performance was attributed to the ultrathin graphene flakes that provide large effective areas, good conductivity and 3D transport paths for both ions and electrons. However, individual graphene sheets begin to aggregate and restack during the fabrication process owing to the interplanar π–π interactions and van der Waals forces between the graphene layers. This agglomeration reduces the surface area of the graphene films and electrolyte ion diffusion, which results in decreased electrochemical performance. Therefore, several strategies have been developed to prevent aggregation of the graphene sheets to increase the surface area and promote electrolyte ion transport. These include adding spacers[42] and crumpling the graphene sheets.[43]

Wang *et al.*[44] reported the synthesis of reduced graphene oxide/carbon black (rGO/CB) hybrid self-standing films by a simple vacuum filtration method. The CB spacers considerably reduced the restacking of individual graphene sheets, resulting in a significant increase in electrochemical performance because of an open structure for charge storage and ion transport. The synthetic effects of the rGO sheets, CB and the interlayer water led to a large accessible surface area for the electrolyte. Moreover, the uniformly distributed CB particles between the graphene layers prevented compact restacking of the rGO sheets and also provided electrical contact between the base planes of the rGO sheets. As-fabricated FSCs with an rGO–CB hybrid film and polyvinyl alcohol (PVA)/H_2SO_4 gel on an Au-coated polyethylene terephthalate (PET) substrate presented a specific capacitance of 112 F g^{-1} at a scan rate of 5 mV s^{-1} and excellent rate performance with a specific capacitance of 79.6 F g^{-1} at a high scan rate of 1 V s^{-1}. Moreover, the FSSC exhibited good cycling stability with 94% capacitance retention after 3000 cycles in the normal state and 2000 cycles in the bent state. However, CB is only an additive and can only contribute a very small amount of capacitance to the whole device. Further, compared with the intercalation method, solution-based strategies could be more effective in reducing graphene sheet agglomeration in terms of simplicity, effectiveness, processing and cost of materials. In this context, Choi *et al.*[45] developed functionalised rGO films by functionalising graphene with Nafion using a supramolecular assembly approach (see Fig. 4(d)). The tight integration of the amphiphilic Nafion species prevents restacking of the individual graphene nanosheets (GNSs) and improves the interfacial wettability between the electrodes and electrolyte. Subsequently, the interconnected functionalised rGO networks provide continuous transport pathways for fast ion transport. FSSCs based on functionalised rGO thin films with solvent-cast Nafion electrolyte membranes were thus fabricated. The specific capacitance for the functionalised rGO species was determined as 118.5 F g^{-1} and remained almost constant (90% retention at 30 A g^{-1}) with changes in current density ranging from 1 to 30 A g^{-1}. Flexibility was demonstrated by bending the device at high tensile strain during the operation as shown in Fig. 4(e). In addition, the bending experiment demonstrated that there was no significant reduction in the initial capacitance at a bending radius of 2.2 mm, indicating good mechanical stability of the rGO-based FSSC (Fig. 4(f)). Yu and Dai[46] reported the synthesis of poly(ethyleneimine)-modified graphene sheet/acid-oxidised CNT hybrid films with interpenetrating network carbon structures and well-defined nanopores. The resulting freestanding multilayered CNT/graphene hybrid film exhibited a near-rectangular CV, even at an exceedingly high scan rate of 1 V s^{-1}, with an average specific capacitance of 120 F g^{-1} (three-electrode configuration).

Due to the dependence of the carbon materials on electrical double-layer charge storage, the electroactive surface area, pore size distribution and transport resistance of the electrolyte ions restricts their reversible capacitance. Thus, the actual gravimetric specific capacitance of carbon materials is usually <300 F g^{-1} and leads to a lower energy density.[47] To further increase the energy density, pseudocapacitive materials, with much higher capacitances than those of carbon materials because of redox reactions, have attracted great interest as potential substitutes for carbonaceous materials.[6] The commonly explored pseudocapacitor materials include transition metal oxides and hydroxides,[48] such as RuO_2,[49] MnO_2,[50] Fe_3O_4[51] and Nb_2O_5,[52] as well as CPs, such as polyaniline (PAni),[53] polypyrrole (PPy)[54] and polythiophene (PT).[55] However, these materials exhibit many disadvantages, including particle aggregation, poor electrical conductivity (metal oxides), structural degradation and poor cycling stability. Conversely, carbon-based materials exhibit high electrical conductivity and a large surface area and provide suitable scaffolds to support these pseudocapacitive materials. Hence, combining these high capacitance materials with flexible carbon materials should improve performance results.

In this context, freestanding metal oxides/nitrides, polymer/CNT and graphene hybrid electrodes were fabricated by simple methods, using synergistic effects from the high electrochemical performance of pseudocapacitive materials and the high conductivity and mechanical consolidation of the CNTs and graphene. Thus, mesoporous vanadium nitride nanowire (VNNW)/CNT hybrid electrodes were fabricated by a simple vacuum filtration method.[56] Notably, the device composed of VNNW/CNT hybrid electrodes and a PVA/H_3PO_4 gel electrolyte only weighed 15 mg (whole device) and exhibited a high volume capacitance of 7.9 F cm^{-3} and energy and power densities of 0.54 mW h cm^{-3} and 0.4 W cm^{-3}, respectively, at a current density of 0.025 A cm^{-3}. Similarly, 3D intertwined nitrogen-doped carbon encapsulated mesoporous vanadium nitride (MVN@NC) NWs were prepared by hydrothermal formation of V_2O_5 NWs and subsequent DA polymerisation, vacuum filtration and annealing under NH_3.[57] Thus, the paper-like freestanding MVN@NC NW electrode exhibited a thickness of 45 μm without any mechanical support or additives. FSSCs were fabricated by sandwiching two freestanding MVN@NC NW film electrodes with PVA, sodium polyacrylate (PAAS) and KOH gel electrolyte

(PVA/PAAS/KOH). This device delivered a remarkable volumetric capacitance of 10.9 F cm^{-3} at a current density of 0.051 A cm^{-3} and a high energy density of 0.97 mW h cm^{-3} with a power density of 2.72 W cm^{-3} based on the entire cell volume. Such excellent electrochemical performance can be attributed to the MVN NWs that provide abundant active sites that are accessible for charge storage and the N-doped carbon shell that suppresses electrochemical dissolution of the inner MVN NWs in an alkaline electrolyte.

In addition to metal oxides/nitrides, many efforts have been made to fabricate self-standing films of CPs, such as PAni, PPy and poly(3,4-ethylenedioxythiophene) (PEDOT). Among these compounds, PAni, known for its ease of synthesis, low cost, environmental friendliness and potentially large pseudocapacitance originating from its redox reactions, is among the most promising electrode materials for SC application.[58] However, PAni exhibits severe mechanical degradation caused by swelling and shrinkage during the doping and dedoping processes, which limits significantly its application as an electrode material for SCs. Therefore, to harvest the high capacitance of PAni while maintaining good cyclic stability, it is usually combined with carbon-based materials, such as graphene and CNTs. Chi *et al.*[59] developed a new type of nanohybrid based on a 3D graphene hydrogel-loaded PANi supported on freestanding graphene paper by an inkjet printing method. The electrochemical performance of the FSSCs based on these electrodes were surprisingly improved with a specific capacitance of 864 F g^{-1} at a current density of 1 A g^{-1} and an areal capacitance of 190.6 mF cm^{-2} at a current density of 0.5 mA cm^{-2}. Owing to the synergistic effect of the different components in this nanohybrid paper, the FSC exhibited an excellent energy density of 24.02 W h kg^{-1} (at a power density of 400.33 W kg^{-1}), remarkable flexibility and 96% cycling performance of over 1000 cycles. Chen *et al.*[60] reported the electrodeposition of PPy on a freestanding vacuum-filtered CNT film as another example of a CP/carbon composite. The CNT/PPy freestanding film exhibited good mechanical properties (ultimate tensile strength: 16 MPa). Thus, FSSCs based on robust CNT/PPy films exhibited good flexibility, a high volumetric capacitance (4.9 F cm^{-3}, considering total volume of the device) and 95% long cycling stability after 10 000 cycles. Further, the FSSC device displayed an energy density of 0.26 mW h cm^{-3} and a power density of 0.15 W cm^{-3}, both of which are acceptable values for practical application.

Poly(3,4-ethylenedioxythiophene)/poly(styrenesulfonate) (PEDOT/PSS) is also considered a promising material for SCs, mainly owing to its high conductivity, good chemical and electrochemical stabilities and excellent dispersibility in various solvents.[61] Liu *et al.*[62] prepared flexible rGO–PEDOT/PSS films by a simple bar-coating method. Notably, the device based on an rGO–PEDOT/PSS electrode retained 100% electrochemical performance under complete bending (180°) and rolled-up (1000-fold) conditions. Moreover, a high areal capacitance of 448 mF cm^{-2} was achieved at a scan rate of 10 mV s^{-1} when using a composite electrode with high mass loading (8.49 mg cm^{-2}), indicating its potential in practical applications.

In addition to graphene and CNT-based freestanding films, Li *et al.*[63] have recently developed a novel method for synthesising thick PEDOT:PSS films with the highest conductivity (1400 S cm^{-1}) and a low sheet resistance of 0.59 Ω sq^{-1}. An FSSC based on the PEDOT:PSS film delivered a volumetric capacitance of 50.1 F cm^{-3} at a current density of 0.1 A cm^{-3}. Interestingly, the device sustained a high volumetric capacitance of 32.9 F cm^{-3}, even at an extremely high current density of 100 A cm^{-3}, suggesting exceptional rate capabilities. Moreover, the device displayed an outstanding volumetric energy density of 6.80 mW h cm^{-3} at a power density of 100 mW cm^{-3}. Surprisingly, the device maintained an energy density of 3.54 mW h cm^{-3} at a high power density of 12 815 mW cm^{-3}, 3.15 mW h cm^{-3} at a power density of 16 160 mW cm^{-3} and 3.15 mW h cm^{-3} at a very high power density of 16 160 mW cm^{-3}. Thus, the outstanding electrochemical properties of the FSCs were attributed to the excellent conductivity of the freestanding PEDOT:PSS films.

3.2 Substrate-supported flexible electrodes

The thickness of the electrode materials used in FSSCs is low (< 50 μm); the freestanding active material films are relatively fragile and can flake off from the electrode after prolonged bending. To overcome this problem, many efforts have been made to support the active materials on flexible substrates. In this section, we briefly describe recent advancements in support substrates. These include coating and growing active materials on flexible, porous and lightweight substrates, such as flexible metal substrates (SS, nickel and titanium), carbon-based electrodes and porous materials (conventional paper, textiles and cable-type electrodes and bendable plastics).

3.2.1 Flexible metal substrates. Metal substrates have been extensively used as electrode substrates for SCs because they exhibit high electrical conductivity and good mechanical properties.[64–67] Various metal substrates, such as SS,[64] copper (Cu),[65] nickel (Ni)[66] and titanium (Ti),[67] provide high strength, good conductivity and ease of preparation. In addition, the electrode configuration of electroactive materials directly synthesised on the substrate surface leads to an increase in SC energy density and flexibility. Conversely, conventional powder-formed materials require additional binders, resulting in low energy density and mechanical durability.[68] Chodankar *et al.*[69] prepared porous nanostructured MnO_2 directly on a flexible SS substrate by chemical bath deposition (Fig. 5(a and b)). FSSCs based on these flexible MnO_2 electrodes were assembled with a carboxymethyl cellulose ((CMC)–Na_2SO_4) gel electrolyte and afforded a specific capacitance of 145 F g^{-1} with a specific energy of 16 W h kg^{-1}. Moreover, the device displayed almost negligible loss in capacitance under different bending conditions as well as long-term stability over 2500 cycles. More importantly, a series combination of two MnO_2-FSC devices easily powered two light-emitting diodes (LEDs) for 135 s, further confirming the significant potential for application in different portable electronic devices. Nanoporous 3D $Cu(OH)_2$ nanorods grown directly on copper foil provide a large number of active sites for redox reactions that can be easily accessed by electrolyte ions.[70] The flexible and foldable asymmetric SCs based on $Cu(OH)_2$ as

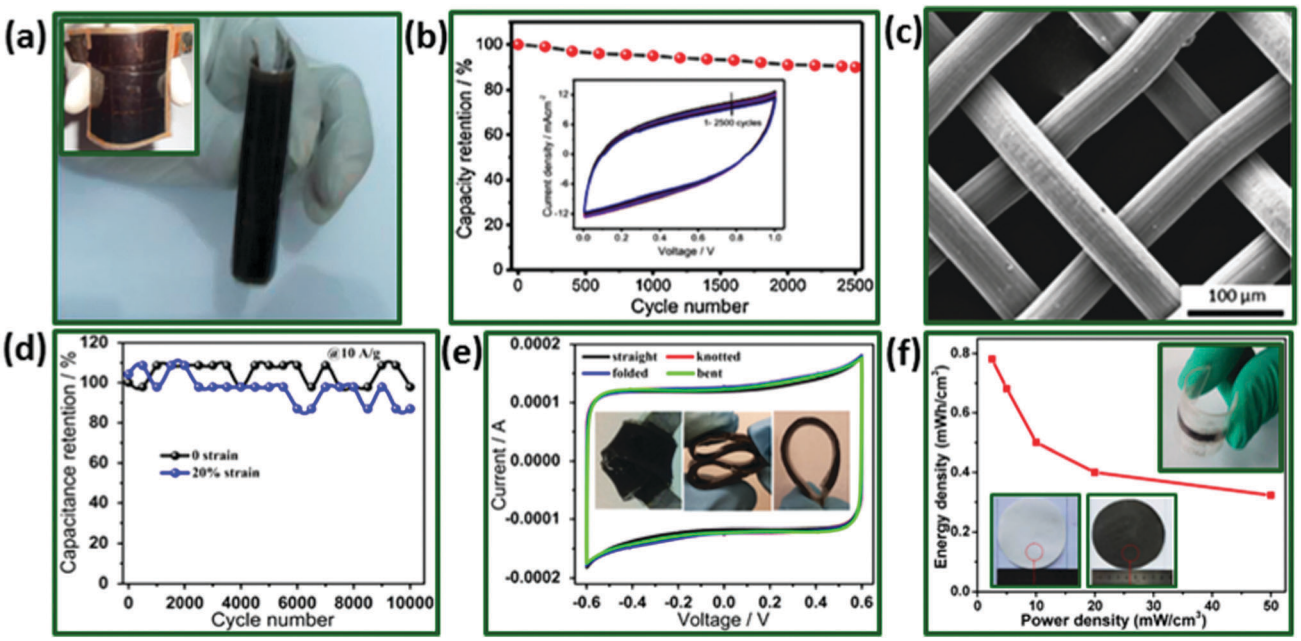

Fig. 5 (a) FSSC device with MnO_2 nanoflakes electrodes in normal and bending conditions. Reprinted with permission from ref. 69*b*, Copyright 2016 Elsevier. (b) Cycling stability of MnO_2 based FSC in bending state using CMC–Na_2SO_4 gel as an electrolyte. Reprinted with permission from ref. 69*a*, Copyright 2015 Elsevier. (c) Low magnified SEM image of polypyrrole deposited on SS mesh, (d) capacitance retentions as functions of cycle number at a specific current of 10 A g^{-1} under 0 (black) and 20% strain (blue). (e) CV curves of the fabricated PPy based stretchable supercapacitors at various kinds of deformation. Reprinted with permission from ref. 73, Copyright 2014 Elsevier. (f) Ragone plot for Ni/MnO_2-FP//Ni/AC-FP FSC, inset shows synthesized Ni/MnO_2-filter paper and digital photograph of final Ni/MnO_2-FP//Ni/AC-FP asymmetric device. Reproduced with permission from ref. 82, Copyright 2016, American Chemical Society.

positive and activated carbon (AC) as negative electrodes delivered a high energy density of 3.68 mW h cm^{-3} and a high power density of 5314 mW cm^{-3}. Practical applicability was displayed by lighting 26 LEDs with the tandem device. Similarly, Sheng *et al.*[71] reported interpenetrating graphene electrodes fabricated by electrochemical deposition of vertical graphene oxide (GO) on gold foil. The double-layer capacitor comprising these graphene electrodes exhibited a specific capacitance of 283 mF cm^{-2} and a short resistor–capacitor time constant of 1.35 ms.

Despite these advances, the conducting substrates used in FSSC electrodes (SS, Cu and Al foil) are usually much thicker and heavier than the coated active material. Therefore, even if the gravimetric specific capacitance based only on the active materials is increased, the low mass loading will only lead to a marginal increase in capacitance for the whole device. Further, the charges in the thick electrode materials cannot be transferred conveniently to the surface of the conducting substrates, thereby greatly decreasing the rate capability and capacitance of SCs with thick electrodes. This problem can be solved by using a 3D conductive structure as substrate to increase the electrode loading mass. Many studies have proposed using porous metallic substrates, such as mesh or foams.[72] Huang *et al.*[73] demonstrated an easy and cost-effective strategy to fabricate stretchable SCs with high performance and excellent cycling stability by electrochemical deposition of PPy on smartly tailored stretchable SS meshes (Fig. 5(c)). The fabricated FSSC exhibited a capacitance up to 170 F g^{-1} at a specific current of 0.5 A g^{-1}, which could be effectively enhanced to 214 F g^{-1} with a 20% strain. Notably, the device can be operated at a very high scan rate of up to 10 V s^{-1} in aqueous electrolytes. This value is significantly higher than that normally employed in PPy-based SCs. Further, under stretching conditions (0% and 20% strains), the device still achieved significant capacitance retentions of 98% and 87%, respectively, at a very high specific current of 10 A g^{-1} after 10 000 cycles (Fig. 5(d)). The CV curves recorded at 10 mV s^{-1} completely overlapped when the device was knotted, folded and bent (Fig. 5(e); inset: corresponding digital photographs). This remarkable performance was attributed to the open porosity of the highly utilised PPy materials and the high electric conductivity of the mesh. Zhou *et al.*[74] prepared a core–shell heterostructure based on layered titanate NWs coated with nickel hydroxide nanosheets on a titanium mesh ($K_2Ti_4O_9$@Ni$(OH)_2$/Ti) by a simple nickel ion exchange reaction. The FSSCs were assembled with a $K_2Ti_4O_9$@Ni$(OH)_2$/Ti flexible electrode and KOH/PVA solid-state electrolyte. The device exhibited a specific capacitance of 5.8 mF cm^{-2} at 5 mV s^{-1} with a retention rate of 92.5% after 2000 cycles and 92.7% after 10 000 cycles. Moreover, the $K_2Ti_4O_9$@Ni$(OH)_2$/Ti FSCs cell displayed an energy density of 4.8 mW h cm^{-3} (0.72 mW h cm^{-2}) at a power density of 1.1 mW cm^{-3} (0.16 mW cm^{-2}) and still retained 7.5 mW h cm^{-3} (1.13 mW h cm^{-2}) at a power density of 0.32 mW cm^{-3} (0.048 mW cm^{-2}).

Notably, FSSCs displayed excellent mechanical integrity with no significant change in electrochemical performance after mechanical stress of more than 200 intentional bends to a

radius of ~1.5 cm. Similarly, Wang *et al.*[75] prepared $NiCo_2O_4$ nanowire arrays (NWAs) on different flexible substrates, including nickel foam, carbon cloth, Ti-foil and polytetrafluoroethylene tape. The FSSC device assembled with the $NiCo_2O_4$ NWs on Ni foam provided an areal capacitance of 161 mF cm^{-2} at 1 mA cm^{-2} with a capacity retention of 82% (137 mF cm^{-2}) after increasing the current density eightfold (8 mA cm^{-2}). In addition, the device exhibited good cycling stability under twisted and bent conditions over 3000 cycles. This high performance was attributed to the highly conductive 3D macroporous Ni foam, which enables efficient charge transport and accessible diffusion of the electrolyte. Recently, a hierarchical PPy@Co–Ni layered double hydroxide (CoNi-LDH) core–shell array was prepared by a two-step electrosynthetic method.[76] In this integrated configuration, the PPy core provided excellent conductivity, while the Co–Ni LDH shell acted as a protection layer to enhance structural stability. The asymmetrical FSSC cell (PPy@LDH//RGO) presented an energy density of 46 W h kg^{-1} at a power density of 2.4 kW kg^{-1} as well as the highest cycling stability (15.4% increase in capacitance after 20 000 cycles). The synergistic effect in this hierarchical core–shell nanostructure contributes towards the promising overall performance of the all-solid-state asymmetric SC device.

3.2.2 Paper-based substrates. Based on their conductivity and porosity, metallic porous substrates are considered good candidates for flexible SC application. However, the lower corrosive resistance of the metal limits this applicability. Moreover, the heavy metallic current collector significantly increases the weight of the whole flexible SC device. Conversely, carbon-based supporting substrates, such as carbon paper, foam and cloth, exhibit higher electrical conductivity, lower corrosive resistance and, most importantly, better flexibility and lower weight. Thus, they are better candidates for flexible SCs application. This section summarises recent advancements in carbon-based flexible substrates for FSSCs.

Carbon paper consists of regular arrangements of carbon microfibres (CMFs) into flat sheets with enormous nanoscale pores that provide a large surface area to host the electrode material. The single carbon fibres present in carbon paper are well connected to each other to form a conducting network that allows appropriate pore channels to be formed. These channels create an efficient electron transportation path as well as effective electrolyte access to the electrochemically active materials. Similarly, carbon nanofoams consist of a cluster assembly of carbon strings in the form of a loose 3D web. Owing to their porosity, mechanical integrity and good conductivity, they have been widely used as substrates in fuel cells, SCs and other applications.[77]

Various forms of paper are widely used in our daily life for hygiene and sanitation purposes, packaging and decorating. In addition, paper applications have been expanded to flexible electronic devices, such as photodiodes, transistors, circuits and displays. Recently, several studies have demonstrated that paper can also be an excellent support for loading active materials to fabricate high-performance SCs. Tao *et al.*[78] reported a solid-state SC with conventional Xerox paper by simple pencil drawing. The thin graphite sheets on paper provided effective channels for electron transmission with a low resistance of 95 Ω sq^{-1}. The conductive organic material of PPy coated onto thin graphite sheets acted as the electrode material of the device. The as-fabricated SC exhibits a high specific capacitance of 52.9 F cm^{-3} at a scan rate of 1 mV s^{-1}. In another investigation, high-purity single-walled carbon nanotube (SWCNT)/graphene flake ink was cast by a rod-rolling method on conventional paper and applied to SCs.[79] Interestingly, at room temperature, the paper with the SWCNT/graphene ink provided lower sheet resistance (90.5 Ω sq^{-1}) than the paper with SWCNT (440.2 Ω sq^{-1}). Similarly, Zhang *et al.*[80] developed a new flexible SC in which the multi-walled carbon nanotubes (MWCNTs) were coated onto microfibrillated cellulose (MFC) doped with solid polyelectrolyte [polyethylene oxide (PEO) and lithium chloride]. In this design, the MWCNTs acted as the active material while the MFC coated with polyelectrolyte served the dual role of electrolyte and separator. The electrode and separator sheets both afforded good conductivities (~8.2×10^{-4} S cm^{-1} and 6.8×10^{-4} S cm^{-1}) and hence an acceptable specific capacitance of 154.5 mF cm^{-2} at 20 mV s^{-1}. In addition, the paper-based device displayed excellent mechanical properties with a tensile strength of 1 MPa and a Young's modulus of 123 MPa, which are significantly better than those observed for conventional liquid or gel-based soft SCs.

The performance of these paper-based SCs remains limited but can be further enhanced by adding pseudocapacitive materials in carbon-based SCs. Yun *et al.*[81] reported an FSSC based on PAni/Au/paper structures that could be easily scaled up to large-scale production. Interestingly, the device enhanced the energy density to 0.01 W h cm^{-3} (comparable with that of AC-based SCs with an aqueous electrolyte) and a power density of ~3 W cm^{-3}. Further, the cell exhibited excellent long-term cycling stability over 10 000 charge/discharge cycles with 100% coulombic efficiency. Conversely, metal oxides are the best pseudocapacitive candidates to combine with carbon materials and hold great promise in increasing the overall device performance. Recently, a paper-based asymmetric device was also developed with Ni/MnO_2 filter paper as the positive electrode and Ni/AC filter paper as the negative electrode, separated by a PVA–Na_2SO_4 electrolyte.[82] Impressively, the asymmetric device exhibited a volumetric energy density of 0.78 mW h cm^{-3} as well as superior flexibility under different bending conditions in a practical demonstration (see Fig. 5(f)). A paper-based all-solid-state flexible planar SC using a PEDOT:PSS–CNT/Ag electrode was accomplished using the inkjet printing technique.[83] The device delivered the best rate capability up to 10 000 mV s^{-1} and a fast frequency response (relaxation time constant τ_0: 8.5 ms). A high volumetric specific capacitance of 23.6 F cm^{-3} with long-cycle stability of ~92% capacitance retention after 10 000 cycles was also displayed.

3.2.3 Textile substrates. Textile-based electronics, such as e-textiles, smart textiles and wearable electronics, can be utilised in the future for high-tech sportswear, workwear, portable energy systems, health monitoring systems and military camouflage.[84] The related integrated devices for wearable electronics need an energy source, and thus, textile-based SCs hold great promise

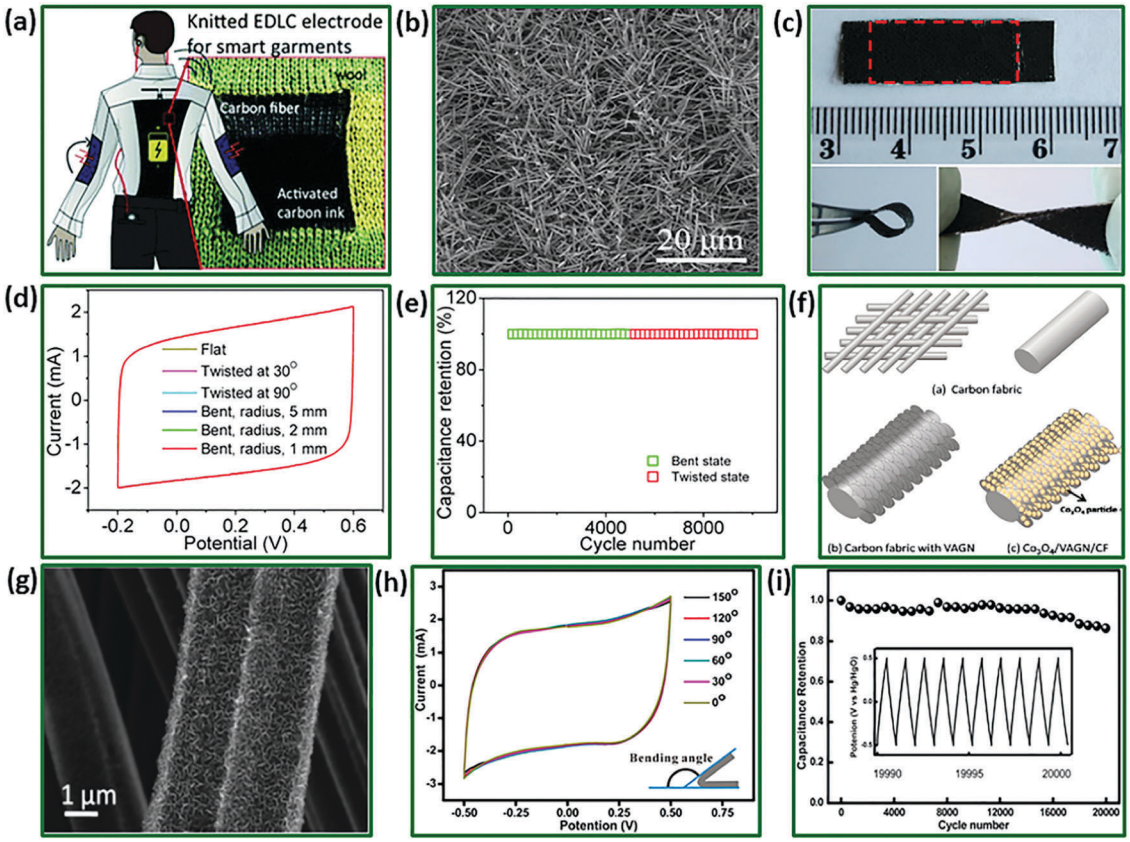

Fig. 6 (a) Schematic of textile based supercapacitors for wearable electronics, reproduced with permission from ref. 85*a*, Copyright 2013, Royal Society of Chemistry. (b–e) SEM image of single crystalline SiC nanowires on carbon fabric, digital photographs of FSSC based on SiC with corresponding CV curves at normal and bending conditions, cycling stability at bent and twisted conditions, respectively, reproduced with permission from ref. 88, Copyright 2015, American Chemical Society. (f–i) Pictorial presentation of steps involved in the synthesis of vertically aligned graphene nanosheets (VAGNs) decoared with Co_3O_4 nanoparticles, SEM image of VAGNs on carbon fabric, CV curves for Co_3O_4/VAGNs/carbon fabric solid-state cell at different bending conditions and cycling stability for 20 000 cycles, respectively, reproduced with permission from ref. 92, Copyright 2015, American Chemical Society.

for application in these systems (Fig. 6(a)). Common textiles, such as cotton, polyester and acrylonitrile, are reusable, cheap, flexible and hydrophilic.[85] When considering flexibility and stretchability, textile-based substrates have many advantages over paper-based substrates.[85] For example, the porous structure of these textiles provides abundant support for loading active materials and facilitates the rapid absorption of electroactive materials because of their hydrophilic nature. This results in a much higher areal mass loading of active materials and therefore a higher areal power and energy density.[86]

Low-cost and highly efficient textile-based SCs are already being integrated into prototype wearable electronics. For instance, CNTs have been grown directly on carbon cloth to fabricate conducting electrodes with 3D porous network architecture.[87] The assembled FSSCs exhibited extraordinary electrochemical performance, including a capacitance of 106 F g^{-1} (areal capacitance: 38.75 mF cm^{-2}), an ultralong cycle life (100 000-fold; 99% capacitance retention), a high energy density (2.4 μW h cm^{-2}) and a high power density (19 mW cm^{-2}). In addition, the device sustained its excellent performance even under very harsh conditions, such as shape deformation (*e.g.*, bending and folding), high mechanical pressure (63 kPa) and a wide temperature window (up to 100 °C). Nitrogen-doped single crystalline silicon carbide nanowires (SiCNWs) were directly grown on flexible carbon fabric by CVD method as shown in Fig. 6(b).[88] The FSSC cell fabricated with this unique material displayed an areal capacitance of 4.7 mF cm^{-2}, which translates into an excellent power density of 72.3 mW cm^{-2} (considerably higher than that observed in electrolytic capacitors) and an energy density of 0.12 μW h cm^{-2} together with superior rate ability and cyclability (~100% after 10 000 cycles; Fig. 6(c–e)). Notably, the SiCNW-based textile FSSC can be operated at an ultrahigh rate (up to 30 V s^{-1}), which is two orders of magnitude higher than that of conventional SCs.

Further attempts were made to improve the electrochemical performance of textile-based SCs by fabricating hybrid composite materials, such as carbon–metal oxides and/or CPs. Jin *et al.*[89] introduced a novel approach for the functionalisation of carbon fabric by a simple acid-oxidation and heat-treatment method. This approach created oxygen-functional groups on the carbon fabric that, in turn, added extra capacitance through a pseudocapacitive mechanism and provided an additional potential window. Thus, the symmetric cells fabricated with these functionalised electrodes could be cycled in a voltage window up to

1.6 V and provided a capacitance of 134.8 F cm^{-2} (or 2.41 F cm^{-3}) with an energy density of 0.83 mW h cm^{-3} and a power density of 1.58 W cm^{-3}. These values are higher than those observed for most previously reported CF-based SCs. MnO_2 is the most successful and promising pseudocapacitive material in terms of cost-effectiveness, high performance and environmental friendliness.

Ko *et al.*[90] developed a lightweight MnO_2/CNT-based textile SC. They implemented a very simple fabrication process comprising the deposition of MWCNTs onto commercial textiles using the 'dip and dry' method and subsequent electrodeposition of MnO_2 nanosheets onto the MWCNTs. Owing to the strong van der Waals forces and carboxyl groups, MWCNTs strongly adhered to the surface of the textile fibres through hydrogen bonds—washing and other mechanical processes did not damage these textiles. Interestingly, the FSSC cell displayed a specific capacitance of 324 F g^{-1} at 0.5 A g^{-1} and an energy density of 7.2 W h kg^{-1} with excellent cycling stability of ~100% capacity retention over 5000 cycles. Recently, Javed *et al.*[91] developed a zinc sulphide-based textile SC using a hydrothermal method. The ZnS-textile-based symmetric SC exhibited excellent electrochemical performance with a high specific capacitance of 540 F g^{-1} (areal capacitance: 56.25 F cm^{-2}) at a scan rate of 5 mV s^{-1} with good rate capability and excellent cycling stability (94.6% retention of the initial capacitance after 5000 cycles) at a constant current density of 0.8 mA cm^{-2}. A high energy density of 51 W h kg^{-1} at a power density of 205 W kg was also achieved, indicating excellent ion accessibility and charge storage ability.

Wang *et al.*[92] reported the growth of vertically aligned graphene nanosheets (VAGNs) decorated with Co_3O_4 nanoparticles directly on the carbon fabric for extraordinary SSCs as illustrated in Fig. 6(f). The Co_3O_4@VAGNs hybrid exhibited an excellent specific capacitance of 3480 F g^{-1} (close to the theoretical value of 3560 F g^{-1}). This value was attributed to the VAGN supported onto the carbon fabric, which served as an excellent backbone. A solid-state symmetric cell based on a Co_3O_4/VAGN/carbon fabric cell delivered a capacitance of 580 F g^{-1} under normal and bending conditions with good cycling ability (86.2% capacitance retention after 20 000 cycles; see Fig. 6(g–i)). Moreover, the cells exhibited an excellent energy density of 80 W h kg^{-1} that was maintained at 27 W h kg^{-1} at a high power density of 20 kW kg^{-1}.

3.2.4 Yarn-like (fibre) substrates. Fibre SCs are small lightweight 1D wires with diameters ranging from micrometres to millimetres. Fibre SCs have several advantages over conventional planar SCs, including considerable design versatility (*i.e.*, fibre SCs allow fabrication into various desired shapes that can be located at different places), high flexibility (*i.e.*, these can be woven or knitted into smart textiles with excellent wearability) and good compatibility with other energy harvesting devices and sensors to form integrated multifunctional systems.[93,94] Generally, planar SCs are fabricated as a bulk powder or thin film. Conversely, the geometrical configuration and mechanical flexibility of the substrates usually constrain yarn-electrode assembly. Normally, highly conductive fibres, such as metal wires and carbon-based fibres, are used as current collectors to grow different nanomaterials that can be directly used as electrodes in SCs. For fibre SCs, the structures are numerous and substantial effort has been made in designing novel device constructions. One simple design consists of two fibre electrodes coated with gel electrolyte in parallel, with a space on the flexible substrate. Graphene-based materials are more suitable for wire- or yarn-based SCs because of their excellent electrical conductivity and mechanical flexibility.

Huang *et al.*[95] developed a graphene fibre-based SC from wet-spun graphene fibres. The graphene fibres, which were several meters in length, were wet spun in a coagulation bath of $CaCl_2$ aqueous ethanol solution and subsequently reduced with hydrazine. Two different-sized fibres (diameters: 35 μm and 100 μm) prepared from hydrogen iodide and dihydrogen dihydride (N_2H_4) reducing agents displayed electrical conductivities of 10 000 S m^{-1} and 700 S m^{-1}, respectively (Fig. 7(a and b)). The planar cell design was used to fabricate fibre-based SCs (Fig. 7(c)) with a capacitance of 2.5 mF cm^{-2} and 3.3 mF cm^{-2} at 0.1 mA cm^{-2} for the 100 μm and 35 μm fibres, respectively, demonstrating the adverse effect of large-sized fibres. Graphene fibre electrode capacitance can be further improved by combining it with a conjugated polymer. To this end, the graphene fibres were uniformly coated with PAni. Surprisingly, the resultant fibre SC displayed a capacitance of 66.6 mF cm^{-2}, representing a 22-fold improvement.

Similarly, Kou *et al.*[96] developed a yarn SC using a coaxial wet-spinning strategy to prepare polyelectrolyte-wrapped (CMC) carbon nanomaterial (graphene, CNTs and a mixture of both) core-sheath fibres that could be directly applied as contactable and interweaving yarn SC electrodes as illustrated in Fig. 7(d and e). The polarised optical image reveals the presence of homogeneous CMC on the GO core sheaths. The CMC is ionically conductive, while the presence of the electrically insulating polyelectrolyte prevents the risk of short circuits. First, GO@CMC core–shell fibres were prepared by mixing aqueous solutions of GO and CMC into a mixture of ethanol/water solution with $CaCl_2$. The GO was further reduced by acid to afford the rGO@CMC fibres. These presented a conductivity of 7000 S m^{-1}, while being completely insulated when measured from the CMC side. The solid-state flexible two-ply yarn SC displayed a capacitance and energy density of 177 mF cm^{-2} (158 F cm^{-3}) and 3.84 μW h cm^{-2} (3.5 mW h cm^{-3}), respectively, which are superior to values afforded by commercial capacitors (Fig. 7(f)). In addition to self-assembled CNT and graphene fibres and their composite fibre electrodes, wire electrodes can be fabricated by directly growing active materials on the fibre conductive current collectors. Carbon, nickel and titanium fibres are commonly employed as conductive substrates, while metal oxides used include $ZnCo_2O_4$, $NiCo_2O_4$, Co_3O_4 and $Ni(OH)_2$.[97]

Although the aforementioned SCs exhibit many advantages, they are not real fibre SCs owing to the use of planar substrates as support. True yarn or fibre SCs should be of single-wire form or cable-type architecture. For example, Wang *et al.*[97] developed a fibre SC by assembling two nickel wires anchored with a $NiCo_2O_4$ nanosheet, whereby one wire was wound around the

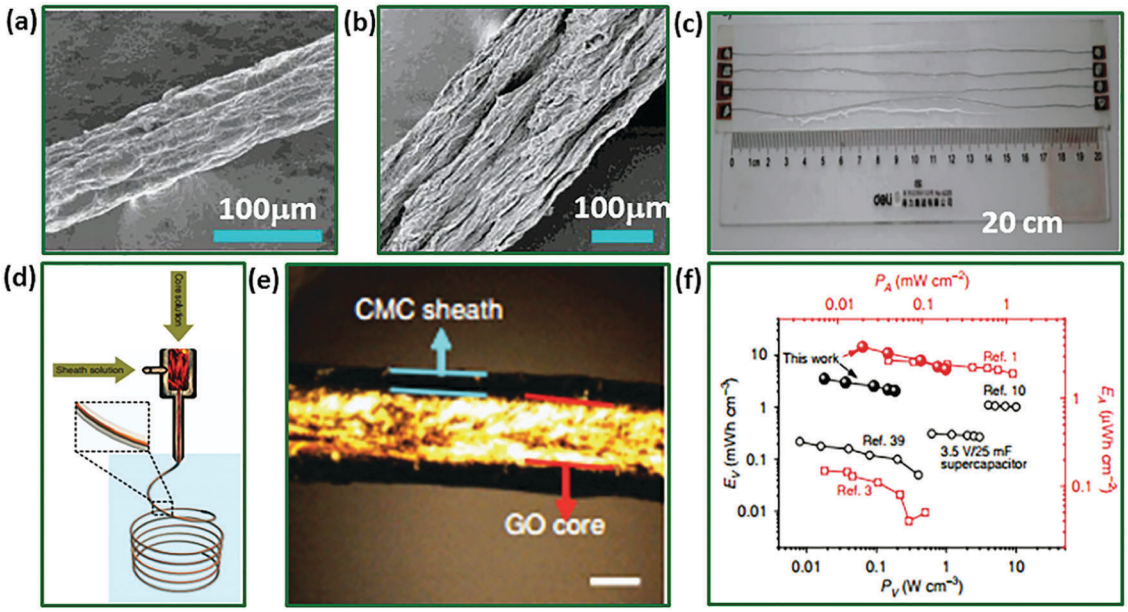

Fig. 7 (a and b) SEM images of graphene fibres of two different sizes such as 100 μm and 35 μm, respectively (c) digital photograph of planar fibre-based SC, reproduced with permission from ref. 95, Copyright 2013, Royal Society of Chemistry. (d) Schematic illustration of preparation of GO@CMC core–shell fibres by coaxial spinning process. (e) Polarized-light optical microscopy image of wet GO@CMC fibre showing the core-sheath structure and the well-aligned GO sheets in the core part, (f) Ragone plots compared with the reported fibre-shaped yarn-SCs with solid electrolyte, reproduced with permission from ref. 96, Copyright 2014, Nature Publishing Group.

other and a PVA–KOH gel electrolyte filled the middle space. No obvious change was recorded in device electrochemical performance under harsh bent conditions because of the unique spring-like structure of the material. However, the electrolyte might be damaged during bending owing to the stress between the metal current collectors. Similarly, titania nanotubes were grown on titanium NWs by the anodisation method.[98] In this configuration, pseudocapacitive titania nanotubes provided a high surface area and also acted as a separator between the Ti-fibre and the outmost CNT yarn or sheet. These electrodes, processed in FSSCs with a CNT sheet electrode, displayed a capacitance of 1.84 mF cm^{-2}, which is approximately triple that afforded with a single CNT yarn electrode. Remarkably, this wire-shaped SC can be woven successfully into various textiles and connected in series or parallel to meet a large variety of specific energy demands.

Fibre SC mechanical stability can be further improved by fabricating cable-type SCs using plastic and carbon fibres instead of metal fibres as the substrate for active materials. A cable-type fibre SC based on PPy–MnO_2/SWCNT-coated carbon fibres as the electrode was assembled with excellent mechanical stability.[99] In this composite, the conducting SWCNT backbone provided excellent conductivity, while the active mesoporous flower-like MnO_2 nanoplates and PPy conductive wrapping layer improved the electrical conductivity and added extra pseudocapacitance. However, this SC design type exhibits low capacitance because the use of active materials is reduced. Therefore, it is very important to choose a proper cell design that maximises such use. To this end, a novel fibre SC with a coaxial structure that has the highest contact area between active materials has attracted significant interest. Yu *et al.* designed a coaxial SC using CuO@AuPd@MnO_2 core–shell nanowhiskers grown on copper wire and foil as inner and outer electrodes, respectively.[100] The as-fabricated coaxial SCs take full advantage of both the inner and outer active materials, thus providing many more electrochemically active sites for reversible redox reactions. Notably, it also exhibited high flexibility and retained electrochemical performance efficiently when tested under different bending angles.

Preparing an industrially weavable and knittable conductive yarn with high capacitance remains a challenge. To this end, soft conductive yarns were produced by a scalable method through the twist-bundle-drawing technique. These yarns are sufficiently mechanically robust to be knitted into cloth using a commercial cloth knitting machine as illustrated in Fig. 8(a and c).[101] Further, these conductive yarns were coated with rGO, and subsequently, MnO_2 nanosheets and PPy were deposited on it. The cable-type SCs fabricated with these composite yarns exhibited capacitances of 31 mF cm^{-1} (length capacitance) and 411 mF cm^{-2} in an all solid-state two-electrode cell, which are considerably higher than previously reported values (Fig. 8(b)). Moreover, the symmetric solid-state SC displayed energy densities of 9.2 μW h cm^{-2} and 1.1 mW h cm^{-3} (both normalised to the whole device) with a long cycle life over 5000 cycles. Finally, a large-sized (15 cm × 10 cm) yarn-type FSSC was assembled on a loom and a woollen wrist band was knitted to form a pattern as demonstrated in Fig. 8(d). Moreover, many yarn FSSCs were fabricated to elucidate the effect of the number of yarns. For example, Le *et al.*[102a] developed a coaxial-fibre FSSC, comprising MWCNTs coated onto CMF bundles as the core electrode,

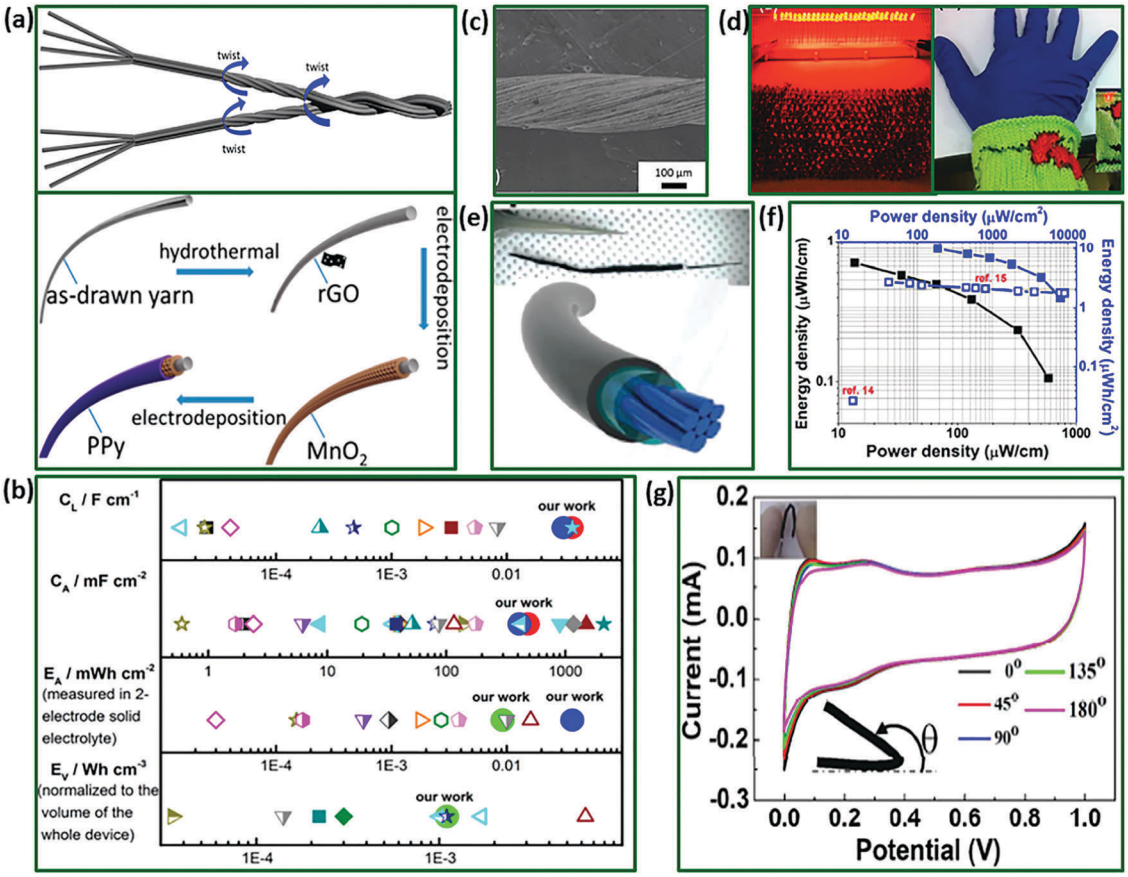

Fig. 8 (a) Steps involved in the fabrication of yarn and subsequent deposition of MnO_2 and PPy thin films on to the yarn. (b) Comparison of electrochemical performance of various fiber/yarn-based electrocapacitive materials (C_L and C_A are length and areal capacitances, E_A and E_V are areal and volumetric energy densities). (c) SEM image of an as-drawn yarn, adopted with permission from ref. 101, Copyright 2013, American Chemical Society. (d) A large-sized (15 cm × 10 cm) yarn-type FSSC assembled on a loom and a woollen wristband knitted to form a pattern. (e) Schematic and digital photo of a coaxial-fiber SC. (f) Ragone plot with energy and power density per length or area of the core electrode. (g) CV curves with different bending angles at a scan rate of 5 mV s^{-1} and inset shows the digital photograph of bended yarn-FSCs. Reprinted with permission from ref. 102, Copyright 2013, American Chemical Society.

with carbon nanofibre (CNF) paper as an outer electrode and polymer gel as the electrolyte (Fig. 8(e)). The devices exhibited a length capacitance of 6.3 mF cm^{-1} with a 230 μm sized core electrode and an energy density of 0.7 μW h cm^{-1} (9.8 μW h cm^{-2}) at a power density of 13.7 μW cm^{-1} (189.4 μW cm^{-2}) as depicted in Fig. 8(f). Moreover, negligible changes in the CV characteristics (Fig. 8(g)) were observed after severe bending (180°), revealing that devices components (CMFs, MWCNTs and CNFs) soaked with polymer gel electrolyte are highly flexible.

In most studies, metal wire/yarn or fibres were used to support active materials. However, these noncapacitive supports increase device volume and weight, which lowers the device performance and mechanical stability. In this context, freestanding elastic SCs using CNT-based fibre springs as electrodes were explored.[102b,102c] A coaxial-fibre SC was assembled using aligned CNTs fibres and sheets as two electrodes with a polymer gel sandwiched between them.[102b] This unique coaxial structure not only decreased contact resistance between the two electrodes, but also achieved a maximum capacitance of 59 F g^{-1} (32 F cm^{-3}) and energy densities up to 1.88 W h kg^{-1}. Significantly, these fibre SCs maintained their high performance under different bending (from 0 to 180°) as well as stretching (0 to 20% strain) conditions. To further improve device performance, Ren *et al.*[102d] developed CNTs and ordered mesoporous carbon (OMC) composite fibre electrodes where CNTs provide high conductivity and OMC offer efficient surface area and tunable pore structure accessible to the electrolyte. Two composite fibres were twisted to fabricate flexible, wire-shaped SCs that exhibited high specific capacitance of 39.7 mF cm^{-2} and energy density of 1.77 μW h cm^{-2}. The mechanical properties were tested by recording CV curves at different bending deformations, which suggests no degradation in the capacitance.

Thus, the use of many fibre/yarn/cable-type SCs has been explored successfully. The discussed results suggest that textile-based energy storage systems with high energy density and mechanical robustness can be achieved using a binder-free approach with nanostructured metal oxides as active materials and CNT graphene fibres as substrates. Moreover, it is critical to develop new nanostructured active materials with high electron conductivity, abundant electrochemical sites and novel fibre

current collectors with strong mechanical stability and ultra-high flexibility to develop fibre-shaped flexible energy storage devices and wire-based integrated energy systems with excellent performance.

3.2.5 Polymer-based nonconducting substrates. Low-cost, comparatively light plastic substrates with excellent bendability, such as PET,[103] polydimethylsiloxane (PDMS)[104] and ethylene/vinyl acetate copolymer films,[105] are considered promising supports for active materials. PET is widely used owing to its easy availability, excellent water and moisture repellent properties and transparent nature. Several studies have examined PET-based flexible SCs.[106] A transparent FSSC based on graphene was also attempted.[107] A cell with an optical transmittance of ~67% at a wavelength range of 500–800 nm was realised, suggesting considerable potential for application in transparent flexible electronics. In addition, the cell exhibited good flexibility, retaining 92.4% of its initial capacitance under a bending angle of 80°. The decrease in capacitance under bending was ascribed to the graphene electrode buckling during compression. Conversely, Choi *et al.*[108] reported a twofold increase in a graphene-based FSSC using functionalised reduced graphene oxide (f-rGO) thin films as the electrode and solvent-cast Nafion electrolyte membranes as the electrolyte and separator. Moreover, the f-rGO cell exhibited a relaxation time that was fourfold faster than that of the rGO-based cell, as well as higher capacitive behaviour at the low-frequency region. These results were attributed to facilitated ionic transport at the electrical double layer because of the interfacial engineering of rGO *via* Nafion.

However, graphene capacitance is still limited, thereby hindering the use of these thin films in a wide range of applications. Fei *et al.*[109] explored a new strategy of mixing CB with graphene and using cross-linked PVA–H_2SO_4 porous gel electrolytes. In this composite, CB nanoparticles were uniformly distributed in the GNSs, thereby greatly improving the active surface area and ion transportation in pristine graphene. Moreover, the porous PVA–H_2SO_4 membrane improved the equilibrium swelling ratio of the electrolyte and provided interconnected ion transport channels. The symmetric cell was designed by casting a graphene/CB composite on PET foil and afforded a specific capacitance of 144.5 F g^{-1} at 0.5 A g^{-1} with good capacitance retention (67.9% from 0.2 to 4 A g^{-1}). More importantly, on investigating the effect of temperature, capacitance retention after 1000 cycles at 70 °C was found to be 78.3%. A new on-chip MSC based on MnO_x/Au multilayers on a PET substrate was introduced by Si *et al.*,[110] A digital photograph of the assembled device is presented in Fig. 9(a). These MSCs exhibited an energy density of 1.75 mW h cm^{-3} and a maximum power density of 3.44 W cm^{-3} (Fig. 9b). Moreover, at a high scan

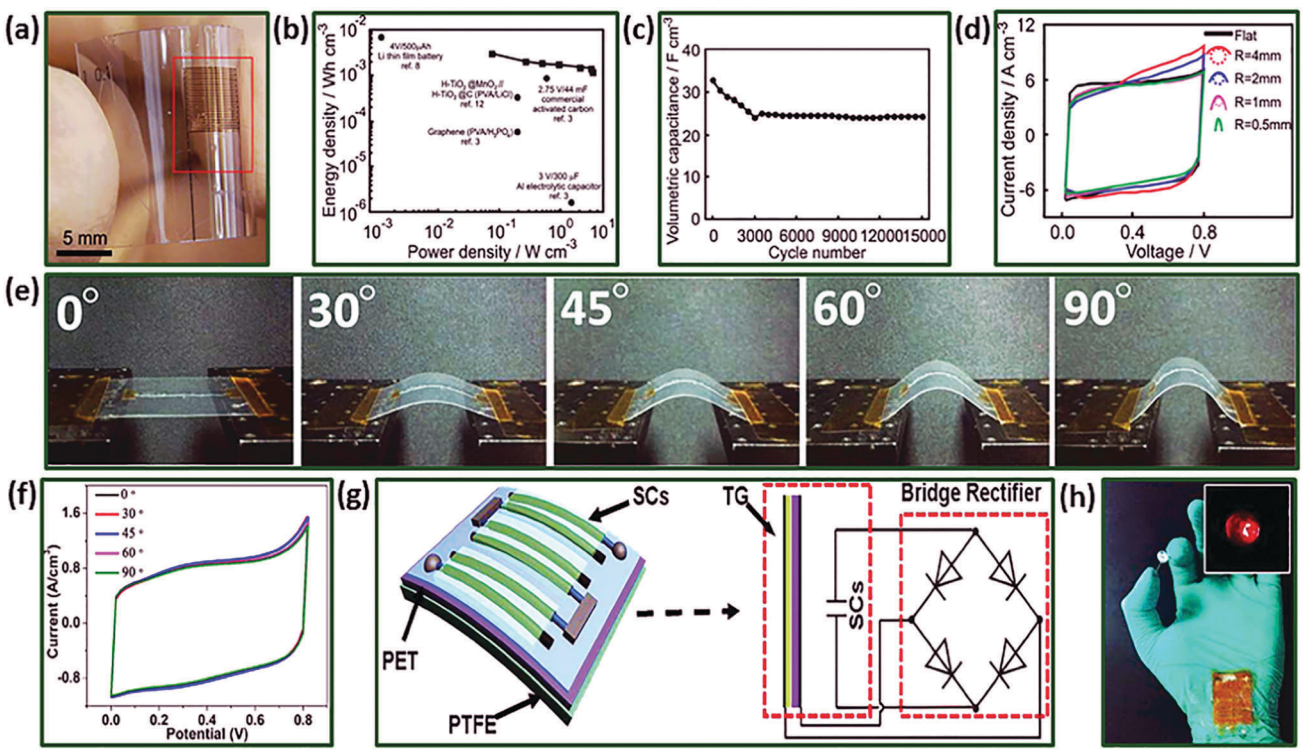

Fig. 9 (a) Photograph of a fabricated flexible micro-supercapacitor on a polyethylene terephthalate (PET) substrate, (b) Ragone plot of the microsupercapacitor, (c) cycling stability of MnO_x/Au multilayer micro-supercapacitors, measured at a scan rate of 1 V s^{-1} (d) CV curves at different bending states, indicated by diameters of curvature, respectively. Reprinted with permission from ref. 110, Copyright 2013, Royal Society of Chemistry. (e) Optical images of MnO_2@carbon fibre single device on PET substrate bended with different angles (f) CV curves for MnO_2@carbon FSCs at different bending conditions (g) schematic diagram of energy modulus integrated by three SCs connected in series and a triboelectric generator. (h) Digital photograph of the energy modulus that is powering commercialized LED. Reprinted with permission from ref. 111, Copyright 2012 American Chemical Society.

rate of 1 V s^{-1}, the device displayed a volumetric capacitance of 32.8 F cm^{-3}, which is almost twofold higher than that of the bare MnO_x electrode (19.23 F cm^{-3}). These excellent electrochemical responses correspond to the improved electrical conductivity of MnO_x owing to incorporating gold. The MnO_x/Au multilayered MSC also exhibited good long-term cycling stability with a capacitance retention rate of 74.1% over 15 000 cycles (Fig. 9(c)). Notably, the cell provides good flexibility with negligible change in the CV shapes under different bending conditions (Fig. 9(d)), suggesting significant potential for application in integrated microdevices.

Conversely, Xiao *et al.*[111] developed a core–shell structure by depositing MnO_2 on carbon fibre and assembled a planar self-powered SC device on a PET substrate. The device exhibited excellent electrochemical performance, including a high rate capability with a scan rate up to 20 V s^{-1}, high volume capacitance of 2.5 F cm^{-3} and an energy density of 0.22 mW h cm^{-3}. Fig. 9(e and f) displays digital photographs of a MnO_2@carbon fibre single cell under different bending conditions and its corresponding CV curves, respectively. Interestingly, in these CV curves, no significant change can be observed under different bending conditions. To meet the energy and power requirements, cells packaged either in series, parallel or a combination of both may be a viable solution. Fig. 9(g) presents a module fabricated from three cells connected in series integrated with a triboelectric generator through which the SC can be charged. Interestingly, a practical demonstration was provided where human hand movement (Fig. 9(h)) charged the SC and powered a LED. These results suggested great potential for application in self-powered micro/nanosystems.

Kurra *et al.*[112] proposed an FSSC fabrication procedure based on PEDOT on a plastic polyethylene naphthalate (PEN) substrate using conventional photolithography and electrochemical deposition techniques. Surfactant-assisted electropolymerisation allows synthesising porous conducting PEDOT electrodes. The electrodes were first tested in aqueous H_2SO_4 electrolytes and displayed excellent electrochemical performance (tunable frequency response and energy density). Specifically, an ultrahigh scan rate capability up to 500 V s^{-1} was achieved with a crossover frequency of 400 Hz at a phase angle of $\sim 45^{\circ}$, values comparable to those afforded by carbonaceous-based materials. When PEDOT SCs were tested with a polymer gel electrolyte, they presented an areal cell capacitance of 5 mF cm^{-2} with a volumetric stack capacitance of 33 F cm^{-3} (retention: $\leq$80% over 10 000 cycles with 100% coulombic efficiency). Moreover, the device exhibited an energy density of 7.7 mW h cm^{-3}, a value that is comparable to that afforded by lithium-based thin-film batteries and superior to the current state-of-the-art carbon and metal oxide-based FSCs.

Polyimide (PI) is another polymeric substrate that has gained significant attention for its potential as a flexible substrate in FSCs.[113] Lately, In *et al.*[114] developed a flexible MSC based on PI sheet laser carbonisation. Localised pulsed laser irradiation rapidly converts the pristine PI surface into an electrically conductive porous carbon structure under ambient conditions. Thus, the PI sheet acts as a flexible substrate as well as a precursor for carbonisation. The electrical properties and morphology of the carbon nanostructure were optimised by various laser parameters. The FSC was fabricated by drawing interdigitated electrode patterns directly on the PI sheets and using a PVA–phosphoric acid mixture as the gel electrolyte. The device exhibited a specific capacitance of 800 μF cm^{-2} at a voltage scan rate of 10 mV s^{-1} with good capacitance retention under mechanical bending. Interestingly, this laser-based patterning technique does not require using tedious photolithographic patterning of porous carbon and metal current collectors. Similarly, Peng *et al.*[115] prepared two FSCs based on porous vertically aligned in-plane graphene on a PI substrate using a laser induction technique. The device displayed a capacitance of 9.11 mF cm^{-2} at a current density of 0.01 mA cm^{-2} with excellent cycle stability (98% retention over 8000 cycles). Moreover, areal capacitance was well maintained after 7000 bending cycles at a radius of 14 mm, suggesting negligible effect from repeated bending.

Several other flexible polymer substrates were tested as substrates for SSCs, such as polycarbonates (PCs),[116] polyethersulfone (PES)[117] and parylene.[118] To date, test results reinforce the assertion that polymersubstrate-based FSCs are promising candidates as energy storage devices in flexible, portable and wearable electronics. However, despite their high flexibility and good ion accessibility, the electrical conductivity of these electrodes has been limited by the insulating properties of the substrates used, which affects the SC charge–discharge rate. In addition, the total SC device weight increased because insulating substrates were used, leading to decreased capacitance per unit weight. Table 1 lists various flexible substrates used for fabricating solid-state devices and their respective electrochemical performance.[70,72,75,76,91,109,110,119–172]

4. Mechanical flexibility of electrodes and devices

Many electronic devices, such as smart clothes, electronic skins, bendable smart phones and implantable medical devices, and their power supplying units (*e.g.*, FSSCs) undergo various severe mechanical deformations. Therefore, it is imperative to assemble bendable, foldable, twistable and stretchable FSSCs without sacrificing their high performance over long cycles. Few methods have been developed so far to investigate electrode flexibility. For instance, the mechanical flexibility of the electrodes can be examined quantitatively using tensile and fatigue tests, the stress–strain curve and *in situ* resistance change ($\Delta R/R$). The stress–strain curve can be found by recording the amount of deformation (strain) at distinct intervals of tensile or compressive loading (stress). This curve reveals many properties of a material (including data to establish the modulus of elasticity). For example, Di *et al.*[173a] prepared ultra-strong and foldable carbon nanotube (CNT) film using aligned few-walled nanotube sheets drawn from spinnable nanotube arrays. The film exhibited tensile strengths up to $\sim$2 GPa and Young's modulus up to $\sim$90 GPa, which is remarkably superior than that of other

Table 1 Various flexible substrates used for the fabrication of flexible solid-state devices and their electrochemical performances

Substrate	Materials	Cell design	Specific capacitance	Cycling stability	Ref.
Ti wire	CNT	Symmetric	1.84 mF cm^{-2} at 1 μA	80% after 1000 cycles	119
Au wire	MnO_2	Asymmetric	12 mF cm^{-2} at 0.3 mA cm^{-2}	90% after 2000 cycles at 0.6 mA cm^{-2}	120
Ni fibres	$Ni(OH)_2$	Symmetric	35.67 mF cm^{-1} at 0.1 mA	70% over 10 000 cycles at 0.5 mA	121
Fibre	MnO_2 nanowire/graphene	Symmetric	66.1 F cm^{-3} at 60 mA cm^{-3}	96% over 10 000 cycles at 0.12 A cm^{-3}	122
Carbon cloth	Activated carbon cloth	Symmetric	161.28 mF cm^{-2} at 12.5 mA cm^{-2}	104% after 30 000 cycles at 12.5 mA cm^{-2}.	123
mCel-membrane	Activated carbon	Symmetric	153 mF cm^{-2} at 10 mV s^{-1}	93.4 after 1000 cycles at 200 mV s^{-1}	124
Carbon cloth	Polyaniline hydrogel	Symmetric	430 F g^{-1} at 5 mV s^{-1}	86% after 1000 at 7.5 A g^{-1}	125
Stainless steel fabrics	Graphene	Symmetric	180.4 mF cm^{-2} at 1 mA cm^{-2}	96.8% after 7500 cycles at 8 mA cm^{-2}	126
Carbon cloth	TiO_2@PANI	Symmetric	775.6 mF cm^{-3} (28.3 F g^{-1}) at 10 mV s^{-1}	97.2% after 10 000 cycles at 100 mV s^{-1}	126
Carbon cloth	$NiCo_2O_4$@CNT/CNT	Asymmetric	—	95% after 5000 cycles at 50 mV s^{-1}	128
Ni Foam	C-$Co_3Si_2O_5(OH)_4$	Asymmetric	352 mF cm^{-2} at 1 mA cm^{-2}	97.3% after 6000 cycles at 4 mA cm^{-2}	129
Carbon fabric	MnO_2//MoO_3	Asymmetric	4.86 mF cm^{-2} at a 0.5 mA cm^{-2}	89% after 3000 cycles at 5 mA cm^{-2}	130
Carbon fabric	MnO_2	Symmetric	—	76.5% after 5000 cycles at 1 mA cm^{-2}	131
PET	$Ti_3C_2T_x$	Symmetric	1.44 F cm^{-3} at 0.288 A cm^{-3}	87% over 1000 cycles at 100 mV s^{-1}	132
Carbon fabric	MnO_2/reduced graphene oxide (RGO)	Symmetric	14 F cm^{-2} (31.8 F g^{-1}) at 2 mV s^{-1}	100% after 5000 cycles at 0.2 mA cm^{-2}	133
Carbon fabric	MoS_2	Symmetric	—	96.5% after 5000 cycles at 0.2 mA	134
PET	SnS/S doped graphene	Symmetric	2.98 mF cm^{-2} at 60 mA cm^{-2}	99% after 10 000 cycles at 120 mA m^{-2}	135
Carbon fabric	MnO_2	Symmetric	0.44 F cm^{-3} (283.9 F g^{-1}) at 0.2 A g^{-1}	83% after 1000 cycles at 0.5 A g^{-1}	136
Carbon fabric	Co_3O_4/vertically aligned graphene nanosheets (VAGNs)	Symmetric	580 F g^{-1} at 1 A g^{-1}	86.3% after 20 000 cycles at 20 A g^{-1}	137
Carbon fabric	CoMn-LDH	Symmetric	—	88.3% after 6000 cycles at 2 A g^{-1}	138*a*
Carbon fabric	Functionalized carbon fabric	Symmetric	134.8 mF cm^{-2} (2.4 F cm^3) at 2 mA cm^{-2}	90% after 5000 cycles at 5 mA cm^{-2}	139
Carbon fabric	$CuCo_2O_4$@MnO_2	Symmetric	714 mF cm^{-2} at 1 mA cm^{-2}	3000 cycles at 2 mA cm^{-2}	140
Carbon fabric	MnO_2	Symmetric	42.4 mF cm^{-2} at 5 mV s^{-1}	96.4% after 2000 cycles at 100 mV s^{-1}	141
Carbon fabric	Cu_7S_4	Symmetric	—	95% after 5000 cycles at 10 mA	142
Carbon textile	ZnS	Symmetric	540 F g^{-1} at 5 mV s^{-1}	96.6% after 5000 cycles at 0.8 mA cm^{-2}	91
Nickel foam	$ZnCo_2O_4$	Symmetric	94 mF cm^{-2} at 0.1 mA cm^{-2}	97.4% after 1400 cycles at 0.5 mA cm^{-2}	72
Nickel foam	MnO_2–CNT–graphene	Symmetric	107 F g^{-1},	—	143
Nickel foam	PPy@LDH core–shell	Asymmetric	88.7 mF cm^{-2} at 20 mA cm^{-2}	115.4% after 20 000 cycles at 20 A g^{-1}	76
Nickel foam	$NiCo_2O_4$	Symmetric	161 mF cm^{-2} at 1 mA cm^{-2}	100% 3000 cycles at 3 mA cm^{-2}	75
Carbon cloth	N/O-Enriched carbon cloth	Symmetric	—	116% 5000 cycles at 5 mA cm^{-1}	144
Commercial textiles	MnO_2/CNT	Symmetric	324 F g^{-1} at 0.5 A g^{-1}	100% 5000 cycles at 10 A g^{-1}	145
Commercial A4-size paper	Graphene sheets	Symmetric	11.3 mF cm^{-2} at 1 mV s^{-1}	—	146
Photo paper	PANI–MnO_x	Symmetric	94.73 mF cm^{-2} at 0.1 mA cm^{-2}	—	147
Xerox printing paper	MnO_2/Au/MnO_2	Symmetric	8.14 mF cm^{-2} (20.35 F cm^3) at 0.2 mA cm^{-2}	88% after 5000 cycles at 100 mV s^{-1}	148
Carbon fiber yarn	MnO_2	Symmetric	—	85% after 10 000 cycles at 0.1 A g^{-1}	149
A4 printing paper	Graphite/polyaniline	Symmetric	77.8 mF cm^{-2} at 0.1 mA cm^{-2}	83% after 10 000 cycles at 1 mA cm^{-2}	150
Filter paper	KCu_7S_4/graphene	Symmetric	—	92% after 5 000 cycles at 0.8 mA cm^{-2}	151

Table 1 (*continued*)

Substrate	Materials	Cell design	Specific capacitance	Cycling stability	Ref.
PET	MnO_x/Au	Symmetric	78.6 F cm^{-3} at 10 mV s^{-1}	74.1% after 15 000 cycles at 1 V s^{-1}	110
PET	Ag/activated carbon	Symmetric	45 mF cm^{-2} at 0.3 mA cm^2	86% after 1200 cycles at 5 mA cm^{-2}	152
PET	Graphene/MWNT	Symmetric	740.9 μF cm^{-2} at 1 μA cm^{-2}	85% after 20 000 cycles at 15 μA cm^{-2}	153
PET	SWCNTs	Symmetric	17.5 F g^{-1} at 2 A g^{-1}	87.5% after 10 000 cycles at 5 A g^{-1}	154
PET	Au/PANI	Symmetric	26.49 mF cm^{-2} (67.06 F cm^{-3}) at 0.5 mA cm^{-2}	72.7% after 1000 cycles at 200 mV s^{-1}	155
Carbon paper	Graphene oxide/ metal–organic framework (GO/MOF)	Symmetric	250 mF cm^{-3} at 6.4 mA cm^{-3}	96.3% after 5000 cycles at 50.4 mA cm^{-3}	156
PET	Au/polyaniline	Symmetric	51.7 mF cm^{-2} at 0.1 mA cm^{-2}	92% after 1000 cycles at 0.2 mA cm^{-2}	157
PET	rGO/PPy	Symmetric	147.9 F cm^{-3} at 5 A cm^3	71.7% after 5000 cycles at 10 A cm^{-3}	158
PET	N-Doped rGO	Symmetric	3.4 mF cm^{-2} at 20 μA cm^{-2}	98.4% after 2000 cycles at 100 μA cm^{-2}	159
PET	MoS_2@$Ni(OH)_2$	Symmetric	14.07 mF cm^{-2} (37.53 F cm^{-3}) at 1 mV s^{-1}	94.2% after 9000 cycles at 1 V s^{-1}	160
PET	rGO/MoO_3	Symmetric	404 F g^{-1} at 0.5 A g^{-1}	80% after 5000 cycles at 2 A g^{-1}	161
Au coated PET	CuSe	Symmetric	30.17 mF cm^{-3} at 0.14 mA cm^{-3}	90% after 10 000 cycles at 0.57 mA cm^{-3}	162
PET	Graphene	Symmetric	56.5 F cm^{-3} at 0.06 A cm^{-3}	—	163
PET	β-$Ni(OH)_2$/graphene	Symmetric	2570 μF cm^{-2} at 0.2 A m^{-1}	98.2% after 2000 cycles at 0.1 A m^{-2}	164
Air-laid paper	PPy	Symmetric	702 mF cm^{-2} at 1 mA cm^{-2}	—	165
PET	Graphene/carbon black nanoparticle	Symmetric	144.5 F g^{-1} at the current density of 0.5 A g^{-1}	—	109
PET or PDMS	Graphene fibres/MnO_2 fibres	Symmetric	42.02 mF cm^{-2} at 0.01 V s^{-1}	92% after 1000 cycles at 1 mA cm^{-2}	166
PDMS	Graphene	Symmetric	4.2 mF cm^{-2} at 0.1 μA	—	167
PDMS	SWCNTs	Symmetric	36.9 F g^{-1} at 10 mV s^{-1}	94% after 500 cycles at 1.25 A g^{-1}	168
Carbon fiber paper	Silver nanoparticle–polyaniline–graphene	Symmetric	142 F g^{-1} at 1.5 A g^{-1}	—	169
Stainless steel	V_2O_5	Symmetric	96 F g^{-1} at 0.5 A g^{-1}	88% after 1000 cycles at 20 mV s^{-1}	170
Carbon nanofibers	$ZnCo_2O_4$//carbon nanofibers	Asymmetric	139.2 F g^{-1} at 2 mV s^{-1}	90% after 3000 cycles at 50 mV s^{-1}	171
Cu foils	Graphene oxide	Symmetric	130 F g^{-1} at 5 mV s^{-1}	—	172
Cu foils	$Cu(OH)_2$//AC	Asymmetric	26.4 F g^{-1} at 4 A g^{-1}	90% after 5000 cycles	70

carbon-based films, including commercial graphite foils, bucky-papers and graphene-related papers (see Fig. 10(a and b)). In addition, the density normalised CNT films (0.9 g cm^{-3}) showed specific tensile strength of around 2000 MPa, which is much greater than that of aluminium foil (483 MPa; density: 2.8 g cm^{-3}) and high-strength steel (AISI 4130 steel; σ: 1110 MPa, 7.85 g cm^{-3}) and comparable with the value for rigid carbon fibre laminate (1600–2000 MPa; density: 1.75 g cm^{-3}). The film can also bear severe bending (even folding) and shows good structural integrity with almost no change in electrical conductivity.

A similar method is adopted to test the flexibility of electrodes supported on flexible substrates, such as paper and PET. The GCP prepared by Weng *et al.*[173b] withstood a stress as high as 8.67 MPa with a 3% elongation. Notably, the GCP strain was also twice as high as that reported for a self-assembled graphite oxide membrane (*ca.* 0.95%). Moreover, increase in resistance was less than 5%, when the strain was as high as 2%, as shown in Fig. 10(c and d). *In situ* change in resistance method was also employed to test GCP electrode flexibility, which showed only 6% increase in resistance of the GCP after 1000 bending cycles at a radius of curvature of about 4 mm. Likewise, El-kady *et al.*[173c] reported hybrid materials based on laser-scribed-graphene (LSG)-MnO_2 on PET substrate for micro-SCs. The change in resistance of electrode was negligible at a bending radius of 5 mm and was completely recovered after straightening during both convex and concave bending (see Fig. 10(e)). Remarkably, the LSG-MnO_2 electrode showed only 2.8% increase in resistance after 1000 cycles of bending and straightening at a concave bend radius of 5.0 mm, demonstrating excellent mechanical integrity under large mechanical deformation.

The mechanical flexibility of FSSC devices is generally evaluated by recording *in situ* electrochemical performance under different mechanical deformations, which we have discussed in each section as appropriate. In this section, we summarised a few of the other methods to evaluate device foldability. Gao *et al.*[173d]

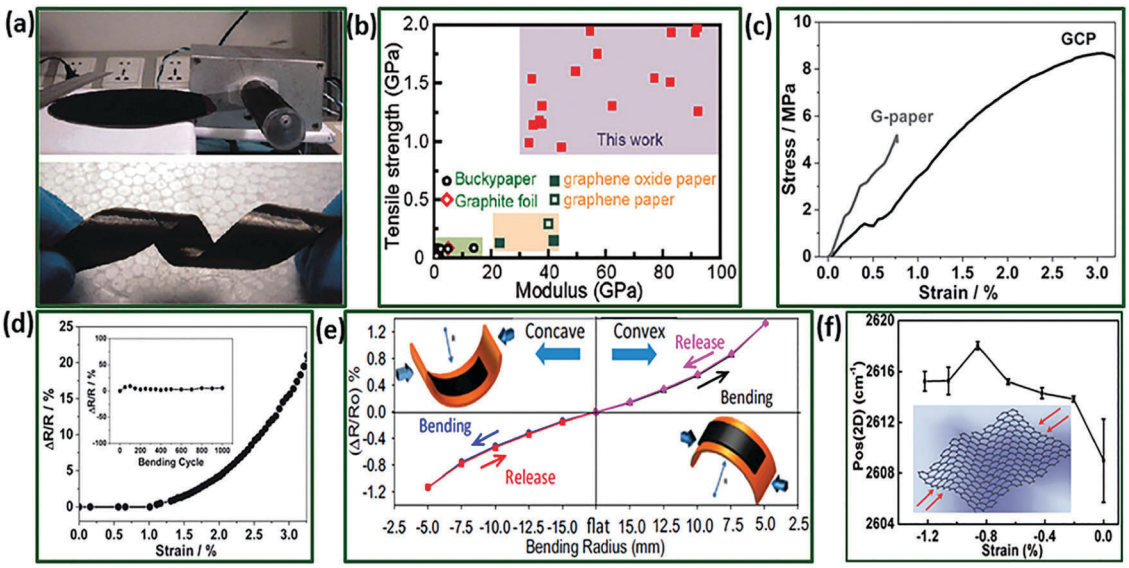

Fig. 10 (a) Experimental setup used for the synthesis of the aligned CNT film with a photograph of flexible CNT film strip in twisted condition. (b) A plot of comparison of flexibility of CNT films with buckypapers, graphite foil, and graphene papers in terms of tensile strength and modulus. Reprinted with the permission from ref. 173*a*, Copyright 2012 American Chemical Society. (c) Stress–strain curves of the graphene cellulose paper (GCP) membrane and graphene (G)-paper. (d) *In situ* variation of resistance of the GCP membrane electrode under different deformations with resistivity changes under repeated bend cycles at a constant radius of curvature of *ca.* 4 mm (inset). Reproduced with the permission from ref. 173*b*, Copyright 2011 Wiley-VCH Verlag GmbH & Co. KGaA, Weinheim. (e) Variation of the resistance of an LSG–MnO_2 electrode as a function of bending radius in concave and convex conditions. Adopted with permission from ref. 173*c*, Copyright 2015 National Academy of Sciences. (f) A plot of variation of Raman 2D peak position as a function of compressive strain in the graphene electrode. Reproduced with the permission from ref. 173*d*, Copyright 2013 American Institute of Physics.

established a unique method through which they recorded Raman 2D peak position at different levels of applied compressive strain using graphene electrodes as shown in Fig. 10(f). They showed that at bending angles (2θ) larger than 40° (strain $>0.86\%$), ripples are generated on the graphene electrodes in compression owing to the weak van der Waals forces between the graphene and the PET substrate. These ripples cause the thickness of the electrical double layer to increase, and hence, capacitance of the compressed device decreases.

Zhang *et al.*,[173e] prepared an interesting architecture of crumpled graphene papers in self-organised patterns using mechanical instabilities in the graphene paper. The idea was that when the substrate would be stretched, the crumpled patterns would unfold, maintaining high reliability of the graphene paper under multiple cycles of large deformation. The FSSCs based on the crumpled graphene papers demonstrated not only good specific capacitance of 28–49 F g^{-1}, but also much larger deformability up to 150% uniaxial strain and 100% × 100% biaxial strain (*i.e.*, 300% areal strain). Using noncapacitive paper or polymer substrates, such as PET and PDMS, increases the volume and weight of the device, which consequently lowers the final performance. In this context, self-standing elastic SCs were designed and assembled using spring-like CNT fibre electrodes where the fibres were twisted in uniform coiled loops.[174a] Flexibility tests were performed by recording electrochemical performance (CV curves) under bending and stretching deformations. The spring-like SC device showed no change in performance at different bending angles (0 to 180°) with 93.5% capacitance retention after 300 bending cycles. Similarly, the cell maintained capacitance at 100% stretching deformation and retained more than 94% capacitance after 300 stretching cycles.

For comfortable electronic devices attachable to the body, energy storage devices should be stretchable to fit the stretchable devices. Highly stretchable micro-SCs were fabricated by designing wave-shaped hybrid MWNTs/PAni electrodes.[174b] The as-assembled stretchable device exhibited a power density of 0.07 mW cm^{-2} at an area energy density of 0.004 mW h cm^{-2}. Owing to the designed wavy electrode structure, the electrochemical features of the stretchable SCs were almost invariable under different stretching deformations from 5% to 40%. It was further demonstrated that the device could power a red LED under different mechanical deformations, such as stretching, twisting, crimping and winding. Recently, Kim *et al.*[174c] developed 3D stretchable SCs using a novel pyramid structure of freestanding CNT films. Remarkably, the devices maintained their electrochemical performance under stretching conditions up to 116% of their initial length along the *x*-, *y*- and *z*-axes. Moreover, the FSSCs exhibited high stability of 93.3% after simultaneous stretching and releasing for 3000 cycles with stretched lengths of 4 mm along the *y*- and *z*-axes. The specific capacitances varied and were less than 7% after stretching to the maximal strain along the *z*-axis for 10 000 cycles.

The flexibility of materials in FSSCs on the support is crucial in addition to that of the substrate. A limited number of investigations have been performed to improve the flexibility of materials and electrolytes.[174d,174e] It is revealed that MnO_2 nanosheets undergo serious strain-induced performance degradation because of their rigid structure, while the performance

of polypyrrole (PPy) is well preserved under strain. Therefore, to enhance tolerance to strain-induced performance degradation of MnO_2 SCs, Huang *et al.*[174d] demonstrated PPy-penetrated MnO_2 nanosheets electrodes. The composite electrode showed a notable enhancement in tolerance to strain-induced performance degradation with well-preserved performance over 93% under strain. In wire-type SCs, the major obstacles emerge from contact failure or a low-adhesion interface between active materials and metal wire/fibre because of the differences in physical properties, leading to breaking and shedding of the active material during assembling and/or a bending test.

This problem can be tackled by adding a buffer layer between active materials and the metal wire to enhance adhesion without sacrificing electrical conductivity. For example, Hu *et al.*[174e] prepared wire-type SCs by wrapping MnO_2 on an Ni wire with multilayer graphene, which is grown directly on the Ni wire, as a buffer layer. The buffer layer effectively eliminated the interface stress and prevented breaking/shedding of the MnO_2. The device showed good electrochemical performance, including length (volumetric) energy density of 0.62 mW h cm^{-1} (0.88 mW h cm^{-3}). Conversely, the electrolyte is another key element that needs to be considered for increasing the stretchability of SCs. The widely used PVA-based electrolytes are neither very stretchable nor compressible therefore, using new electrolytes is highly desirable. Recently, the use of hydrogel polyelectrolyte containing proton-incorporated polyacrylamide (PAM) cross-linked by vinyl hybrid silica nanoparticles (VSNPs) was reported.[174d] Here, the cross-linking VSNPs served as stress buffers to dissipate energy when strain was applied. The prepared polyelectrolyte with PPy–CNTs paper demonstrated excellent electrochemical performance, including high capacitance (equivalent to the highest results obtained with the same electrode), intrinsic super-stretchability (unprecedented 1000% stretch with a 2.6-fold capacitance enhancement) and intrinsic high compressibility (50% compression with 99.4% capacitance retention).

In summary, the foldability of electrodes can be evaluated using the stress–strain curve and *in situ* change in resistance while device flexibility can be tested by *in situ* electrochemical performance under different mechanical deformations. However, very few reports on the effect of deformations on the nanostructure of materials and electrolytes/electrode interface are available. Conducting more investigations, such as *in situ* microscopic analysis, under different mechanical deformations is highly desirable to identify suitable electrode materials and electrolytes, using which stretchable SCs that achieve high performance and show great tolerance to strain can be assembled for developing next-generation stretchable electronics.

5. Recent trends in the development of gel electrolytes

Solid-state electrolytes are key components in SCs and considerably affect electrochemical properties, such as energy density, rate capability and cycling stability.[14,15,20,26] The advantages of SCs based on solid-state electrolytes over those based on conventional liquid electrolytes include easy and inexpensive packaging, simple fabrication steps and no leakage of toxic electrolytes. In addition, solid-state electrolytes provide good mechanical stability, which allows successful assembly of different flexible and bendable SCs in various applications. They also play a dual role in SC devices, such as ionic conducting media and electrode separators. The key to developing high-performance FSSCs is a suitable solid-state electrolyte that exhibits high ionic conductivity; high chemical, electrochemical and thermal stabilities; good mechanical strength; and dimensional stability. Three main types of solid-state electrolytes are used in SCs, namely ceramic electrolytes (CEs),[175a,b] gel polymer electrolytes (GEs)[174c,d] and polyelectrolytes (PE).[174f] Among these, GEs are extensively employed in SCs owing to their relatively high ionic conductivity (10^{-4} to 10^{-3} S cm^{-1} under ambient conditions).[175c,d]

Normally, GEs are composed of a polymeric host (PVA), a solvent as the plasticiser and a conducting electrolytic salt; the polymer serves as a medium that swells in the solvent and the ions travel through the solvent.[175e] Some studies have termed these GEs as quasi-solid-state electrolytes because of the presence of a liquid phase.[176–178] Polymer matrices are also commonly used to prepare GEs for FSCs. These include PVA,[176] poly(methyl methacrylate) (PMMA),[177] poly(polyacrylate) (PAA),[178] poly(amine-ester) (PAE),[179] PEO,[180] polyacrylonitrile (PAN), poly-(ethylene glycol) blending poly(acrylonitrile) (PAN-*b*-PEG-*b*-PAN),[181] poly-(vinylidene fluoride) (PVDF) and poly(vinylidene fluoride-*co*-hexafluoropropylene) (PVDF-*co*-HFP).[182] Conversely, based on the electrolyte salts, the GEs are classified as Li-ion GEs (*e.g.*, LiCl), proton-conducting GEs (*e.g.*, H_2SO_4, H_3PO_4) and alkaline GEs (*e.g.*, KOH). These exhibit a low dissociation energy and provide free/mobile ions. In this section, we discuss current advancements in GEs to develop different-shaped and high-performance FSCs. The section is divided into four subsections: (1) aqueous GEs (AGEs), (2) organic GEs (OGEs), (3) ionic liquid GEs (ILGEs) and (4) redox-active GEs.

5.1 Aqueous gel polymer electrolytes

As specified before, AGEs have been studied extensively for their potential in FSSC application owing to their high ionic conductivity, low cost and nontoxicity. AGEs comprise a host polymer matrix (PVA, PMMS, PAA and PEO), water as a plasticiser and an electrolytic salt that can be a strong acid (H_2SO_4 and H_3PO_3), strong alkali (KOH), or neutral (LiCl, Na_2SO_4). AGEs are also known as hydrogel polymer electrolytes, in which 3D polymeric networks trap water molecules through surface tension. The degree of plasticisation depends on the compositional polymer/plasticiser ratio that affects the AGE glass-transition temperature.

Generally, high-performance FSSCs require good interfacial contact between the electrode and gel electrolyte; thus, the interfacial features of the AGE and electrode materials are key components. PVA has been widely investigated as a polymer matrix for AGEs because of its ease of preparation, high hydrophilicity, good film-forming properties, nontoxic characteristics

and low cost.[183] Conversely, the selection of the electrolyte salt generally depends on the electrode materials. Several neutral AGEs, such as PVA/LiCl,[184] PVA/Na_2SO_4[185] and PVA/$NaNO_3$,[186] have been investigated as promising electrolytes for FSSCs for different electrode materials. For instance, Li *et al.*[187] developed a neutral AGE with PVA as the polymer host, LiCl as the electrolyte and water as the plasticiser for CNF-based films. The resultant symmetric device could be cycled reversibly in a wide voltage window of 1.8 V with a specific capacitance of 137.5 F g^{-1} at a scan rate of 5 mV s^{-1}. Moreover, ~93.1% capacitance retention was observed with almost constant coulombic efficiency over 5000 cycles at 1 A g^{-1}, demonstrating ideal movement of charge carriers and excellent electrochemical capacitive behaviour.

Subsequently, a practical demonstration was provided by fabricating internal series-connected SCs that afforded an extended voltage range up to 3.6 V. The Nyquist plot suggested that the equivalent series resistance (R_s) of the device was 3.35 Ω, illustrating the excellent effective interfacial area of active materials for the electrolyte and low internal resistance of the series-connected device. Thus, this neutral LiCl/PVA AGE effectively suppressed the chemical dissolution and irreversible electrochemical oxidation reaction of the electrode and mechanically stabilised the electrode during cycling. Similarly, PVA/LiCl AGE was recently used in a polypyrrole/carbon quantum dot (PPy/CQD) composite material synthesised on carbon cloth.[188] The device exhibited good capacitance (315 mF cm^{-2}) and good cycling stability (85.7% after 2000 cycles at 2 mA cm^{-2}). Other PVA-based neutral electrolytes, such as PVA/$LiNO_3$ and PVA/LiOH, have been developed to enhance the intercalation/deintercalation performance of metal oxide and polymer electrodes.[184,189] Notably, for some electrode materials, such as vanadium oxide and vanadium nitride (VN), the AGEs provided greatly enhanced cycling stability over aqueous electrolytes, suggesting the importance of interfacial contacts between the electrode and AGE electrolyte. In addition to PVA-based Li-ion AGEs. Lian *et al.*[190] have recently developed a polyacrylamide–LiCl (PAM/LiCl) AGE for CNT-coated graphite electrodes. The as-prepared PAM/LiCl AGE exhibited an amorphous structure with excellent ionic conductivity (<10 mS cm^{-1}). Moreover, this neutral electrolyte system exhibited a high overpotential for both hydrogen and oxygen evolution reactions, providing a wide voltage window of 1.5 V for the CNT-graphite-based symmetric cell. The device also displayed excellent cycling stability with 90% capacitance retention over 10 000 cycles and excellent rate capability up to 5 V s^{-1}.

The higher mobility of protons compared with that of Li^+ ions shows great promise for transporting charges at ultrafast rates during charge/discharge processes in SCs. The proton-conducting AGEs are prepared by mixing a polymer matrix with water (plasticiser) and proton-donor salts, such as H_3PO_4 and H_2SO_4. To date, many proton-conducting AGEs, including PVA/H_3PO_4[191] and PVA/H_2SO_4,[192] have been investigated. These AGEs exhibit ionic conductivities ranging from 10^{-4} to 10^{-2} S cm^{-1} at ambient temperature. Normally, proton-conducting AGEs are applied to carbon-based materials, such as graphene,[193] CNTs,[87] graphene ribbons,[194] AC cloths[195] and graphene/porous carbon aerogels.[196] These advanced carbon nanostructures facilitate proton transport into the porous electrodes, suggesting enhancement in electrochemical performance and high utilisation of active materials. Recently, Chen *et al.*[197] tested different electrolytes (H_2SO_4, H_3PO_4, KOH, NaOH, KCl and NaCl) with a PVA-based AGE for application to graphene-based FSCs. Electrochemical analyses suggested that the PVA/H_3PO_4 AGE exhibited a relatively high capacitive performance. Lian *et al.* developed a novel proton-conducting heteropoly acid AGE for high rate SCs.[198,199] For example, the SiWA/PVA/H_3PO_4 AGE developed for a graphite-based device exhibited excellent performance and shelf life.[198] Compared with Nafion, the SiWA/PVA/H_3PO_4 gel electrolyte displayed significantly higher conductivity, achieving a value of 8 mS cm^{-1} at room temperature. Moreover, the as-assembled device was successfully charged/discharged at a very high rate (20 V s^{-1}) with a time constant of 10 ms. To improve the environmental stability of the SiWA/PVA/H_3PO_4 gel electrolyte further, nano-SiO_2 was incorporated into the AGE.[200] In gel electrolytes, SiO_2 can function as a plasticiser, cross-linker and water-retaining agent.[201] The addition of SiO_2 in SiWA/PVA/H_3PO_4 significantly enhanced water retention and displayed consistent proton conductivity (16 mS cm^{-1}) over the parent gel electrolyte. It also exhibited a cross-linking effect on the PVA polymer. The symmetric cell was assembled from SS foils as electrodes and a nano-SiO_2-incorporated SiWA/PVA/H_3PO_4 AGE and demonstrated a high rate capability of 5000 V s^{-1} in CV curves with good environmental stability and excellent cycle life (up to 100 000 cycles).

Similarly, Lian *et al.* developed another heterpoly acid AGE based on PVA and phosphotungstic acid ($H_3PW_{12}O_{40}$, PWA) and applied it to an asymmetric cell based on graphite and RuO_2.[202] The PVA/PWA electrolyte provided a wide voltage window of 1.5 V and also contributed extra capacitance through the pseudocapacitance of the electrochemical reactions. Thus, the PVA–HPA electrolyte shows great promise for application in both symmetric and asymmetric FSCs owing to its good ionic conductivity and stability. Recently, $H_5BW_{12}O_{40}$ (BWA)/PVA was developed as an effective electrolyte for FSSCs based on CNT-graphite electrodes and its electrochemical properties were compared with those of the SiWA/PVA electrolyte.[203] The comparison of BWA and SiWA (Fig. 11(a)) suggests that except for the central atoms, the overall structures of both are the same. The electrolytes exhibited an ionic conductivity trend of BWA (78 mS cm^{-1}) > SiWA (60 mS cm^{-1}) > H_2SO_4 (30 mS cm^{-1}) as illustrated in Fig. 11(b). Because of the high ionic movements and number of dissociated ions, the device with the BWA/PVA electrolyte exhibited high capacitance. Moreover, this device was successfully cycled in a wide voltage window of 1.6 V (higher than that of the SiWA/PVA electrolyte at 1.4 V) while maintaining its high proton conductivity. It also displayed a very stable performance with no significant decay in capacitance after 5000 cycles (Fig. 11(c)). Several other polymer matrices have been investigated. Kim *et al.*[204] tested the electrochemical performance of RuO_2-based FSSCs using different acrylic hydrogel electrolytes, such as poly(acrylic acid) (PAA), potassium polyacrylate (PAAK)

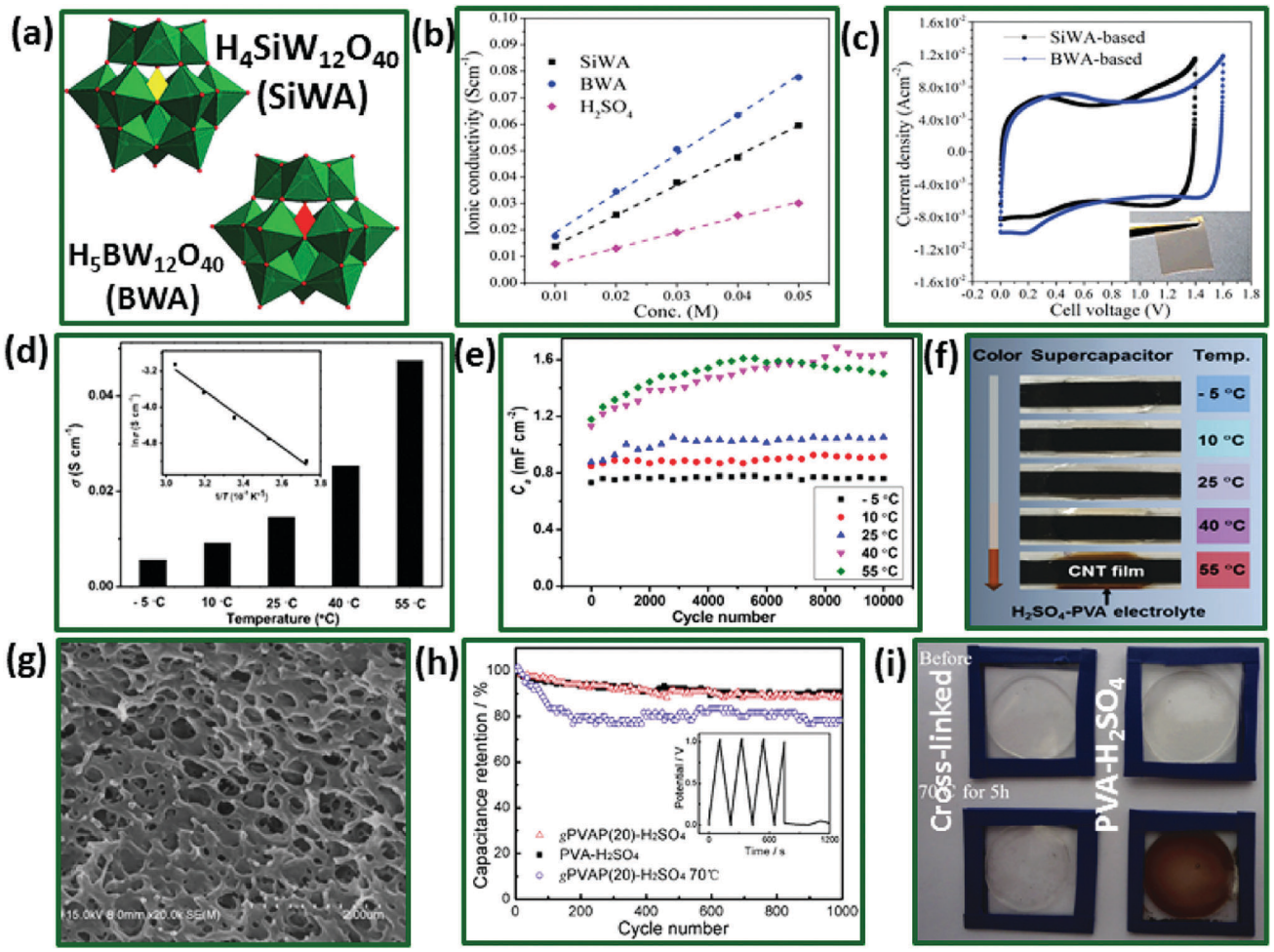

Fig. 11 (a) Structures of SiWA and BWA heteropolyacids, adopted with the permission from ref. 203*a*, Copyright 2016, Royal Society of Chemistry. (b) Ionic conductivities of SiWA, BWA, and H_2SO_4 at different electrolyte concentrations (c) CVs curves of CNT–graphite electrodes with SiWA- and BWA-based gel electrolytes at 1 V s^{-1}, inset shows a picture of a polymer electrolyte film. Reprinted with permission from ref. 203*b*, Copyright 2015, Royal Society of Chemistry. (d) Ionic conductivities of H_2SO_4–PVA electrolyte at various temperatures with corresponding plot of log σ *vs.* 1/*T*. (e) Variations in areal specific capacitances of CNTs and H_2SO_4–PVA with cycle number at different temperatures. (f) Change in the colour of cells after 10 000 cycles at different temperatures, suggesting aging of electrolyte. Reprinted with permission from ref. 205, Copyright 2017, Elsevier. (g) Cross-sectional SEM image of cross-linked H_2SO_4–PVA gel–electrolyte (h) cycling stability of graphene/carbon black electrode with and without cross-linked H_2SO_4–PVA gel–electrolyte at room temperature and 70 °C. (i) Photographs of with and without cross linked H_2SO_4–PVA gel–electrolytes before and after thermal treatment at 70 °C for 5 h. Reprinted with permission from ref. 109, Copyright 2014, Elsevier.

and poly(2-acrylamido-2-methyl-1-propanesulfonic acid) (PAMPS). They discovered that the capacitance of RuO_2 decreased in the following trend: PAMPS/H_2O > PAA/H_2SO_4 > PAAK/H_2SO_4 > PAMPS/H_2SO_4. Moreover, owing to the favourable proton hosting in the PAMPS side chain, RuO_2-based SCs with PAMPS exhibited a relatively high specific capacitance.

PVA-based electrolytes exhibit fluidity and thermal ageing problems at high temperatures. Recently, Chen *et al.*[205] investigated the effect of temperature (between −5 °C and 55 °C) on the electrochemical performance of CNT-based FSCs with a PVA/H_2SO_4 gel electrolyte. They observed that the conductivity of the gel electrolyte increased (from 5.52 mS cm^{-1} to 46 mS cm^{-1}) with an increase in temperature (Fig. 11(d)). Consequently, the capacitance was also enhanced with an increase in temperature because of the reduction in internal resistance *via* the acceleration of electrolyte ion transport/adsorption and surface modification of the electrode. About 24.3% and 32.6% enhancement was observed when the temperature changed from −5 °C to 25 °C and 25 °C to 55 °C, respectively, at 0.2 mA cm^{-2}. It was further concluded that the PVA-based gel electrolyte exhibited excellent cycling stability at low temperatures but was not suitable at temperatures >40 °C owing to ageing of the electrolyte (Fig. 10(e)). The digital photograph of the device at 55 °C displayed a colour change in the PVA–H_2SO_4 gel electrolyte from transparent to brown, suggesting such ageing, as shown in Fig. 10(f). To limit the fluidity of the PVA-based gel electrolytes at high temperatures, Fei *et al.*[109] developed a cross-linked PVA/H_2SO_4 hydrogel (SEM image in Fig. 11(g)). The PVA/H_2SO_4 membrane was modified by poly(vinyl pyrrolidone) (PVP) as a pore-forming agent to enhance its swelling ratio in the H_2SO_4 electrolyte; glutaraldehyde (GA) was employed as cross-linking agent. The ionic conductivity of the cross-linked PVA/H_2SO_4

electrolyte was determined as 24.9 mS cm^{-1} at 20 °C and further increased with an increase in temperature. The as-fabricated cell with a graphene/CB nanocomposite electrode and cross-linked PVA/H_2SO_4 gel electrolyte exhibited good cycling stability with 78.3% capacitance retention after 1000 cycles at a high temperature of 70 °C (Fig. 11(h)). The photographs did not display any significant change in the colour of cross-linked PVA/H_2SO_4 gel, while the bare PVA–H_2SO_4 turned brown suggesting ageing at high temperatures (Fig. 11(i)).

With recent advancements in alkaline rechargeable batteries and SCs, the development of alkaline GEs is of great importance.[206] Among the different electrolyte salts, KOH is by far the most widely investigated salt for OH^- ion-conducting AGE application, because of its low-cost and environmentally friendly nature.[207] Several noteworthy investigations on KOH-based gel electrolytes for FSSCs have been reported.[208] For instance, Yang *et al.* prepared a PVA/KOH gel electrolyte for SCs as well as Ni–MH and Zn–air batteries.[209] These alkaline PVA/KOH electrolytes exhibited a high ionic conductivity of 10^{-2} S cm^{-1}. Similarly, Zhang *et al.*[210] developed self-standing α-Fe_2O_3/rGO hybrid films by a vacuum filtration method and assembled symmetric FSSCs with a PVA/KOH gel electrolyte. The device exhibited a high volumetric capacitance of 16.45 F cm^{-3}, leading to an energy density of 1.46 mW h cm^{-3} and a power density of 199.8 mW cm^{-3}. In addition, the device with the AGE displayed excellent flexibility with almost no change in capacitance, even when the cell was bent to 180°. Similarly, Lewandowski *et al.*[211] developed a PEO/KOH gel electrolyte and reported good ionic conductivity ranging from 10^{-4} to 10^{-3} S cm^{-1} by controlling the PEO/KOH/water ratio. To further improve the ionic conductivity of the PVA/KOH gel electrolyte, additives or fillers, such as SiO_2[212] and GO,[213] were incorporated. Thus, to improve ionic conduction, Huang *et al.* incorporated electrically insulating GO in a boron cross-linked PVA/KOH gel electrolyte for AC-based SCs. They discovered that at low levels of GO doping, the ionic conductivity of the cross-linked PVA/KOH gel increased (from 100 to 200 mS cm^{-1}), while high GO doping afforded a decreasing trend. This decrease in ionic conductivity with an increase in GO doping was attributed to ion channel blocking owing to aggregation of the GO nanosheets. Interestingly, the device with GO-doped boron cross-linked PVA/KOH exhibited 29% higher specific capacitance than that with the parent KOH aqueous electrolyte. Various investigations with KOH as salt and different polymer matrices as host, such as poly(epichlorohydrin-*co*-ethylene oxide) P(ECH-*co*-EO)/KOH,[214] PEO/KOH[215] and PAAK/KOH,[216] have been reported.

Despite significant advancements in KOH-based alkaline gel electrolytes, these compounds still exhibit KOH crystallisation under ambient conditions, suggesting environmental instability. The performance of SCs with PVA/KOH gel electrolytes degrades considerably over time because of the hydration of the KOH/PVA electrolyte.[217] To tackle the issue of environmental instability, Li and Lian[218] replaced KOH with tetraethylammonium hydroxide (TEAOH). Moreover, OH^- ion transportation in the polymer matrix depends on the crystallinity, hydrophilicity and functional group electronegativity of the polymer hosts. Thus, different polymer host matrices, such as PVA, PEO and PAA, were tested to check their compatibility with TEAOH and achieve a gel electrolyte with high ionic conductivity TEAOH–PVA- and TEAOH–PAA-based SCs achieved ionic conductivity of 5 mS cm^{-1} and an ultrahigh rate of 5000 V s^{-1} that was attributed to the amorphous nature of TEAOH–PVA and TEAOH–PAA polymers with high water content (12% and 46%, respectively). Moreover, no significant change in ionic conductivity was observed after six weeks of shelf storage, suggesting excellent environmental stability.

5.2 Organic gel electrolytes

GEs are promising candidates for FSSCs; however, their narrow operating voltage window limits their wide application. The focus has therefore shifted to OGEs. The synthetic strategy for OGEs plays an important role in determining the mechanical properties and ionic conductivity of the systems. Generally, an OGE comprises a physical blend of a high molecular weight polymer (*e.g.*, PMMA and PVDF–HFP) gelated with a conducting salt dissolved in a nonaqueous solvent. Such OGEs overcome low interface formation and improve ionic conductivity. Organic solvents, such as propylene carbonate (PC),[177] ethylene carbonate (EC), dimethyl formamide (DMF)[219] and their mixtures (PC–EC[220] and PC–EC–DMC[221]), have been used as common plasticisers to improve the working voltage range. Thus, the cell voltage was increased to 2.5–3 V,[222] a value that is significantly higher than that observed for AGE-based cells. This increase in cell voltage consequently improves the device energy density.[223]

For example, Huang *et al.*[224] developed an OGE using a PEO–PAN blend (PAN-*b*-PEG-*b*-PAN) as host, DMF as plasticiser and $LiClO_4$ as an electrolytic salt for an AC-based SC. This OGE exhibited an ionic conductivity of 6.9 mS cm^{-1} and excellent compatibility with carbon electrodes. The fabricated cell exhibited a capacitance of 101 F g^{-1} at 0.125 A g^{-1} and delivered an energy level of 11.5 W h kg^{-1} at a high power of 10 kW kg^{-1} over a voltage window of 2.1 V. Moreover, the cell displayed good stability with very small decay in capacitance over 30 000 cycles. The ionic conductivity is strongly influenced by the electrolyte salt and salt/host polymer ratio.[225] Thus, several different salts, such as $LiClO_4$,[226] $LiPF_6$[227] and $TBAPF_6$,[228] have been investigated in OGEs. For instance, Ramasamy *et al.*[229] investigated two different OGEs, namely, PEO/PC-sodium bis(trifluoromethanesulfonyl)imide (NaTFSI) and PEO/PC–EC–DMC–NaTFSI, for use in AC-based SCs. Both gel electrolytes exhibited good ionic conductivity (0.54 mS cm^{-1} and 0.76 mS cm^{-1}, respectively), while the mixed gel electrolyte displayed higher ionic conductivity and thus better electrochemical performance. Moreover, the cells operated in a wide voltage window of 2.5 V with high specific capacitance and good efficiency at a low charge rate (specific capacitance: 24 F g^{-1}; power: 0.52 kW kg^{-1}; energy density: 18.7 W h kg^{-1}).

Other alkali metal ions, such as Mg, have been investigated in OGEs.[230] To improve ionic conductivity, Jain *et al.*[231] incorporated SiO_2 particles into a PVDF–HFP/$Mg(ClO_4)_2$–PC electrolyte

for carbon-based SCs. The resulting OGE exhibited ionic conductivity of 5.4 mS cm^{-1} at room temperature as well as good mechanical and dimensional stability. Although these OGEs performed better than dry polymer electrolytes in terms of ionic conductivity, their mechanical stability was generally compromised. Therefore, considerable effort has been made to improve the mechanical stability of OGEs with particular interest in mimicking the liquid-like electrode–electrolyte interface.[232] An interesting new strategy to prepare high ionic conducting and mechanically stable OGEs has recently been proposed in which a liquid electrolyte ($LiClO_4$/PC) is entrapped in a poly(2-hydroxy-3-phenoxypropyl acrylate) matrix *via* an *in situ* polymerisation method.[233] Thus, this new OGE integrates the qualities of liquid, dry polymer and quasi-solid electrolytes in a single system. Moreover, it entrapped ~80% (v/v) of the liquid electrolyte (3 M $LiClO_4$/PC) and had ionic conductivity of 4.7 mS cm^{-1}, comparable to those of nonaqueous liquid electrolytes. Large-scale FSSC cells (area 16 cm^2) with high AC and OGE mass loading (4 mg cm^{-2}) were designed and these demonstrated a capacitance of 111 F g^{-1} at a current density of 1 mA cm^{-2} in a potential window of 2.5 V, indicating the industrial potential of the system.

5.3 Ionic liquid-based gel polymer electrolytes

Ionic liquid-based gel electrolytes exhibit some additional advantages over aqueous and organic electrolytes, including high ionic conductivities, nonvolatility, nonflammability and wide potential windows (up to 3.5 V); therefore, they are considered suitable for use in flexible and stretchable energy storage devices. Several ILGEs have been investigated for use in FSSCs,[234] with the ILGE properties (conductivity and working voltage window) relying on the nature of the IL and polymer host matrix. Similar to AGE and OGE, various polymer hosts were investigated for ILGE, including PVDF–HFP,[235] PVA[236] and PEO.[237] Recently, Tamilarasan *et al.*[238] prepared an ILGE using 1-butyl-3-methylimidazolium bis(trifluoromethylsulfonyl)imide as supporting electrolyte and PAN as polymer host (PAN/[BMIM][TFSI]). This electrolyte exhibited an ionic conductivity of 2.42 mS cm^{-1} at ambient temperature along with good mechanical strength and thermal stability. The graphene-based FSSC comprising the PAN/[BMIM][TFSI] ILGE displayed a maximum energy density of 32.3 W h kg^{-1} and power density 82 kW kg^{-1} with good cycling stability.

Zhang *et al.*[239] developed a flexible ILGE using 1-butyl-3-methylimidazolium chloride (BMIMCl) as ionic liquid, Li_2SO_4 as additive and PVA as polymer host. The afforded ILGE presented a high ionic conductivity of 37 mS cm^{-1} and high fracture strain at 100% elongation. Moreover, the fabricated FSSC with AC as electrode and a PVA–Li_2SO_4:BMIMCI gel electrode displayed a maximum energy density of 10.6 W h kg^{-1} and a power density of 3400 W kg^{-1}. Notably, the ionic conductivity remained stable even after bending at an angle of 180°. To improve the conductivity of the gel electrolyte, Yang *et al.*[240] made two major contributions by preparing GO-doped ILGEs, such as with (PVDF–HFP) as the polymer matrix, the ionic liquid 1-ethyl-3-methylimidazolium tetrafluoroborate ($EMIMBF_4$) as the supporting electrolyte and GO as the ionic conducting promoter. The ionic conductivity for 1 wt% GO-doped (PVDF–HFP)–$EMIMBF_4$ ILGE was determined as ~25 mS cm^{-1}, which was attributed to the 3D distribution of the GO network throughout the gel that acts as an ion 'highway' to facilitate ionic transportation. Interestingly, the device based on the AC electrode and (PVDF–HFP)–$EMIMBF_4$ ILGE displayed an energy density of 32.4 W h kg^{-1} at a power density of 6.6 kW kg^{-1}, suggesting excellent performance.

For patterned MSCs, it is important to select a polymer that can be patterned easily on any substrate. Poly(ethylene glycol) diacrylate (PEGDA) is a nondegradable hydrophilic polymer that in an ILGE can be patterned on any substrate using a photolithographic process.[241] Kim *et al.*[242] developed an ILGE using 1-ethyl-3-methylimidazolium bis(trifluoromethylsulfonyl)-imide ([EMIM][TFSI]) as IL electrolyte and PEGDA as polymer host. The afforded ILGE presented an ionic conductivity of 9.4 mS cm^{-1} at room temperature and demonstrated excellent electrochemical performance when used in CNT-based FSCs. The flexible MSC exhibited a stack capacitance of 5.3 F cm^{-3} at a scan rate of 10 mV s^{-1} and an energy density of 2.9 mW h cm^{-3} at a power density of 50 mW cm^{-3} and a high potential window of 2 V. Moreover, it exhibited excellent cyclability with ~80% capacitance retention over 30 000 cycles. However, the preparation of an IL-gel electrolyte with high ionic conductivity and good mechanical properties is still challenging. Zhong *et al.*[243] prepared a cross-linked [EMIM][TFSI] ionic liquid with PEO and benzophenone (Bp) followed by ultraviolet (UV) irradiation. The resultant [EMIM][TFSI]-based ILGE exhibited an ionic conductivity of 6.7 mS cm^{-1} with a high capacitance of 70.84 F g^{-1}, a wide and stable electrochemical window of 3.5 V and an energy density of 30.13 W h kg^{-1}.

An ideal IL-gel electrolyte should exhibit good compressive stress, good tensile strength and puncture resistance. Liu *et al.*[244] developed an IL-mask hybrid gel electrolyte using $BMIMBF_4$ as ionic liquid, *N*,*N*-dimethylacrylamide (DMAA) and methylene-bis-acrylamide as polymer host, and TiO_2 nanoparticles. These nanoparticles initiated *in situ* polymerisation through UV irradiation to form a hybrid ILGE that comprised the high mechanical strength of the masked substance and the good thermal characteristics of the ILGE. The fabricated FSC exhibited a stable capacitive performance, even under a high pressure of 3236 kPa. Moreover, owing to the good thermal stability of the composite gel electrolyte, the FSSC comprising an AC electrode could be operated at high temperatures ranging from 25 °C to 200 °C.

Many pseudocapacitive materials require proton conducting gel electrolytes, such as RuO_2, PANi and PPy.[245] In this respect, Lian *et al.*[246] developed protic ionic liquids (PILs) and binary systems of PILs with different cations and PIL eutectic compositions. Three PILs, namely 1-ethyl-3-methylimidazolium hydrogen sulfate ($EMIHSO_4$), 1-methylimidazolium hydrogen sulfate ($MIHSO_4$) and imidazolium hydrogen sulfate ($ImHSO_4$), were prepared. The ILGEs comprising $EMIHSO_4$–$MIHSO_4$ and $EMIHSO_4$–$ImHSO_4$ binary mixtures with a PEO polymer host exhibited ionic conductivities of 1.7 mS cm^{-1} and 2.5 mS cm^{-1}, respectively.

Moreover, the eutectic binary PIL mixtures exhibited a liquidus range from −70 °C to +150 °C. The specific capacitances of the RuO_2-based cell using $MIHSO_4$–$ImHSO_4$, $EMIHSO_4$–$ImHSO_4$ and $EMIHSO_4$ were determined as 67 mF cm^{-2}, 44 mF cm^{-2} and 26 mF cm^{-2}, respectively, suggesting a higher proton contribution of the MI and Im cations (over that of EMI) to the electrochemical oxidation and reduction of RuO_2. Similarly, Gao *et al.*[247] prepared a 1-ethyl-3-methylimidazolium bis(trifluoromethylsulfonyl)imide–poly(vinylidene fluoride)-hexafluoropropylene {[EMIM][NTf2]–PVdF(HFP)} ILGE and applied it to MnO_2/CNT/carbon nano-onions. The FSSCs exhibited an energy density of 16.4 W h kg^{-1} at a power density of 33.3 kW kg^{-1} when using the [EMIM][NTf2]–PVdF(HFP) gel electrolyte. Moreover, these SCs exhibited high electrochemical performance under large mechanical stress, making the devices suitable for application to flexible electronics.

5.4 Redox-active gel electrolytes

An emerging strategy to improve the electrochemical performance of a device is to modify/add redox-active species to the electrolyte to maximise the capacitance and consequently the energy density of the device. Redox additives can add extra pseudocapacitance through reversible faradaic reactions and fast electron transfer at the electrode–electrolyte interface, resulting in significant enhancement of the specific capacitance.[248] A typical charge storage mechanism in a redox-active electrolyte is presented in Fig. 12(a) using potassium iodide (KI) as an example. Notably, the iodide can produce redox pairs (I^-/I_3^- and I_2/IO_3^-) during the electrochemical process. The ionic sizes of I^-, I_3^- (I_3^- solvated by four water molecules) and IO_3^- (IO_3^- solvated by three water molecules) are 0.39 nm, 0.63 (1.8) nm and 0.57 (1.4) nm, respectively.[249] Thus, because of their small ionic sizes, these ions can easily access the micropores and small mesopores of the porous electrode.

Numerous redox couples, such as iodides (KI),[183,250] $K_3Fe(CN)_6$[251] and Na_2MoO_4;[252] organic redox mediators, such as hydroquinone,[253] P-phenylenediamine (PPD)[254] and p-benzenediol;[250] and methylene blue (MB);[255] anthraquinone-2,7-disulfonate (AQDS);[256] and indigo carmine (IC)[257] have been investigated in solid-state gel electrolytes (Fig. 12(b–e)). This approach of adding redox-species in gel electrolytes effectively improves the performance of the device. Feng *et al.*[258] prepared a bromamine acid sodium (BAAS)-doped PVA–H_2SO_4 gel electrolyte that presented good ionic conductivity (21.4 mS cm^{-1}). The FSSC device assembled with AC electrodes displayed a good energy density (30 W h kg^{-1}) for PVA–H_2SO_4–BAAM that was almost twofold higher than that without BAAM doping. They also investigated the redox additive 1-anthraquinone sulfonic acid sodium (AQQS) incorporated with a PVA–H_2SO_4 gel electrolyte.[259] The resultant redox-gel electrolyte exhibited excellent mechanical strength and a high ionic conductivity of 28.5 mS cm^{-1}. Notably, the device exhibited a remarkably stable capacitive performance with the gel electrolyte, even under a large tensile strain (100%), a high pressure of 2000 kPa and fold states.

In our previous investigation, we demonstrated a double hybrid strategy using hybrid electrodes (rGO–POMs, such as PMo_{12} and PW_{12}) and a hybrid electrolyte (HQ-doped PVA–H_2SO_4 gel electrolyte).[260] The symmetric cells based on rGO–PMo_{12} and rGO–PW_{12} could be reversibly cycled in a wide voltage window of 1.6 V and exhibited energy densities of 1.7 mW h cm^{-3} and 2.38 mW h cm^{-3}, respectively; these values are double those

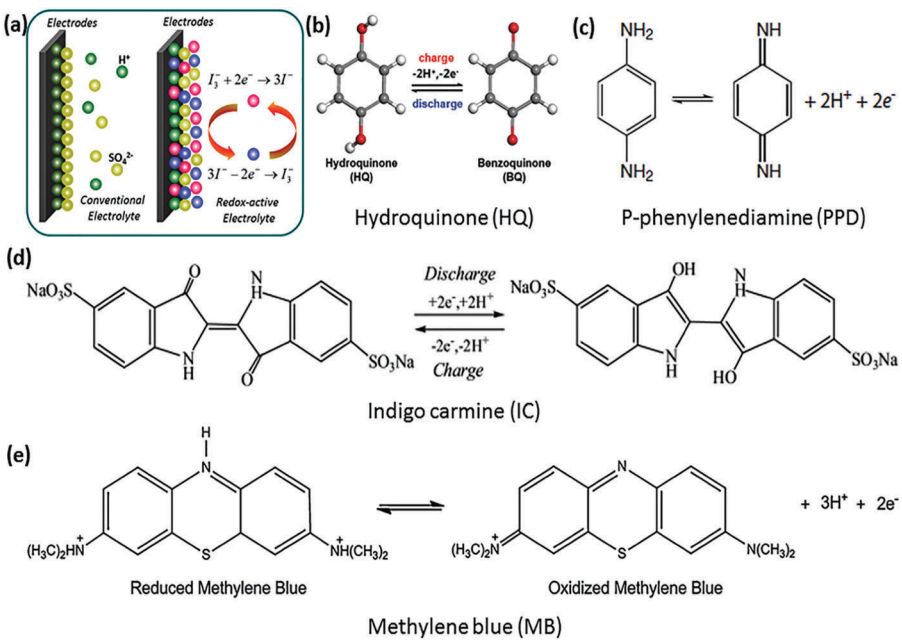

Fig. 12 (a) Schematics illustration of charge storing mechanism in conventional and redox-active electrolytes (*e.g.* KI). Reaction mechanisms of different organic redox-active electrolytes during charge/discharge process (b) hydroquinone (HQ) (c) *p*-phenylenediamine (PPD) (d) indigo carmine (IC) and (e) methylene blue (MB).

afforded in the absence of the HQ electrolyte. Yarn and fibre SCs have gained considerable attention for application in wearable applications. Pan *et al.*[261] assembled a CNT–mesoporous carbon (CNT–MC) fibre SC using a 2-mercaptopyridine (PySH)-doped PVA–H_2SO_4 gel electrolyte. The resulting FSC, based on two aligned CNT–MC hybrid electrodes with a redox-gel electrolyte, exhibited excellent capacitances (length, areal and volumetric capacitances of 17.51 mF cm^{-1}, 507.02 mF cm^{-2} and 184.37 mF cm^{-3}, respectively) that were nine times higher than those afforded in the absence of PySH.

Kim *et al.*[262] utilised a *p*-nitroaniline-doped PVA–KOH (PVA–KOH–PNA) gel electrolyte in an asymmetric cell with SiC/Fe_3O_4 negative and SiC positive electrodes. Notably, the unique integration of hybrid electrode materials with a redox-active gel electrolyte into a single device manifested several excellent features, such as good specific capacitance (97.6 F g^{-1} at a scan rate of 5 mV s^{-1}) and good rate capability (72.58% retention after increasing the scan rate from 5 to 500 mV s^{-1}). Moreover, the cell could deliver an enhanced energy of 48.94 W h kg^{-1} at a power density of 463.64 W kg^{-1} and excellent mechanical flexibility. Similarly, the specific capacitance of a fibre SC based on RGO exhibited a threefold improvement on using sodium molybdate (Na_2MoO_4) as a redox-active electrolyte.[263] The molybdate species (MoO_4^{2-}) form polymeric ions (H_2MoO_4) in an acidic medium (PVA/H_3PO_4 gel electrolyte) with a +VI oxidation state. H_2MoO_4 can react with H^+ ions *via* Mo(VI)/Mo(V) and Mo(VI)/Mo(IV) as possible redox couples.

To increase the operation cell voltage, Zhang *et al.*[264] investigated two redox mediators, namely ferrocene (fc) and 4-oxo-2,2,6,6-tetramethylpiperidinooxy (4-oxo-TEMPO), with a tetraethylammonium tetrafluoroborate/PMMA-PC gel electrolyte for PEDOT-based SCs. The resultant gel exhibited ionic conductivities of 1.89 and 1.73 mS cm^{-1}, respectively, suggesting that the introduction of a redox mediator also improves the gel electrolyte ionic conductivity. The maximum energies and power densities for fc- and 4-oxo TEMPO-based OGEs were determined as 27.4 W h kg^{-1} and 17.3 kW kg^{-1}, and 20.8 W h kg^{-1} and 14.8 kW kg^{-1}, respectively. Zhou *et al.*[265] developed a PEO/$LiClO_4$-acetonitrile organic gel with two different redox mediators, NaI/I_2 and $K_3Fe(CN)_6$/$K_4Fe(CN)_6$. The cells with NaI/I_2 and $K_3Fe(CN)_6$/$K_4Fe(CN)_6$ could deliver specific energy densities of 49.1 W h kg^{-1} and 33.6 W h kg^{-1}, respectively. Recently, Kim *et al.* fabricated flexible MSCs using an OGE with a redox-active species (HQ) based on PMMA–PC–$LiClO_4$ and MWCNTs on a PET substrate.[266] Incorporating HQ significantly enhanced MSC specific capacitance and energy density, with the latter being ~35-fold higher than that of MSCs without HQ.

As described in Section 5.3, ILGEs are of special interest in the FSSC field owing to their wide voltage window, inflammability and good flexibility. Jang *et al.*[267] prepared a redox-active $EMIMBF_4$–IL-incorporated PVA–H_3PO_4 gel electrolyte and investigated the ionic conductivity of the PVA/H_3PO_4/IL-gel polymer electrolyte at various $EMIMBF_4$ weight percentages. They discovered that the ionic conductivity of the GE increased with an increase in $EMIMBF_4$ inclusion from 27.3 mS cm^{-1} (PVA/H_3PO_4) to a maximum of 39.3 mS cm^{-1} for 100 wt% $EMIMBF_4$ addition. The improved ionic conductivity was attributed to the plasticising effect of the ionic liquid. The incorporation of $EMIMBF_4$ in the PVA/H_3PO_4 electrolyte effectively increased the specific capacitance of the AC-based FSC to 271 F g^{-1} at 0.5 A g^{-1}, a much higher value than that of the bare PVA/H_3PO_4 cell (103 F g^{-1}). Moreover, the FSC with the PVA/H_3PO_4/$EMIMBF_4$ (50%) electrolyte exhibited high energy and power density values of 54.3 W h kg^{-1} and 23.88 kW kg^{-1}, respectively.

In summary, this section described the benefits and disadvantages of using different GEs, namely aqueous, organic, ionic liquid and redox-active species-based gel electrolytes. It revealed that different parameters, such as ionic conductivity, nature of electrolyte and mechanical stability, affected the overall device electrochemical performance. Thus, to assemble high-performance flexible SCs, suitable gel electrolytes with good ionic conductivity and mechanical stability must be used. Different combinations of polymer host matrices and electrolytic salts together with their corresponding ionic conductivities are summarised in Table 2.[176,226,230,268–274] This list can serve as a guide for selecting suitable gel electrolytes in FSSCs.

6. Electrode materials: introduction to novel materials

FSSC device performance is strongly dependant on electrode materials and electrolytes. Conversely, device configuration is a factor defining FSSC device performance. Thus, according to the arrangement of electrodes, FSSCs can be classified into two categories: solid-state symmetric SCs (SSCs) and solid-state asymmetric SCs (ASCs). Several materials, such as nanocarbons (*e.g.*, CNTs and graphene), transition metal oxide/hydroxides/sulphides and conducting polymers, have been widely investigated as promising electrode materials for FSSCs. Additionally, several new electrode materials, such as MXenes, MOFs, POMs and BP, have been introduced recently as frontrunners as shown in Fig. 13. This section briefly summarises the recent progress in these two configurations and strategies to improve the overall device performance with new designs and emerging new materials.

6.1 Solid-state symmetric supercapacitors

6.1.1 Carbon-based materials in SSCs. A symmetric device is fabricated from electrodes of the same material with the same mass. Carbon materials exhibit excellent properties, including electrical conductivity, flexibility, low cost and light weight, which make them ideal candidates for SSC application. To date, several works have reported on SSCs based on carbon materials, such as CNTs[37,275] and graphene.[40,41,44,45] Miao *et al.*[276] developed a flexible SSC based on freestanding nitrogen-doped porous CNFs derived from electrospun PAN/polyaniline core–shell composite nanofibres. The device achieved a specific capacitance of 260 F g^{-1} at a current density of 0.5 A g^{-1} (areal capacitance: 0.35 F cm^{-2}; volume capacitance: 4.3 F cm^{-3}) as well as a high rate capability with 54% capacitance retention of the initial capacitance at 8 A g^{-1}. Moreover, it delivered an

Table 2 Advances in gel–polymer electrolytes based on combinations of different plasticizers and polymer host matrices with their corresponding room temperature ionic conductivities

Polymer host	Electrolytic salt	Type of electrolyte	Ionic conductivity (mS cm^{-1})	Ref.
PAM	LiCl	Aqueous	10	180
PVA	SiWA–H_3PO_4	Aqueous	8	198
PVA	SiO_2–SiWA–H_3PO_4	Aqueous	16	201
PVA	BWA	Aqueous	78	203
PVA	H_2SO_4	Aqueous	30	203
PVA	KOH	Aqueous	0.1	209
PEO	KOH	Aqueous	1 to 10	210
PVA	GO doped KOH	Aqueous	200	213
PEO	TEAOH	Aqueous	11.2	218
PAA	TEAOH	Aqueous	0.9	218
PAN-*b*-PEG-*b*-PAN	DMF–$LiClO_4$	Organic	6.9	219
PEO	PC–NaTFSI	Organic	0.54	229
PEO	PC–EC–DMC–NaTFSI	Organic	0.76	229
PVDF–HFP	PC–$Mg(ClO_4)_2$	Organic	5.4	231
PVA	BMIMCl–Li_2SO_4	Ionic liquid	37	239
PVDF–HFP	GO doped $EMIMBF_4$	Ionic liquid	25	240
PEGDA	[EMIM][TFSI]	Ionic liquid	9.4	242
PEO	$EMIHSO_4$–$MIHSO_4$	Ionic liquid	1.7	246
PEO	$EMIHSO_4$–$ImHSO_4$	Ionic liquid	2.5	246
PVA	BAAS doped H_2SO_4	Redox-active aqueous	21.4	258
PVA	AQQS doped H_2SO_4	Redox-active aqueous	28.5	259
PMMA	PC-Fc doped $TEABF_4$	Redox-active organic	1.89	264
PMMA	PC-4-oxo TEMPO doped $TEABF_4$	Redox-active organic	1.73	264
PVA	$EMIMBF_4$ doped H_3PO_4	Redox-active ionic liquid	39.3	258
PAN-*b*-PEG-*b*-PAN	$LiClO_4$	Organic	11	226
PEO	$LiClO_4$–TiO_2–Al_2O_3	Organic	0.03	268
PEOEMA	$BMIPF_6$ and $LiPF_6$	Ionic liquid	0.94	269
PHEMA/chitosan	EMIMCl	Ionic liquid	25	270
PVdF–HFP	EMITf	Ionic liquid	13	271
PVdF–HFP	EMITf	Ionic liquid	5.19	272
PVdF–HFP	EMITf–NH_4Tf	Ionic liquid	0.23	273
PMMA	PC–EC–$LiClO_4$ OR PC–EC–$NaClO_4$ OR PC–EC–$TEAClO_4$	Organic	1	274
PAN	[BMIM][TFSI]	Ionic liquid	2.42	238
PEGDA	[EMIM][TFSI]	Ionic liquid	9.4	242
PVA	*p*-Benzenediol (PB) doped H_2SO_4	Redox active aqueous	34.8	176

energy density of 9.2 W h kg^{-1} (0.61 mW h cm^{-3}) at 0.25 kW kg^{-1} (17 mW cm^{-3}) and exhibited good cycling stability with 86% capacitance retention after 10 000 cycles. The flexibility test did not reveal any significant changes in device performance after repeated deformation (bindings).

SWCNTs are considered the best candidates for SSCs because of their good electrical and mechanical properties as well as their good corrosion resistance. Yuksel *et al.*[228] cast SWCNT onto PDMS substrates to assemble transparent and flexible SSCs as illustrated in Fig. 14(a and b). Interestingly, the flexible SSCs exhibited an optical transmittance of 82% for 0.02 mg SWCNTs, while the high conductance of the SWCNT thin films eliminated the use of extra charge collectors. The specific capacitance, maximum power and energy density were determined as 34.2 F g^{-1}, 21.1 kW kg^{-1} and 18 W h kg^{-1}, respectively, for 0.08 mg SWCNT devices (see Fig. 14(b)). Moreover, high bendability without any significant deterioration in device properties was attained (<6% loss in the initial capacitance over 500 charge/discharge cycles). Similarly, an interdigitated pattern of vertically aligned CNTs was coated on a thin PC substrate *via* a maskless laser-assisted dry transfer method.[277] The flexible SSC was fabricated with an ionogel, an ionic liquid in a semi-solid matrix gel electrolyte. The assembled SC device reached a maximum specific capacitance of 430 μF cm^{-1} at a scan rate of 0.1 V s^{-1}. Moreover, a flexibility test suggested a capacitance retention >90% over the full 1000 bending cycles, implying great potential for application in foldable energy storage devices. Paper-based substrates show greater promise as supports than other polymer substrates, such as PPET and PDMS, owing to their porous nature that readily integrates with carbon materials.

Graphene is another promising carbon isotope that has attracted considerable attention in the field of flexible SSCs because of its higher mechanical and electrical properties and exceptionally larger surface areas compared with other carbon materials. Recently, El-Kady *et al.*[278] developed a new strategy to fabricate graphene-based flexible SCs whereby they effectively avoided restacking of graphene. The GO was directly reduced by using a standard LightScribe DVD optical drive. The afforded graphene films exhibited a high electrical conductivity (1738 S m^{-1}) and SSA (1520 m^2 g^{-1}), allowing their direct use as SCs electrodes. The flexible SSC was assembled with PVA–H_3PO_4 as a gel electrolyte and displayed an ultrahigh energy density value while maintaining the high power density and excellent cycle stability of the SCs (>97% over 10 000 cycles). Moreover, the as-fabricated device exhibited an excellent calendar life since no

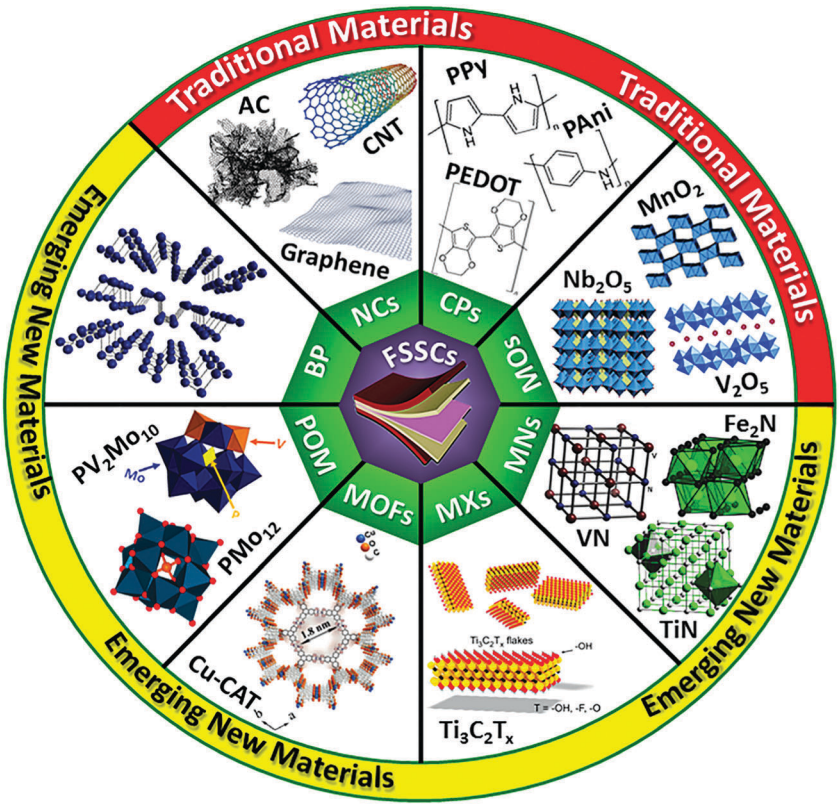

Fig. 13 An overview of promising electrode materials used so far for flexible solid-state supercapacitors (FSSCs). The materials are divided into two sub-sections such as traditional materials (NCs-nanocarbons, CPs-conducting polymers, MOs-metal oxides) and emerging new materials (MNs – metal nitrides, MXs – MXenes, MOFs – metal organic frameworks, POMs – polyoxometalates, BP – black phosphorous). Modified and reprinted with the permission from ref. 6*b*, 260*a*, 311*b*, 321*c*, 335 and 337 Wiley-VCH Verlag GmbH & KGaA, Royal society of chemistry, Elsevier.

significant decay in capacitance was observed after 4 months. In addition, the device exhibited only 5% loss in the initial capacitance when tested in the bent state for more than 1000 cycles. This was attributed to the high mechanical flexibility of the electrodes along with the interpenetrating network structure between the graphene electrodes and gel electrolyte.

Similarly, Xu *et al.*[279] developed an interconnected 3D graphene hydrogel with exceptional electrical conductivity (192 S m^{-1}) and mechanical robustness. Initially, silver paste was coated on the PI substrate, onto which 3D graphene and a gel electrolyte were sequentially cast. The steps involved in the preparation of the electrodes and FSC are presented in Fig. 14(c). Exceptional electrochemical properties, including a high gravimetric specific capacitance of 186 F g^{-1} for a 120 μm thick electrode (up to 196 F g^{-1} for a 42 μm thick electrode) and an unprecedented areal specific capacitance of 372 mF cm^{-2} ($\leq$402 mF cm^{-2} for a 185 μm thick electrode), were afforded. Moreover, no considerable change in the CV curves was observed, even under harsh bending conditions (Fig. 14(d)), suggesting excellent flexibility. Notably, only 8.4% decay in specific capacitance was observed after 10 000 charge/discharge cycles with a coulombic efficiency of 98.8–100% throughout testing under the bent state (150°) (Fig. 14(e)). Gao *et al.*[280] fabricated a flexible SSC based on a CNF–rGO hybrid aerogel with a PVA–H_2SO_4 gel electrolyte. The assembled SSC device displayed a specific capacitance of 203 F g^{-1} at a current density of 0.7 mA cm^{-2} that was maintained at 134 F g^{-1} after an increase in current density to 11.2 mA cm^{-2}, suggesting excellent rate capability (66%). These characteristics were attributed to the highly open continuous pore structure that facilitates ionic diffusion. Moreover, the device exhibited excellent performance with an areal capacitance, maximum areal power and areal energy density of 158 mF cm^{-2}, 15.5 mW cm^{-2} and 20 mW h cm^{-2}, respectively.

6.1.2 Metal oxide/nitride/sulphide in SSCs. Normally, carbon-based materials exhibit a lower capacitance than pseudocapacitive/faradaic materials owing to their electrostatic (nonfaradaic) charge storage mechanism. Conversely, pseudocapacitive/faradaic materials store charge through fast, reversible surface redox reactions and hence exhibit considerably large capacitance values (300–2000 F g^{-1}).[281] This category normally comprises transition metal oxides/hydroxides/sulphides/nitrides[282] and CPs, such as PANi, PPy and PEDOT.[283] Among the different transition metal oxides, RuO_2 is the first and most studied material because of its wide potential window of 1.2 V, highly reversible redox reactions spanning three distinct oxidation states, high proton conductivity, remarkably high specific capacitance and a long cycle life.[49]

Ferris *et al.*[284] prepared a porous gold/RuO_2 electrode through a two-step procedure under which the gold current collectors

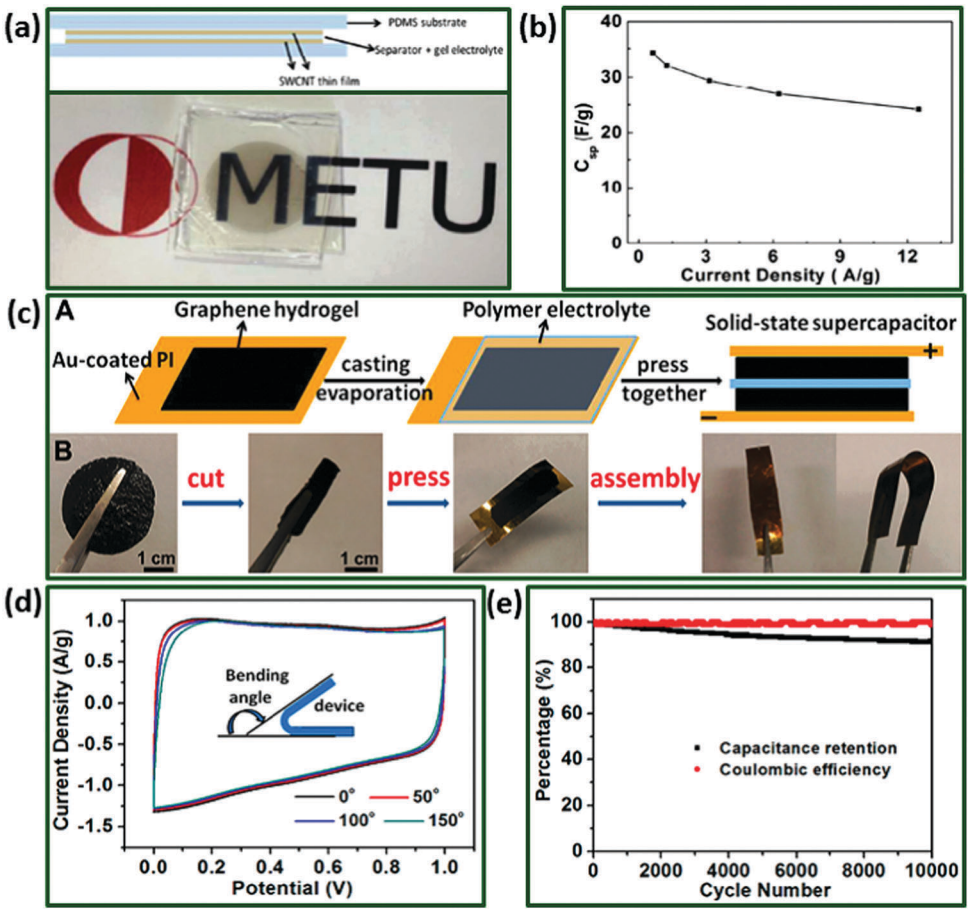

Fig. 14 (a) Schematic and photograph of the fabricated supercapacitors without carbon paste current collectors. (b) Variation of specific capacitance with current density of SSC cell. Reprinted with permission from ref. 228, Copyright 2014 American Chemical Society. (c) Schematic illustrations and photographs of the fabrication process of flexible solid-state supercapacitors based on graphene hydrogel films. (d) CV curves of FSC device at 10 mV s^{-1} for different bending angles. (e) Cycling stability of the device at a current density of 10 A g^{-1} with Coulombic efficiency. Adopted with permission from ref. 279, Copyright 2013 American Chemical Society.

were sculptured using hydrogen bubble dynamic template synthesis followed by electrodeposition of the hydrous ruthenium oxide. Fig. 15(a and b) illustrates the top side and cross-sectional SEM images of the electrodeposited RuO_2, suggesting a cracked mud-like morphology. Subsequently, a flexible SSC was assembled using gold/RuO_2 electrodes with a PVA–H_3PO_4 gel electrolyte comprising silicotungstic acid. A remarkable cell capacitance of 1220 mF cm^{-2} with a very low IR-drop voltage (38 mV) was afforded at 1.5 mA cm^{-2}. Moreover, the cell delivered an excellent specific energy density of 0.126 mW h cm^{-2} (7.9 mW h cm^{-3}) and a maximum power density of 7.9 mW cm^{-2} (493.8 mW cm^{-3}) (Fig. 15(c)) with a significant capacitance retention of ~95% after 2000 cycles. These encouraging electrochemical properties were attributed to the porous current collectors that provide a mechanical and conductive framework to afford durable 3D hydrous RuO_2. Similarly, they fabricated vertically aligned carbon nanowalls decorated with porous ruthenium oxide for SSCs.[285] The RuO_2-decorated carbon nanowalls electrode, consisting of thin carbon sheets assembled from graphene domains, delivered a specific energy density of 49 μW h cm^{-2}, comparable with that of state-of-the-art lithium ion micro batteries but with much higher power (10–20 mW cm^{-2}) and lifetime (up to 2000 cycles at 1.5 mA cm^{-2}) values (Fig. 15(d–f)).

However, the high cost, toxic nature, use of acidic electrolytes and lower natural abundance of RuO_2 hampers its potential for practical application. Thus, significant efforts have been directed towards finding suitable low-cost metal oxides as alternatives. Manganese-based oxides are widely recognised as highly promising alternative electrode materials for RuO_2 because of their low cost and high theoretical specific capacitance (~1400 F g^{-1}). Owing to the significant potential of MnO_2, several SSCs have been developed in recent years.[86,105] Chodankar *et al.*[69] fabricated an SSC with MnO_2 nanoflakes grown on an SS substrate and a PVP–$LiClO_4$ gel electrolyte. Interestingly, the cell could be cycled in a wide voltage window of 1.6 V and hence exhibited an energy density of 23 W h kg^{-1} at a power density of 1.9 kW kg^{-1}. Recently, flexible SSCs were fabricated by electrodeposition of ultrathin MnO_2 nanosheets on commercial carbon fibre yarns.[286] Two hybrid MnO_2-coated carbon fibre electrodes were assembled together in parallel with a PVP–Na_2SO_4 gel electrolyte. The assembled flexible device exhibited a high volumetric energy

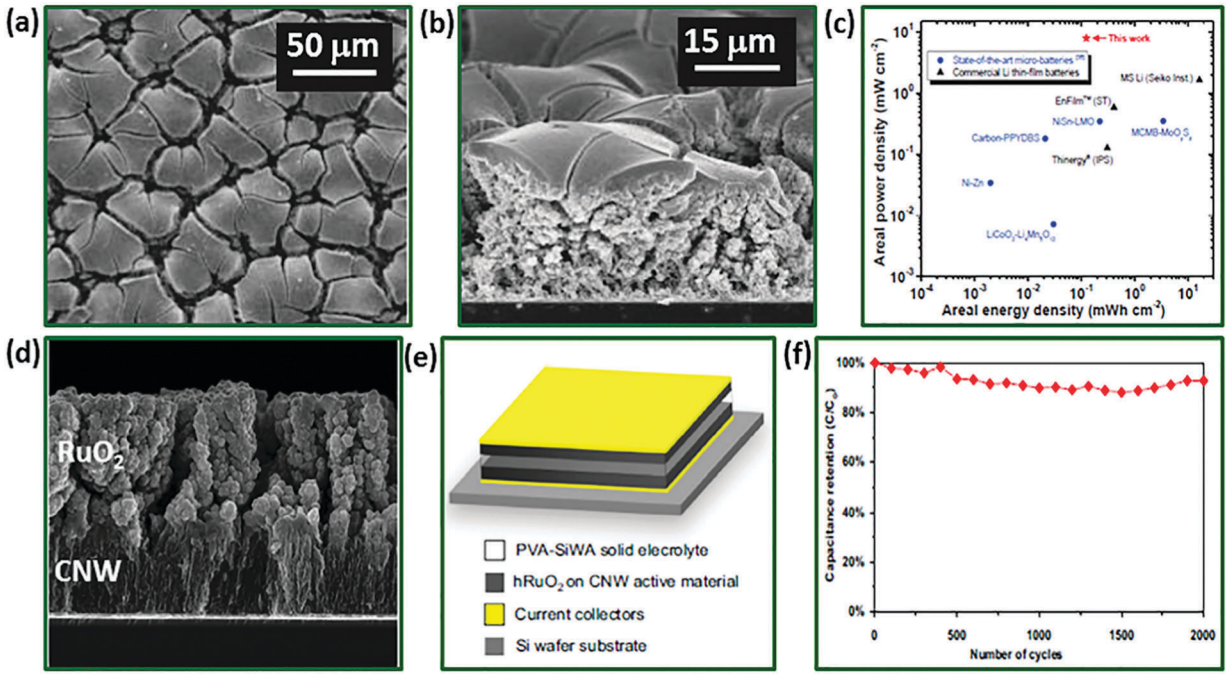

Fig. 15 (a and b) SEM image (top-view and cross-section) of RuO_2 electrode after 300 electrodeposition cycles, respectively, (c) Ragone plot of the solid-state device based on RuO_2. Reproduced with the permission from ref. 284, Copyright 2013 Wiley-VCH Verlag GmbH & KGaA. (d) Cross-section SEM image of a carbon nanowalls (CNW) film loaded with RuO_2, suggesting different morphologies such as cauliflower RuO_2 and vertically aligned CNW (e) schematic diagram of fabrication of SSC based on RuO_2 on CNW electrodes, (f) capacity retention with number of cycles for SSC device. Reproduced with the permission from ref. 285, Copyright 2014 Elsevier.

density of 3.8 mW h cm^{-3} at a power density of 89 mW cm^{-3} with good flexibility, (no significant change in CV curves over 2000 cycles in the bending state). In addition, the device displayed superior long-cycle stability with a capacity retention of 85.8% over 10 000 cycles. A practical demonstration was also provided by lightning a commercial LED using the integrated SCs, suggesting strong potential for application as flexible energy storage devices. However, the relatively low electrical conductivity of MnO_2 (10^{-5} to 10^{-6} S cm^{-1}) and its cycling stability limit its electrochemical performance. An effective approach to improve the electrical conductivity and stability of MnO_2 electrodes is to combine them with other highly conductive materials, such as carbon-based materials and/or CPs. Shi *et al.*[287] decorated an amorphous MnO_2 nanoparticle on MWCNT fibre and applied it to SSC devices. This unique fibre provided good mechanical reliability, high electrical conductivity and fast ion diffusion. Impressively, the volumetric capacitance for the amorphous MnO_2@MWCNT fibre-based device was determined as 10.9 F cm^{-3} (specific length capacitance: 28.9 μF cm^{-1}; gravimetric capacitance: 10.3 F g^{-1}) at a current density of 0.1 A cm^{-3}. Notably, the device retained ~63% of its initial capacitance when the current density was increased from 0.1 A cm^{-3} to 5 A cm^{-3}, suggesting excellent rate capability. Moreover, the device could deliver an energy density of 1.5 mW h cm^{-3} at a power density of 50 mW cm^{-3}. The flexibility test did not display any significant changes in the CV curves for the MnO_2@MWCNT fibre-based cell in a highly curved shape (180° folded). Moreover, very little decay (<10%) in the initial capacitance was observed over 15 000 charge–discharge cycles.

Graphene can also be combined with MnO_2 to improve the overall electrochemical performance of the SSC cell. Ma *et al.*[288] developed hierarchical MnO_2 NW/graphene hybrid fibres with a mesoporous structure and large SSA (139.9 m^2 g^{-1}) using the wet-spinning method. Synergic charge storage from both the pseudocapacitive MnO_2 and EDLC graphene improved the final device performance. The SSC cell fabricated by twisting two MnO_2/graphene fibres with a PVA–H_3PO_4 gel electrolyte exhibited a volumetric capacitance of 66.1 F cm^{-3} (normalised by the total volume of the two fibre electrodes) and excellent cycling stability with 96% capacitance retention over 10 000 cycles. Further, high energy (5.8 mW h cm^{-3}) and power (510 mW cm^{-3}) densities were achieved, suggesting great potential for application in wearable electronics. Many other MnO_2-based hybrid devices were investigated for SSCs.[289]

Owing to their high specific capacitance, vanadium-based oxides are also considered promising alternative materials to RuO_2 in flexible SSCs.[290] Kim *et al.*[291] fabricated an on-chip SSC on a PET substrate with hybrid electrodes of MWNT/V_2O_5 NW composites. The patterned SSC based on MWNT/V_2O_5 electrodes exhibited an excellent volumetric capacitance of 80 F cm^{-3} with an energy density of 6.8 mW h cm^{-3} in a PVA–LiCl electrolyte. The cell maintained 82% of the capacitance over 10 000 cycles at a current density of 11.6 A cm^{-3}. Further, bending analysis suggested a small capacitance loss of only 6% over 1000 bending cycles at a bending radius of 7 mm. Finally,

a practical demonstration was provided by operating a SnO_2 NW UV sensor.

Nickel- and cobalt-based binary and ternary materials have gained significant attention as electrode materials for SSCs because of their high capacitance through faradaic reactions. Recently, Qian *et al.* prepared NiO nanosheets on flexible carbon fibres using pre-deposited ZnO nanoparticle films as a seed-layer that was subsequently removed.[292] The device displayed a specific capacitance of 20 mF cm^{-2} at 0.1 mA cm^{-2} that was maintained over 10 000 cycles (100% retention), suggesting excellent cycling stability. The CV curves tested under different curvature conditions (bending angles: 60°, 90°, 120°, 180° and twist) afforded very small changes to the CV curves, confirming outstanding mechanical flexibility. Ni-Co-based oxides ($NiCo_2O_4$) are low-cost ternary metal oxides with superior conductivity (from 0.05 to 10^{-6} S cm^{-1}) over that of single component nickel (2×10^{-2} S cm^{-1}) or cobalt oxides (333 S cm^{-1}), which makes them suitable for SCs.

Wang *et al.*[75] designed flexible SSCs using two $NiCo_2O_4$ NWAs supported on Ni foam as the electrodes and PVA/KOH as electrolyte. The as-fabricated SSCs displayed a high cell areal capacitance of 161 mF cm^{-2} at 1 mA cm^{-2}. In addition, good cycling stability (100% capacity retention) over 3000 cycles was achieved, even after the device was subjected to harsh mechanical conditions, including both twisted and bent states. Similarly, Zheng *et al.*[293] assembled SSCs with a CNT/$NiCo_2O_4$ hybrid paper electrode and PVA/KOH gel electrolyte. They prepared a sandwich-like CNT/$NiCo_2O_4$ hybrid paper from a layer of conductive CNT buckypaper coated with honeycomb-like $NiCo_2O_4$ nanosheets on both sides. This CNT/$NiCo_2O_4$ SSC device delivered a high areal capacitance of 337.3 mF cm^{-2} (specific capacitance: 268.4 F g^{-1}) at a discharge current density of 0.1 mA cm^{-2}. An excellent volumetric energy of 1.17 mW h cm^{-3} and a power density of 2430 mW cm^{-3} were also demonstrated.

Conversely, a porous vanadium-doped zinc–nickel–cobalt ternary oxide (VZnNiCo) was grown on nickel foil for flexible SSCs.[294] Interestingly, the SSC based on VZnNiCo-based electrodes exhibited a capacitance of 590 mF g^{-1}, which is fourfold higher and twofold higher than that of $NiCo_2O_4$/$NiCo_2O_4$- and of ZnNiCo//ZnNiCo-based SSCs, respectively. This significant increase in capacitive response was attributed to the synergistic redox reactions of all the ions and the direct growth of the unique porous nanostructure on the flexible current collector that provides excellent ion diffusion efficiency with a high electrochemically active surface area. Moreover, the device delivered a volumetric capacitance of 0.463 mF cm^{-2} with an energy density of 0.93 mW h cm^{-2} and a power density of 75 mW cm^{-2}. The SSC also revealed excellent cycling stability with 94% capacitance retention after 5000 cycles. The constant area under the CV curves at different bending angles suggests that mechanical deformation has no effect on the electrochemical activity of the flexible SC, thereby providing a stable capacitive response.

Several other materials, including $ZnCo_2O_4$,[97,295] $MnFe_2O_4$/graphene[296] and CoMn-layered double hydroxide,[138a] have been investigated as promising electrode materials for SSCs. 2D transition metal hydroxide (TMH) ultrathin, atomic-thick nanosheets have received considerable attention in FSSCs because of extra contribution of abundant electroactive sites from various kinds of inorganic atoms or ions with unique physicochemical properties. However, the presence of strain in pure TMH causes cracking of the electrode during the charge–discharge process, resulting in poor cyclic performance. To mitigate these practical problems, composite electrodes from hybrid structures have been used intensively instead of a single ingredient. For example, Xie *et al.*[138b] demonstrated a facile one-step approach to prepare β-$Ni(OH)_2$/graphene nanohybrids using the layer-by-layer method. They fabricated a two-electrode cell by sandwiching PVA–KOH gel electrolyte between gold-coated flexible PET sheet (served as counter) and β-$Ni(OH)_2$/graphene nanohybrids electrodes. The as-fabricated device showed a high specific capacitance of 660.8 F cm^{-3} with negligible degradation even after 2000 cycles, suggesting good cycling stability. Recently, Jagadale *et al.*[138c] assembled yarn SCs by loading electroactive CoAl-layered double hydroxides (CoAl LDH) on carbon fibre (CF) yarns. They investigated the effect of mass loading on electrochemical performance of yarn SCs. Interestingly, CoAl LDH@CF-based yarns-SC offers excellent areal capacitance (195 mF cm^{-2}) and volumetric energy density of 1.6 mW h cm^{-3} with 94% cyclic stability after 4000 charge/discharge cycles.

Metal nitrides, such as titanium nitride (TiN) and VN, are an emerging class of electrode materials for high-performance SCs owing to their excellent electrical conductivity (4000–55 500 S cm^{-1}).[297] Xiao *et al.*[298] prepared flexible freestanding mesoporous VNNWs on CNTs to realise MVNN/CNT hybrid electrodes. A synergic combination of the high electrochemical performance of MVNNs and high conductivity and mechanical consolidation of CNTs was achieved. The SSC cell was constructed based on freestanding MVNN/CNT hybrid electrodes with an H_3PO_4–PVA electrolyte and exhibited a high volume capacitance of 7.9 F cm^{-3} and energy and power density values of 0.54 mW h cm^{-3} and 0.4 W cm^{-3}, respectively, at a current density of 0.025 A cm^{-3}. In addition, the device displayed 82% capacity retention over 10 000 cycles and demonstrated excellent flexibility with almost no change in the CV shapes under different bending conditions. Recently, Ma *et al.*[299] developed a freestanding multilayered film electrode with alternately stacked mesoporous Mo_2N nanobelts and rGO nanosheets (MMNNB/rGO). The SSC was then fabricated by sandwiching two thin and flexible freestanding MMNNB/rGO hybrid electrodes with PVA–H_3PO_4–silicotungstic acid (SiWA) gel electrolyte. The cell exhibited a high volumetric capacitance of 15.4 F cm^{-3} as well as energy and power densities of 1.05 mW h cm^{-3} and 0.035 W cm^{-3}, respectively, based on the volume of the entire cell. Moreover, the flexible SC retained 85.7% of the initial capacitance after 4000 cycles, suggesting good cycling stability. However, most of these metal nitrides exhibited poor cycling stabilities because of the irreversible electrochemical oxidation of metal nitrides during the charging/discharging cycles. Lu *et al.*[300] demonstrated the electrochemical cycling stabilisation of TiN NWs by using a PVA/KOH gel electrolyte. The polymer electrolyte suppressed the oxidation reaction on the

electrode surface. As a result, the TiN NW-based SSCs displayed extraordinary stability up to 15 000 cycles (82% capacity retention) and a high volumetric energy density of 0.05 mW h cm^{-3}. These results open up new opportunities in the development of high-performance metal nitride-based SSCs. Similarly, many other metal sulphides[301] and metal phosphates[302] have been explored for their excellent potential as electrode materials for SSCs.

6.1.3 Conducting polymers in SSCs. CPs, such as PANi, PPy and PEDOT, are another class of pseudocapacitive materials with great potential to provide excellent specific capacitance.[303] Xiao *et al.*[304] designed a new rGO/PANi/rGO sandwich-structured nanohybrid paper and explored its potential as an electrode for SSCs. Initially, the freestanding graphene paper was prepared by a printing technique and bubbling delamination method and displayed high electrical conductivity (340 S cm^{-2}), light weight (1 mg cm^{-2}) and excellent mechanical properties. Subsequently, PANi was electropolymerised on graphene paper with successive deposition of a thin graphene layer by dip coating to form a sandwich-structured graphene/PAni/graphene paper. Interestingly, this unique approach improved the energy storage capacity, the rate performance and cycling stability of the electrode. Thus, the as-obtained SSC exhibited an excellent capacitance of 120 mF cm^{-2}, which was maintained at 62% after an increase in current density from 0.1 to 10 mA cm^{-2}, and an energy density of 5.4 mW h cm^{-3} (10.79 W h kg^{-1}).

PPy is another CP extensively used as an electrode material in SCs. This compound has good environmental stability, a low-cost synthetic procedure, good conductivity, unusual doping/dedoping chemistry and high redox pseudocapacitive charge storage.[54] A simple 'soak and polymerisation' method was employed to prepare highly conductive paper through PPy coating on common printing paper.[305] The as-fabricated porous flexible paper exhibited an electrical conductivity of 15 S cm^{-1} and a low sheet resistance of 4.5 Ω sq^{-1}. The flexible SSC cell assembled from the PPy/paper composite exhibited an areal capacitance of 0.42 F cm^{-2} with an energy density of 1 mW h cm^{-3} at a power density of 0.27 W cm^{-3} (normalised to the volume of the whole cell). The electrode for the SSC was prepared by decorating PPy NWs on rGO sheets.[306] The maximum capacitance for the PPy NW/graphene composite-based SSC was determined as 434.7 F g^{-1} at a current density of 1 A g^{-1}; this is almost quadruple that observed for the rGO-based SSC (117.2 F g^{-1}). Notably, a specific capacitance of 361.1 F g^{-1} (83%) was retained after an increase in current density to 20 A g^{-1}, suggesting excellent rate capability attributed to the high dispersibility, large effective surface area and high electric conductivity (457.6 S m^{-1}) of the composite. In addition, the as-fabricated SSC exhibited an energy density of 60.37 W h kg^{-1} at a power density of 0.5 kW kg^{-1} and excellent cycling stability with 88.1% capacitance retention over 5000 cycles, suggesting exceptional mechanical flexibility. Recently, Liu *et al.*[307] proposed a chemical polymerisation and filtering method to coat flexible bacterial cellulose (BC) paper with PANi and graphene. BC paper with a 3D fibrous network exhibited an appreciable areal capacitance (4.16 F cm^{-2}), excellent tensile strength (65.4 MPa) and high flexibility. Moreover, the SSC cell exhibited stable behaviour in the bent state and provided an energy density of 0.12 mW h cm^{-2} at a power density of 0.1 W cm^{-2}.

6.1.4 MXenes in SSCs. The revolutionary discovery of graphene realised the unusual electronic, mechanical and optical properties of 2D materials.[308] MXenes, the term collectively used for transition metal carbides, carbonitrides and nitrides (*e.g.*, Nb_2C, Ti_3C_2, Ti_3CN and Ti_4N_3) are the latest addition to the family of 2D materials and have received extensive attention since their discovery in 2011.[309] These compounds have a general formula of $M_{n+1}X_nT_x$ (n = 1–3), where M represents an early transition metal (Ti, V, Nb, Cr and Mo), X is carbon and/or nitrogen and T_x corresponds to the surface terminations (hydroxyl, oxygen and fluorine).[309,310] Their various unique properties, such as high conductivity, good mechanical properties and hydrophilicity, make them promising candidates for energy storage applications. For example, depending on its synthetic route, $Ti_3C_2T_x$ displays an electronic conductivity ranging from $<$1000 S cm^{-1} to 6500 S cm^{-1}.[311]

MXenes are commonly prepared by selective etching of element 'A' (mostly Al) from their layered precursors (MAX phases) using wet chemistry routes, such as etching in HF[309,312] or acidic solutions of fluoride salts (LiF in HCl).[313] Among the many MXenes, $Ti_3C_2T_x$ is one of the most widely studied materials for FSSC application.[314,315] Recently, transparent, thin films of $Ti_3C_2T_x$ nanosheets with transmittance values of 93% ($\sim$4 nm) and 29% ($\sim$88 nm) and respective conductivities of $\sim$5736 and $\sim$9880 S cm^{-1} were fabricated.[314] Subsequently, a transparent solid-state asymmetric cell (72% transmittance) was assembled using $Ti_3C_2T_x$ and SWCNT films as positive and negative electrodes, respectively (Fig. 16a and b). Notably, the cell displayed a capacitance of 1.6 mF cm^{-2} with a long cycle life (no capacitance decay over 20 000 cycles) (Fig. 16(c)). Moreover, almost fivefold improvement in the energy density was recorded when compared with the symmetric cell based on $Ti_3C_2T_x$.

The exclusive layered structure of MXenes is thought to effectively prevent dense stacking in graphene and CPs, resulting in relatively porous structures that are favourable for ion transport. In this context, an ultrathin SSC (size of the whole device: 149 μm based on a PPy intercalated Ti_3C_2 film was assembled (Fig. 16d)). Notably, the intercalated Ti_3C_2 effectively prevented dense stacking in PPy and the electrochemical performance (Fig. 16e), including the capacitance (35 mF cm^{-2}), cycling stability and deformation tolerance, was significantly advanced (Fig. 16f).[315] Moreover, the strong interconnections between the PPy backbones and Ti_3C_2 layers offer highways for charge-carrier transport, greatly facilitating the pseudocapacitive process. Similarly, a freestanding film comprising hybrid inks based on $Ti_3C_2T_x$ nanosheets and graphene was developed and applied to the SSCs.[316] The assembled SSCs with the MXene/graphene hybrid film delivered a volumetric capacitance of 216 F cm^{-3} at a current density of 0.1 A cm^{-3}. Moreover, the device exhibited a volumetric energy density of 3.4 mW h cm^{-3} at a power density of 200 mW cm^{-3}, maintained at 1.4 mW h cm^{-3} at a high power density of 1600 mW cm^{-3}. In this unique

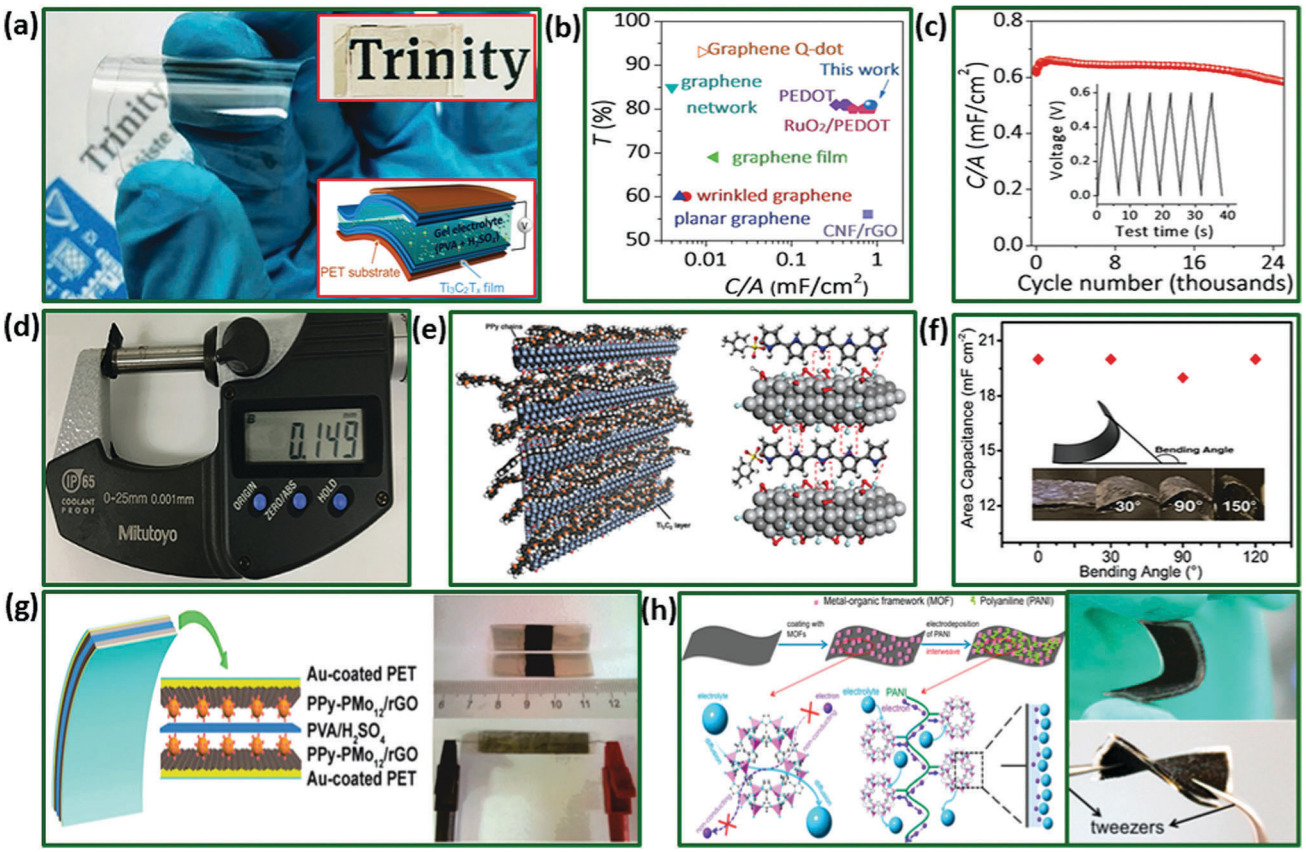

Fig. 16 (a) Digital photographs of flexible, transparent $Ti_3C_2T_x$ film on PET substrate and inset shows schematic diagram and photograph of SSCs cell. (b) Comparison of areal capacitances with various transparent supercapacitors. (c) Cycling stability of a $Ti_3C_2T_x$ SSCs with the typical GCD curves upon cycling (inset). Reproduced with the permission from ref. 314, Copyright 2017 Wiley-VCH Verlag GmbH & Co. KGaA, Weinheim. (d) Photograph of thickness of the as-prepared PPy/Ti_3C_2 SSC complete cell. (e) Schematic of intercalated PPy in the interlayers of Ti_3C_2 with corresponding atomic-scale presentation. (f) Performance of the PPy/Ti_3C_2 SSC under bending. Reprinted with the permission from ref. 315, Copyright 2016 Wiley-VCH Verlag GmbH & Co. KGaA, Weinheim. (g) Schematic illustration of PPy–PMo_{12}/rGO SSCs with actual photographs of the device. Adopted from ref. 322, Copyright 2015, Royal Society of Chemistry. (h) Steps involved in synthesis of PANI-ZIF-67-CC electrode with schematic representation of electron and electrolyte conduction in MOF (left) and MOF interwoven by PANI (right). Reprinted with the permission from ref. 331, 2015, American Chemical Society.

hybrid electrode, the small-sized MXene between the graphene layers acted as an active material and ideal 'buffer' for enhanced electrolyte shuttling as well as a conducting spacer that prevented the irreversible π–π stacking between the graphene sheets.

6.1.5 Polyoxometalates (POM) in SSCs. A new class of faradaic electrode materials known as POMs is emerging as a molecular frontrunner in the field of energy storage systems.[317] POMs are nanometric oxide clusters with reversible redox activities that can be used as building blocks for energy storage applications. These materials comprise a 3D framework of redox-active molecular clusters that combine oxygen and early transition metals (Mo, V, Nb, Ta and W) at their highest oxidation states. POMs are molecular oxides that contain tens to hundreds of metal atoms that reach nuclearities as high as 368 metal atoms in one single cluster molecule. Moreover, they are well suited to achieve a high capacity for energy storage applications because of their fast and reversible multi-electron redox reactions.[318] Nonetheless, the best known, most stable and widely investigated species are solid acids (or anions in their deprotonated form) with the general formula $H_n[AM_{12}O_{40}]$ (A: Si or P; M: V, Mo or W). Notably, POM clusters (simple Keggin type), phosphomolybdate (PMo_{12}) and phosphotungstate (PW_{12}) represent the ultimate degree of dispersion for an oxide nanocluster because all 12 MO_6 moieties (M: Mo or W) are at the surface of the cluster; this makes them ideal active materials for SCs.[319]

In fact, the development of hybrid materials made of CPs and POMs for SSCs has been tackled by our group[317,320] and others.[319,321] The anchoring of anionic POMs within the network of CPs and/or on the surface of nanocarbons (graphene and CNTs) has led to the synthesis of hybrid materials in which the inorganic clusters maintain their integrity and activity while benefiting from the conducting properties of the hybrid composite structure. A ternary nanocomposite based on polypyrrole–phosphomolybdic acid/reduced graphene oxide (PPy–PMo_{12}/rGO) was developed for the realisation of a high-performance SSC.[322] The flexible cell assembled on an Au-coated PET and a PVA/H_2SO_4 electrolyte (Fig. 16(g)) displayed a specific capacitance of 2.61 mF cm^{-2} at a current density of 150 mA m^{-2}. An ion soft

landing deposition technique has been recently developed to prepare high-density CNTs decorated with monodisperse POM (PMo_{12}) anions and the agglomeration of the active species (POMs) has been proven to affect the performance and stability of SSCs strongly.[323] The direct evidence of the uniform distribution of the individual redox-active species (PMo_{12}) on complex commercially relevant electrodes (CNT) was provided using atomically resolved STEM imaging. The FSC device was fabricated from CNT/PMo_{12}-coated carbon paper as electrode and $EMIMBF_4$/PVDF–HFP as gel electrolyte. Uniform deposition of small amounts of intact active species (PMo_{12}) on CNT electrodes was found to substantially improve the device performance.

6.1.6 MOF-derived material in SSCs. MOFs, a new class of functional materials with high porosity and chemical tunability, comprise nanosized cavities and open channels that make them promising candidates as sacrificial templates or precursors of nanostructured materials.[324] MOFs were first introduced by Yaghi[325] in 1995 and are extremely light materials with very high SSAs (up to 46 000 $m^2\ g^{-1}$), large pore volumes and well-defined pore sizes. MOFs consist of metal ions or cluster units coordinated by electron-donating organic ligands, which are commonly prepared using solvothermal, hydrothermal, microwave-assisted and surfactant-mediated synthetic methods.[324] The mass production of MOFs was recently realised by some companies (BASF and MOF Technologies).[326] MOFs hold great promise as electrode materials in SCs owing to their controlled pore sizes (0.6–2 nm) as well as their ability to incorporate redox-metal centres.

As-synthesised MOFs are usually nonconducting, thereby limiting their practical application in SCs. Hence, high temperature carbonisation methods are implemented to convert them into nanoporous carbon materials. The first practical realisation of MOFs as an electrode in SCs was demonstrated in 2011, using some Co-based MOFs in liquid electrolytes.[327] Recently, they have been used as promising electrode materials in FSSCs.[328–331] An FSSC with MOF-5-derived nanoporous carbon delivered a high energy density of 17.37 W h kg^{-1} and high power density of 13 kW kg^{-1} with 94.8% capacity retention over 10 000 cycles using Na_2SO_4/PVA electrolyte.[329] Another effective strategy to improve MOF conductivity is to prepare nanocomposites with other conducting materials, such as carbon-based species (*e.g.*, CNT and RGO) and CPs (*e.g.*, PANi and PPy).[330] For example, Co-based MOF crystals (ZIF-67) were interwoven with electrochemically deposited PANi chains on carbon cloth to realise a flexible conductive porous electrode without altering the underlying structure of the MOF (Fig. 16h and i).[331] The SSC with the PAni-ZIF-67-CC electrode yielded a remarkable areal capacitance of 35 mF cm^{-2} (stack capacitance: 116 mF cm^{-3}) and a power density of 0.833 W cm^{-3} at a current density of 0.05 mA cm^{-2} and retained more than 80% of its initial capacitance after 2000 cycles.

As previously mentioned, MOFs are ideal templates for the construction of carbons, metal nanoparticles, metal oxide nanoparticles and their composites under thermolysis conditions. The tribasic composite MoO_2@Cu@C was prepared using the POM (PMo_{12})@MOF (Cu-based MOF) as template by a thermolysis method and subsequently applied to SSCs.[332] The device displayed a charge capacity of 7.49 mA h g^{-1} at 0.25 A g^{-1} and 91% capacity retention over 5000 cycles. Moreover, the cell delivered an energy density of 2.58 W h kg^{-1} at a power density of 86.8 W kg^{-1}. Recently, rGO/Fe_2O_3 and rGO/NiO/Ni composite aerogels were also prepared using GO/MOF composites (Fe-MOF and Ni-MOF, respectively) as precursors.[156] The flexible SSC device assembled with the rGO/Fe_2O_3 composite aerogel exhibited a volumetric capacitance of 250 mF cm^{-3} at 6.4 mA cm^{-3} and a capacity retention of 96.3% after 5000 cycles at 50.4 mA cm^{-3}. It also displayed excellent mechanical flexibility.

In addition to producing nanocomposites, several efforts have been made to design and prepare conducting MOFs.[333] In 2016, Dinca *et al.*[334] applied the conductive MOF Ni_3(2,3,6,7,10,11-hexaiminotriphenylene)$_2$ (Ni_3(HITP)$_2$) as freestanding electrode material in an EDLC without conductive additives or other binders. This was the first material of its kind. Moreover, the team claimed a bulk electrical conductivity >5000 S m^{-1}, exceeding that of ACs and holey graphite (1000 S m^{-1}). Inspired by this pioneering work, Li *et al.* have developed conductive MOF NWAs (Cu-CAT) on CF paper and demonstrated their potential as electrodes in SSCs. Typically, Cu-CAT is constructed by coordinating Cu ions with 2,3,6,7,10,11-hexahydroxytriphenylene (HHTP) ligands in the *ab* plane to create a 2D hexagonal lattice.[335] This structure further packs along the *c*-axis with a slipped-parallel AB stacking model to form a honeycomb-like porous structure as illustrated in Fig. 13. Moreover, Cu-CAT exhibited 1D channels along the *c*-axis with an open-window size of $\approx$1.8 nm and good charge transportation because of the effective orbital overlap between the Cu ions and organic ligands. The Cu-CAT NW-based SSC displayed an EDL capacitance of 120 F g^{-1} at a current density of 0.5 A g^{-1} and good cycling stability, retaining 85% of its initial capacitance after 5000 cycles. Notably, the device delivered a surface area normalised capacitance of $\approx$22 μF cm^{-2} (BET surface area: 540 $m^2\ g^{-1}$), which is twofold higher than values observed for AC- and SWCNT-based cells (10 μF cm^{-2}) and comparable to those observed for graphene-based SSCs (18.9–25 μF cm^{-2}).

6.1.7 Black phosphorous in SSCs. BP is a new member of the large family of 2D materials and is the most stable allotrope of phosphorous. It comprises a layered structure with corrugated planes of P atom puckered layers weakly bonded *via* van der Waals interactions.[336] Similar to other layered materials, single- and few-layered BP nanoflakes can be readily formed by mechanical exfoliation (high-energy ball-milling of red phosphorus) and liquid exfoliation.[337] Few-layered BP (phosphorene) is a p-type direct-bandgap semiconducting layered material. Moreover, BP has a large spacing of 5.3 Å between adjacent puckered layers that is larger than the 3.6 Å spacing observed in graphite and comparable to the 6.15 Å spacing in the 1T MoS_2 phase. This makes it a promising candidate for energy storage applications.[338] The utilisation of BP in SCs is still in its infancy. Recently, a liquid-exfoliated BP nanoflake-based SSC on a PET substrate was fabricated using PVA/H_3PO_4 as gel electrolyte.[338] The cell displayed a volumetric capacitance of 17.78 F cm^{-3} (59.3 F g^{-1}) at a scan rate of 5 mV s^{-1} with energy densities

ranging from 0.123 to 2.47 mW h cm^{-3} and a maximum power density of 8.83 W cm^{-3}. The cycling stability study revealed ~71.8% capacitive retention after 30 000 cycles.

6.1.8 Other emerging materials in SSCs. In addition to traditional electrode materials, a few works have reported recently on FSSCs with selenium (Se)- and tellurium (Te)-based transition metal dichalcogenides.[339,340] These materials are considered promising electrode materials for FSSCs owing to their large effective surface area, remarkable electrochemical performance and good flexibility, guaranteeing maximum functionality. Very recently, atomically thin WTe_2 nanosheets were applied to SSCs for the first time.[341] WTe_2 was initially prepared using the CVD method followed by liquid-phase exfoliation to afford single crystals 2–7 layers WTe_2 nanosheets. The resulting SSCs delivered energy and power densities of 0.01 W h cm^{-3} and 83.6 W cm^{-3}, respectively, values superior to those observed for the commercial 4 V/500 μA h Li thin-film battery and 3 V/300 μA h electrolytic capacitor. These positive results were attributed to good mechanical flexibility and superior cycling stability (capacitance retention of ≈91% after 5500 cycles). Table 3 lists recent advancements in symmetric SCs based on different materials with their corresponding electrochemical performance.[191,342–376]

6.2 Solid-state asymmetric supercapacitors

SSCs usually exhibit low voltage (~1 V), leading to low energy density. Thus, to expand the practical applications of SCs, the energy density and operating voltage of FSSCs need to be improved without sacrificing their device power density and cycling stability. An emerging approach to attain these results is to assemble ASCs.[377] Contrary to SSCs, ASCs comprise two electrodes of different charge storage mechanisms, such as a faradaic/pseudocapacitive positive electrode and a nonfaradaic capacitor-type negative electrode.[378] Thus, in ASCs, both electrodes work in different potential windows, resulting in an extended voltage range up to 2.0 V for the cell, even in aqueous electrolytes. This range is much larger than that of SSCs and hence significantly improves energy density.

6.2.1 Carbon-based negative electrodes. Generally, carbon-based nanomaterials are used as negative electrodes in ASCs because of their excellent electrical conductivity and high surface area and power density.[379] Conversely, faradaic/pseudocapacitve materials, such as transition metal oxides and CPs, are used as positive electrodes owing to their high capacitance and energy density.[380] AC has been widely studied as a negative electrode material in ASC because of its high SSA (2000 to 3000 m^2 g^{-1}) and controlled porosity. Recently, Pang *et al.*[381] fabricated ASCs with a Co_3O_4-nanocube/$Co(OH)_2$-nanosheet hybrid as a positive electrode and AC as a negative electrode with PVA/KOH as gel electrolyte. The Co_3O_4/$Co(OH)_2$//AC device delivered a specific capacitance of 210 mF cm^{-1} at a current density of 0.3 mA cm^{-2}, which is almost twice as high as that of Co_3O_4-nanocube//AC (111 mF cm^{-2}), fivefold higher than that of $Co(OH)_2$ microplate//AC (43 mF cm^{-2}) and twice as high as that of Co_3O_4 + $Co(OH)_2$ hybrid//AC (133 mF cm^{-2}) cells. Interestingly, the Co_3O_4/$Co(OH)_2$ hybrid//AC cell maintained a capacitance of 159 mF cm^{-2} at a current density of 10 mA cm^{-2}, suggesting excellent rate capability (75% capacitance retention).

Notably, the as-assembled ASC cell exhibited a maximum energy density of 9.4 mW h cm^{-3} with very little capacitance decay over 5000 cycles (97.4% retention). Graphene is another carbon-based negative electrode material widely investigated for application in ASCs owing to its high electrical conductivity and mechanical strength.[382] Pan *et al.*[383] developed ASCs by pairing MnO_x (as a positive electrode) with chemically converted graphene as a negative electrode. A nanoporous Ni architecture was first constructed on the surface of a flexible carbon cloth (Ni@CC) to prepare a 3D porous current collector. This unique 3D architecture effectively enhanced the energy density per surface area because of its ability of high mass loading of active materials and efficient electron and ion transport. Subsequently, ultrathin MnO_x nanosheets were electrodeposited onto the 3D Ni@CC nanoporous current collectors, which exhibited an areal specific capacitance of 906.6 mF cm^{-2} at 1 mA cm^{-2} in an aqueous electrolyte. When 3D MnO_x@Ni@CC was employed as the positive electrode and chemically converted graphene (CCG) as the negative electrode in an ASC, with Na_2SO_4/PVA as gel electrolyte, a superior energy density of 1.16 mW h cm^{-3} was achieved. In addition, the device exhibited excellent cyclic stability with 81.5% capacity retention after 10 000 charge/discharge cycles. More importantly, the ASC cell maintained over 85.7% of its original capacitance, even after 200 bending cycles, suggesting potential application in flexible high-performance wearable electronics and energy storage devices.

A novel 1D $Co_{2.18}Ni_{0.82}Si_2O_5(OH)_4$ ultrathin nanoflake architecture was paired with GNSs to realise an ASC.[384] Interestingly, the as-assembled $Co_{2.18}Ni_{0.82}Si_2O_5(OH)_4$//graphene ASC cell displayed a specific capacitance of 194.3 mF cm^{-2} at a current density of 0.50 mA cm^{-2}, while retaining a value of 141.6 mF cm^{-2} at a current density of 6.0 mA cm^{-2} (~73% capacitance retention). Further, the cell could deliver a maximum energy density of 0.496 mW h cm^{-3} and excellent cycle stability with 96.3% retention over 10 000 cycles. Hierarchical core/shell nanostructures are of great interest owing to their large surface area, short diffusion paths, fast ion/electron transport pathway and component synergistic effects that are feasible for high-performance SCs. Zhu *et al.*[385] prepared well-aligned hierarchical $Cu(OH)_2$@$Ni_2(OH)_2CO_3$ core/shell NWAs on copper foam as a positive electrode combined with rGO as negative electrode to assemble ASCs. Impressively, the device could be cycled up to 1.6 V and exhibited a specific capacitance of 785 mF cm^{-2} (based on the area of the device) at a current density of 10 mA cm^{-2}. Moreover, an energy density of 1.01 W h cm^{-2} at a power density of 57 W cm^{-2} was attained. A practical demonstration was provided by powering a 'five-point star' pattern on a shoulder bag using two of the fabricated asymmetric SC devices with an area of 1 × 3 cm^2 in series for more than 45 s, indicating great potential for application as a portable and wearable energy storage device.

The common electrochemical performance-limiting factor for metal oxides is their low electrical conductivity; hence, it is essential to combine them with conducting carbon or

Table 3 Comparison of electrochemical performances of flexible solid-state symmetric designs based on different materials

Electrode material	Electrolyte	Specific capacitance	Energy density	Power density	Capacitance retention	Ref.
Treated carbon cloth	PVA–H_2SO_4	920 mF cm^{-2} at 2 mA cm^{-2}	1.4 mW h cm^{-3}	280 mW cm^{-3}	100% after 10 000 cycles	342
Graphene	PVA–H_2SO_4	80 F g^{-1} at 5 mV s^{-1}	8.87 W h kg^{-1}	7.142 kW kg^{-1}	100% over 10 000 cycles (0.5 mA cm^{-2})	343
Polyaniline	PVA–H_2SO_4	237.5 mF cm^{-2} at 10 mV s^{-1}	24.31 mW h cm^{-3}	140 mW cm^{-3}	95.2% over 2000 cycles (1 mA cm^{-2})	344
α-Fe_2O_3/rGO	PVA–KOH	32.9 mF cm^{-2} at 1 mA cm^{-2}	1.46 mW h cm^{-3}	2011.8 mW cm^{-3}	79.1% over 1000 cycles (2.5 mA cm^{-2})	345
Carbon quantum dots/polypyrrole	PVA–LiCl	315 mF cm^{-2} at 0.2 mA cm^{-2}	—	—	85.7% over 2000 cycles (2 mA cm^{-2})	346
N/O co-doped graphene quantum dots	PVA–H_2SO_4	461 mF cm^{-2} at 0.5 mA cm^{-2}	0.032 mW h cm^{-2}	—	87.5% over 2000 cycles (15 mA cm^{-2})	347
MWCNTs	PVA–H_3PO_4	2.02 F cm^{-3} at 10 mV s^{-1}	0.18 mW h cm^{-3}	400 mW cm^{-3}	94.1% over 6000 cycles (0.17 A cm^{-3})	348
MWCNTs	PVA–H_3PO_4	26.8 F g^{-1} at 1 A g^{-1}	3.5 W h kg^{-1}	28.1 kW kg^{-1}	92% over 5000 cycles (4 A g^{-1})	349
CNTs/$NiCo_2O_4$	PVA–KOH	337.3 mF cm^{-2} at 0.1 mA cm^{-2}	1.17 mW h cm^{-3}	2430 mW cm^{-3}	95.6% over 2000 cycles (2 A g^{-1})	350
CuO/3D graphene	PVA–LiCl	64 mF cm^{-2} at 0.25 mA cm^{-2}	0.0059 mW h cm^{-2}	110 μW cm^{-2}	86% over 5000 cycles (5 mA cm^{-2})	351
Expanded graphite foil	PVA–H_2SO_4	30.5 mF cm^{-2} at 1 mA cm^{-2}	0.163 mW h cm^{-3}	447 mW cm^{-3}	92% over 10 000 cycles (20 mA cm^{-2})	352
$FeCo_2S_4$–$NiCo_2S_4$	PVA–KOH	—	46 W h kg^{-1}	4.723 kW kg^{-1}	92% over 3000 cycles (10 mA cm^{-2})	353
MXene/graphene	PVA–H_3PO_4	216 F cm^{-3} at 0.1 A cm^{-2}	3.4 mW h cm^{-3}	1600 mW cm^{-3}	85.2% over 2500 cycles (1 A cm^{-3})	354
MnO_2	PVA–LiCl	776 F g^{-1} at 0.5 A g^{-1}	0.17 mW h cm^{-3}	—	91% over 20 000 cycles (4 A g^{-1})	355
Graphene/MoS_2	PVA–H_3PO_4	19.44 F cm^{-3} at 0.3 mA	1.728 mW h cm^{-3}	62 mW cm^{-3}	95% over 1000 cycles	191
Graphene/polyaniline	PVA–H_2SO_4	665 F g^{-1} at 1 A g^{-1}	14.2 mW h cm^{-3}	—	100% over 1000 cycles (5 A g^{-1})	356
N-Doped cotton-derived carbon frameworks (NCCF)-rGO	PVA–KOH	200 F g^{-1} at 0.1 A g^{-1}	20 W h kg^{-1}	—	94% over 10 000 cycles (3 A g^{-1})	357
Graphene	PVA–H_2SO_4	4.21 mF cm^{-2} at 0.1 mA cm^{-2}	0.552 mW h cm^{-3}	561.9 mW cm^{-3}	94.8% over 20 000 cycles (0.1 mA cm^{-2})	358
MnO_2	PVA–KOH	847.22 mF cm^{-2} at 0.41 mA cm^{-2}	0.0188 mW h cm^{-2}	16.33 mW cm^{-2}	92.7% over 5000 cycles (0.1 mA cm^{-2})	359
MnO_2/CNT	PVA–H_3PO_4	830 F g^{-1} at 1 mV s^{-1}	115.2 W h kg^{-1}	73.9 kW kg^{-1}	89% over 3000 cycles (20 mA)	360
MoS_2/CNT	PVA–H_2SO_4	16.3 mF cm^{-2} at 20 mV s^{-1}	0.92 mW h cm^{-3}	2100 mW cm^{-3}	95.1% over 20 000 cycles (100 mV s^{-1})	361
$MoSe_2$	PVA–KOH	133 F g^{-1} at 2 A g^{-1}	36.2 W h kg^{-1}	1.4 kW kg^{-1}	92% over 2000 cycles (100 mV s^{-1})	362
PEDOT:PSS/MWCNT	PVA–KOH	380 F g^{-1} at 0.25 A g^{-1}	13.2 W h kg^{-1}	4.99 kW kg^{-1}	90% over 1000 cycles (1 A g^{-1})	363
PANI/N-carbon	PVA–H_2SO_4	122 mF cm^{-2} at 0.05 mA cm^{-2}	0.22 mW h cm^{-2}	—	91.3% over 1000 cycles (1 A g^{-1})	364
PEDOT:PSS	PVA–H_2SO_4	202 F cm^{-3} at 0.54 A cm^{-3}	—	—	100% over 10 000 cycles (11 A cm^{-3})	365
rGO/PANI	PVA–H_2SO_4	6.4 mF cm^{-2} at 0.08 mA cm^{-2}	7.07 W h kg^{-1}	—	72% over 2000 cycles (0.1 mA cm^{-2})	366
ZnS/CNTs	PVA–KOH	159.6 F g^{-1} at 1 A g^{-1}	22.3 W h kg^{-1}	5 kW kg^{-1}	91.8% over 3000 cycles (1 A g^{-1})	367
$ZnCo_2O_4$/rGO	PVA–KOH	143 F g^{-1} at 1 A g^{-1}	11.44 W h kg^{-1}	1.382 kW kg^{-1}	93.4% over 5000 cycles (3 A g^{-1})	368
Pt/n-CNT@PANI	PVA–H_3PO_4	217.7 F g^{-1} at 0.2 A g^{-1}	30.22 W h kg^{-1}	9.072 kW kg^{-1}	96% over 5000 cycles (1.8 A g^{-1})	369
Waste paper fibers-RGO–MnO_2	PVA–Na_2SO_4	220 F g^{-1} at 1 A g^{-1}	19.6 W h kg^{-1}	2.4 kW kg^{-1}	85.3% over 2000 cycles (1 A g^{-1})	370
Porous carbon	PVA–KOH	81.3 F g^{-1} at 0.5 A g^{-1}	7.22 W h kg^{-1}	—	—	371
SWCNTs/TiO_2	PVA–LiCl	28 F g^{-1} at 20 mV s^{-1}	—	66.7 kW kg^{-1}	100% over 1000 cycles	372
SnS/S-doped Graphene	PVA–H_2SO_4	2.98 mF cm^{-2} at 60 mA m^{-2}	—	—	99% over 10 000 cycles	373
rGO/Mn_3O_4	PVA–H_3PO_4	45.5 F cm^{-3} at 50 mA cm^{-3}	4.05 mW h cm^{-3}	268 mW cm^{-3}	85% over 10 000 cycles (20 mV s^{-1})	374
rGO/PPy	PVA–H_3PO_4	0.51 F cm^{-2} at 0.1 mA cm^{-2}	1.18 mW h cm^{-3}	—	—	375
$MoSe_2$	PVA–KOH	133 F g^{-1} at 2 A g^{-1}	36.2 W h kg^{-1}	1.4 kW kg^{-1}	92% over 2000 cycles (2 A g^{-1})	339*c*
$SnSe_2$	PVA–H_2SO_4	406 μF cm^{-2} at 20 mA m^{-2}	—	—	100% over 1000 cycles (50 mA m^{-2})	340
SnSe	PVA–H_2SO_4	1176 μF cm^{-2} at 45 mA m^{-2}	—	—	100% over 1000 cycles (60 mA m^{-2})	340
rGO/$Ti_3C_2T_x$	PVA–KOH	—	63 mW h cm^{-3}	60 mW cm^{-3}	100% over 10 000 cycles (5 A g^{-1})	376*a*

polymer-based materials. Recently, a $ZnCo_2O_4$/ZnO@multiwall carbon nanotube hybrid was prepared as a positive electrode for ASCs.[386] Initially, $ZnCo_2O_4$/ZnO was deposited onto Ni foam by the hydrothermal method, with subsequent MWCNT deposition by a dip and dry process. The ASC cell was then fabricated by pairing a $ZnCo_2O_4$/ZnO@MWCNT positive electrode and AC negative electrode with PVA/KOH as electrolyte. The ASC device displayed a high specific capacitance of 111.8 F g^{-1} (at 1 A g^{-1}), a high energy density of 48.1 W h kg^{-1} (at 900 W kg^{-1}) and good cycling stability with a capacitance retention of 92.9% after 3000 cycles. Moreover, two serial connected $ZnCo_2O_4$/ZnO@MWCNT//AC ASCs were utilised to light four parallel connected LEDs, which remained bright for 23 min. Similarly, Shao *et al.*[387] produced a solid-state ASC device based on a graphene/MnO_2 nanorod as the positive electrode and a graphene/Ag combination as the negative electrode. The device exhibited a maximum energy density of 50.8 W h kg^{-1} and a high power density of 90.3 kW kg^{-1}, even at an energy density of 7.53 W h kg^{-1}. The bent hybrid nanostructured asymmetric SC was used to spin a fan, which also proved the high power density of the fabricated asymmetric SC. Notably, the unique graphene sheet-MnO_2 nanorod structure and 3D network architecture of the graphene/Ag species provided a higher specific surface and richer porous structure than those of traditional constructions, enabling high rates of charge propagation and short electron transport paths that improved the electrochemical performance of the electrodes.

Yang *et al.*[388] also developed ASCs based on a 3D Al@Ni@MnO_x nanospike (NSP) as the positive electrode, CCG as the negative electrode and Na_2SO_4/PVA as the polymer gel electrolyte. Owing to the different working potential windows of the Al@Ni@MnO_x NSP and CCG electrodes, the ASC cell exhibited ideal capacitive behaviour with a cell voltage up to 1.8 V, capable of lighting up a red LED indicator (nominal voltage: 1.8 V). Moreover, the device delivered an energy density of 23.02 W h kg^{-1} (1.29 mW h cm^{-3}) at a power density of 947.5 W kg^{-1} (53.02 mW cm^{-3}); it maintained an energy density of 6.57 W h kg^{-1} even at a maximum power density of 59 kW kg^{-1}. Interestingly, the device preserved 96.3% of its initial capacitance over 10 000 charging/discharging cycles at a current density of 2 A g^{-1}. Several other ASCs with carbon-based negative electrodes have also been explored.[389]

CPs are also promising candidates to combine with metal oxides to increase conductivity and add extra pseudocapacitance. Recently, a positive electrode for ASCs was fabricated by coating $NiCo_2O_4$ NWAs on carbon textiles with a PPy nanosphere shell layer.[390] The $NiCo_2O_4$@PPy electrode exhibited a high specific capacitance of 2244 F g^{-1} in an aqueous electrolyte. This was attributed to the synergistic effect between the conductive PPy and short ion transport channels in the ordered $NiCo_2O_4$ mesoporous NW. Moreover, a lightweight and flexible ASC device assembled with $NiCo_2O_4$@PPy (positive) and AC (negative) electrodes achieved a high energy density of 58.8 W h kg^{-1} at 365 W kg^{-1}, outstanding power density of 10.2 kW kg^{-1} at 28.4 W h kg^{-1} and good cycling stability ($\sim$89.2% retention after 5000 cycles) as well as high flexibility. Similarly, ASC was fabricated from PPy-wrapped MnO_2 nanoflowers on carbon cloth and AC on carbon cloth as positive and negative electrodes, respectively.[391] The ASC displayed an areal capacitance of 1.41 F cm^{-2} and an energy density of 0.63 mW h cm^{-2} at a power density of 0.9 mW cm^{-2}. An energy storage unit fabricated using multiple ASCs could drive an LED segment display, a mini motor and even a toy car after full charging. PEDOT is another promising CP that can be used as a pseudocapacitive material in combination with a metal oxide. Yang *et al.*,[392] developed a fibre-shaped ASC with NiO/$Ni(OH)_2$ nanoflowers encapsulated in 3D interconnected PEDOT on contra wires as the positive electrode and ordered mesoporous carbon (CMK3) as the negative electrode. The as-formed flexible ASC device exhibited an areal capacitance of 31.6 mF cm^{-2} (3.16 F cm^{-3}) at a current density of 0.4 mA cm^{-2} with an energy density of 0.011 mW h cm^{-2} at a power density of 0.33 mW cm^{-2} in an operating voltage window of 1.45 V. The as-fabricated ASC only displayed a slight fluctuation during charge/discharge cycling over 1400 cycles, demonstrating the outstanding stability of the device.

As described in Section 6.1.6, MOF-based materials can be used as templates or precursors for the synthesis of nanoporous carbon and nanostructured metal oxides with tunable surface properties. A new 'one for two' strategy has been proposed to prepare positive (Co_3O_4) and negative (N-doped carbon) electrodes on carbon cloth for flexible ASCs using a single 2D MOF precursor.[393] The device exhibited fast kinetics by retaining almost 66% capacitance when the current density was increased eightfold and also demonstrated robust mechanical flexibility. Moreover, an energy density of 41.5 W h kg^{-1} at a power density of 6.2 kW kg^{-1} was delivered with 85.5% capacitance retention after 20 000 cycles under different bending and twisting conditions.

6.2.2 Metal oxide-based negative electrodes. Metal oxides have also been widely explored as negative electrodes in ASCs because of their higher capacitance and energy density compared with carbon-based materials.[394] The working potential window of metal oxides for asymmetric SCs can be defined as follows:

$$E = E_0 + \Delta E_1 + \Delta E_2 = \frac{1}{F(\omega^{\beta} - \omega^{\alpha})N_A} + \Delta E_1 + \Delta E_2 \quad (4)$$

where ω^{α} and ω^{β} are the work functions of the positive and negative electrodes, respectively; N_A is Avogadro's constant; and ΔE_1 and ΔE_2 are the surface dipole potential of the positive and negative electrodes, respectively.[395] For SSCs, both electrodes have the same charge storage mechanisms so that $\Delta E_1 = -\Delta E_2$ and $\omega^{\beta} = \omega^{\alpha}$. Hence, the additional potential window is zero and the operation voltage of symmetric SCs is defined by the dissociation energy of the electrolyte. Conversely, for asymmetric SCs, the work function difference of the two metal oxides (positive and negative electrodes) defines the operating potential. Therefore, to assemble large voltage asymmetric SCs, it is essential to choose two different metal oxide electrodes with the largest work function difference. This results in an extended operating voltage window, even larger than the dissociation energy of the

electrolyte, which improves the energy density over that of symmetric SCs. Water dissociation is kinetically limited by hydrogen and oxygen evolution reactions on the surface of the metal oxides in the aqueous electrolytes.

Fig. 17 presents the work functions and working potential windows for different metal oxides[396,397] and can be used as a guide when choosing suitable positive and negative electrodes for high-performance ASCs. In metal oxides with a higher work function, oxygen vacancy defects are more prone to decrease the work function of the oxide because they act as n-type dopants, shifting the Fermi level closer to the conduction band edge. Further, the chemisorption of proton and hydroxide ions on the surface of the metal oxides will further extend the potential window by modifying the work function of the electrode. Several metal oxides, such as MoO_3[397] and iron oxide,[398] have been widely studied as negative electrodes for ASCs owing to certain advantages, including high theoretical capacitance, a suitable potential window, low cost, abundance and nontoxicity.

Yang *et al.*[399] developed a low-cost high-performance ASC with α-MnO_2 NWs and amorphous Fe_2O_3 nanotubes on flexible carbon fabric with PVA–LiCl as the gel electrolyte. Taking advantage of the different operating potential ranges of MnO_2 NWs and Fe_2O_3 nanotubes, the ASC cell can be cycled up to 1.6 V. The MnO_2//Fe_2O_3 ASC cell exhibited high specific and volumetric capacitances of 91.3 F g^{-1} and 1.5 F cm^{-3}, respectively, at a current density of 2 mA cm^{-2} that was maintained at 0.88 F cm^{-3} when the current density was increased to 10 mA cm^{-2}, suggesting good rate performance (58.6% retention). Moreover, the MnO_2//Fe_2O_3 cell displayed a high energy density of 0.55 mW h cm^{-3} and a high power density of 139.1 mW cm^{-3} with moderate stability (80%) over 6000 cycles. A simple application to light a commercial blue LED was demonstrated by connecting two MnO_2//Fe_2O_3 devices in series. These encouraging results were attributed to the unique nanostructure of the carbon fabric with a large surface area and high electrical conductivity.

Ma and co-workers[400] designed $ZnCo_2O_4$@MnO_2 core–shell nanotube arrays on Ni foam as a positive electrode for an ASC and paired it with 3D porous α-Fe_2O_3 on Fe foil as the negative electrode. The as-designed ASC device exhibited an extended operating voltage window of 1.3 V with a specific capacitance of 161 F g^{-1} at 2.5 mA cm^{-2}, a maximum energy density of 37.8 W h kg^{-1} and excellent stability with 91% capacitance retention after 5000 cycles. Similarly, a novel core–shell nanoarchitecture based on Co_3O_4@RuO_2 nanosheet arrays was developed on woven carbon fabrics to use as negative electrodes in ASCs.[401] The positive electrode Co_9S_8 nanorod array was prepared by hydrothermal sulphuration treatment of acicular Co_3O_4 nanorod arrays. Thus, the Co_3O_4@RuO_2//Co_9S_8 ASC cell was fabricated with a PVA–KOH gel electrolyte that can be reversibly cycled in a voltage window up to 1.6 V. The as-fabricated cell exhibited an energy density of 1.21 mW h cm^{-3} at a power density of 13.29 W cm^{-3} in aqueous electrolyte and an energy density of 1.44 mW h cm^{-3} at a power density of 0.89 W cm^{-3} in a solid-state electrolyte. However, the intrinsic semiconducting nature of metal oxides presents poor electrical conductivity, eventually leading to low power density in ASCs.[402] To tackle this issue, Yu *et al.*[403] recently developed a novel coil-type ASC based on Fe_2O_3@C nanorods on carbon cloth as the negative electrode and MnO_2 NWs on copper wire as the positive electrode with PVA–LiCl as the gel electrolyte. The thin carbon coating on the Fe_2O_3 nanorods improved the electrical conductivity. For the MnO_2 NW positive electrode, the copper wire was first annealed to prepare insulating CuO NWs on the Cu-wire and subsequently an MnO_2 layer was electrodeposited onto it. The coil-type ASC was assembled by simply winding the Fe_2O_3@C negative electrode onto the MnO_2@CuO NW positive electrode separated by a PVA–LiCl electrolyte. The as-assembled device exhibited an excellent volumetric capacitance of 2.46 F cm^{-3} with extraordinary rate capability (95.4%), high energy density (0.85 mW h cm^{-3}) (Fig. 18(a)) and remarkable flexibility and bendability with superior bending cycle stability (≈93.0% after 4000 cycles at different bending states). The digital photographs of the different bending states of the device and the corresponding capacity retention against the number of cycles are illustrated in Fig. 18(b and c), respectively.

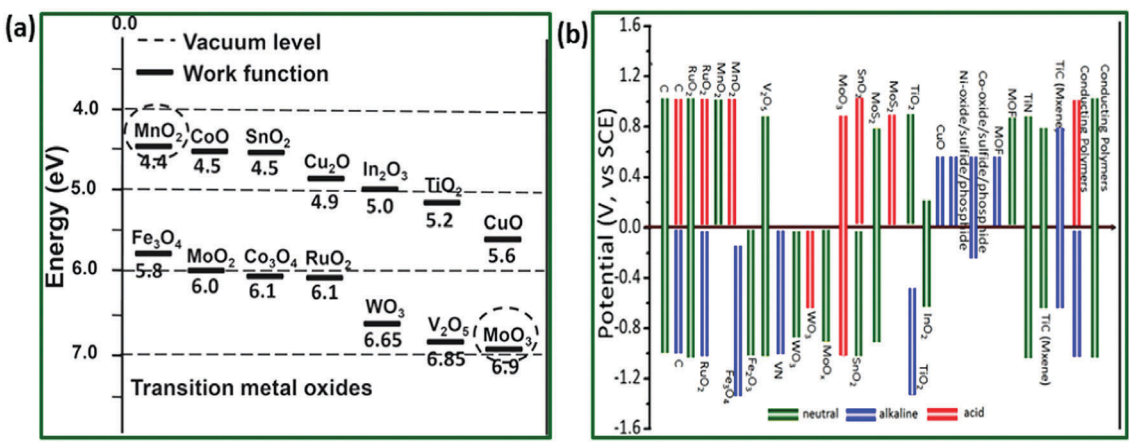

Fig. 17 (a) Schematic illustration of work function of different metal oxides, reprinted with permission from ref. 397*b*, Copyright 2013 Wiley-VCH Verlag GmbH & KGaA. (b) Potential window of various electrode materials in aqueous electrolyte. Reproduced with the permission from ref. 398*c*, Copyright 2015, Royal Society of Chemistry.

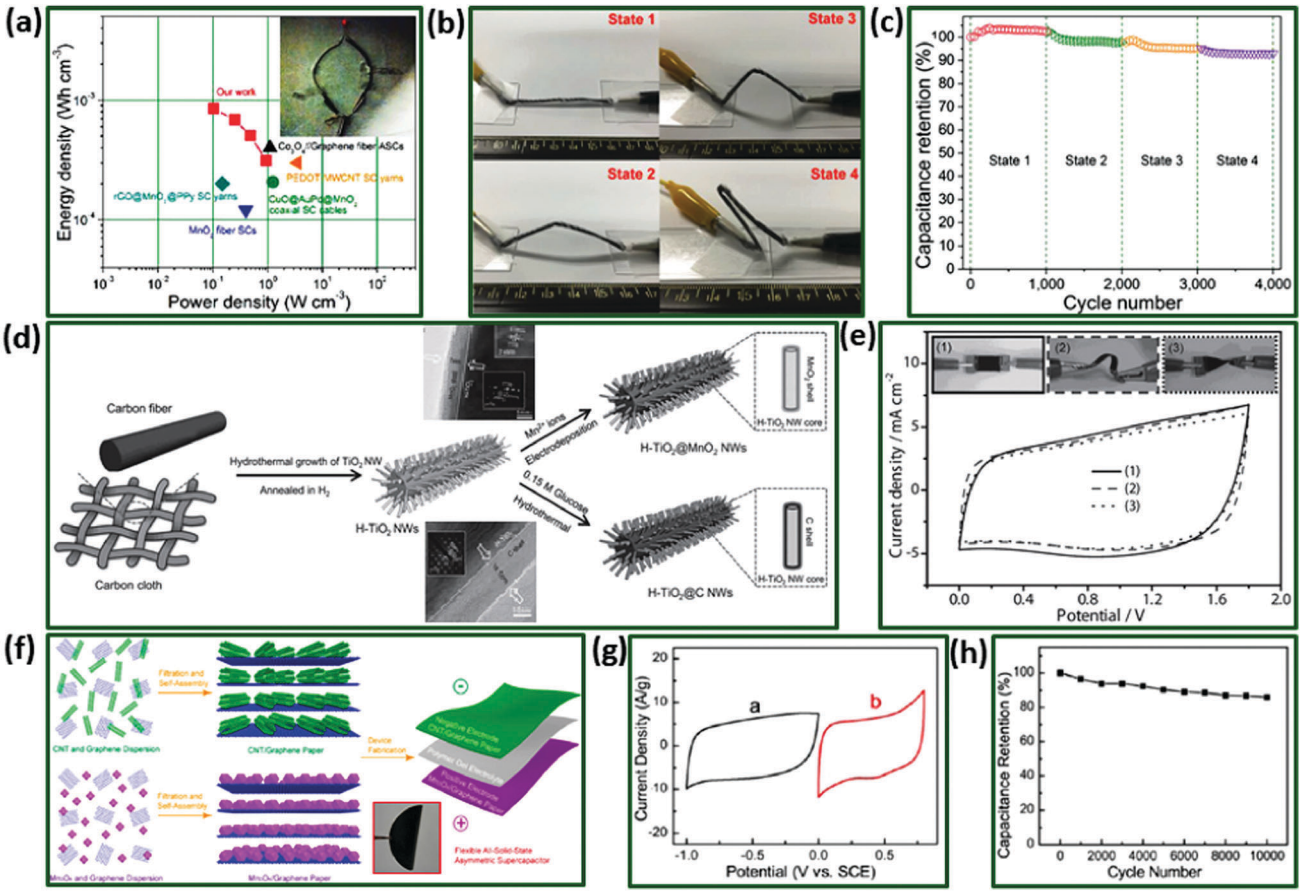

Fig. 18 (a) Ragone plots of Fe_2O_3@C//MnO_2@CuO ASC compared with other recently reported values of ASCs. The inset shows a LED powered by ASC. (b) Photographs of cable-type ASC at different bending states. (d) Long-term cycling stability at different bending states. Adopted with the permission from ref. 403, Copyright 2013 Wiley-VCH Verlag GmbH & KGaA. (d) Pictorial presentation of synthesis of hydrogenated (H)-TiO_2@MnO_2 and H-TiO_2@C core–shell NWs on a carbon cloth substrate as positive and negative electrodes for ASC respectively with corresponding TEM images. (e) CV curves recorded at a scan rate of 100 mV s^{-1} for (H)-TiO_2@MnO_2//H-TiO_2@C under different bending conditions with photographs of the device (inset). Reproduced with the permission from ref. 405, Copyright 2013 Wiley-VCH Verlag GmbH & KGaA. (f) Schematic presentation of synthesis steps of freestanding films of CNTs–graphene as negative and Mn_3O_4–graphene as a positive electrode, inset shows photograph of free-standing Mn_3O_4–graphene film, (g) CV curves of CNTs–graphene and Mn_3O_4–graphene in different working potential ranges, (d) cycling stability of CNTs–graphene//Mn_3O_4–graphene ASC over 10 000 cycles at 50 mV s^{-1} scan rate. Reprinted with permission from ref. 409, Copyright 2012 American Chemical Society.

Another approach to improve the conductivity of metal oxide electrodes is to combine them with carbon materials, such as CNTs and graphene. Thus, ASCs with wrinkled MnO_2/CNT as the positive electrode and a wrinkled Fe_2O_3/CNT composite as the negative electrode were assembled.[404] The optimised ASC could be reversibly cycled in a voltage window up to 2 V and displayed an energy density of 45.8 W h kg^{-1} at a power density of 0.41 kW kg^{-1}. Additionally, the ASC exhibited exceptional cycling stability and durability, with 98.9% specific capacitance retention after 10 000 cycles at multiple strains. Such excellent electrochemical performance was attributed to the synergistic effects of the two electrodes with an optimised potential window. Lu *et al.* explored a novel approach to improve the conductivity of MnO_2 by fabricating a hydrogenated TiO_2@MnO_2 core–shell nanostructure as presented in Fig. 18(d).[405] Interestingly, TiO_2 is an inexpensive and electrochemically stable semiconductor with higher electrical conductivity (10^{-5}–10^{-6} S cm^{-1})[406] than that of MnO_2 (10^{-5}–10^{-2} S cm^{-1}).[407] More importantly, the carrier density of pristine TiO_2 can be increased by three orders of magnitude upon hydrogenation. Thus, hydrogen-treated TiO_2 (H-TiO_2) NWs were employed as the core (conducting scaffold) to support electrochemically active MnO_2 and carbon shells (H-TiO_2@C) (Fig. 18(b and c)) and an ASC device based on H-TiO_2@MnO_2 (positive electrode)//H-TiO_2@C (negative electrode) core–shell NW electrodes was fabricated. This could be reversibly cycled in a potential window up to 1.8 V and exhibited maximum volumetric and specific capacitance values of 0.71 F cm^{-3} and 141.8 F g^{-1}, respectively, at 10 mV s^{-1}. Moreover, the device displayed a good capacitance rate, with 56% volumetric capacitance retention when the scan rate increased from 10 to 400 mV s^{-1}. It delivered a volumetric energy density of 0.30 mW h cm^{-3} (59 W h kg^{-1}) and a volumetric power density of 0.23 W cm^{-3} (45 kW kg^{-1}). Additionally, the device exhibited excellent cycling performance with 8.8% capacitance loss over 5000 cycles and good flexibility as illustrated by the CV curves measured under different bending conditions (Fig. 18(e)).

Because of their diverse crystal structures, Mn-based oxides can be used as both positive and negative electrodes. For example, a novel ASC cell based on amorphous porous Mn_3O_4 on conducting paper (nickel/graphite/paper, NPG; Mn_3O_4/NGP) as a negative electrode and an $Ni(OH)_2$ on NGP ($Ni(OH)_2$/NGP) positive electrode were assembled.[408] In the ASC negative electrode, Mn_3O_4 exhibits +2 and +3 Mn valences and provides rich redox reactions for pseudocapacitance generation. In addition, Mn_3O_4 has a suitable working window at negative potential and is also low in cost, highly abundant and nontoxic. Interestingly, the devices could be cycled reversibly in a wide voltage window (1.3 V) and displayed a high energy density of 0.35 mW h cm^{-3}, high power density of 32.5 mW cm^{-3} and a superior cycling performance (<17% capacitance loss after 12 000 cycles at a high scan rate of 100 mV s^{-1}). Conversely, Gao *et al.*[409] prepared a freestanding Mn_3O_4-graphene (Mn_3O_4-G) paper electrode and applied it as a positive electrode in an ASC cell with freestanding carbon nanotube-graphene (CNT-G) as negative electrode and a PAAK/KCl electrolyte. Fig. 18(f) is a schematic illustration of the systematic fabrication process of the ACS. Compared with pristine graphene paper, the composite paper electrodes with carbon nanotubes or Mn_3O_4 nanoparticles uniformly intercalated between the GNSs exhibited excellent mechanical stability, greatly improved active surface areas and enhanced ion transportation. As expected, the CNT-G//Mn_3O_4-G cell could be cycled reversibly with a cell voltage window up to 1.8 V (Fig. 18(g)) and achieved a specific capacitance of 72.6 F g^{-1} at a current density of 0.5 A g^{-1} while still retaining 50.8 F g^{-1} at a higher current density of 10 A g^{-1}. Moreover, the cell presented an energy density of 32.7 W h kg^{-1}, which is almost threefold higher than that of the CNT-G//CNT-G (10.5 W h kg^{-1}) and Mn_3O_4-G//Mn_3O_4-G (7.1 W h kg^{-1}) SCs. More importantly, when the power density increased to 9.0 kW kg^{-1}, the energy density of CNT-G//Mn_3O_4-G was still as high as 22.9 W h kg^{-1}, suggesting that the ASC cell can concurrently provide high energy and power densities. Finally, the cell displayed remarkable cycling stability and retained 86% of its initial capacitance after 10 000 cycles as illustrated in Fig. 18(h).

6.2.3 Metal nitride-based negative electrodes. The limited electrical conductivity of the metal oxide-based negative electrode hampers the resulting energy storage capacity of ASCs. Therefore, to further improve the efficiency of ASCs, a new class of redox-active metal nitrides with superb electrical conductivity (4000–55 500 S cm^{-1}) has been recently explored.[410] Lu *et al.*[411] developed vanadium nitrides (VN) as a new class of negative electrodes for ASCs. Vanadium nitride (VN) shows great potential as a negative electrode for ASCs owing to its large specific capacitance (1340 F g^{-1}), high electrical conductivity (σ_{bulk} = 1.67 × 10^6 Ω^{-1} m^{-1}) and wide operation windows at negative potentials. The ASC cell was fabricated with porous VN NW as the negative electrode and VO_x NW as the positive electrode with LiCl/PVA as electrolyte. Initially, porous VN NWs were fabricated through a two-step approach that comprised growing VO_x NWs on a carbon cloth substrate by the hydrothermal method followed by post-annealing in ammonia at 600 °C.

Notably, the VO_x//VN-ASC device exhibited a stable electrochemical window of 1.8 V and achieved a volumetric capacitance of 1.35 F cm^{-3} (based on the volume of the entire device; 60.1 F g^{-1}, based on the total mass of active materials) at a current density of 0.5 mA cm^{-2}. More importantly, the ASC cell demonstrated remarkable rate capability with 74.7% retention of the initial capacitance (1.01 F cm^{-3}) as the current density increased to 5 mA cm^{-2}. Indeed, a high energy density of 0.61 mW h cm^{-3} and a high power density of 0.85 W cm^{-3} were achieved with excellent cycling stability (12.5% reduction in capacitance over 10 000 cycles). The mechanical flexibility test indicated that the electrochemical performance of the device was not affected by folding and twisting, which confirms its potential for application as a flexible energy storage device.

However, metal nitrides usually oxidise in aqueous solutions, and therefore, to circumvent this problem, these materials have been combined with more stable materials by different processes, including CNT encapsulation[412] and graphene wrapping.[413] Among these, vertically aligned graphene nanosheets (GNS) are more effective as substrates because of their large surface area, high conductivity and light weight. Zhu *et al.*[414] fabricated an all metal nitrides ASC using titanium nitride (TiN) as positive and iron nitride (Fe_2N) as negative electrode grown on GNS substrate. The schematic illustration of the steps involved in the fabrication process for both electrodes is presented in Fig. 19(a). Initially, thin layers (20 nm) of TiO_2 and ZnO were coated on the GNS substrate by atomic layer deposition. Next, the Fe_2N@GNS negative electrode was produced by converting ZnO into FeOOH *via* an ion exchange reaction and subsequent thermal treatment in NH_3. Conversely, the TiN@GNS positive electrode was prepared by annealing TiO_2@GNS under NH_3 atmosphere. The TiN@GNS//Fe_2N@GNS ASC assembled with PVA/LiCl gel electrolyte could be reversibly cycled up to 1.6 V. The device delivered a stable capacitance of 60 F g^{-1} at 10 mV s^{-1} with <2% capacity drop after an increase in scan rate to 100 mV s^{-1}, suggesting extraordinary rate capability. Moreover, the cycling stability of the device was tested under bending conditions from cycle 5000 to 15 000 and subsequently under natural state in the last 5000 cycles, suggesting that bending had negligible effect on the capacitance of the device. Interestingly, the device maintained 100% coulombic efficiency within 20 000 cycles (Fig. 19(b)). This result was ascribed to the structure stability of the electrode material in the gel electrolyte. In addition, the device achieved both a high volumetric energy density of 0.55 mW h cm^{-3} and a high power density of 220 mW cm^{-3} (Fig. 19(c)).

6.2.4 Conducting polymer-based negative electrodes. CPs comprise a large family of pseudocapacitive materials that can provide stable and impressive energy storage performance in both positive and negative working potentials because of their good conductivities, reversible redox reactions and environmental friendliness. However, during charging/discharging processes, the CPs may swell and shrink, resulting in mechanical degradation of the electrodes. Thus, poor cycling stability is always observed, especially when they are used as negative electrodes. Therefore, different strategies have been developed

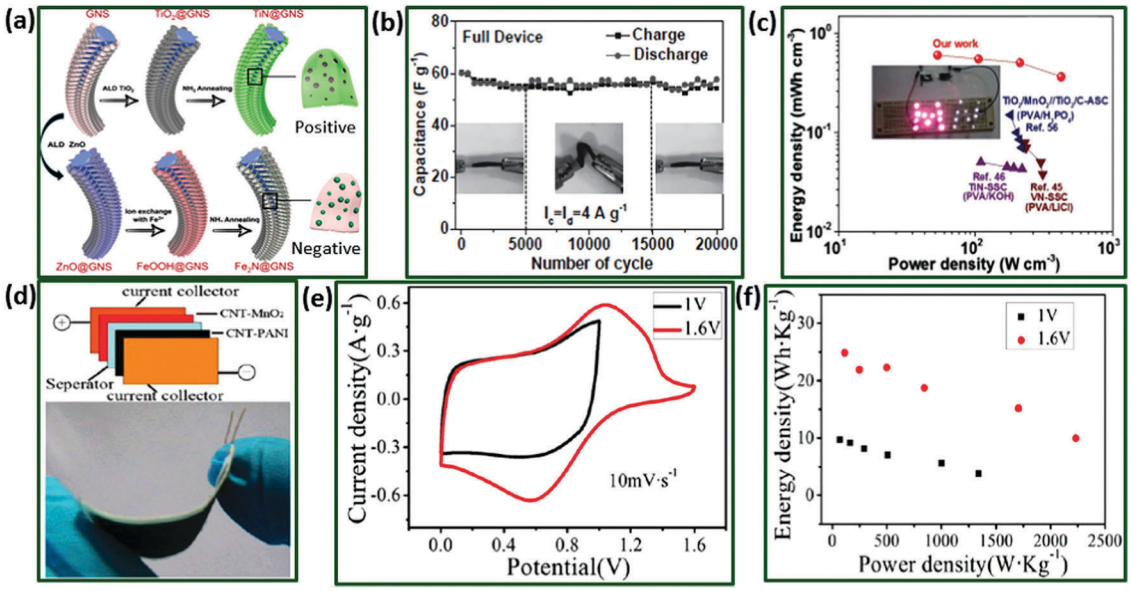

Fig. 19 (a) Schematics of the fabrication of negative electrode (Fe_2N@GNS) and positive electrode (TiN@GNS) for ASC, (b) cycling performance of Fe_2N@GNS//TiN@GNS device at 4 A g^{-1} in 20 000 cycles with different bending situations. (c) Ragone plots of quasi-solid-state Fe_2N@GNS//TiN@GNS ASC in comparison with other PVA-based solid electrolyte SSCs and ASCs with practical demonstration (inset). Reproduced with the permission from ref. 414, Copyright 2015 Wiley-VCH Verlag GmbH & KGaA. (d) Schematic diagram of design of ASC based on CNT–MnO_2 as positive electrode and CNT–PAni as negative electrode with corresponding photograph of final ASC device. (e) CV curves and (f) Ragone plots of the CNT–MnO_2//CNT–PAni ASCs under different potential ranges. Reprinted with permission from ref. 416, Copyright 2013 American Chemical Society.

to enhance the pseudocapacitance of CPs, such as optimising the nanostructures, doping with surfactant ions and fabricating composites with other species. Lu *et al.*[415] synthesised highly ordered 3D α-Fe_2O_3@PANi core–shell NWAs as negative electrodes for ASCs. The α-Fe_2O_3 NWAs were electrodeposited on carbon cloth with subsequent annealing in air. A thin layer of PANi was then electrodeposited on the α-Fe_2O_3 NWs to produce the 3D α-Fe_2O_3@PANi core–shell NW. This unique α-Fe_2O_3@PANi core–shell nanoarchitecture provided a large reaction surface area, fast ion and electron transfers and good structure stability, all of which improved the electrochemical performance. The ASC cell was then assembled with α-Fe_2O_3@PANi as negative and PANi on carbon cloth as positive electrodes. The ASC cell displayed a high volumetric capacitance of 2.02 mF cm^{-3} (based on the volume of device), a high energy density of 0.35 mW h cm^{-3} at a power density of 120.51 mW cm^{-3} and very good cycling stability with a capacitance retention of 96% after 10 000 cycles.

Similarly, Jin *et al.*[416] assembled an ASC using CNT/PANi and CNT/MnO_2/graphene paper as negative and positive electrodes, respectively, with a PVP–Na_2SO_4 gel electrolyte as presented in Fig. 19(d). The assembled ASC operated in a higher voltage range up to 1.6 V and achieved an energy density of 24.8 W h kg^{-1} and a high power density of 2230 W kg^{-1} (Fig. 19(e and f)). PEDOT is another promising candidate for application as a negative electrode in ASC owing to its higher reduction potential ascribed to the electron-donating nature of its oxygen groups. Further, the high stability of PEDOT in its oxidised state enables it to exhibit electrochemical activity in a wide potential window. For example, an ASC device was fabricated on Au-coated PEN plastic substrates using PEDOT and PANi as negative and positive electrodes, respectively.[417] This ASC device could be cycled in a wide voltage window of 1.6 V and exhibited a volumetric stack capacitance of 34 F cm^{-3} at a current density of 0.5 mA cm^{-2}. Moreover, the PANi//PEDOT ASC device displayed the highest energy density (12 mW h cm^{-3}), which was sixfold higher than that for the symmetric PEDOT cell (E = 2 mW h cm^{-3}) and twofold higher than the PANi-based cell (E = 5 mW h cm^{-3}). Finally, the cycling stability of the ASC was determined as 80% over 10 000 cycles at a current density of 2 mA cm^{-2}.

6.2.5 Some other negative electrodes. In addition to the aforementioned materials, some new promising materials have been recently employed as negative electrodes in ASCs. Specifically, metal phosphides, having both metalloid characteristics and good electric conductivity, have been considered advanced electrode materials for ASCs. A 3D cobalt phosphide (CoP) NW on carbon cloth was presented as the negative electrode with a MnO_2 NW as the positive electrode and LiCl/PVA as the gel electrolyte.[418] Interestingly, the resultant ASC cell could be successfully cycled in a voltage window up to 1.6 V and delivered good supercapacitive characteristics, including a volumetric capacitance of 1.94 F cm^{-3} and energy and power densities of 0.69 mW h cm^{-3} and 114.20 mW cm^{-3}, respectively. Iron selenide ($FeSe_2$) is another suitable candidate for ASC application because of its excellent electrochemical activities and an appropriate operating window at negative potentials.[419] The assembled ASC was based on $NiCo_2O_4$ and $FeSe_2$ as positive and negative electrodes, respectively, and a KOH/PVA electrolyte exhibited an energy density of 10.4 W h kg^{-1} and a maximum

power density of 1.2 kW kg^{-1} (operating window: 1.5 V). Phytic acid has a strong chelating ability and can easily bond with metal ions to generate cross-linked metal phytate complexes. Thus, using phytic acid treatment, NiZn-phytate and Fe-phytate were developed to serve as positive and negative electrodes, respectively.[420] The resultant Ni/Fe cell delivered excellent electrochemical properties with long-term stability (~86% retention after 8000 cycles at 20.83 A g^{-1}). Moreover, the ASC cell maintained its electrochemical performance under various bending conditions, suggesting great potential for application as a power supply for wearable smart products. A summary of the electrochemical performance of flexible solid-state asymmetric designs based on different positive and negative electrodes with their corresponding gel electrolytes is presented in Table 4.[421–468]

7. Innovations in cell designs

It is highly desirable that FSSCs have flexibility and a compact design so that they can be easily incorporated in wearable electronics. However, further investigations must focus on breakthroughs for new designs of the SCs itself, rather than solely focusing on the electrode materials. As shown in Fig. 20, several innovative cell designs were developed in the recent past for use in wearable/bendable electronics, as discussed in this section.

7.1 Sandwich-type design

This is the most common FSSC cell structure as it is easy to assemble. The design consists of two layers of planar flexible electrodes with a gel electrolyte layer sandwiched between them and a flexible packaging material as shown in Fig. 20. The mechanical flexibility of sandwich-type FSSCs can be tested by evaluating their electrochemical performance in bent, folded and twisted conditions. As it is the most widely used structure, many such sandwich-type flexible SCs have been studied in recent years.[434] However, because the device does not have a separator, prevention of short circuits is not guaranteed.

7.2 Planar or on-chip design

Planar SCs, as an emerging cell design of SCs, enable the entire device to be much thinner and more flexible than existing SCs owing to their unique structural design.[2c,469a] The device integrates three important components into a two-dimensional configuration in the same horizontal plane, including the electrode material, electrolyte and current collector. The planar configuration design offers planar channels for electrolyte ions, facilitating fast ion transport in the two-dimensional direction. Further, the planar configuration would not affect the ion transport when the SCs are under different bending states, such as folded and rolled.

7.3 Fibre supercapacitor design

Fibre SCs have drawn considerable attention in the past few years because of the popularisation of wearable and portable devices. Compared with conventional cell designs, such as sandwich or planar-type, fibre SCs exhibit some unique benefits in terms of flexibility, light weight and structural variety. Excitingly, they also show large specific volume power density, which planar SCs cannot match. For fibre SCs, the structures are numerous and substantial effort has been devoted in developing novel constructions. One simple design involves merely placing two fibre electrodes coated with gel electrolyte in parallel, with space in between, on a flexible substrate (see Fig. 20).[97a] These fibre SCs can be easily integrated in the single fibre SC in series or in parallel, which can enhance the current and potential to meet the power and energy requirements for practical microelectronics. Carbon-based materials, such as CFs, CNTs, graphene and mesoporous carbon, can be made into various fibre and yarn forms. They can be also hybridised with selected electrical active materials with faradaic pseudocapacitance, namely, metal oxides, hydroxides and conducting polymers.

7.4 Wire-type design

The rise of wearable electronics necessitates developing wire-shaped SCs that can be easily weaved into the wearables. Although the aforementioned SCs have many advantages, they are not true fibre SCs in the strict sense, because planar substrates are commonly used for support. True fibre SCs should be presented as a single-wire architecture in which one fibre electrode is wound around the other with a gel electrolyte filling in between.[445] For instance, wire-type SCs are assembled using two nickel fibre/$NiCo_2O_4$ fibres where one fibre is wound around the other with PVA–KOH gel electrolyte.[97b] This cell design is also recognised as coil-type SCs (as presented in Fig. 20). Its electrochemical performance can be examined under different mechanical deformations, such as stretching, bending, folding and winding. However, the gel electrolyte might be destroyed and the two electrodes separated from each other when bent owing to the stress between the metal current collectors. Therefore, optimised structures should be designed to increase mechanical stability.

7.5 Cable-type design

The unreliable device structure of wire-type SCs, which can cause serious short-circuit and leakage problems because the fibre electrodes are in direct contact makes them unsuitable for practical applications. In this context, a novel cable-type SC has been developed. It has a similar structure to wire-type SCs, but has an additional spacer wire as shown in Fig. 20. The spacer wire is evenly twisted onto the surface of one fibre electrode with a specific pitch. A spacer is required in traditional flat SCs to effectively prevent short circuits caused by the direct contact of two electrodes. Common spacers also require a porous structure for ion transport, and hence, they usually have porous polymer membranes. In 2012, a cable-type SC that had a commercial pen ink-coated fibre electrode, gel electrolyte and helical spacer wire was demonstrated.[469b] It was found that the spacer wire not only prevents short circuiting during bending, but also plays a key role in efficiently transporting ions and allows easy preparation of large-size FSCs.

Table 4 Summary of electrochemical performances of flexible solid-state asymmetric designs based on different positive and negative electrodes with corresponding gel–electrolytes

Positive electrode	Negative electrode	Electrolyte	Voltage window	Specific capacitance	Max. energy density	Max. power density	Cycling stability	Ref.
$Co_{2.18}Ni_{0.82}Si_2O_5(OH)_4$	Graphene	KOH/PVA	1.75 V	194.3 mF cm^{-2} at 0.50 mA cm^{-2}	0.496 mW h cm^{-3}	38.8 mW cm^{-3}	96.3% after 10 000 cycles	421
Graphene/MnO_2	Graphene/polypyrrole	KOH/PVA	1.8 V	2.69 F cm^{-3} (175.2 F g^{-1}) at 1 mA cm^{-2}	1.23 mW h cm^{-3}	—	90.2% after 10 000 cycles	422
CW/PNC/PEDOT	CW/CMK-3	KOH/PVA	1.45 V	31.6 mF cm^{-2} (3.16 F cm^{-3}) at 0.4 mA cm^{-2}	0.011 mW h cm^{-2}	7.8 mW cm^{-2}	106% 1400 cycles	423
Mn_3O_4/NGP	$Ni(OH)_2$/NGP	NaOH/PVA	1.3 V	1.96 F cm^{-3} at 50 mV s^{-1}	0.35 mW h cm^{-3}	32.5 mW cm^{-3}	83% after 12 000 cycles	424
TiN@GNSs	Fe_2N@GNSs	LiCl/PVA	1.6 V	60 F g^{-1} at 50 mV s^{-1}	15.4 W h kg^{-1}	6.4 kW kg^{-1}	98% after 20 000 cycles	414
$Ni_{20}[(OH)_{12}(H_2O)_6][(HP_4)_8(PO_4)_4]\cdot12H_2O$	Graphene	KOH/PVA	1.47 V	148 F cm^{-2} at 0.5 mA cm^{-2}	0.446 mW h cm^{-3}	44.1 mW cm^{-3}	97.4% after 5000 cycles	425
$NaCoPO_4$–Co_3O_4	Graphene	KOH/PVA	1.0 V	28.6 mF cm^{-2} at 0.1 mA cm^{-2}	0.39 mW h cm^{-3}	50 mW cm^{-3}	94.5% after 5000 cycles	426
$NiCo_2O_4$@PPy	Activated carbon (AC)	KOH/PVA	1.6 V	165.4 F g^{-1} at 1 mA cm^{-2}	58.8 W h kg^{-1}	10.2 kW kg^{-1}	89.2% after 5000 cycles	427
Co_3O_4@C@Ni_3S_2	AC	KOH/PVA	1.8 V	—	1.52 mW h cm^{-3}	60 000 mW cm^{-3}	91.43% after 10 000 cycles	428
MoS_2–rGO/MWCNT	rGO/MWCNT	H_2SO_4/PVA	1.4 V	5.2 F cm^{-3} at 0.16 A cm^{-3}	—	—	100% after 7000 cycles	429
Carbon fiber (CF)–$Ni(OH)_2$	CF–CNT	KOH–PVA	1.3 V	—	41.1 W h kg^{-1}	3.5 kW kg^{-1}	98% after 3000 cycles	430
$K_2Co_3(P_2O_7)_2\cdot2H_2O$	Graphene	KOH/PVA	1.07 V	6 F cm^{-3} at 10 mA cm^{-3}	0.96 mW h cm^{-3}	54.5 mW cm^{-3}	94.4% after 5000 cycles	431
MnO_2/graphene/CF	Graphene hydrogel (GH)/copper wire (CW)	KCl/PAAK	1.6 V	2.54 F cm^{-3} at 0.2 mA cm^{-2}	0.9 mW h cm^{-3}	200 mW cm^{-3}	90% after 10 000 cycles	432
CF@RGO@MnO_2	CF@TRGO	KCl/PAAK	1.6 V	—	1.23 mW h cm^{-3}	270 mW cm^{-3}	91% after 10 000 cycles	433
MnO_2	$CoSe_2$	LiCl/PVA	1.6 V	1.77 F cm^{-3} at 1 mA cm^{-2}	0.588 mW h cm^{-3}	282 mW cm^{-3}	94.8% after 2000 cycles	434
$NiCo_2O_4$/CC	Porous graphene papers (PGP)	LiOH/PVA	1.8 V	71.32 F g^{-1} at 5 mA cm^{-2}	60.9 W h kg^{-1}	11.36 kW kg^{-1}	96.8% after 5000 cycles	435
$Co_{11}(HPO_3)_8(OH)_6$–Co_3O_4	Graphene	KOH/PVA	1.38 V	1.84 F cm^{-3} at 0.5 mA cm^{-2}	0.48 mW h cm^{-3}	105 mW cm^{-3}	98.7% after 2000 cycles	436
$CoMoO_4$/PPy	AC	KOH/PVA	1.7 V	—	104.7 W h kg^{-1}	971.43 W kg^{-1}	95% after 2000 cycles	437
MnO_2	Fe_2O_3	$LiClO_4$/PVA	2.0	147 F g^{-1} at 5 mV s^{-1}	41 W h kg^{-1}	10 kW kg^{-1}	95% after 2500 cycles	438
CuO	Fe_2O_3	Na_2SO_4/CMC	2.0	79 F g^{-1} at 2 mA cm^{-2}	23 W h kg^{-1}	19 kW kg^{-1}	90% after 1000 cycles	439
Ni/MnO_2	AC	Na_2SO_4/PVA	2.5 V	2.0 F cm^{-3} at 5 mV s^{-1}	0.78 mW h cm^{-3}	50 mW cm^{-3}	96.3% after 500 bending Cycles	82
Cobalt carbonate hydroxide/N-doped graphene	N-Doped graphene	KOH/PVA	1.9 V	153.5 mF cm^{-2} at 1.0 mA cm^{-2}	0.077 mW h cm^{-2}	2.5 mW cm^{-2}	93.6% after 2000 cycles	440
γ-MnS	Eggplant derived AC (EDAC)	—	1.6 V	110.4 F g^{-1} at 1.0 mA	37.6 W h kg^{-1}	181.2 W kg^{-1}	89.87% after 5000 cycles	441
$NiCo_2Se_4$	$NiCo_2O_4$@PPy	KOH/PVA	1.7 V	14.2 F cm^{-3} at 63.7 mA cm^{-3}	5.18 mW h cm^{-3}	260 W cm^{-3}	94% after 5000 cycles	442
CoS	AC	KOH/PVA	1.8 V	47 F g^{-1} at 2 A g^{-1}	5.3 W h kg^{-1}	1.8 kW kg^{-1}	92% after 5000 cycles	443
Human hair/Ni/Graphene/MnO_2	Human hair/Ni/Graphene	KOH/PVA	1.8 V	4.10 F cm^{-3} at 100 mV s^{-1}	1.81 mW h cm^{-3}	—	83.3% after 5000 cycles	444
Carbon fiber/MnO_2	Carbon fiber/MoO_3	KOH/PVA	2.0 V	3.20 mF cm^{-2} at 5 mA cm^{-2}	0.0027 mW h cm^{-2}	0.53 mW cm^{-2}	89% after 3000 cycles	445
Co_3O_4/$Co(OH)_2$	AC	KOH/PVA	1. 4 V	210 mF cm^{-2} at 0.3 mA cm^{-2}	9.4 mW h cm^{-3}.	354 mW cm^{-3}	97.6% after 5000 cycles	446

Table 4 (*continued*)

Positive electrode	Negative electrode	Electrolyte	Voltage window	Specific capacitance	Max. energy density	Max. power density	Cycling stability	Ref.
MnO_2	CoP	LiCl/PVA	1.6 V	1.94 F cm^{-3} at 1 mA cm^{-2}	0.69 mW h cm^{-3}	114.2 mW cm^{-3}	82% after 5000 cycles	447
$CoMoO_4$	Fe_2O_3	KOH/PVA	1.5 V	3.6 F cm^{-3} at 1 mA cm^{-2}	1.13 mW h cm^{-3}	150 mW cm^{-3}	93.1% after 5000 cycles	448
$CoMoO_4$@$NiMoO_4{\cdot}xH_2O$	Fe_2O_3	KOH/PVA	1.6 V	153.6 F g^{-1} at 1 A g^{-1}	41.8 W h kg^{-1}	12 kW kg^{-1}	89.3% after 5000 cycles	449
CuS/3D graphene	3D graphene	KOH/PVA	1.6 V	32 F g^{-1} at 1 A g^{-1}	5 W h kg^{-1}	3.2 kW kg^{-1}	77% after 1000 cycles	450
Co_3O_4	AC	KOH/PVA	1.5 V	215 mF cm^{-2} at 1.5 mA cm^{-2}	—	—	90.7% after 1000 cycles	451
MnO_2	Porous carbon cloth	PVA/LiCl	2 V	1515 mF cm^{-2} at 2 mA cm^{-2}	0.841 mW h cm^{-2}	—	96% after 20 000 cycles	452
MnO_2@CNTs@3D graphene foams	Ppy@CNTs@3D graphene foams	Na_2SO_4/PVA	1.8 V	8.56 F cm^{-3} (950 mF cm^{-2}) at 1 mA cm^{-2}	3.85 mW h cm^{-3}	630 mW cm^{-3}.	84.6% after 20 000 cycles	453
MnO_2@PANI	3D graphene foam (GF)	KOH/PVA	1.5 V	95.3 F g^{-1} at 1 A g^{-1}	37 W h kg^{-1}	386 W kg^{-1}	89% after 5000 cycles	454
$Ni(OH)_2$–N-doped graphene (NG)	NG	H_2SO_4/PVA	1.45 V	255 mF cm^{-2} at 1.0 mA cm^{-2}	79.5 mW h cm^{-2}	944 mW cm^{-2}	92% after 10 000 cycles	455
Ni-Co LDHs/pen ink/nickel/CF	Pen ink/nickel/CF	KOH/PVA	1.55 V	28.67 mF cm^{-2} at 0.5 A g^{-1}	0.00957 mW h cm^{-2}	1.841 mW cm^{-2}	86% after 5000 cycles	456
Ni–Co@Ni–Co LDH	Carbon fibers	KOH/PVA	1.5 V	319 F g^{-1} at 2 A g^{-1}	100 W h kg^{-1}	15 kW kg^{-1}	98.6% after 3000 cycles	457
Co_3O_4-nanocube/$Co(OH)_2$-nanosheet	AC	KOH/PVA	1.4 V	210 mF cm^{-2} at 0.3 mA cm^{-2}	9.4 mW h cm^{-3}	354 mW cm^{-3}	97.6% after 5000 cycles	458
$NiCo_2S_4$@$NiCo_2O_4$	AC	KOH/PVA	1.6 V	0.41 F cm^{-2} at 2 mA cm^{-2}	44.6 W h kg^{-1}	6.4 kW kg^{-1}	92.5% after 6000 cycles	459
$NiCo_2S_4$/polyaniline	AC	KOH/PVA	1.6 V	152.1 F g^{-1} at 1 A g^{-1}	54.06 W h kg^{-1}	27.1 kW kg^{-1}	84.5% after 5000 cycles	460
NiCo-LDH	Carbon nanorods	KOH/PVA	1.7 V	147.6 F g^{-1} at 1 A g^{-1}	59.2 W h kg^{-1}	34 kW kg^{-1}	82% after 5000 cycles	461
MnO_2	Carbon	LiCl/PVA	2.0 V	71.856 mF cm^{-2} at 0.5 mA cm^{-2}	0.766 mW h cm^{-3}	142.56 mW cm^{-3}	91.4% after 4000 cycles	462
MnO_2 nanorods/rGO	MoO_3 nanorods/rGO	H_3PO_4/PVA	1.6 V	51.2 F cm^{-3} at 2 mV s^{-1}	18.2 mW h cm^{-3}	3269 mW cm^{-3}	96.8% after 3000 cycles	463
$Ni(OH)_2$/RGO/Ni	RGO aerogel/Ni	KOH/PVA	1.6 V	69 F g^{-1} at 2 A g^{-1}	24.5 W h kg^{-1}	10.3 kW kg^{-1}	83% after 6000 cycles	464
$ZnCo_2O_4$	VN	KOH/PVA	1.6 V	196.43 mF cm^{-2} at 1 mA cm^{-2}	64.76 mW h cm^{-3}	8000 mW cm^{-3}	87.9% after 4000 cycles	465
MOF–MnO_x	AC	KOH/PVA	1.2 V	175 mF cm^{-2} at 0.5 mA cm^{-2}	5.1 mW h cm^{-3}	120 mW cm^{-3}	94.5% after 10 000 cycles	393
CuO nonowires@ CoFe-layered double hydroxide (CoFe-LDH)	Cu–AC	KOH/PVA	1.2 V	9.38 F cm^{-3} at 0.25 A cm^{-3}	1.857 mW h cm^{-3}	914.5 mW cm^{-3}	99.5% after 2000 cycles	466
rGO/CoAl-LDH	rGO	KOH/PVA	1.2 V	99.5 F g^{-1} at 1 A g^{-1}	22.6 W h kg^{-1}	1.5 kW kg^{-1}	94% after 5000 cycles	467
ZnO@C@CoNi-LDH	Fe_2O_3@C	KOH/PVA	1.6 V	30.9 mF cm^{-2} at 1 mA cm^{-2}	1.078 mW h cm^{-3}	0.4 W cm^{-3}	95% after 10 000 cycles	468

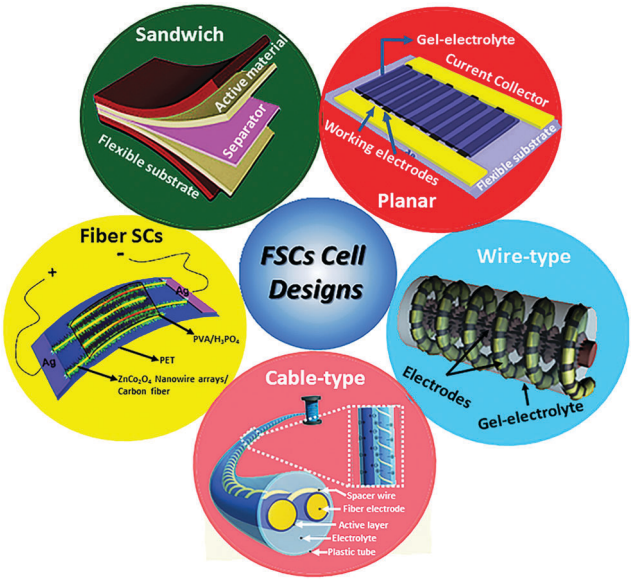

Fig. 20 Recently developed innovative cell designs conventional sandwich-type, planar, fiber, wire-type and cable-type. Reprinted with the permission from ref. 2c, 97a, 434, 445 and 466, Copyrights Royal Society of Chemistry, Wiley-VCH Verlag GmbH & Co. KGaA, Weinheim, and Elsevier, respectively.

In summary, the three main cell designs are sandwich-type, planar and fibre SCs. Fibre SCs can be categorised into fibre on plane, wire-type and cable-type SCs. Sandwich-type SCs are the most common cell design as these can be fabricated easily. Planar SCs are of high volumetric capacitances and considered promising power sources for implantable medical devices and active radio frequency identification tags. Wire-shaped and cable-type SCs are suitable for wearable energy textiles and can be designed to stretch. Thus, all the three cell structures are important depending on the application perspective. Thus, the design of FSSCs to integrate into a wearable electronics require to be safe, must exhibits good mechanical flexibility and store sufficient amount of energy to satisfy the application requirements. More essentially, flexibility is frequently mentioned as a strict requirement for wearable electronics.

8. Some practical applications

8.1 Piezoelectric supercapacitors

In recent years, various novel implantable/wearable healthcare devices (*e.g.*, spirometers, sphygmomanometers and wristbands) have been employed in a broad range of applications ranging from physical activity monitoring to more analytical applications, such as diet tracking, mental stress detection and rehabilitation.[470] However, the flexible efficiency of the power supply unit remains a bottleneck for wearable electronics. Thus, a new self-sustainable energy storage device that can harvest/store body energy (such as that generated through breathing, arm pressing and chest compression) and power smart electronics shows great potential for application in next-generation implantable/wearable electronics. The recent discovery of electricity generation using piezoelectric ZnO NWs has attracted significant attention to the use of piezoelectric materials in energy harvesting and transducer technology.[471] Piezoelectric materials can convert ubiquitously irregular and low-frequency mechanical vibrations into electricity and have been extensively studied for their use as nanogenerators.[472] Thus, mechanical vibrations (energy) can be efficiently converted and stored in piezoelectric SCs using a piezoelectric film to replace traditional separators. Owing to their excellent piezoelectric properties and mechanical flexibility, polyamide (PA) and PVDF films have been demonstrated as wearable flexible energy generators.[473]

The piezoseparator (piezoelectric film) is a key component in piezoelectric SCs and is typically a well-polarised PVDF film placed between the electrodes. In the piezo-electrochemical mechanism, the external mechanical impact develops a piezoelectric potential across the PVDF films and drive ions in the electrolyte to migrate towards the SC electrode interface (forming an electronic double layer or pseudocapacitance at the interface), storing the electricity as electrochemical energy (Fig. 21(a)). Thus, the integration of energy generation (mechanical generation of energy from a piezoelectric potential) and storage (storing in SCs) systems can effectively supply power without using an external DC source.[474]

An FSSC was assembled using functionalised carbon cloth as positive and negative electrodes with polarised PVDF films coated with a H_2SO_4/PVA gel electrolyte.[475] The integrated piezoelectric SC exhibited a specific capacitance of 357.6 F m^{-2} (current density: 8 A m^{-2}), a power density of 49.67 mW h m^{-2} and an energy density of 400 mW m^{-2}. Moreover, when the SSC was charged under a continuous compressive force with an average frequency of 4.5 Hz, the voltage of the piezoelectric SC increased to 100 mV within 40 s. The stored electric energy was determined from the discharge curve as 0.25 mA h at a constant current of 100 mA. More recently, the integration of a pseudo-SC and piezoelectric materials as a hybrid energy harvesting and storage device was realised using pseudocapacitive MnO_2 NWs as positive and negative electrodes and PVDF–ZnO coated with H_3PO_4/PVA film as the separator (as well as a piezoelectric).[476] The addition of ZnO NWs in the PVDF matrix induced polarisation of ions in the composite film without electrical poling. When a compressive force with palm impact was applied, the voltage of the device increased from 35 to 145 mV (110 mV charged) in 300 s. In addition, after realising the compression force, the device sustained the stored energy for ~150 s. The fabrication of flexible piezoelectric SCs using a laser engraving technique by integrating a triboelectric nanogenerator and an MSC array into a single device was recently reported.[477] A high degree of integration was realised through double-faced laser engraving of the PI substrate. The triboelectric nanogenerator and MSC were fabricated by using two sides of the laser-induced graphene. The nanogenerator generated electricity from ambient mechanical vibrations with high output, while the rectified electrical energy was directly stored in the MSC that could be charged to 3 V in 117 min.

8.2 Photo-supercapacitors

Solar energy, the cleanest and most easily available energy source to date, is unfortunately limited by access to sunlight. Integrating solar

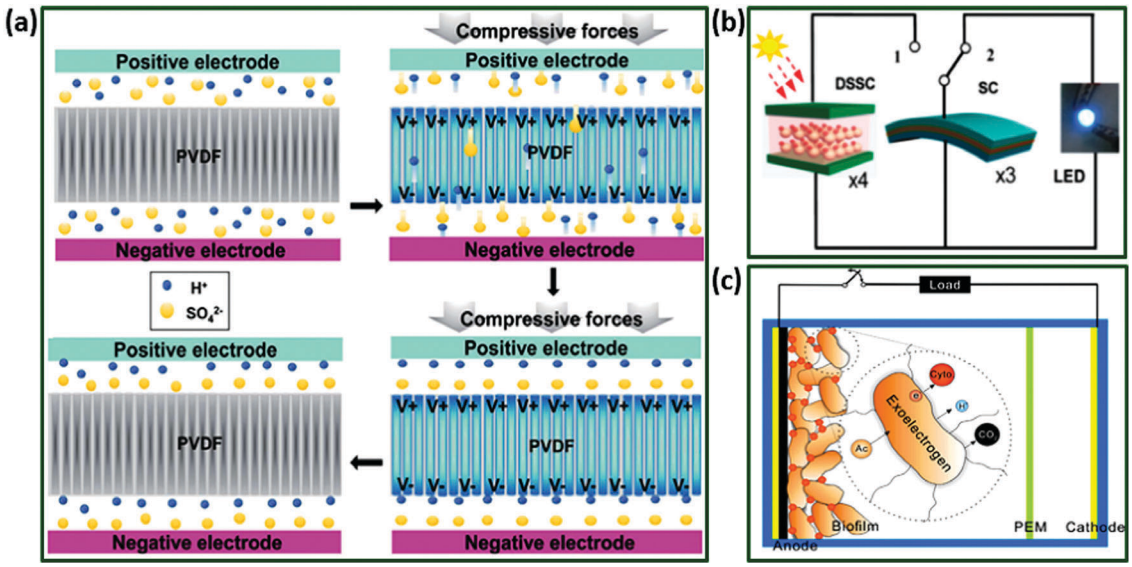

Fig. 21 (a) Proposed working mechanism of the piezo-supercapacitor. Reproduced with the permission from ref. 471, Copyright 2015, Royal Society of Chemistry. (b) Schematic of a self-powered system consisting of DSSCs and FSSCs, and one LED. Reproduced with the permission from ref. 474*b*, Copyright 2015, Elsevier. (c) Working principle of the microbial supercapacitor (MSC): when a high-speed switch is off, electrons are stored in the biofilm on graphene anode, and when it is on, electrons stored inside biofilm are discharged very quickly, resulting an extremely high current and power density. Reproduced with the permission from ref. 485, Copyright 2015, Elsevier.

cells with energy storage devices is an exclusive strategy to extend the practical applications of solar energy beyond the restrictions imposed by sunlight availability.[376] A complete energy conversion and storage device, known as photo-supercapacitors (photo-SCs), can be fabricated by coupling solar cells and SCs, whereby solar energy can be efficiently transferred and converted to electrical energy by adopting an SC as the energy delivery system (schematically shown in Fig. 21(b)[478]).

A coaxial, all-solid-state 'energy fibre' was introduced by integrating a dye-sensitised solar cell (DSSC) with SCs comprising CNTs@Ti wire electrodes and a PVA–H_3PO_4 gel electrolyte.[479] The photoelectric conversion efficiency was determined as 2.73%, while the energy storage efficiency reached 75.7% with specific capacitances up to 0.156 mF cm^{-1} (3.32 mF cm^{-2}) and power densities up to 0.013 mW cm^{-1} (0.27 mW cm^{-2}) at a current of 50 mA. Similarly, Zhang *et al.*[480] assembled coaxial SCs by coupling P3HT:PCBM@TiO_2@Ti wire (PCBM: [6,6]-phenyl-C61-butyric acid methyl ester) and PEDOT/PSS as the photo-electrode and MWCNTs as the SC electrode with a PVA/H_3PO_4 electrolyte. The photo-conversion and energy storage efficiencies were investigated as a function of MWCNT length in the SCs, achieving 0.4% and 0.82 optimum performance, respectively. Further, the coaxial structure offers good effective contact area and favours rapid charge transport. It can be easily woven into various structures, such as lightweight textiles.

In addition to DSSC, a wearable energy-smart ribbon photo-SC was recently demonstrated by integrating a perovskite solar cell (PSC) on top of a symmetric SC.[481*a*] This flexible integrated device displayed the highest photo-conversion efficiency (10.41%), while the energy storage efficiency was ~67%. The SC held an energy density of 1.15 mW h cm^{-3} and a power density of 243 mW cm^{-3} under solar illumination. Even with their stability and the need for appropriate sealing to prevent fast environmental ageing of the PSCs concerned, DSSCs represent a more reliable technology for integrated devices. In this context, Chen *et al.*[481*b*] reported a high-performance fibre-shaped integrated energy wire, comprising a DSSC and FSSC. In this case, they used radially grown titania nanotubes on a titanium wire as the core electrode for both the solar cell and SCs and wrapped an aligned CNT fibre around the titanium wire, after coating with electrolytes, as the top electrode for the solar cell and SC. Interestingly, the SC in this integrated cell was rapidly charged to a voltage close to the open-circuit voltage of the DSSC upon light irradiation. An entire energy conversion and storage efficiency of up to 1.5% was obtained.

8.3 Shape-memory supercapacitors

Many recent applications (wearable electronics, bendable smart phones and biomedical devices) and their energy storage devices undergo irreversible deformation. Therefore, electronic devices and their power units need to exhibit mechanically deformable ability. Thus, stretchable, compressible and shape-memory (shape-recoverable) SCs have attracted considerable attention for use in future applications.[12]

The shape-memory materials incorporated SCs can recuperate back to their original dimensions after severe deformations. Typically, shape-memory materials can be classified into two types such as shape-memory alloys (SMAs) and polymers (SMPs).[482] For SMAs materials, shape-memory effect is raised through a reversible crystalline phase change called as a martensite-austenite transformation. When heated to a certain temperature, the deformed SMAs return to their original shape and all plastic deformations are removed. The most prominent SMAs are based on nickel-titanium (NiTi) owing to its superior mechanical and electrical characteristics.

A shape-memory SC was realised using graphene coated on TiNi alloy flakes as the negative electrode and an ultrathin MnO_2/Ni film as the positive electrode in gel electrolytes.[482] It displayed a specific capacitance of 53.8 F g^{-1} at 0.5 A g^{-1}. The bent device regained its original planar shape within 550 s when heated to ambient temperature. The recovery speed of this SC was relatively low. Recently, NiTi wires were applied as current collectors and substrates for active materials (MnO_2 and PPy) in a twisted fibre shape-memory SC, whereby serious plastic deformations were restored to an undistorted state within a few seconds[483] while maintaining near-identical capacitive performance.

Above the glass-transition temperature (T_g; amorphous polymers) and melting temperature (T_m; crystalline polymers), SMPs are soft and lightweight and can be extended to several hundred per cent. SMPs can memorise more than one shape and recover their original form when subjected to various stimuli, such as temperature, light, magnetic fields and electric currents. Wrapping aligned CNT sheets onto a shape-memory polyurethane (SMPU) substrate enabled a shape-memory and fibre-shaped MSC.[484] After 500 cycles of deformation and recovery at a strain of 50%, its electrochemical properties exhibited no significant decrease, suggesting excellent stability of the device structure. However, its maximum specific capacitance was only 42.3 mF cm^{-1}, which could be enhanced by introducing pseudocapacitve materials. Densely compacted CNT layers and PANi layers were coated on the PVA/CNT SMPU fibres through layer-by-layer technology.[485] The resulting shape-memory SCs possessed shape-memory properties and exhibited outstanding specific capacitance values exceeding 427 F cm^{-3}.

8.4 Microbial supercapacitors

A microbial electrochemical technique converts biomass directly to electricity or fuel, harvesting electrons from specific bacterial species known as '*exoelectrogens*' ('exo:' out of; 'electrogene:' bacteria-producing electrons) *via* their unique extracellular electron transport. The schematic representation of working mechanism of microbial SCs (MSC) is presented in Fig. 21(c). Exoelectrogens have been implemented in various microbial electrochemical technologies, such as microbial fuel cells (MFCs), microbial electrolysis cells and microbial reverse electrodialysis cells (MRCs).[486] Recently, several reports have demonstrated that exoelectrogens, such as geobacter, shewanella and proteobacteria, store electrons and can be used as capacitors[487] with a current density in the range of 1.2–90 A m^{-2}. The high current density observed in these reports demonstrated the ability to use biological pseudocapacitance as a potential renewable method for energy generation and storage.

In 2012, Malvankar *et al.*[488] demonstrated the pseudocapacitive redox nature of *c*-type cytochrome biofilms. These biofilms displayed low self-discharge and good charge/discharge reversibility. The capacitance of *G. sulfurreducens* biofilms was determined as 620 μF cm^{-2} at the open-circuit potential. A novel bio-inspired microbial SC was recently presented utilising pseudocapacitance generated by an exoelectrogen, *Geobacter* spp., grown on a single-layer graphene film and 3D graphene-scaffold electrodes.[489] Charging and discharging the microbial SC were performed by regulating the exoelectrogen respiration (Fig. 21(c)). The microbial SC delivered a specific capacitance of 17.85 mF cm^{-2} with outstanding cycling stability over one million cycles. It also demonstrated maximum current and power densities of 531.2 A m^{-2} (1 060 000 A m^{-3}) and 197.5 W m^{-2} (395 000 W m^{-3}), respectively. Notably, its areal power density was 2.5-fold, 19-fold, three orders of magnitude and four orders of magnitude greater than those of solar cell (outdoor), enzymatic fuel cell, thermoelectric energy harvester and radio frequency (RF) energy harvester, respectively.[490]

8.5 Electrochromic supercapacitors

Some electrode materials have the ability to change their colour reversibly during the electrochemical reduction/oxidation processes, and this phenomenon is clearly observed when the material is deposited over the transparent current collectors, such as fluorine-doped tin oxide (FTO) and tin-doped indium oxide (ITO).[491] Electrochromism is a phenomenon discovered 50 years ago.[492] Since then, considerable progress has been achieved in synthesising electrochromic (EC) materials to fabricate EC devices, improving EC properties and applying EC materials that have been extended to smart windows, displays, antiglare mirrors and active camouflage gear.[493] Some electrode materials have the ability to store electrical charge by reversible changing of their colours. Such materials can be used to develop an integrated energy storage and EC device. Some transition metal oxides or conductive polymers (*e.g.*, polyaniline) can serve as active materials for SCs as well as EC devices because they use fast faradaic reactions between the active materials and electrolytes.[494]

Among different electrode materials, tungsten oxides (WO_3) have been reported to be suitable for use as smart materials for SCs as well as for EC devices.[495] Yang *et al.*[496] developed multifunctional glass windows through the facile thermal evaporation and electrodeposition method that combines energy storage and electrochromism in a single device. The prepared WO_3 films on FTO glass exhibited a high specific capacitance of 639.8 F g^{-1}. During electrochemical CV or galvanostatic CD measurements, the WO_3 reveals its EC property by changing its colour. Both the pseudocapacitive behaviour and the electrochromic response are because of the redox reactions between W^{6+} and W^{5+}, which are accompanied by H^+ insertion/extraction. During the electrochemical reaction, WO_3 optical transmittance abruptly decreased from 91.3% to 15.1% at a wavelength of 633 nm when a voltage of 0.6 V *vs.* Ag/AgCl was applied. Similarly, some reports compare the electrochromic SC with different materials, such as the NiO,[497] PANi[498] and V_2O_5[499] with conventional rigid current collectors.

However, ITO and FTO are unsuitable for flexible electronics applications owing to their brittleness and the high cost of the preparation procedure. Few reports are available on the flexible EC supercapacitors (ECSCs). Chen *et al.*[500] developed EC fibre-shaped SCs where CNTs were wound onto a stretched elastic fibre (with a strain of 100%) to form sheet-like structures of aligned CNTs and PANI was then electrodeposited on the

two separated CNT sheets to prepare CNT/PANI composite electrodes. The two CNT/PANI composite electrodes were further coated with PVA/H_3PO_4 gel electrolyte to produce the desired fibre-shaped SC. In this SC, charges are stored and released mainly through the redox reaction of PANI, with a small contribution from the electrical double layers at the electrode/electrolyte interface. During the charge/discharge processes, the composite electrodes changed colour in response to the varying potentials. Both the electrodes of symmetric EC supercapacitor demonstrated rapid and reversible chromatic transitions between blue, green and light yellow under different working states. Apart from the chromatic transition properties, the SC delivered a decent electrochemical performance. A specific capacitance of 255.5 F g^{-1} (0.1890 mF cm^{-1}) was achieved with energy density of 12.75 W h kg^{-1} and power density of 1494 W kg^{-1}.

Yao *et al.*[501a] designed a flexible ITO-free ECSC using a hybrid graphene/CuS network on PET (G-CuS) as the transparent conductive electrode (TCE) with PVA–H_2SO_4 gel electrolyte. This new type of TCE was produced by photolithography, CVD and a low temperature solvothermal reaction. It exhibited an R_s of $\sim$20 Ω sq^{-1} at $\sim$85% transmittance, which is superior to sputtered CuS films. In addition, the G-CuS TCE displayed remarkable mechanical flexibility and excellent chemical stability under bending stress and PANi electrodeposition in acid solution, respectively. Further, they assembled a symmetrical SC, which showed excellent electrochromic response during the galvanostatic charge/discharge process. Likewise, Zhang and co-workers[501b] fabricated first stimulus-responsive FSSCs (SR-FSSC) with a reversible electrochromic window. A hybrid nanopaper based on exfoliated graphene (EG) and V_2O_5 nanoribbons (EG/V_2O_5) was prepared as an electrode for FSSC. The device delivered a capacitance of 130.7 F cm^{-3} at 10 mV s^{-1} with energy density of 20 mW h cm^{-3}. After solidification of the electrolyte together with methyl viologen, the resulting SR-FSSC manifested a remarkable reversible electrochromic effect during the charge/discharge process within 0–1 V, which provided a direct visual observation of the charge/discharge state of the FSSCs. Despite these advancements, numerous opportunities are available for development of flexible ECSCs for real practical application by exploring the different transparent flexible substrates and electrode materials.

8.6 Self-healing supercapacitors

During the long life cycling, SCs inevitably suffer from all types of local stress under bending or other deformations, which may cause permanent mechanical failure over time. Such unavoidable failure would seriously limit the SC lifespan and reliability, resulting in device malfunction.[502] Therefore, it is necessary to develop an SC device that can restore its configuration and electrical properties after mechanical damage. Self-healable SCs are recently developed to overcome these issues by using the self-healable materials. These materials are able to heal and repair damages autonomically or in response to external stimuli, such as changes in pH, heat or light. Huang *et al.*[503] developed a self-healable yarn-based SC by wrapping magnetic electrodes around a self-healing polymer shell. The strong force from magnetic attraction between the broken yarn electrodes allows reconnection of fibres in the yarn electrodes during self-healing and thus offers an effective strategy for the restoration of electric conductivity, whereas the polymer shell recovers the configuration integrity and mechanical strength. In their construction, stainless steel yarn was treated with the microwave-assisted hydrothermal method several times to ensure enough magnetic Fe_3O_4 particles to nucleate and crystallise on the surface of the yarn. Then, a 2 μm thick layer of polypyrrole (PPy) serving as the active material was electrodeposited on the annealed black yarn, which not only guarantees adequate SC performance, but also wraps up the Fe_3O_4 magnetic particles and protects them from being ripped off during applications. Two Fe_3O_4/PPy-coated yarns were integrated to form a device with PVA–H_3PO_4 gel electrolyte. Lastly, self-healing carboxylated polyurethane (PU) was introduced to the outermost SC layer as a protection shell to make the device self-healable. The self-healing performance is attributed to the existence of a large amount of hydrogen bond acceptors and donors in the supramolecular network of carboxylated PU. Moreover, the solid electrolyte, PVA gel, is a type of self-adhering material and can self-heal to some degree. Once the SC is subjected to mechanical damage, the external movement of the self-healing shell brings the broken areas into contact and realises mechanical self-healing autonomically, while the broken magnetic electrodes are electrically reconnected and aligned with the assistance of their own magnetic force. The synergistic effects between the self-healing shell and magnetic electrodes enable the device to restore its configuration and electrochemical performance. Up to 71.8% of the specific capacitance is recovered even after four breaking–healing cycles. Moreover, the mechanical properties of the whole device can be well maintained after multiple such cycles.

Similarly, Wang *et al.*[504] developed a mechanically and electrically self-healing SC by spreading SWCNT and flower-like TiO_2 nanostructures onto self-healing substrates. The interaction between TiO_2 nanospheres and supramoleculars by hydrogen bonds can retain the shape of supramolecular networks and enhance their transition temperature (T_g). The as-prepared SCs exhibited excellent electrochemically self-healing performance by restoring 85.7% of initial capacitance even after the fifth cutting. Sun *et al.*[505] also developed self-healable wire-shaped SCs using self-healing polymer (SHP) fibres with scrolled CNTs added onto it. When the broken parts were brought back into contact, tensile strengths were maintained at 79.1 and 72.5% after self-healing for one and five cycles, respectively. Its mechanical flexibility was also tested by recording change in resistance before and after self-healing. It is observed that upon breaking, the resistance of a CNT/SHP fibre with a length of approximately 1.5 cm increased from about 200 to over 10^7 Ω. After the two broken cross-sections regained contact, resistance recovered to approximately 600 Ω as a result of the reconstruction of the conducting CNT layer on the surface. Notably, resistance further decreased to 250 Ω when the two cross-sections in contact were pressed together gently. Further,

the electrochemical performance of the self-healable wire-shaped SCs was improved by introducing PANI onto the CNTs. Introducing PANI was not detrimental to self-healing performance, and the specific capacitance was maintained up to 92% after one self-healing process.

The electrolyte is the component that determines the performance of self-healable SCs. Recently, a new electrolyte that consists of polyacrylic acid dual cross-linked by hydrogen bonding and vinyl hybrid silica nanoparticles (VSNPs-PAA)[506] was developed for self-healable SCs. The prepared polyelectrolyte possesses the advantages of tunable ionic conductivity, self-healability and high stretchability. Additionally, the movable protons in the polyelectrolyte provide an equivalent electrode capacitance compared with the commonly used PVA/H_3PO_4 electrolyte. It can be easily self-repaired at room temperature and can be stretched over 3700% without it cracking, suggesting effectively reversible cross-linking interactions through stress transfer and energy dissipation. When this polyelectrolyte was applied in PPy/CNT paper SCs, the device demonstrated over 100% self-healability after 20 breaking–healing cycles with excellent stretchability (600% strain with enhanced performance).

8.7 Integrated supercapacitor-sensor device

On account of increasing social concerns, wearable sensing systems, such as body-attached sensors to monitor health and the environment, UV sensors and body-temperature sensors, are gaining considerable attention. Generally, these sensing systems are externally connected to a power supplying unit, which increases their weight and volume and hinders their applications in wearable electronics. To tackle this problem, an integrated FSSC-sensor device has been developed in which the energy generator, FSSC and sensor were combined on a single platform. Critical requirements to develop such an integrated device are the use of multifunctioning electrode materials and unique device geometry. Several such integrated designs have been developed for different sensing applications.[507,508] For instance, Huang *et al.*[507a] developed integrated wearable devices taking advantages of supercapacitive and photo-sensitive functions of PPy material. In addition, using fabric geometry, SCs and strain sensors were integrated by which energy is generated through piezoresistive properties. A wire-type SC-photodetector integrated device was assembled using PPy-coated CNF electrodes with PVA–H_3PO_4 gel electrolyte. When the device is exposed to visible light, electron–hole pairs are generated in PPy and then separated by an external field that arises from the charged SC. Later, to integrate SCs and a strain sensor in a single device, knitted conducting fabrics comprising PPy@SWCNT-coated cellulose yarn electrodes were prepared. When the device is stretched, the resistance decreases because of increased and closer contact between the conducting yarns, which results in improved discharging current of this wire-type SC. Thus, light or strain stimuli can be detected without external power supply by using these multifunctional PPy materials or fabric geometry.

Kim *et al.*,[507b] fabricated body-attachable multi-sensors operated by integrated SCs, which were repeatedly charged by an integrated wireless RF power receiver. The power receiver wirelessly received energy from the RF power source and stably charged the connected FSSCs made of MWCNTs electrodes and (PEGDA)/[EMIM][TFSI] gel electrolyte. Further, 12.6 W cm^{-3} and 1.5 mW h cm^{-3} were the maximum power and energy densities recorded, respectively. A strain sensor based on fragmentised graphene foam powered by FSSCs successfully detected repeated body motion, voice, swallowing of saliva and carotid artery pulse. In addition, the MWNT/SnO_2 nanowire (NW) hybrid film sensor was integrated with FSSCs to detect both toxic NO_2 gas and UV light. The fabricated sensor integrated with 1.5 V charged FSSCs detected 200 ppm of NO_2 gas under various applied uniaxial strains up to 50% with 76.6 and 17.8 s response and recovery times, respectively. Additionally, the UV sensor had UV sensitivity of approximately 1.0 under 0–50% strain. Response and recovery times for sensing UV light of 312 nm were 5.3 and 6.4 s, respectively, while those for UV light of 254 nm were 4.1 and 4.3 s, respectively. Similarly, an integrated device was assembled using a graphene/ZnO nanoparticle UV sensor and asymmetric micro-SCs (AMSCs) based on MnO_2/MWNTs (positive) and V_2O_5/MWNTs (negative) electrodes on a paper substrate.[507c] The resistor type UV sensor based on graphene/ZnO nanoparticles was patterned to be driven by the stored energy of the integrated AMSCs. The UV sensor and AMSCs were easily integrated on a liquid metal (Galinstan) patterned waterproof mineral paper and showed mechanically stable UV sensing, even after repetitive folding cycles. These AMSCs provided a window up to 1.6 V and demonstrated high cyclic stability with retention of initial capacitance by 86% after 10 000 charge/discharge cycles. Moreover, the fabricated UV sensor was stably operated by the AMSCs, integrated on the same foldable paper substrate with patterned liquid metal interconnections, to detect UV for longer than 1500 s regardless of folding deformation.

9. Prospective applications

9.1 Implantable healthcare/portable devices

A recently invented triboelectric nanogenerator (TENG) is a powerful technique to convert low-frequency mechanical vibrations into electricity. However, because of irregular and fluctuating output electric power of TENGs, they cannot be directly used to drive most electronic devices, which require stable and continuous input power. Given the nature of the pulsed output of TENG, FSSCs are a good choice for developing a self-powered system with TENGs owing to the advantages of ultrafast charging/discharging rates, long life cycles and environmental safety. Thus, integrating nanogenerators and FSSCs can open several opportunities to develop self-sustainable power supplying units for large applications as described below.

- Piezo-SCs can be used in many implantable healthcare devices, such as cardiac pacemaker and insulin pumps, which requires power in the range of microwatts to milliwatts (see Fig. 22(a)). For example, lung motion through breathing can generate up to 1 W of power, which is sufficient to drive pacemakers.

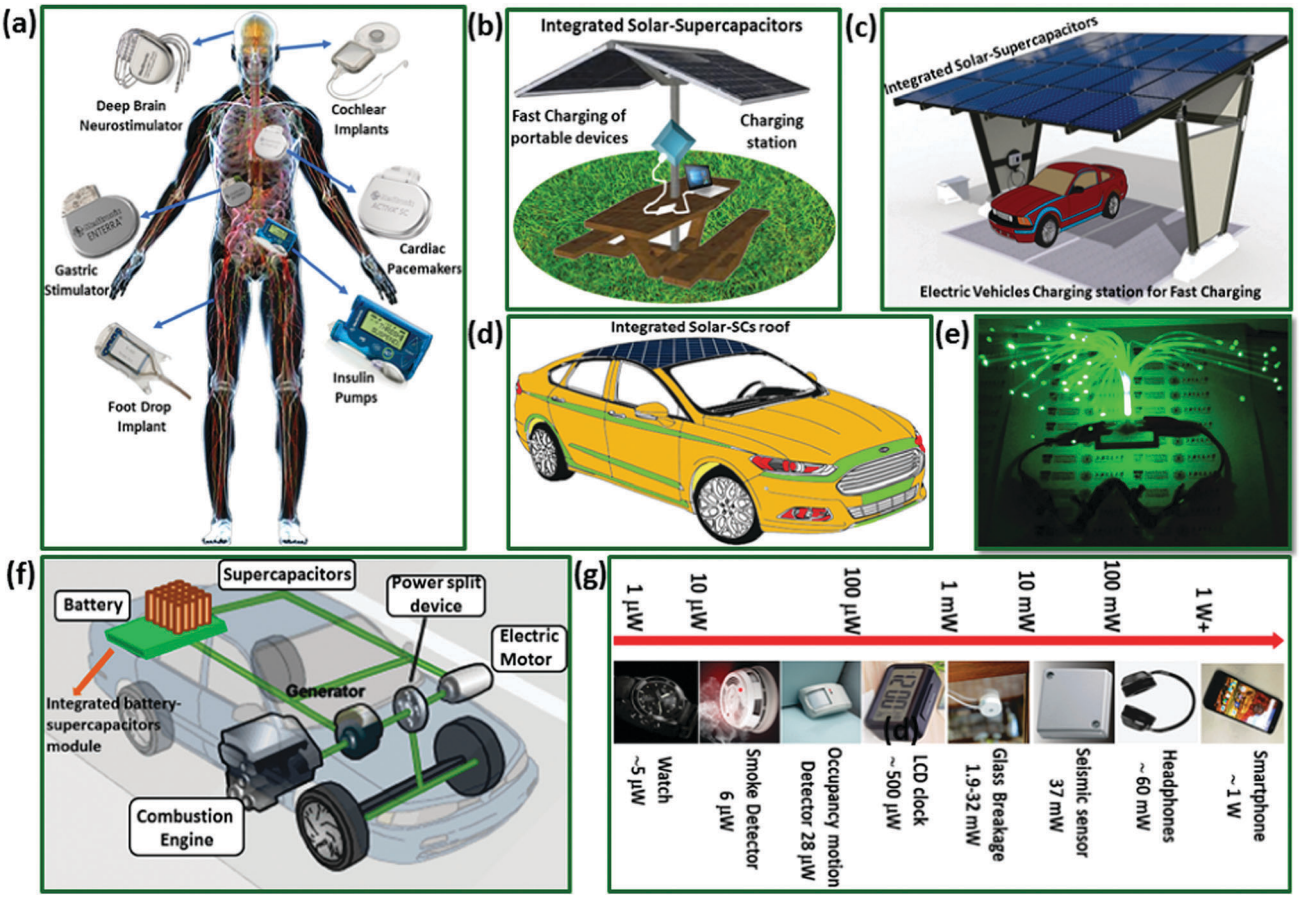

Fig. 22 An overview of several new applications of FSSCs such as (a) implantable medical devices (b and c) solar cell-SCs integrated systems can be implemented as charging stations for fast charging of portable electronic devices, electric vehicles and so on. (d) Integrated solar cell-SCs device mounted on the roof of cars can be used for the fast charging of battery. (e) FSSCs can also be implement for decoration such as LEDs showers as well as LED displays in bus, train and at the bus/train platforms. Reprinted with permission from ref. 58c Nature Publishing Group. (f) SCs-battery integrated system for "regenerative braking" as well as extra energy source in hybrid electric vehicles (HEV) and plug in hybrid electric vehicles (PHEV). (g) Applications of FSSCs in many smart and portable electronic devices such as watch, sensors, mobiles and so on.

In addition, the impact from heels striking the ground when walking is a particularly rich source of energy with 67 W of power available from a brisk walker. Harvesting/storing even 1–5% of that power would be sufficient to run many body-worn multimedia devices.[509]

• TENG-SCs can be employed for a large range of applications, from small-scale wearable electronics (microwatts), such as devices interconnected through the Internet of Things; sensors; wireless communication devices; and devices connected to smart floors with new functions, including for indoor location tracking, activity recognition, home security and energy optimisation[2–5] to large-scale wave energy (ocean wave motions, kW h) harvesting and storage on the grid.

9.2 Solar-supercapacitor charging stations

Integrated solar-SC systems can be used as charging stations on streets or in other public places, such as gardens and parking areas, for quick charging of portable electronic devices and EVs (see Fig. 22(b and c)). Further, solar-SCs systems can be implemented on the roof of cars to power many electronic components in the car, such as sensors, multimedia devices, car wipers and indicators, and to quickly charge the vehicle battery (Fig. 22(d)). A long-time goal has been to install SCs in EVs and HEVs, providing high power capabilities for stop-start and engine starting, torque assist and longer battery life. SCs-battery integrated system can also be used for "regenerative braking" application in HEVs as shown in Fig. 22(f). Many applications of these integrated devices should be available in the near future.

9.3 Defence and aerospace applications

The unique characteristics of FSSCs, including quick power delivery, superior low temperature operation and the ability to handle up to a million cycles, makes them a strong candidate for various military and aerospace applications, such as backup power for electronics in military vehicles, fire control systems in tanks and armoured vehicles, black box on helicopters, backup power/memory hold-up for emergency handheld radios, GPS guided missiles and projectiles and bridge power for switching from a ground system to one onboard an aircraft for data retention.

FSSCs can also be used in many aerospace applications, such as actuator systems for stage separation devices in launch vehicles,

and other functions in satellites and spacecraft systems in which on-board systems require high power density.

9.4 Other applications

Various other very interesting applications using SCs are possible, which also emphasises the economically interesting aspects of SCs for applications of high power density. Additional areas of application include elevators, cranes or pallet trucks in the electric transportation domain, hand tools or flashlights, pulsed laser and welding in the industry and memory supplies in phones or computers. Last but not the least, FSSCs can be applied in many portable electronic devices such as watch, sensors, mobile and so on as displayed in Fig. 22(e and g).

10. Conclusion and future challenges

FSSCs are emerging as breakthrough miniaturised energy storage systems with diverse technological applications, such as wearable electronics, smart clothes, electronic skins and implantable medical devices. This review introduced recent progress in the fundamentals of charge storage mechanisms, emerging new electrode materials and electrolytes, and novel cell designs of FSSCs. To date, studies have demonstrated that excellent progress has been made in developing new flexible electrodes and cell designs (symmetric and asymmetric) for FSSCs. Moreover, the latest discoveries of new materials with controlled architecture hold great promise towards performance improvement in terms of high power, energy densities and cycle life. FSSC performance is commonly defined in terms of gravimetric and volumetric scales that foster new electrode design development, such as freestanding and substrate-supported designs. The former is lightweight and utilises the entire electrode material to achieve high performance, thereby avoiding the extra weight of current collectors and additives however, it is fragile and difficult to handle.

Conversely, a large variety of flexible substrates, such as metal foils/wires, paper, textiles, PETs and fibres have been investigated to achieve high-performance FSSCs. Owing to their porous structure, light weight and high flexibility, textile- and paper-based current collectors are considered promising substrates for FSSC application. In addition, extensive efforts have been devoted towards exploring new gel electrolytes that improve overall SC performance. Thus, various new POM-incorporated gels, such as SiWA, PWA and BWA, have been found to be promising electrolytes for FSSC application because of their good conductivity and pseudocapacitance. A new strategy of designing redox-active electrolyte-enhanced devices has emerged through the introduction of pseudocapacitive contribution in electrolytes.

Several new promising materials, such as MXenes, MOFs, POMs and metal nitrides, with properties, such as high electronic conductivity and surface controlled porosity, have been adopted in the FSSC field. Moreover, the very recent discovery of MXenes has demonstrated great potential for designing FSSCs with enhanced volumetric energy density. The application of other layered materials (phosphorene) as electrodes in FSSCs is still in its infancy and needs further development, including the identification of new reducing agents, etchants and intercalants to synthesise high-quality large-scale materials. Various potential practical applications have been introduced, including piezoelectric, photo- and shape-memory SCs. This is a significant step towards achieving smart SCs.

Despite the many achievements and encouraging results, the development of a new generation of miniaturised FSSCs remains at an early stage. Extensive effort is needed before real technological implementations can emerge. To summarise, some of the current challenges and future directions for the practical realisation of FSSCs are as follows:

(1) A detailed analysis is necessary to understand energy storage mechanisms at the electrode/polymer gel electrolyte interface. Many theoretical studies have focused on liquid electrolytes; however, the theoretical basis of the charge storage mechanism in gel electrolytes is complicated and difficult to understand because ions are trapped in polymer chains. Therefore, advanced *in situ* characterisation (microscopic and spectroscopic) and simulation techniques need to be developed to elucidate FSSC charge storage mechanisms.

(2) A standardised method to evaluate FSSC electrochemical features and mechanical flexibility is yet to be developed. It is essential to report volumetric electrochemical features for FSSC and thin-film based systems since the mass of the active material is negligible when compared with the mass of the whole device. Similarly, different approaches have been undertaken to analyse FSSC mechanical integrity, thereby highlighting the need for standard methods of comparison.

(3) FSSC performance relies entirely on the electrode material and electrolytes. As discussed in Section 4, the unusual electronic, chemical and surface properties of 2D materials other than graphene (MXenes, phosphorene, germanene and tinene,) make them promising for use in FSSC electrodes. However, mass production of high-quality 2D materials is still challenging, and therefore, more effort should be taken to elucidate new synthesis methods that meet industrial requirements.

(4) Several new investigations on gel electrolytes resolved the initial problems of low ionic conductivity (10^{-3}–10^{-1} S cm^{-1}) and thermal instability. However, more research on improving device performance in terms of capacitance, energy density, stability and operating cell voltage using new redox-active electrolytes is required. In addition, the issues related to redox-active electrolytes such as high self-discharge need to be resolved.

(5) Standard methods need to be developed to investigate the mechanical flexibility of FSSCs. In addition, the effect of mechanical deformations on electrode materials and polymer gel electrolytes of the device should be explored using "*in situ*" and/or "*ex situ*" characterisation techniques.

(6) High production cost is another challenge for the practical implementation of FSSC technology. Therefore, future studies should focus on developing highly flexible and energetic FSSCs using cost-effective raw materials. Due consideration should be given to the fact that single-step processing materials and electrolytes are more favourable for practical application.

(7) The rapid advancement in electronic gadgets demands for efficient power sources with integrated stimulus-response. In this context, new flexible, bendable, foldable and stretchable device designs need to be explored.

(8) Integrating different functional electronic devices in a single component is of great interest. However, more investigations are required to further explore the potential of integrated devices in many application. Following increased efforts on optimisation, smart SCs would play an important role in the emergence of lightweight, flexible and wearable capacitive devices in the near future.

Conflicts of interest

There are no conflicts to declare.

Acknowledgements

DPD acknowledges the support of the University of Adelaide, Australia for the grant of a Research Fellowship (VC Fellow), the Secretary for Universities and Research of the Ministry of Economy and Knowledge of the Government of Catalonia, and the Co-fund program of the Marie Curie Actions of the 7th R&D Framework Program of the European Union. DPD and PGR acknowledges support from MINECO-FEDER (MAT2015-68394-R) and AGAUR (NESTOR 2014_SGR_1505). ICN2 acknowledges support from the Severo Ochoa Program (MINECO, Grant SEV-2013-0295) and funding from the CERCA Programme/Generalitat de Catalunya. This work was also supported by the National Research Foundation of Korea (NRF-2015M3A7B 4050 424).

References

1 (*a*) N. A. Kyeremateng, T. Brousse and D. Pech, *Nat. Nanotechnol.*, 2017, **12**, 7–15; (*b*) H. Sun, Y. Zhang, J. Zhang, X. Sun and H. Peng, *Nat. Rev. Mater.*, 2017, **2**, 17023; (*c*) M. Beidaghi and Y. Gogotsi, *Energy Environ. Sci.*, 2014, **7**, 867–884; (*d*) Z. Liu, J. Xu, D. Chen and G. Shen, *Chem. Soc. Rev.*, 2015, **44**, 161–192; (*e*) D. Yu, Q. Qian, L. Wei, W. Jiang, K. Goh, J. Wei, J. Zhang and Y. Chen, *Chem. Soc. Rev.*, 2015, **44**, 647–662.

2 (*a*) H. He, Y. Fu, T. Zhao, X. Gao, L. Xing, Y. Zhang and X. Xue, *Nano Energy*, 2017, **39**, 590–600; (*b*) D. Qi, Y. Liu, Z. Liu, L. Zhang and X. Chen, *Adv. Mater.*, 2017, **29**, 1602802; (*c*) X. Peng, L. Peng, C. Wu and Y. Xie, *Chem. Soc. Rev.*, 2014, **43**, 3303–3323; (*d*) D. Pech, M. Brunet, H. Durou, P. H. Huang, V. Mochalin, Y. Gogotsi, P. L. Taberna and P. Simon, *Nat. Nanotechnol.*, 2010, **5**, 651–654.

3 (*a*) F. Wang, X. Wu, X. Yuan, Z. Liu, Y. Zhang, L. Fu, Y. Zhu, Q. Zhou, Y. Wu and W. Huang, *Chem. Soc. Rev.*, 2017, **46**, 6816–6854; (*b*) F. Bonaccorso, L. Colombo, G. Yu, M. Stoller, V. Tozzini, A. C. Ferrari, R. S. Ruoff and V. Pellegrini, *Science*, 2015, **347**, 1246501; (*c*) L. Hu and Y. Cui, *Energy Environ. Sci.*, 2012, **5**, 6423–6435; (*d*) L. Li, C. Fu, Z. Lou, S. Chen, W. Han, K. Jiang, D. Chen and G. Shen, *Nano Energy*, 2017, **41**, 261–268.

4 (*a*) S. Bauer, *Nat. Mater.*, 2013, **12**, 871–872; (*b*) E. Gibney, *Nature*, 2015, **528**, 26–28; (*c*) I. M. Mosa, A. Pattammattel, K. Kadimisetty, P. Pande, M. F. El-Kady, G. W. Bishop, M. Novak, R. B. Kaner, A. K. Basu, C. V. Kumar and J. F. Rusling, *Adv. Energy Mater.*, 2017, **7**, 1700358.

5 (*a*) X. Pu, L. Li, M. Liu, C. Jiang, C. Du, Z. Zhao, W. Hu and Z. L. Wang, *Adv. Mater.*, 2016, **28**, 98–105; (*b*) F. R. Fan, W. Tang and Z. L. Wang, *Adv. Mater.*, 2016, **28**, 4283–4305; (*c*) D. Son, J. Lee, S. Qiao, R. Ghaffari, J. Kim, J. E. Lee, C. Song, S. J. Kim, D. J. Lee, S. W. Jun, S. Yang, M. Park, J. Shin, K. Do, M. Lee, K. Kang, C. S. Hwang, N. S. Lu, T. Hyeon and D. H. Kim, *Nat. Nanotechnol.*, 2014, **9**, 397–404; (*d*) T. Q. Trung and N. E. Lee, *Adv. Mater.*, 2016, **28**, 4338–4372.

6 (*a*) M. Salanne, B. Rotenberg, K. Naoi, K. Kaneko, P.-L. Taberna, C. P. Grey, B. Dunn and P. Simon, *Nat. Energy*, 2016, **1**, 16070; (*b*) D. P. Dubal, O. Ayyad, V. Ruiz and P. Gomez-Romero, *Chem. Soc. Rev.*, 2015, **44**, 1777–1790; (*c*) M. R. Lukatskaya, B. Dunn and Y. Gogotsi, *Nat. Commun.*, 2016, **7**, 12647–12659; (*d*) Y. Wang, Y. Song and Y. Xia, *Chem. Soc. Rev.*, 2016, **45**, 5925–5950; (*e*) Z. Yu, L. Tetard, L. Zhai and J. Thomas, *Energy Environ. Sci.*, 2015, **8**, 702–730.

7 (*a*) Y. Wang, Y. Song and Y. Xia, *Chem. Soc. Rev.*, 2016, **45**, 5925–5950; (*b*) D. P. Dubal, P. Gomez-Romero, B. R. Sankapal and R. Holze, *Nano Energy*, 2015, **11**, 377–399; (*c*) G. P. Wang, L. Zhang and J. J. Zhang, *Chem. Soc. Rev.*, 2012, **41**, 797–828; (*d*) Q. Lu, J. G. Chen and J. Q. Xiao, *Angew. Chem., Int. Ed.*, 2013, **52**, 1882–1889.

8 (*a*) S. Yang, R. E. Bachman, X. Feng and K. Mullen, *Acc. Chem. Res.*, 2013, **46**, 116–128; (*b*) H. B. Wu, G. Zhang, L. Yu and X. W. Lou, *Nanoscale Horiz.*, 2016, **1**, 27–40; (*c*) C. Zhang, W. Lv, Y. Tao and Q. H. Yang, *Energy Environ. Sci.*, 2015, **8**, 1390–1403.

9 (*a*) Z. Wu, L. Li, J. Yan and X. Zhang, *Adv. Sci.*, 2017, **4**, 1600382; (*b*) Z. Yang, J. Ren, Z. Zhang, X. Chen, G. Guan, L. Qiu, Y. Zhang and H. Peng, *Chem. Rev.*, 2015, **115**, 5159–5223; (*c*) K. Naoi, W. Naoi, S. Aoyagi, J. Miyamoto and T. Kamino, *Acc. Chem. Res.*, 2013, **46**, 1075–1083.

10 (*a*) B. E. Conway, *Electrochemical Supercapacitors Scientific Fundamentals and Technological Applications*, Kluwer Academic/Plenum Publishers, New York, 1999; (*b*) A. Yu, V. Chabot and J. Zhang, *Electrochemical supercapacitor for energy storage and delivery: fundamentals and application*, CRC Press, by Taylor & Francis Group, 2013.

11 (*a*) C. Yan and P. S. Lee, *Small*, 2014, **10**, 3443–3460; (*b*) S. Y. Lee, K. H. Choi, W. S. Choi, Y. H. Kwon, H. R. Jung, H. C. Shin and J. Y. Kim, *Energy Environ. Sci.*, 2013, **6**, 2414–2423; (*c*) S. Yao and Y. Zhu, *Adv. Mater.*, 2015, **27**, 1480–1511; (*d*) Y. Zhang, Y. Huang and J. A. Rogers, *Curr. Opin. Solid State Mater. Sci.*, 2015, **19**, 190–199.

12 (*a*) W. Liu, M. S. Song, B. Kong and Y. Cui, *Adv. Mater.*, 2017, **29**, 1603436; (*b*) K. Guo, N. Yu, Z. Hou, L. Hu, Y. Ma, H. Li and T. Zhai, *J. Mater. Chem. A*, 2017, **5**, 16–30;

(*c*) T. Q. Trung and N. E. Lee, *Adv. Mater.*, 2017, **29**, 1603167.

13 (*a*) Y. Matsuda, M. Morita, M. Ishikawa and M. Ihara, *J. Electrochem. Soc.*, 1993, **140**, L109–L110; (*b*) A. Clemente, S. Panero, E. Spila and B. Scrosati, *Solid State Ionics*, 1996, **85**, 273–277; (*c*) S. A. Hashmi, R. J. Latham, R. G. Linford and W. S. Schlindwein, *Polym. Int.*, 1998, **47**, 28–33.

14 (*a*) A. Lewandowski, M. Zajder, E. Frachowiak and F. Beguin, *Electrochim. Acta*, 2001, **46**, 2777–2780; (*b*) K. R. Prasad and N. Munichandraiah, *Electrochem. Solid-State Lett.*, 2002, **5**, A271–A274; (*c*) Y. G. Wang and X. G. Zhang, *Solid State Ionics*, 2004, **166**, 61–67.

15 (*a*) L. Liu, Z. Niu and J. Chen, *Chem. Soc. Rev.*, 2016, **45**, 4340–4363; (*b*) X. Wang, K. Jiang and G. Shen, *Mater. Today*, 2015, **18**, 265–272; (*c*) Y. Z. Zhang, Y. Wang, T. Cheng, W. Y. Lai, H. Pang and W. Huang, *Chem. Soc. Rev.*, 2015, **44**, 5181–5199; (*d*) X. Wang, X. Lu, B. Liu, D. Chen, Y. Tong and G. Shen, *Adv. Mater.*, 2014, **26**, 4763–4782.

16 (*a*) P. Yang and W. Mai, *Nano Energy*, 2014, **8**, 274–290; (*b*) X. Lu, M. Yu, G. Wang, Y. Tong and Y. Li, *Energy Environ. Sci.*, 2014, **7**, 2160–2181; (*c*) A. Tyagi, K. M. Tripathi and R. K. Gupta, *J. Mater. Chem. A*, 2015, **3**, 22507–22541; (*d*) L. Li, Z. Wu, S. Yuan and X. B. Zhang, *Energy Environ. Sci.*, 2014, **7**, 2101–2122.

17 (*a*) H. Chen, S. Zeng, M. Chen, Y. Zhang and Q. Li, *Carbon*, 2015, **92**, 271–296; (*b*) X. Wang and G. Shi, *Energy Environ. Sci.*, 2015, **8**, 790–823; (*c*) G. Xiong, C. Meng, R. G. Reifenberger, P. P. Irazoqui and T. S. Fisher, *Electroanalysis*, 2014, **26**, 30–51.

18 (*a*) W. K. Chee, H. N. Lim, Z. Zainal, N. M. Huang, I. Harrison and Y. Andou, *J. Phys. Chem. C*, 2016, **120**, 4153–4172; (*b*) T. Chen and L. Dai, *J. Mater. Chem. A*, 2014, **2**, 10756–10775; (*c*) Y. Huang, H. Li, Z. Wang, M. Zhu, Z. Pei, Q. Xue, Y. Huang and C. Zhi, *Nano Energy*, 2016, **22**, 422–438.

19 (*a*) J. Sun, Y. Huang, Y. N. S. Sea, Q. Xue, Z. Wang, M. Zhu, H. Li, X. Tao, C. Zhi and H. Hu, *Mater. Today Energy*, 2017, **5**, 1–14; (*b*) S. T. Senthilkumar, Y. Wang and H. Huang, *J. Mater. Chem. A*, 2015, **3**, 20863–20879; (*c*) K. Jost, G. Dion and Y. Gogotsi, *J. Mater. Chem. A*, 2014, **2**, 10776–10787.

20 (*a*) H. Wang, A. C. Forse, J. M. Griffin, N. M. Trease, L. Trognko, P. L. Taberna, P. Simon and C. P. Grey, *J. Am. Chem. Soc.*, 2013, **135**, 18968–18980; (*b*) F. Béguin, V. Presser, A. Balducci and E. Frackowiak, *Adv. Mater.*, 2014, **26**, 2219–2251; (*c*) P. Simon and Y. Gogotsi, *Acc. Chem. Res.*, 2013, **46**, 1094–1103.

21 (*a*) V. Augustyn, P. Simon and B. Dunn, *Energy Environ. Sci.*, 2014, **7**, 1597–1614; (*b*) J. R. Miller and A. F. Burke, *Electrochem. Soc. Interface*, 2008, 53–57; (*c*) P. Simon and Y. Gogotsi, *Nat. Mater.*, 2008, **7**, 845–854; (*d*) J. R. Miller and P. Simon, *Science*, 2008, **321**, 651–652.

22 (*a*) S. Zheng, Z. S. Wu, S. Wang, H. Xiao, F. Zhou, C. Sun, X. Bao and H. M. Cheng, *Energy Storage Mater.*, 2017, **6**, 70–97; (*b*) H. Xiao, Z. S. Wu, L. Chen, F. Zhou, S. Zheng, W. Ren, H. M. Cheng and X. Bao, *ACS Nano*, 2017, **11**, 7284–7292; (*c*) N. A. Choudhury, S. Sampath and A. K. Shukla, *Energy Environ. Sci.*, 2009, **2**, 55–67; (*d*) G. Lota and E. Frackowiak, *Electrochem. Commun.*, 2009, **11**, 87–90.

23 (*a*) J. Chmiola, G. Yushin, Y. Gogotsi, C. Portet, P. Simon and P. L. Taberna, *Science*, 2006, **313**, 1760–1763; (*b*) C. Largeot, C. Portet, J. Chmiola, P. L. Taberna, Y. Gogotsi and P. Simon, *J. Am. Chem. Soc.*, 2008, **130**, 2730–2731.

24 H. Shi, *Electrochim. Acta*, 1996, **41**, 1633–1639.

25 S. Kondrat, N. Georgi, M. V. Fedorov and A. A. Kornyshev, *Phys. Chem. Chem. Phys.*, 2011, **13**, 11359–11366.

26 (*a*) C. Merlet, B. Rotenberg, P. A. Madden, P. L. Taberna, P. Simon, Y. Gogotsi and M. Salanne, *Nat. Mater.*, 2012, **11**, 306–310; (*b*) M. Deschamps, E. Gilbert, P. Azais, E. R. Pinero, M. R. Ammar, P. Simon, D. Massiot and F. Beguin, *Nat. Mater.*, 2013, **12**, 351–358.

27 (*a*) T. Brousse, D. Bélanger and J. W. Long, *J. Electrochem. Soc.*, 2015, **162**, A5185–A5189; (*b*) D. P. Dubal and P. Gomez-Romero, *Metal oxides in supercapacitors*, Elsevier, 2017, ISBN: 9780128111697.

28 E. Herrero, L. J. Buller and H. D. Abruna, *Chem. Rev.*, 2001, **101**, 1897–1930.

29 X. Wang and G. Yushin, *Energy Environ. Sci.*, 2015, **8**, 1889–1904.

30 (*a*) M. D. Stoller and R. S. Ruoff, *Energy Environ. Sci.*, 2010, **3**, 1294–1301; (*b*) S. Roldan, D. Barreda, M. Granda, R. Menendez, R. Santamaria and C. Blanco, *Phys. Chem. Chem. Phys.*, 2015, **17**, 1084–1092; (*c*) Y. Gogotsi and P. Simon, *Science*, 2011, **334**, 917–918; (*d*) Y. J. Kang, S.-J. Chun, S.-S. Lee, B.-Y. Kim, J. H. Kim, H. Chung, S.-Y. Lee and W. Kim, *ACS Nano*, 2012, **6**, 6400–6406.

31 J. Bae, M. K. Song, Y. J. Park, J. M. Kim, M. Liu and Z. L. Wang, *Angew. Chem., Int. Ed.*, 2011, **50**, 1683–1687.

32 (*a*) Y. Cheng, S. Lu, H. Zhang, C. V. Varanasi and J. Liu, *Nano Lett.*, 2012, **12**, 4206–4211; (*b*) X. Xiao, T. Li, Z. Peng, H. Jin, Q. Zhong, Q. Hu, B. Yao, Q. Luo, C. Zhang, L. Gong, J. Chen, Y. Gogotsi and J. Zhou, *Nano Energy*, 2014, **6**, 1–9.

33 (*a*) D. Feng, Y. Lv, Z. Wu, Y. Dou, L. Han, Z. Sun, Y. Xia, G. Zheng and D. Zhao, *J. Am. Chem. Soc.*, 2011, **133**, 15148–15156; (*b*) K. Xiao, L. X. Ding, G. Liu, H. Chen, S. Wang and H. Wang, *Adv. Mater.*, 2016, **28**, 5997–6002.

34 (*a*) Y. He, W. Chen, X. Li, Z. Zhang, J. Fu, C. Zhao and E. Xie, *ACS Nano*, 2013, **7**, 174–182; (*b*) K. Qin, J. Kang, J. Li, C. Shi, Y. Li, Z. Qiao and N. Zhao, *ACS Nano*, 2015, **9**, 481–487.

35 V. L. Pushparaj, M. M. Shaijumon, A. Kumar, S. Murugesan, L. Ci, R. Vajtai, R. J. Linhardt, O. Nalamasu and P. M. Ajayan, *Proc. Natl. Acad. Sci. U. S. A.*, 2007, **104**, 13574–13577.

36 (*a*) Z. Cao and B. B. Wei, *Energy Environ. Sci.*, 2013, **6**, 3183–3201; (*b*) Z. Zhang, T. Zhai, X. Lu, M. Yu, Y. Tong and K. Mai, *J. Mater. Chem. A*, 2013, **1**, 505–509; (*c*) J. Chang, S. Adhikari, T. H. Lee, B. Li, F. Yao, D. T. Pham, V. T. Le and Y. H. Lee, *Adv. Energy Mater.*, 2015, **5**, 1500003.

37 Y. J. Kang, S. J. Chun, S. S. Lee, B. Y. Kim, J. H. Kim, H. Chung, S. Y. Lee and W. Kim, *ACS Nano*, 2012, **6**, 6400–6406.

38 (*a*) A. K. Geim and K. S. Novoselov, *Nat. Mater.*, 2007, **6**, 183–191; (*b*) A. K. Geim, *Science*, 2009, **324**, 1530–1534; (*c*) L. Dai, *Acc. Chem. Res.*, 2012, **46**, 31–42.

39 (*a*) L. L. Zhang, R. Zhou and X. Zhao, *J. Mater. Chem.*, 2010, **20**, 5983–5992; (*b*) C. Xu, B. Xu, Y. Gu, Z. Xiong, J. Sun and X. Zhao, *Energy Environ. Sci.*, 2013, **6**, 1388–1414.

40 Z. Weng, Y. Su, D. W. Wang, F. Li, J. Du and H.-M. Cheng, *Adv. Energy Mater.*, 2011, **1**, 917–922.

41 N. Li, G. Yang, Y. Sun, H. Song, H. Cui, G. Yang and C. Wang, *Nano Lett.*, 2015, **15**, 3195–3203.

42 (*a*) G. K. Wang, X. Sun, F. Y. Lu, H. T. Sun, M. P. Yu, W. L. Jiang, C. S. Liu and J. Lian, *Small*, 2012, **8**, 452–459; (*b*) Z. Lei, N. Christov and X. S. Zhao, *Energy Environ. Sci.*, 2011, **4**, 1866–1873.

43 C. Liu, Z. Yu, D. Neff, A. Zhamu and B. Z. Jang, *Nano Lett.*, 2010, **10**, 4863–4868.

44 Y. Wang, J. Chen, J. Cao, Y. Liu, Y. Zhou, J. H. Ouyang and D. Jia, *J. Power Sources*, 2014, **271**, 269–277.

45 B. G. Choi, J. Hong, W. H. Hong, P. T. Hammond and H. Park, *ACS Nano*, 2011, **5**, 7205–7213.

46 D. Yu and L. Dai, *J. Phys. Chem. Lett.*, 2009, **1**, 467–470.

47 (*a*) Y. Shao, M. F. El-Kady, L. J. Wang, Q. Zhang, Y. Li, H. Wang, M. F. Mousaviae and R. B. Kaner, *Chem. Soc. Rev.*, 2015, **44**, 3639–3665; (*b*) A. Borenstein, O. Hanna, R. Attias, S. Luski, T. Brousse and D. Aurbach, *J. Mater. Chem. A*, 2017, **5**, 12653–12672.

48 (*a*) G. Zhang, X. Xiao, B. Li, P. Gu, H. Xue and H. Pang, *J. Mater. Chem. A*, 2017, **5**, 8155–8186; (*b*) F. Shi, L. Li, X. Wang, C. Gu and J. Tu, *RSC Adv.*, 2014, **4**, 41910–41921.

49 (*a*) C. Zhang, T. M. Higgins, S. H. Park, S. E. O'Brien, D. Long, J. N. Coleman and V. Nicolosi, *Nano Energy*, 2016, **28**, 495–505; (*b*) Z. Peng, X. Liu, H. Meng, Z. Li, B. Li, Z. Liu and S. Liu, *ACS Appl. Mater. Interfaces*, 2017, **9**, 4577–4586.

50 (*a*) M. Huang, F. Li, F. Dong, Y. X. Zhang and L. L. Zhang, *J. Mater. Chem. A*, 2015, **3**, 21380–21423; (*b*) J. Cao, X. Li, Y. Wang, F. C. Walsh, J. H. Ouyang, D. Jia and Y. Zhou, *J. Power Sources*, 2015, **293**, 657–674.

51 (*a*) S. Gu, Z. Lou, L. Li, Z. Chen, X. Ma and G. Shen, *Nano Res.*, 2016, **9**, 424–434; (*b*) K. Chi, Z. Zhang, Q. Lv, C. Xie, J. Xiao, F. Xiao and S. Wang, *ACS Appl. Mater. Interfaces*, 2017, **9**, 6044–6053.

52 (*a*) C. H. Lai, D. Ashby, M. Moz, Y. Gogotsi, L. Pilon and B. Dunn, *Langmuir*, 2017, **33**, 9407–9415; (*b*) L. Kong, C. Zhang, J. Wang, W. Qiao, L. Ling and D. Long, *ACS Nano*, 2015, **9**, 11200–11208.

53 (*a*) W. Li, F. Gao, X. Wang, N. Zhang and M. Ma, *Angew. Chem., Int. Ed.*, 2016, **12**, 9342–9347; (*b*) E. Feng, H. Peng, Z. Zhang, J. Lia and Z. Lei, *New J. Chem.*, 2017, **41**, 9024–9032; (*c*) A. Khosrozadeh, M. A. Darabi, M. Xing and Q. Wang, *ACS Appl. Mater. Interfaces*, 2016, **8**, 11379–11389.

54 (*a*) C. Yang, L. Zhang, N. Hu, Z. Yang, H. Wei and Y. Zhang, *J. Power Sources*, 2016, **302**, 39–45; (*b*) Y. Zhou, X. Hu, Y. Shang, C. Hua, P. Song, X. Li, Y. Zhang and A. Cao, *RSC Adv.*, 2016, **6**, 62062–62070; (*c*) C. Yang, L. Zhang, N. Hu, Z. Yang, H. Wei, Y. Wang and Y. Zhang, *Appl. Surf. Sci.*, 2016, **387**, 666–673.

55 (*a*) R. B. Ambade, S. B. Ambade, R. R. Salunkhe, V. Malgras, S. H. Jin, Y. Yamauchi and S. H. Lee, *J. Mater. Chem. A*, 2016, **4**, 7406–7415; (*b*) Y. Li, G. Ren, Z. Zhang, C. Teng, Y. Wu, X. Lu, Y. Zhu and L. Jiang, *J. Mater. Chem. A*, 2016, **4**, 17324–17332; (*c*) Z. S. Wu, Y. Zheng, S. Zheng, S. Wang, C. Sun, K. Parvez, T. Ikeda, X. Bao, K. Müllen and X. Feng, *Adv. Mater.*, 2017, **29**, 1602960.

56 X. Xiao, X. Peng, H. Jin, T. Li, C. Zhang, B. Gao, B. Hu, K. Huo and J. Zhou, *Adv. Mater.*, 2013, **25**, 5091.

57 B. Gao, X. Li, X. Guo, X. Zhang, X. Peng, L. Wang, J. Fu, P. K. Chu and K. Huo, *Adv. Mater. Interfaces*, 2015, **2**, 1500211.

58 (*a*) S. Mondal, U. Rana and S. Malik, *J. Phys. Chem. C*, 2017, **121**, 7573–7583; (*b*) J. Li, W. Lu, Y. Yand and T. W. Chou, *J. Mater. Chem. A*, 2017, **5**, 11271–11277; (*c*) N. Hu, L. Zhang, C. Yang, J. Zhao, Z. Yang, H. Wei, H. Liao, Z. Feng, A. Fisher, Y. Zhang and Z. J. Xu, *Sci. Rep.*, 2016, **6**, 19777; (*d*) L. Negre, B. Daffos, V. Turq, P. L. Taberna and P. Simon, *Electrochim. Acta*, 2016, **206**, 490–495.

59 K. Chi, Z. Zhang, J. Xi, Y. Huang, F. Xiao, S. Wang and Y. Liu, *ACS Appl. Mater. Interfaces*, 2014, **6**, 16312–16319.

60 Y. Chen, L. Du, P. Yang, P. Sun, X. Yu and W. Mai, *J. Power Sources*, 2015, **287**, 68–74.

61 (*a*) H. Zhou, H. J. Zhai and G. Han, *J. Power Sources*, 2016, **323**, 125–133; (*b*) T. Cheng, Y. Z. Zhang, J. D. Zhang, W. Y. Lai and W. Huang, *J. Mater. Chem. A*, 2016, **4**, 10493–10499; (*c*) S. Lehtimäki, M. Suominen, P. Damlin, S. Tuukkanen, C. Kvarnström and D. Lupo, *ACS Appl. Mater. Interfaces*, 2015, **7**, 22137–22147; (*d*) I. Shown, A. Ganguly, L. C. Chen and K. H. Chen, *Energy Sci. Eng.*, 2015, **3**, 2–26.

62 Y. Liu, B. Weng, J. M. Razal, Q. Xu, C. Zhao, Y. Hou, S. Seyedin, R. Jalili, G. G. Wallace and J. Chen, *Sci. Rep.*, 2015, **5**, 17045.

63 Z. Li, G. Ma, R. Ge, F. Qin, X. Dong, W. Meng, T. Liu, J. Tong, F. Jiang, Y. Zhou, K. Li, X. Min, K. Huo and Y. Zhou, *Angew. Chem., Int. Ed.*, 2016, **55**, 979–982.

64 (*a*) J. Yu, J. Wu, H. Wang, A. Zhou, C. Huang, H. Bai and L. Li, *ACS Appl. Mater. Interfaces*, 2016, **8**, 4724–4729; (*b*) J. Cao, T. Huang, R. Liu, X. Xi and D. Wu, *Electrochim. Acta*, 2017, **230**, 265–270; (*c*) P. A. Shinde, N. R. Chodankar, V. C. Lokhande, A. M. Patil, T. Ji, J. H. Kim and C. D. Lokhande, *RSC Adv.*, 2016, **6**, 113442.

65 (*a*) A. Lamberti, M. Fontana, S. Bianco and E. Tresso, *Int. J. Hydrogen Energy*, 2016, **41**, 11700–11708; (*b*) P. Pazhamalai, K. Krishnamoorthy and S. J. Kim, *Int. J. Hydrogen Energy*, 2016, **41**, 14830–14835.

66 (*a*) Y. Wang, S. Wang, Y. Wu, Z. Zheng, K. Hong, B. Li and Y. Sun, *Electrochim. Acta*, 2017, **246**, 1065–1074; (*b*) X. Yang, Z. Lin, J. Zheng, Y. Huang, B. Chen, Y. Mai and X. Feng, *Nanoscale*, 2016, **8**, 8650–8657; (*c*) V. S. Kumbhar, Y. R. Lee, C. S. Ra, D. Tum, B. K. Min and J. J. Shim, *RSC Adv.*, 2017, **7**, 16348–16359.

67 (*a*) H. Xia, D. D. Zhu, Z. T. Luo, Y. Yu, X. Q. Shi, G. L. Yuan and J. P. Xie, *Sci. Rep.*, 2013, **3**, 2978; (*b*) L. T. Le,

M. H. Ervin, H. Qiu, B. E. Fuchs and W. Y. Lee, *Electrochem. Commun.*, 2011, **13**, 355.
68 (*a*) N. R. Chodankar, D. P. Dubal, A. C. Lokhande and C. D. Lokhande, *J. Colloid Interface Sci.*, 2015, **460**, 370–376; (*b*) S. K. Shinde, D. P. Dubal, G. S. Ghodake, D. Y. Kim and V. J. Fulari, *Nano-Struct. Nano-Objects*, 2016, **6**, 5–13.
69 (*a*) N. R. Chodankar, D. P. Dubal, G. S. Gund and C. D. Lokhande, *Electrochim. Acta*, 2015, **165**, 338–347; (*b*) N. R. Chodankar, D. P. Dubal, G. S. Gund and C. D. Lokhande, *J. Energy Chem.*, 2016, **25**, 463–471.
70 J. Chen, J. Xu, S. Zhou, N. Zhao and C. P. Wong, *J. Mater. Chem. A*, 2015, **3**, 17385–17391.
71 K. Sheng, Y. Sun, C. Li, W. Yuan and G. Shi, *Sci. Rep.*, 2012, **2**, 247.
72 (*a*) R. K. Gupta, J. Candler, S. Palchoudhury, K. Ramasamy and B. K. Gupta, *Sci. Rep.*, 2015, **5**, 15265; (*b*) G. Zhu, Z. He, J. Chen, J. Zhao, X. Feng, Y. Ma, Q. Fan, L. Wang and W. Huang, *Nanoscale*, 2014, **6**, 1079–1085; (*c*) B. Liu, B. Liu, Q. Wang, X. Wang, Q. Xiang, D. Chen and G. Shen, *ACS Appl. Mater. Interfaces*, 2013, **5**, 10011–10017.
73 Y. Huang, J. Tao, W. Meng, M. Zhu, Y. Huang, Y. Fu, Y. Gao and C. Zhi, *Nano Energy*, 2015, **11**, 518–525.
74 W. Zhou, X. Liu, Y. Sang, Z. Zhao, K. Zhou, H. Liu and S. Chen, *ACS Appl. Mater. Interfaces*, 2014, **6**, 4578–4586.
75 Q. Wang, X. Wang, B. Liu, G. Yu, X. Hou, D. Chen and G. Shen, *J. Mater. Chem. A*, 2013, **1**, 2468–2473.
76 M. Shao, Z. Li, R. Zhang, F. Ning, M. Wei, D. G. Evans and X. Duan, *Small*, 2015, **11**, 3530–3538.
77 (*a*) W. Liu, C. Lu, H. Li, R. Y. Tay, L. Sun, X. Wang, W. L. Chow, X. Wang, B. K. Tay, Z. Chen, J. Yan, K. Feng, G. Lui, R. Tjandra, L. Rasenthiram, G. Chiu and A. Yu, *J. Mater. Chem. A*, 2016, **4**, 3754–3764; (*b*) Z. Liu, Z. S. Wu, S. Yang, R. Dong, X. Feng and K. Müllen, *Adv. Mater.*, 2016, **28**, 2217–2222.
78 J. Tao, W. Ma, N. Liu, X. Ren, Y. Shi, J. Su and Y. Gao, *Nano-Micro Lett.*, 2015, **7**, 276–281.
79 J. Li, X. Cheng, J. Sun, C. Brand, A. Shashurin, M. Reeves and M. Keidar, *J. Appl. Phys.*, 2014, **115**, 164301.
80 X. Zhang, Z. Lin, B. Chen, S. Sharma, C. Wong, W. Zhang and Y. Deng, *J. Mater. Chem. A*, 2013, **1**, 5835–5839.
81 L. Yuan, X. Xiao, T. Ding, J. Zhong, X. Zhang, Y. Shen, B. Hu, Y. Huang, J. Zhou and Z. L. Wang, *Angew. Chem., Int. Ed.*, 2012, **51**, 4934–4938.
82 L. Zhang, P. Zhu, F. Zhou, W. Zeng, H. Su, G. Li, J. Gao, R. Sun and C. Wong, *ACS Nano*, 2016, **10**, 1273–1282.
83 K. H. Choi, J. T. Yoo, C. K. Lee and S. Y. Lee, *Energy Environ. Sci.*, 2016, **9**, 2812–2821.
84 (*a*) M. Mao, J. Hu and H. Liu, *Int. J. Energy Res.*, 2015, **39**, 727–740; (*b*) S. Zhai, H. E. Karahan, L. Wei, Q. Qian, A. T. Harris, A. I. Minett, S. Ramakrishna, A. K. Ng and Y. Chen, *Energy Storage Mater.*, 2016, **3**, 123–139; (*c*) Q. Xue, J. Sun, Y. Huang, M. Zhu, Z. Pei, H. Li, Y. Wang, N. Li, H. Zhang and C. Zhi, *Small*, 2017, **13**, 1701827.
85 (*a*) K. Jost, D. Stenger, C. R. Perez, J. K. McDonough, K. Lian, Y. Gogotsi and G. Dion, *Energy Environ. Sci.*, 2013, **6**, 2698–2705; (*b*) W. Y. Ko, Y. F. Chen, K. M. Lu and K. J. Lin, *Sci. Rep.*, 2016, **6**, 18887; (*c*) X. Yu, X. Su, K. Yan, H. Hu, M. Peng, X. Cai and D. Zou, *Adv. Mater. Technol.*, 2016, **1**, 1600009; (*d*) X. Li, J. Wang, Y. Zhao, F. Ge, S. Komarneni and Z. Cai, *ACS Appl. Mater. Interfaces*, 2016, **8**, 25905–25914.
86 (*a*) A. M. Abdelkader, N. Karim, C. Vallés, S. Afroj, K. S. Novoselov and S. G. Yeates, *2D Mater.*, 2017, **4**, 035016; (*b*) Q. Lu, L. Liu, S. Yang, J. Liu, Q. Tian, W. Yao, Q. Xue, M. Li and W. Wu, *J. Power Sources*, 2017, **361**, 31–38; (*c*) N. Yu, H. Yin, W. Zhang, Y. Liu, Z. Tang and M. Q. Zhu, *Adv. Energy Mater.*, 2016, **6**, 1501458.
87 C. Zhou and J. Liu, *Nanotechnology*, 2014, **25**, 035402.
88 Y. Chen, X. Zhang and Z. Xie, *ACS Nano*, 2015, **9**, 8054–8063.
89 H. Y. Jin, Z. H. Peng, W. M. Tang and H. L. W. Chan, *RSC Adv.*, 2014, **4**, 33022–33028.
90 W. Y. Ko, Y. F. Chen, K. M. Lu and K. J. Lin, *Sci. Rep.*, 2016, **6**, 18887.
91 M. S. Javed, J. Chen, L. Chen, Y. Xi, C. Zhang, B. Wan and C. Hu, *J. Mater. Chem. A*, 2016, **4**, 667–674.
92 Q. Liao, N. Li, S. Jin, G. Yang and C. Wang, *ACS Nano*, 2015, **9**, 5310–5317.
93 (*a*) Q. Wang, Y. Wu, T. Li, D. Zhang, M. Miao and A. Zhang, *J. Mater. Chem. A*, 2016, **4**, 3828–3834; (*b*) J. Sun, Y. Huang, C. Fu, Z. Wang, Y. Huang, M. Zhu, C. Zhi and H. Hu, *Nano Energy*, 2016, **27**, 230–237; (*c*) L. Gao, X. Li, X. Li, J. Cheng, B. Wang, Z. Wang and C. Li, *RSC Adv.*, 2016, **6**, 57190–57198.
94 (*a*) C. Choi, H. J. Sim, G. M. Spinks, X. Lepró, R. H. Baughman and S. J. Kim, *Adv. Energy Mater.*, 2016, **6**, 1502119; (*b*) Q. Wang, D. Zhang, Y. Wu, T. Li, A. Zhang and M. Miao, *Energy Technol.*, 2017, **5**, 1449–1456; (*c*) Q. Xue, J. Sun, Y. Huang, M. Zhu, Z. Pei, H. Li, Y. Wang, N. Li, H. Zhang and C. Zhi, *Small*, 2017, 1701827.
95 T. Huang, B. Zheng, L. Kou, K. Gopalsamy, Z. Xu, C. Gao, Y. Meng and Z. Wei, *RSC Adv.*, 2013, **3**, 23957–23962.
96 L. Kou, T. Huang, B. Zheng, Y. Han, X. Zhao, K. Gopalsamy, H. Sun and C. Gao, *Nat. Commun.*, 2014, **5**, 3754.
97 (*a*) B. Liu, D. Tan, X. Wang, D. Chen and G. Shen, *Small*, 2013, **9**, 1998–2004; (*b*) Q. Wang, X. Wang, J. Xu, X. Ouyang, X. Hou, D. Chen, R. Wang and G. Shen, *Nano Energy*, 2014, **8**, 44–51; (*c*) X. Dong, Z. Guo, Y. Song, M. Hou, J. Wang, Y. Wang and Y. Xia, *Adv. Funct. Mater.*, 2014, **24**, 3405–3412.
98 T. Chen and L. Dai, *Energy Storage Mater.*, 2016, **2**, 21–26.
99 N. Liu, W. Ma, J. Tao, X. Zhang, J. Su, L. Li, C. Yang, Y. Gao, D. Golberg and Y. Bando, *Adv. Mater.*, 2013, **25**, 4925–4931.
100 Z. Yu and J. Thomas, *Adv. Mater.*, 2014, **26**, 4279–4285.
101 Y. Huang, H. Hu, Y. Huang, M. Zhu, W. Meng, C. Liu, Z. Pei, C. Hao, Z. Wang and C. Zhi, *ACS Nano*, 2015, **9**, 4766–4775.
102 (*a*) V. T. Le, H. Kim, A. Ghosh, J. Kim, J. Chang, Q. A. Vu, D. T. Pham, J. H. Lee, S. W. Kim and Y. H. Lee, *ACS Nano*, 2013, **7**, 5940–5947; (*b*) X. Chen, L. Qiu, J. Ren, G. Guan, H. Lin, Z. Zhang, P. Chen, Y. Wang and H. Peng, *Adv. Mater.*, 2013, **25**, 6436–6441; (*c*) J. Ren, L. Li, C. Chen, X. Chen, Z. Cai, L. Qiu, Y. Wang, X. Zhu and H. Peng, *Adv.*

Mater., 2013, **25**, 1155–1159; (*d*) J. Ren, W. Bai, G. Guan, Y. Zhang and H. Peng, *Adv. Mater.*, 2013, **25**, 5965–5970.
103 (*a*) X. Cao, B. Zheng, W. Shi, J. Yang, Z. Fan, Z. Luo, X. Rui, B. Chen, Q. Yan and H. Zhang, *Adv. Mater.*, 2015, **27**, 4695–4701; (*b*) Y. J. Kang, H. Chung, M. S. Kim and W. Kim, *Appl. Surf. Sci.*, 2015, **355**, 160–165; (*c*) X. Peng, H. Liu, Q. Yin, J. Wu, P. Chen, G. Zhang, G. Liu, C. Wu and Y. Xie, *Nat. Commun.*, 2016, **7**, 11782.
104 (*a*) T. Gu and B. Wei, *ACS Appl. Mater. Interfaces*, 2016, **8**, 25243–25250; (*b*) X. Fan, T. Chen and L. Dai, *RSC Adv.*, 2014, **4**, 36996–37002; (*c*) E. A. Nagelli, L. Huang, A. Q.-Z. Dai, F. Du and L. Dai, *Part. Part. Syst. Charact.*, 2017, **34**, 1700131.
105 Z. S. Zhang, T. Zhai, X. H. Lu, M. H. Yu, Y. X. Tong and K. C. Mai, *J. Mater. Chem. A*, 2013, **1**, 505.
106 (*a*) Z. Liu, Z. S. Wu, S. Yang, R. Dong, X. Feng and K. Müllen, *Adv. Mater.*, 2016, **28**, 2217–2222; (*b*) P. Yu, W. Fu, Q. Zeng, J. Lin, C. Yan, Z. Lai, B. Tang, K. Suenaga, H. Zhang and Z. Liu, *Adv. Mater.*, 2017, **29**, 1701909.
107 Y. Gao, Y. S. Zhou, W. Xiong, L. J. Jiang, M. Mahjouri-samani, P. Thirugnanam, X. Huang, M. M. Wang, L. Jiang and Y. F. Lu, *APL Mater.*, 2013, **1**, 012101.
108 B. G. Choi, J. Hong, W. H. Hong, P. T. Hammond and H. S. Park, *ACS Nano*, 2011, **5**, 7205–7213.
109 H. Fei, C. Yang, H. Bao and G. Wang, *J. Power Sources*, 2014, **266**, 488–495.
110 W. Si, C. Yan, Y. Chen, S. Oswald, L. Hana and O. G. Schmidt, *Energy Environ. Sci.*, 2013, **6**, 3218–3223.
111 X. Xiao, T. Li, P. Yang, Y. Gao, H. Jin, W. Ni, W. Zhan, X. Zhang, Y. Cao, J. Zhong, L. Gong, W. C. Yen, W. Mai, J. Chen, K. Huo, Y. L. Chueh, Z. L. Wang and J. Zhou, *ACS Nano*, 2012, **6**, 9200–9206.
112 N. Kurra, M. K. Hota and H. N. Alshareef, *Nano Energy*, 2015, **13**, 500–508.
113 (*a*) Y. Xu, Z. Lin, X. Huang, Y. Liu, Y. Huang and X. Duan, *ACS Nano*, 2013, **7**, 4042–4049; (*b*) J. Cai, C. Lv and A. Watanabe, *J. Mater. Chem. A*, 2016, **4**, 1671–1679.
114 J. B. In, B. Hsi, J. H. Yoo, S. Hyun, C. Carraro, R. Maboudian and C. P. Grigoropoulos, *Carbon*, 2015, **83**, 144–151.
115 Z. Peng, J. Lin, R. Ye, E. L. G. Samuel and J. M. Tour, *ACS Appl. Mater. Interfaces*, 2015, **7**, 3414–3419.
116 (*a*) S. Li, C. Zhao, K. Shu, C. Wang, Z. P. Guo, G. G. Wallace and H. K. Liu, *Carbon*, 2014, **79**, 554–562; (*b*) B. Hsia, J. Marschewski, S. Wang, J. B. In, C. Carraro, D. Poulikakos, C. P. Grigoropoulos and R. Maboudian, *Nanotechnology*, 2014, **25**, 055401.
117 Y. S. Moon, D. Kim, G. Lee, S. Y. Hong, K. K. Kim, S. M. Park and J. S. Ha, *Carbon*, 2015, **81**, 29–37.
118 J. Maeng, C. Meng and P. P. Irazoqui, *Biomed. Microdevices*, 2015, **17**, 7.
119 T. Chen and L. Dai, *Energy Storage Mater.*, 2016, **2**, 21–26.
120 H. Xu, X. Hu, Y. Sun, H. Yang, X. Liu and Y. Huang, *Nano Res.*, 2015, **8**, 1148–1158.
121 X. Dong, Z. Guo, Y. Song, M. Hou, J. Wang, Y. Wang and Y. Xia, *Adv. Funct. Mater.*, 2014, **24**, 3405–3412.
122 W. Ma, S. Chen, S. Yang, W. Chen, Y. Cheng, Y. Guo, S. Peng, S. Ramakrishn and M. Zhu, *J. Power Sources*, 2016, **306**, 481–488.
123 S. Jiang, T. Shi, X. Zhan, H. Long, S. Xi, H. Hu and Z. Tang, *J. Power Sources*, 2014, **272**, 16–23.
124 D. Zhao, C. Chen, Q. Zhang, W. Chen, S. Liu, Q. Wang, Y. Liu, J. Li and H. Yu, *Adv. Energy Mater.*, 2017, **7**, 1700739.
125 K. Wang, X. Zhang, C. Li, H. Zhang, X. Sun, N. Xu and Y. Ma, *J. Mater. Chem. A*, 2014, **2**, 19726–19732.
126 J. Yu, J. Wu, H. Wang, A. Zhou, C. Huang, H. Bai and L. Li, *ACS Appl. Mater. Interfaces*, 2016, **8**, 4724–4729.
127 P. Zhang, Z. Liu, Y. Liu, H. Fan, Y. Jiao and B. Chen, *Electrochim. Acta*, 2015, **184**, 1–7.
128 P. Wu, S. Cheng, M. Yao, L. Yang, Y. Zhu, P. Liu, O. Xing, J. Zhou, M. Wang, H. Luo and M. Liu, *Adv. Funct. Mater.*, 2017, **27**, 1702160.
129 X. Li, S. Ding, X. Xiao, J. Shao, J. Wei, H. Pang and Y. Yu, *J. Mater. Chem. A*, 2017, **5**, 12774–12781.
130 J. Noh, C. Yoon, Y. Kim and J. Jang, *Carbon*, 2017, **116**, 470–478.
131 M. Yu, T. Zhai, X. Lu, X. Chen, S. Xie, W. Li, C. Liang, W. Zhao, L. Zhang and Y. Tong, *J. Power Sources*, 2013, **239**, 64–71.
132 B. S. Shen, H. Wang, L. J. Wu, R. S. Guo, Q. Huang and X. B. Yan, *Chin. Chem. Lett.*, 2016, **27**, 1586–1591.
133 K. Ye, Z. Liu, C. Xu, N. Li, Y. Chen and Y. Su, *Inorg. Chem. Commun.*, 2013, **30**, 1–4.
134 M. S. Javed, S. Dai, M. Wang, D. Guo, L. Chen, X. Wang, C. Hu and Y. Xi, *J. Power Sources*, 2015, **285**, 63–69.
135 C. Liu, S. Zhao, Y. Lu, Y. Chang, D. Xu, Q. Wang, Z. Dai, J. Bao and M. Han, *Small*, 2017, **13**, 1603494.
136 P. Yang, Y. Li, Z. Lin, Y. Ding, S. Yue, C. P. Wong, X. Cai, S. Tan and W. Mai, *J. Mater. Chem. A*, 2014, **2**, 595–599.
137 Q. Liao, N. Li, S. Jin, G. Yang and C. Wang, *ACS Nano*, 2015, **9**, 5310–5317.
138 (*a*) J. Zhao, J. Chen, S. Xu, M. Shao, D. Yan, M. Wei, D. G. Evans and X. Duan, *J. Mater. Chem. A*, 2013, **1**, 8836–8843; (*b*) J. Xie, X. Sun, N. Zhang, K. Xu, M. Zhou and Y. Xie, *Nano Energy*, 2013, **2**, 65–74; (*c*) A. D. Jagadale, G. Guan, X. Li, X. Du, X. Ma, X. Hao and A. Abudula, *Energy Technol.*, 2016, **4**, 997–1004.
139 H. Y. Jin, Z. H. Peng, W. M. Tang and H. L. W. Chan, *RSC Adv.*, 2014, **4**, 33022–33028.
140 Q. Wang, J. Xu, X. Wang, B. Liu, X. Hou, G. Yu, P. Wang, D. Chen and G. Shen, *ChemElectroChem*, 2014, **1**, 559–564.
141 X. F. Lu, A. L. Wang, H. Xu, X. J. He, Y. X. Tong and G. R. Li, *J. Mater. Chem. A*, 2015, **3**, 16560–16566.
142 M. S. Javed, S. Dai, M. Wang, Y. Xi, Q. Lang, D. Guo and C. Hu, *Nanoscale*, 2015, **7**, 13610–13618.
143 G. Zhu, Z. He, J. Chen, J. Zhao, X. Feng, Y. Ma, Q. Fan, L. Wang and W. Huang, *Nanoscale*, 2014, **6**, 1079–1085.
144 T. Qin, S. Peng, J. Hao, Y. Wen, Z. Wang, X. Wang, D. He, J. Zhang, J. Hou and G. Cao, *Adv. Energy Mater.*, 2017, 1700409.
145 W. Y. Ko, Y. F. Chen, K. M. Lu and K. J. Lin, *Sci. Rep.*, 2015, **6**, 18887.

146 K. Parvez, Z. Wu, R. Li, X. Liu, R. Graf, X. Feng and K. Müllen, *J. Am. Chem. Soc.*, 2014, **136**, 6083–6091.

147 X. Wang, A. Sumboja, W. L. Foo, C. Yan, K. Tsukagoshi and P. Lee, *RSC Adv.*, 2013, **3**, 15827–15833.

148 Y. Gao, H. Jin, Q. Lin, X. Li, M. Tavakoli, S. Leung, W. Tang, L. Zhou, H. Chan and Z. Fan, *J. Mater. Chem. A*, 2015, **3**, 10199–10204.

149 J. Zhang, X. Zhao, Z. Huang, T. Xu and Q. Zhang, *Carbon*, 2016, **107**, 844–851.

150 B. Yao, L. Yuan, X. Xiao, J. Zhang, Y. Qi, J. Zhou, J. Zhou, B. Hub and W. Chen, *Nano Energy*, 2013, **2**, 1071–1078.

151 S. Dai, W. Xu, Y. Xin, M. Wang, X. Gun, D. Guo and C. Hun, *Nano Energy*, 2016, **19**, 363–372.

152 H. Lee, S. Hong, J. Kwon, Y. Suh, J. Lee, H. Moon, J. Yeo and S. Ko, *J. Mater. Chem. A*, 2015, **3**, 8339–8345.

153 J. Yun, D. Kim, G. Lee and J. Ha, *Carbon*, 2014, **79**, 156–164.

154 Y. Kang, H. Chung, M. Kim and W. Kim, *Appl. Surf. Sci.*, 2015, **355**, 160–165.

155 H. Hu, K. Zhang, S. Li, S. Jia and C. Ye, *J. Mater. Chem. A*, 2014, **2**, 20916–20922.

156 X. Xu, W. Shi, P. Li, S. Ye, C. Ye, H. Ye, T. Lu, A. Zheng, J. Zhu, L. Xu, M. Zhong and X. Cao, *Chem. Mater.*, 2017, **29**, 6058–6065.

157 K. Zhang, H. Hu, W. Yao and C. Ye, *J. Mater. Chem. A*, 2015, **3**, 617–623.

158 X. Liu, T. Qian, N. Xu, J. Zhou, J. Guo and C. Yan, *Carbon*, 2015, **92**, 348–353.

159 S. Liu, J. Xie, H. Li, Y. Wang, H. Yang, T. Zhu, S. Zhang, G. Cao and X. Zhao, *J. Mater. Chem. A*, 2014, **2**, 18125–18131.

160 C. Hao, F. Wen, J. Xiang, L. Wang, H. Hou, Z. Su, W. Hu and Z. Liu, *Adv. Funct. Mater.*, 2014, **24**, 6700–6707.

161 X. Cao, B. Zheng, W. Shi, J. Yang, Z. Fan, Z. Luo, X. Rui, B. Chen, Q. Yan and H. Zhang, *Adv. Mater.*, 2015, **27**, 4695–4701.

162 L. Li, J. Gong, C. Liu, Y. Tian, M. Han, Q. Wang, X. Hong, Q. Ding, W. Zhu and J. Bao, *ACS Omega*, 2017, **2**, 1089–1096.

163 G. Sun, J. An, C. Chua, H. Pang, J. Zhang and P. Chen, *Electrochem. Commun.*, 2015, **51**, 33–36.

164 J. Xie, X. Sun, N. Zhang, K. Xu, M. Zhou and Y. Xie, *Nano Energy*, 2013, **2**, 65–74.

165 Y. Chen, K. Cai, C. Liu, H. Song and X. Yang, *Adv. Energy Mater.*, 2017, **7**, 1701247.

166 X. Li, T. Zhao, Q. Chen, P. Li, K. Wang, M. Zhong, J. Wei, D. Wu, B. Weief and H. Zhu, *Phys. Chem. Chem. Phys.*, 2013, **15**, 17752–17757.

167 X. Fan, T. Chen and L. Dai, *RSC Adv.*, 2014, **4**, 36996–37002.

168 R. Yuksel, Z. Sariob, A. Cirpan, P. Hiralal and H. Unalan, *ACS Appl. Mater. Interfaces*, 2014, **6**, 15434–15439.

169 M. Sawangphruk, M. Suksomboon, K. Kongsupornsak, J. Khuntilo, P. Srimuk, Y. Sanguansak, P. Klunbud, P. Suktha and P. Chiochan, *J. Mater. Chem. A*, 2013, **1**, 9630–9636.

170 B. Pandit, D. P. Dubal and B. R. Sankapal, *Electrochim. Acta*, 2017, **242**, 382–389.

171 H. Niu, X. Yang, H. Jiang, D. Zhou, X. Li, T. Zhang, J. Liu, Q. Wang and F. Qu, *J. Mater. Chem. A*, 2015, **3**, 24082–24094.

172 Y. Shao, H. Wang, Q. Zhang and Y. Li, *NPG Asia Mater.*, 2014, **6**, 119.

173 (*a*) J. Di, D. Hu, H. Chen, Z. Yong, M. Chen, Z. Feng, Y. Zhu and Q. Li, *ACS Nano*, 2012, **6**, 5457–5464; (*b*) Z. Weng, Y. Su, D. W. Wang, F. Li, J. Du and H. M. Cheng, *Adv. Energy Mater.*, 2011, **1**, 917–922; (*c*) M. F. El-Kady, M. Ihns, M. Li, J. Y. Hwang, M. F. Mousavi, L. Chaney, A. T. Lech and R. B. Kaner, *Proc. Natl. Acad. Sci. U. S. A.*, 2015, **112**, 4233–4238; (*d*) Y. Gao, Y. S. Zhou, W. Xiong, L. J. Jiang, M. Mahjouri-samani, P. Thirugnanam, X. Huang, M. M. Wang, L. Jiang and Y. F. Lu, *APL Mater.*, 2013, **1**, 012101; (*e*) J. Zang, C. Cao, Y. Feng, J. Liu and X. Zhao, *Sci. Rep.*, 2014, **4**, 6492.

174 (*a*) Y. Zhang, W. Bai, X. Cheng, J. Ren, W. Weng, P. Chen, X. Fang, Z. Zhang and H. Peng, *Angew. Chem., Int. Ed.*, 2014, **53**, 14564–14568; (*b*) L. Li, Z. Lou, W. Han, D. Chen, K. Jiang and G. Shen, *Adv. Mater. Technol.*, 2017, **2**, 1600282; (*c*) S. He, L. Qiu, L. Wang, J. Cao, S. Xie, Q. Gao, Z. Zhang, J. Zhang, B. Wang and H. Peng, *J. Mater. Chem. A*, 2016, **4**, 14968–14973; (*d*) Y. Huang, Y. Huang, W. Meng, M. Zhu, H. Xue, C. S. Lee and C. Zhi, *ACS Appl. Mater. Interfaces*, 2015, **7**, 2569–2574; (*e*) M. Hu, Y. Liu, M. Zhang, H. Wei and Y. Gao, *J. Power Sources*, 2016, **335**, 113–120; (*f*) Y. Huang, M. Zhong, F. Shi, X. Liu, Z. Tang, Y. Wang, Y. Huang, H. Hou, X. Xie and C. Zhi, *Angew. Chem., Int. Ed.*, 2017, **56**, 9141–9145.

175 (*a*) B. E. Francisco, C. M. Jones, S. H. Lee and C. R. Stoldt, *Appl. Phys. Lett.*, 2012, **100**, 103902; (*b*) A. S. Ulihin, Y. G. Mateyshina and N. F. Uvarov, *Solid State Ionics*, 2013, **251**, 62–65; (*c*) N. A. Choudhury, S. Sampath and A. K. Shukla, *Energy Environ. Sci.*, 2009, **2**, 55–67; (*d*) H. Gao and K. Lian, *RSC Adv.*, 2014, **4**, 33091–33113; (*e*) C. Zhong, Y. Deng, W. Hu, J. Qiao, L. Zhang and J. Zhang, *Chem. Soc. Rev.*, 2015, **44**, 7484–7539.

176 (*a*) C. Meng, C. Liu, L. Chen, C. Hu and S. Fan, *Nano Lett.*, 2010, **10**, 4025; (*b*) H. J. Yu, J. H. Wu, L. Q. Fan, Y. Z. Lin, K. Q. Xu, Z. Y. Tang, C. X. Cheng, S. Tang, J. M. Lin, M. L. Huang and Z. Lan, *J. Power Sources*, 2012, **198**, 402–407.

177 J. Duay, E. Gillette, R. Liu and S. B. Lee, *Phys. Chem. Chem. Phys.*, 2012, **14**, 3329.

178 K. T. Lee and N. L. Wu, *J. Power Sources*, 2008, **179**, 430.

179 X. L. Hu, G. M. Hou, M. Q. Zhang, M. Z. Rong, W. H. Ruan and E. P. Giannelis, *J. Mater. Chem.*, 2012, **22**, 18961.

180 P. Sivaraman, A. Thakur, R. K. Kushwaha, D. Ratna and A. B. Samui, *Electrochem. Solid-State Lett.*, 2006, **9**, A435–A438.

181 C. W. Huang, C. A. Wu, S. S. Hou, P. L. Kuo, C. T. Hsieh and H. S. Teng, *Adv. Funct. Mater.*, 2012, **22**, 4677–4685.

182 Y. S. Lee, S. H. Ju, J. H. Kim, S. S. Hwang, J. M. Choi, Y. K. Sun, H. Kim, B. Scrosati and D. W. Kim, *Electrochem. Commun.*, 2012, **17**, 18–21.

183 L. Q. Fan, J. Zhong, J. H. Wu, J. M. Lin and Y. F. Huang, *J. Mater. Chem. A*, 2014, **2**, 9011–9014.

184 G. M. Wang, X. H. Lu, Y. C. Ling, T. Zhai, H. Y. Wang, Y. X. Tong and Y. Li, *ACS Nano*, 2012, **6**, 10296–10302.

185 Y. J. Kang, H. Chung and W. Kim, *Synth. Met.*, 2013, **166**, 40–44.

186 M. Sawangphruk, P. Srimuk, P. Chiochan, A. Krittayavathananon, S. Luanwuthi and J. Limtrakul, *Carbon*, 2013, **60**, 109–116.

187 X. Li, M. Zhou, J. Wang, F. Ge, Y. Zhao, S. Komarneni and Z. Cai, *J. Power Sources*, 2017, **342**, 762–771.

188 X. Jian, H. Yang, J. Li, E. Zhang, L. Cao and Z. Liang, *Electrochim. Acta*, 2017, **228**, 483–493.

189 T. Qian, N. Xu, J. Zhou, T. Yang, X. Liu, X. Shen, J. Liang and C. Yan, *J. Mater. Chem. A*, 2015, **3**, 488–493.

190 A. Virya and K. Lian, *Electrochem. Commun.*, 2017, **74**, 33–37.

191 N. Li, T. Lv, Y. Yao, H. Li, K. Liu and T. Chen, *J. Mater. Chem. A*, 2017, **5**, 3267.

192 Y. Yu, J. Zhong, W. Sun, R. Kumar and N. Koratkar, *Adv. Funct. Mater.*, 2017, **27**, 1606461.

193 Y. Xu, Z. Lin, X. Huang, Y. Wang, Y. Huang and X. Duan, *Adv. Mater.*, 2013, **25**, 5779–5784.

194 G. Huang, C. Hou, Y. Shao, B. Zhu, B. Jia, H. Wang, Q. Zhang and Y. Li, *Nano Energy*, 2015, **12**, 26–32.

195 G. M. Wang, H. Y. Wang, X. H. Lu, Y. C. Ling, M. H. Yu, T. Zhai, Y. X. Tong and Y. Li, *Adv. Mater.*, 2014, **26**, 2676–2682.

196 H. F. Ju, W. L. Song and L. Z. Fan, *J. Mater. Chem. A*, 2014, **2**, 10895–10903.

197 Q. Chen, X. M. Li, X. B. Zang, Y. C. Cao, Y. J. He, P. X. Li, K. L. Wang, J. Q. Wei, D. H. Wu and H. W. Zhu, *RSC Adv.*, 2014, **4**, 36253–36256.

198 H. Gao and K. Lian, *J. Power Sources*, 2011, **196**, 8855–8857.

199 H. Gao and K. Lian, *J. Mater. Chem.*, 2012, **22**, 21272–21278.

200 H. Gao and K. Lian, *J. Electrochem. Soc.*, 2013, **160**, A505–A510.

201 (*a*) B. Scrosati, F. Croce and L. Persi, *J. Electrochem. Soc.*, 2000, **147**, 1718–1721; (*b*) J. A. Kerres, *Fuel Cells*, 2005, **5**, 230–247; (*c*) Y. Jin, S. Qiao, L. Zhang, Z. P. Xu, S. Smart, J. C. D. d. Costa and G. Q. Lu, *J. Power Sources*, 2008, **185**, 664–669.

202 K. Lian and Q. Tian, *Electrochem. Commun.*, 2010, **12**, 517–519.

203 (*a*) W. Li, T. Li, X. Ma, Y. Li, L. An and Z. Zhang, *RSC Adv.*, 2016, **6**, 12491–12496; (*b*) H. Gao, A. Virya and K. Lian, *J. Mater. Chem. A*, 2015, **3**, 21511–21517.

204 K. M. Kim, J. H. Nam, Y. G. Lee, W. I. Cho and J. M. Ko, *Curr. Appl. Phys.*, 2013, **13**, 1702–1706.

205 D. Z. Chen, J. Yu, W. Lu, Y. Zhao, Y. Yan and T. W. Chou, *Electrochim. Acta*, 2017, **233**, 181–189.

206 (*a*) X. H. Lu, G. M. Wang, T. Zhai, M. H. Yu, S. L. Xie, Y. C. Ling, C. L. Liang, Y. X. Tong and Y. Li, *Nano Lett.*, 2012, **12**, 5376–5381; (*b*) C. C. Yang and S. J. Lin, *J. Appl. Electrochem.*, 2003, **33**, 777–784.

207 (*a*) J. Qiao, J. Fu, R. Lin, J. Ma and J. Liu, *Polymer*, 2010, **51**, 4850–4859; (*b*) C. C. Yang, S. J. Lin and G. M. Wu, *Mater. Chem. Phys.*, 2005, **92**, 251–255; (*c*) J. M. Yang and S. A. Wang, *J. Membr. Sci.*, 2015, **477**, 49–57.

208 I. K. Moon, S. Yoon and J. Oh, *Chem. – Eur. J.*, 2017, **23**, 597–604.

209 C. C. Yang, S. T. Hsu and W. C. Chien, *J. Power Sources*, 2005, **152**, 303–310.

210 H. Zhang, C. Lu, C. Chen, L. Xie, P. Zhou and Q. Kong, *ChemElectroChem*, 2017, **4**, 1990–1996.

211 A. Lewandowski, M. Zajder, E. Frackowiak and F. Beguin, *Electrochim. Acta*, 2001, **46**, 2777–2780.

212 H. Gao and K. Lian, *J. Electrochem. Soc.*, 2013, **160**, A505–A510.

213 Y. F. Huang, P. F. Wu, M. Q. Zhang, W. H. Ruan and E. P. Giannelis, *Electrochim. Acta*, 2014, **132**, 103–111.

214 N. Vassal, E. Salmon and J. F. Fauvarque, *Electrochim. Acta*, 2000, **45**, 1527–1532.

215 D. Kalpana, N. G. Renganathan and S. Pitchumani, *J. Power Sources*, 2006, **157**, 621–623.

216 (*a*) C. Iwakura, H. Wada, S. Nohara, N. Furukawa, H. Inoue and M. Morita, *Electrochem. Solid-State Lett.*, 2003, **6**, A37–A39; (*b*) H. Wada, S. Nohara, N. Furukawa, H. Inoue, N. Sugoh, H. Iwasaki, M. Morita and C. Iwakura, *Electrochim. Acta*, 2004, **49**, 4871–4875.

217 H. Gao, J. Li and K. Lian, *RSC Adv.*, 2014, **4**, 21332–21339.

218 J. Li and K. Lian, *Polymer*, 2016, **99**, 140–146.

219 C. W. Huang, C. A. Wu, S. S. Hou, P. L. Kuo, C. T. Hsieh and H. S. Teng, *Adv. Funct. Mater.*, 2012, **22**, 4677–4685.

220 Y. N. Sudhakar, M. Selvakumar and D. K. Bhat, *Ionics*, 2013, **19**, 277–285.

221 C. Ramasamy, J. P. del Vel and M. Anderson, *J. Solid State Electrochem.*, 2014, **18**, 2217–2223.

222 M. Schroeder, P. Isken, M. Winter, S. Passerini, A. Lex-Balducci and A. Balducci, *J. Electrochem. Soc.*, 2013, **160**, A1753–A1758.

223 P. M. DiCarmine, T. B. Schon, T. M. McCormick, P. P. Klein and D. S. Seferos, *J. Phys. Chem. C*, 2014, **118**, 8295–8307.

224 C. W. Huang, C. A. Wu, S. S. Hou, P. L. Kuo, C. T. Hsieh and H. Teng, *Adv. Funct. Mater.*, 2012, **22**, 4677–4685.

225 J. Rodrıguez, E. Navarrete, E. A. Dalchiele, L. Sanchez, J. R. Ramos-Barrado and F. Martın, *J. Power Sources*, 2013, **237**, 270–276.

226 M. F. Hsueh, C. W. Huang, C. A. Wu, P. L. Kuo and H. Teng, *J. Phys. Chem. C*, 2013, **117**, 16751–16758.

227 Y. D. Chiou, D. S. Tsai, H. H. Lam, C. H. Chang, K. Y. Lee and Y. S. Huang, *Nanoscale*, 2013, **5**, 8122–8129.

228 R. Yuksel, Z. Sarioba, A. Cirpan, P. Hiralal and H. E. Unalan, *ACS Appl. Mater. Interfaces*, 2014, **6**, 15434–15439.

229 C. Ramasamy, J. Palma and M. Anderson, *J. Solid State Electrochem.*, 2014, 18, 2903–2911.

230 S. N. Syahidah and S. R. Majid, *Electrochim. Acta*, 2013, **112**, 678–685.

231 A. Jain and S. K. Tripathi, *Ionics*, 2013, **19**, 549–557.

232 B. Anothumakkool, A. T. Arun Torris, S. Veeliyath, V. Vijayakumar, M. V. Badiger and S. Kurungot, *ACS Appl. Mater. Interfaces*, 2016, **8**, 1233–1241.

233 V. Vijayakumar, B. Anothumakkool, A. T. Arun Torris, S. B. Nair, M. V. Badiger and S. Kurungot, *J. Mater. Chem. A*, 2017, **5**, 8461–8476.

234 (*a*) Y. Lim, J. Yoon, J. Yun, D. Kim, S. Y. Hong, S. J. Lee, G. Zi and J. S. Ha, *ACS Nano*, 2014, **8**, 11639–11650; (*b*) S. Wang, B. Hsia, C. Carraro and R. Maboudian, *J. Mater. Chem. A*, 2014, **2**, 7997–8002.

235 (*a*) G. P. Pandey and S. A. Hashmi, *J. Mater. Chem. A*, 2013, **1**, 3372–3378; (*b*) M. Suleman, Y. Kumar and S. A. Hashmi, *J. Phys. Chem. B*, 2013, **117**, 7436–7443.

236 C. W. Liew, S. Ramesh and A. K. Arof, *Int. J. Hydrogen Energy*, 2014, **39**, 2953–2963.

237 S. Ketabi and K. Lian, *Electrochim. Acta*, 2013, **103**, 174–178.

238 P. Tamilarasan and S. Ramaprabhu, *Energy*, 2013, **51**, 374–381.

239 X. Zhang, L. Wang, J. Peng, P. Cao, X. Cai, J. Li and M. Zhai, *Adv. Mater. Interfaces*, 2015, **2**, 1500267.

240 (*a*) Y. J. Kang, S. J. Chun, S. S. Lee, B. Y. Kim, J. H. Kim, H. Chung, S. Y. Lee and W. Kim, *ACS Nano*, 2012, **6**, 6400–6406; (*b*) X. Yang, F. Zhang, L. Zhang, T. Zhang, Y. Huang and Y. Chen, *Adv. Funct. Mater.*, 2013, **23**, 3353–3360.

241 A. Revzin, R. J. Russell, V. K. Yadavalli, W. G. Koh, C. Deister, D. D. Hile, M. B. Mellott and M. V. Pishko, *Langmuir*, 2001, **17**, 5440–5447.

242 D. Kim, G. Lee, D. Kim and J. S. Ha, *ACS Appl. Mater. Interfaces*, 2015, **7**, 4608–4615.

243 X. Zhong, J. Tang, L. Cao, W. Kong, Z. Sun, H. Cheng, Z. Lu, H. Pan and B. Xu, *Electrochim. Acta*, 2017, **244**, 112–118.

244 X. Liu, B. Wu, N. Brandon and Q. Wang, *Energy Technol.*, 2017, **5**, 220–224.

245 G. P. Pandey, A. C. Rastogi and C. R. Westgate, *J. Power Sources*, 2014, **245**, 857–865.

246 S. Ketabi, B. Decker and K. Lian, *Sol. State Ionics*, 2016, **298**, 73–79.

247 Y. Gao, Y. S. Zhou, M. Qian, H. M. Li, J. Redepenning, L. S. Fan, X. N. He, W. Xiong, X. Huang, M. Majhouri-Samani, L. Jiang and Y. F. Lu, *RSC Adv.*, 2013, **3**, 20613–20618.

248 (*a*) N. R. Chodankar, D. P. Dubal, A. C. Lokhande, A. M. Patil, J. H. Kim and C. D. Lokhande, *Sci. Rep.*, 2016, **6**, 39205; (*b*) E. Frackowiak, K. Fic, M. Meller and G. Lota, *ChemSusChem*, 2012, **5**, 1181–1185; (*c*) E. Frackowiak, M. Meller, J. Menzel, D. Gastol and K. Fic, *Faraday Discuss.*, 2014, **172**, 179–198; (*d*) B. Akinwolemiwa, C. Peng and G. Z. Chena, *J. Electrochem. Soc.*, 2015, **162**, A5054–A5059.

249 (*a*) G. Lota, K. Fic and E. Frackowiak, *Electrochem. Commun.*, 2011, **12**, 38–41; (*b*) K. Fic, G. Lota, M. Meller and E. Frackowiak, *Energy Environ. Sci.*, 2012, **5**, 5842–5850.

250 (*a*) H. Yu, J. Wu, L. Fan, K. Xu, X. Zhong, Y. Lin and J. Lin, *Electrochim. Acta*, 2011, **56**, 6881–6886; (*b*) S. T. Senthilkumar, R. Kalai Selvan, Y. S. Lee and J. S. Melo, *J. Mater. Chem. A*, 2013, **1**, 1086–1095.

251 G. Ma, J. Li, K. Sun, H. Peng, J. Mu and Z. Lei, *J. Power Sources*, 2014, **256**, 281–287.

252 (*a*) K. Sun, E. Feng, H. Peng, G. Ma, Y. Wu, H. Wang and Z. Lei, *Electrochim. Acta*, 2015, **158**, 361–367; (*b*) S. T. Senthilkumar, R. K. Selvan, J. S. Melo and C. Sanjeeviraja, *ACS Appl. Mater. Interfaces*, 2013, **5**, 10541–10550.

253 S. T. Senthilkumar, R. K. Selvan, N. Ponpandian and J. S. Melo, *RSC Adv.*, 2012, **2**, 8937–8940.

254 G. F. Ma, E. K. Feng, K. J. Sun, H. Peng, J. J. Li and Z. Q. Lei, *Electrochim. Acta*, 2014, **135**, 461–466.

255 F. D. Yu, M. L. Huang, J. H. Wu, Z. Y. Qiu, L. Q. Fan, J. M. Lin and Y. B. Lin, *J. Appl. Polym. Sci.*, 2014, **131**, 39784.

256 Y. Tian, R. Xue, X. Zhou, Z. Liu and L. Huang, *Electrochim. Acta*, 2015, **152**, 135–139.

257 S. Roldán, Z. González, C. Blanco, M. Granda, R. Menéndez and R. Santamaría, *Electrochim. Acta*, 2011, **56**, 3401–3405.

258 E. Feng, G. Ma, K. Sun, F. Ran, H. Peng and Z. Lei, *New J. Chem.*, 2017, **41**, 1986–1992.

259 E. Feng, G. Ma, K. Sun, Q. Yang, H. Peng and Z. Lei, *RSC Adv.*, 2016, **6**, 75896–75904.

260 (*a*) D. P. Dubal, J. Suarez-Guevara, D. Tonti, E. Enciso and P. Gomez-Romero, *J. Mater. Chem. A*, 2015, **3**, 23483–23492; (*b*) D. P. Dubal, B. Nagar, J. Suarez-Guevara, D. Tonti, E. Enciso, P. Palomino and P. Gomez-Romero, *Mater. Today Energy*, 2017, **5**, 58–65.

261 S. Pan, J. Deng, G. Guan, Y. Zhang, P. Chen, J. Ren and H. Peng, *J. Mater. Chem. A*, 2015, **3**, 6286–6290.

262 M. Kim, J. Yoo and J. Kim, *Chem. Eng. J.*, 2017, **324**, 93–103.

263 G. K. Veerasubramani, K. Krishnamoorthy, P. Pazhamalai and S. J. Kim, *Carbon*, 2016, **105**, 638–648.

264 H. Zhang, J. Li, C. Gu, M. Yao, B. Yang, P. Lu and Y. Ma, *J. Power Sources*, 2016, **332**, 413–419.

265 J. Zhou, J. Cai, S. Cai, X. Zhou and A. N. Mansour, *J. Power Sources*, 2011, **196**, 10479–10483.

266 D. Kim, G. Lee, D. Kim, J. Yun, S. S. Lee and J. S. Ha, *Nanoscale*, 2016, **8**, 15611–15620.

267 H. S. Jang, C. J. Raj, W. G. Lee, B. C. Kim and K. H. Yu, *RSC Adv.*, 2016, **6**, 75376–75383.

268 J. K. Lee, Y. J. Lee, W. S. Chae and Y. M. Sung, *J. Electroceram.*, 2006, **17**, 941.

269 J. Reiter, J. Vondrak, J. Michalek and Z. Micka, *Electrochim. Acta*, 2006, **52**, 1398.

270 X. Liu, D. Wu, H. Wang and Q. Wang, *Adv. Mater.*, 2014, **26**, 4370.

271 G. P. Pandey, S. A. Hashmi and Y. Kumar, *Energy Fuels*, 2010, **24**, 6644.

272 D. Kumar and S. A. Hashmi, *Solid State Ionics*, 2010, **181**, 416–423.

273 Sellam and S. A. Hashmi, *J. Solid State Electrochem.*, 2014, **18**, 465–475.

274 S. A. Hashmi, A. Kumar and S. K. Tripathi, *Eur. Polym. J.*, 2005, **41**, 1373–1379.

275 T. Chen, H. Peng, M. Durstock and L. Dai, *Sci. Rep.*, 2014, **4**, 3612.

276 F. Miao, C. Shao, X. Li, K. Wang and Y. Liu, *J. Mater. Chem. A*, 2016, **4**, 4180–4187.

277 B. Hsia, J. Marschewski, S. Wang, J. B. In, C. Carraro, D. Poulikakos, C. P. Grigoropoulos and R. Maboudian, *Nanotechnology*, 2014, **25**, 55401.
278 M. F. El-Kady, V. Strong, S. Dubin and R. B. Kaner, *Science*, 2012, **335**, 1326.
279 Y. Xu, Z. Lin, X. Huang, Y. Liu, Y. Huang and X. Duan, *ACS Nano*, 2013, **7**, 4042–4049.
280 K. Gao, Z. Shao, J. Li, X. Wang, X. Peng, W. Wang and F. Wang, *J. Mater. Chem. A*, 2013, **1**, 63–67.
281 (*a*) J. Sun, C. Wu, X. Sun, H. Hu, C. Zhi, L. Hou and C. Yuan, *J. Mater. Chem. A*, 2017, **5**, 9443–9464; (*b*) Y. Zhang, L. Li, H. Su, W. Huang and X. Dong, *J. Mater. Chem. A*, 2015, **3**, 43–59; (*c*) K. Wang, H. Wu, Y. Meng and Z. Wei, *Small*, 2014, **10**, 14–31.
282 (*a*) Y. Zhong, X. Xia, F. Shi, J. Zhan, J. Tu and H. J. Fan, *Adv. Sci.*, 2016, **3**, 1500286; (*b*) X. Rui, H. Tan and Q. Yan, *Nanoscale*, 2014, **6**, 9889–9924; (*c*) M. S. Balogun, W. Qiu, W. Wang, P. Fang, X. Lu and Y. Tong, *J. Mater. Chem. A*, 2015, **3**, 1364–1387.
283 (*a*) Y. Shi, L. Peng, Y. Ding, Y. Zhao and G. Yu, *Chem. Soc. Rev.*, 2015, **44**, 6684–6696; (*b*) F. Wolfart, B. M. Hryniewicz, M. S. Góes, C. M. Corrêa, R. Torresi, M. A. O. S. Minadeo, S. I. Córdoba de Torresi, R. D. Oliveira, L. F. Marchesi and M. Vidotti, *J. Solid State Electrochem.*, 2017, **21**, 2489–2515; (*c*) R. Holze and Y. P. Wu, *Electrochim. Acta*, 2014, **122**, 93–107; (*d*) A. Eftekhari, L. Li and Y. Yang, *J. Power Sources*, 2017, **347**, 86–107.
284 A. Ferris, S. Garbarino, D. Guay and D. Pech, *Adv. Mater.*, 2015, **27**, 6625–6629.
285 T. M. Dinha, A. Achour, S. Vizireanu, G. Dinescu, L. Nistor, K. Armstrong, D. Guay and D. Pech, *Nano Energy*, 2014, **10**, 288–294.
286 J. Zhang, X. Zhao, Z. Huang, T. Xu and Q. Zhang, *Carbon*, 2016, **107**, 844–851.
287 P. Shi, L. Li, L. Hua, Q. Qian, P. Wang, J. Zhou, G. Sun and W. Huang, *ACS Nano*, 2017, **11**, 444–452.
288 W. Ma, S. Chen, S. Yang, W. Chen, Y. Cheng, Y. Guo, S. Peng, S. Ramakrishna and M. Zhu, *J. Power Sources*, 2016, **306**, 481–488.
289 S. Yang, X. Song, P. Zhang and L. Gao, *J. Mater. Chem. A*, 2015, **3**, 6136–6145.
290 (*a*) B. Pandit, D. P. Dubal, P. Gómez-Romero, B. B. Kale and B. R. Sankapal, *Sci. Rep.*, 2017, **7**, 43430; (*b*) B. Pandit, D. P. Dubal and B. R. Sankapal, *Electrochim. Acta*, 2017, **242**, 382–389.
291 D. Kim, J. Yun, G. Lee and J. S. Ha, *Nanoscale*, 2014, **6**, 12034–12041.
292 Y. Qian, R. Liu, Q. Wang, J. Xu, D. Chen and G. Shen, *J. Mater. Chem. A*, 2014, **2**, 10917–10922.
293 Y. Zheng, Z. Lin, W. Chen, B. Liang, H. Du, R. Yang, X. He, Z. Tang and X. Gui, *J. Mater. Chem. A*, 2017, **5**, 5886–5894.
294 B. D. Boruah and A. Misra, *J. Mater. Chem. A*, 2016, **4**, 17552–17559.
295 H. Niu, X. Yang, H. Jiang, D. Zhou, X. Li, T. Zhang, J. Liu, Q. Wang and F. Qu, *J. Mater. Chem. A*, 2015, **3**, 24082–24094.
296 W. Cai, T. Lai, W. Dai and J. Ye, *J. Power Sources*, 2014, **255**, 170–178.
297 (*a*) D. Choi, G. E. Blomgren and P. N. Kumta, *Adv. Mater.*, 2006, **18**, 1178–1182; (*b*) P. Pande, P. G. Rasmussen and L. T. Thompson, *J. Power Sources*, 2012, **207**, 212–215.
298 X. Xiao, X. Peng, H. Jin, T. Li, C. Zhang, B. Gao, B. Hu, K. Huo and J. Zhou, *Adv. Mater.*, 2013, **25**, 5091–5097.
299 G. Ma, Z. Wang, B. Gao, T. Ding, Q. Zhong, X. Peng, J. Su, B. Hu, L. Yuan, P. K. Chu, J. Zhou and K. Huo, *J. Mater. Chem. A*, 2015, **3**, 14617–14624.
300 X. Lu, G. Wang, T. Zhai, M. Yu, S. Xie, Y. Ling, C. Liang, Y. Tong and Y. Li, *Nano Lett.*, 2012, **12**, 5376–5381.
301 M. S. Javed, S. Dai, M. Wang, Y. Xi, Q. Lang, D. Guo and C. Hu, *Nanoscale*, 2015, **7**, 13610–13618.
302 (*a*) X. Li, A. M. Elshahawy, C. Guan and J. Wang, *Small*, 2017, **13**, 1701530; (*b*) M. C. Liu, Y. M. Hu, W. Y. An, Y. X. Hu, L. Y. Niu, L. B. Kong and L. Kang, *Electrochim. Acta*, 2017, **232**, 387–395; (*c*) C. Yang, L. Dong, Z. Chen and H. Lu, *J. Phys. Chem. C*, 2014, **118**, 18884–18891.
303 (*a*) R. Soni, B. Anothumakkool and S. Kurungot, *ChemElectroChem*, 2016, **3**, 1329–1336; (*b*) C. Yang, L. Zhang, N. Hu, Z. Yang, H. Wei, Z. J. Xu, Y. Wang and Y. Zhang, *Appl. Surf. Sci.*, 2016, **379**, 206–212; (*c*) J. M. DArcy, M. F. El-Kady, P. P. Khine, L. Zhang, S. H. Lee, N. R. Davis, D. S. Liu, M. T. Yeung, S. Y. Kim, C. L. Turner, A. T. Lech, P. T. Hammond and R. B. Kaner, *ACS Nano*, 2014, **8**, 1500–1510.
304 F. Xiao, S. Yang, Z. Zhang, H. Liu, J. Xiao, L. Wan, J. Luo, S. Wang and Y. Liu, *Sci. Rep.*, 2015, **5**, 9359.
305 L. Yuan, B. Yao, B. Hu, K. Huo, W. Chen and J. Zhou, *Energy Environ. Sci.*, 2013, **6**, 470–476.
306 C. Yu, P. Ma, X. Zhou, A. Wang, T. Qian, S. Wu and Q. Chen, *ACS Appl. Mater. Interfaces*, 2014, **6**, 17937–17943.
307 R. Liu, L. Ma, S. Huang, J. Mei, J. Xu and G. Yuan, *New J. Chem.*, 2017, **41**, 857–864.
308 (*a*) R. Dong, M. Pfeffermann, H. Liang, Z. Zheng, X. Zhu, J. Zhang and X. Feng, *Angew. Chem., Int. Ed.*, 2015, **54**, 12058–12063; (*b*) M. Chhowalla, H. S. Shin, G. Eda, L. J. Li, K. P. Loh and H. Zhang, *Nat. Chem.*, 2013, **5**, 263–275; (*c*) S. Liu, F. Wang, R. Dong, T. Zhang, J. Zhang, X. Zhuang, Y. Mai and X. Feng, *Adv. Mater.*, 2016, **28**, 8365–8370; (*d*) P. Xiong, J. Zhu, L. Zhang and X. Wang, *Nanoscale Horiz.*, 2016, **1**, 340–374.
309 (*a*) B. Anasori, M. R. Lukatskaya and Y. Gogotsi, *Nat. Rev. Mater.*, 2017, **2**, 16098; (*b*) M. Naguib, M. Kurtoglu, V. Presser, J. Lu, J. Niu, M. Heon, L. Hultman, Y. Gogotsi and M. W. Barsoum, *Adv. Mater.*, 2011, **23**, 4248–4253; (*c*) V. M. H. Ng, H. Huang, K. Zhou, P. S. Lee, W. Que, J. Z. Xu and L. B. Kong, *J. Mater. Chem. A*, 2017, **5**, 3039–3068.
310 (*a*) B. Anasori, Y. Xie, M. Beidaghi, J. Lu, B. C. Hosler, L. Hultman, P. R. C. Kent, Y. Gogotsi and M. W. Barsoum, *ACS Nano*, 2015, **9**, 9507–9516; (*b*) J. C. Lei, X. Zhang and Z. Zhou, *Front. Phys.*, 2015, **10**, 107303.
311 (*a*) F. Shahzad, M. Alhabeb, C. B. Hatter, B. Anasori, S. M. Hong, C. M. Koo and Y. Gogotsi, *Science*, 2016, **353**,

1137–1140; (*b*) A. Lipatov, M. Alhabeb, M. R. Lukatskaya, A. Boson, Y. Gogotsi and A. Sinitskii, *Adv. Electron. Mater.*, 2016, **2**, 1600255.
312 M. R. Lukatskaya, O. Mashtalir, C. E. Ren, Y. Dall Agnese, P. Rozier, P. L. Taberna, M. Naguib, P. Simon, M. W. Barsoum and Y. Gogotsi, *Science*, 2013, **341**, 1502–1505.
313 M. Ghidiu, M. R. Lukatskaya, M. Q. Zhao, Y. Gogotsi and M. W. Barsoum, *Nature*, 2014, **516**, 78–81.
314 C. Zhang, B. Anasori, A. Seral-Ascaso, S. H. Park, N. McEvoy, A. Shmeliov, G. S. Duesberg, J. N. Coleman, Y. Gogotsi and V. Nicolosi, *Adv. Mater.*, 2017, **29**, 1702678.
315 M. Zhu, Y. Huang, Q. Deng, J. Zhou, Z. Pei, Q. Xue, Y. Huang, Z. Wang, H. Li, Q. Huang and C. Zhi, *Adv. Energy Mater.*, 2016, **6**, 1600969.
316 H. Li, Y. Hou, F. Wang, M. R. Lohe, X. Zhuang, L. Niu and X. Feng, *Adv. Energy Mater.*, 2017, **7**, 1601847.
317 (*a*) J. Suarez-Guevara, V. Ruiz and P. Gomez-Romero, *J. Mater. Chem. A*, 2014, **2**, 1014–1021; (*b*) J. Suarez-Guevara, V. Ruiz and P. Gomez-Romero, *Phys. Chem. Chem. Phys.*, 2014, **16**, 20411–20414.
318 (*a*) A. K. Cuentas-Gallegos, M. Lira-Cantú, N. Casañ-Pastor and P. Gómez-Romero, *Adv. Funct. Mater.*, 2005, **15**, 1125–1133; (*b*) Y. Ji, L. Huang, J. Hu, C. Streb and Y. F. Song, *Energy Environ. Sci.*, 2015, **8**, 776–789.
319 (*a*) M. Ammam, *J. Mater. Chem. A*, 2013, **1**, 6291–6312; (*b*) M. Genovese and K. Lian, *Electrochem. Commun.*, 2014, **43**, 60–62; (*c*) T. Akter, K. W. Hu and K. Lian, *Electrochim. Acta*, 2011, **56**, 4966–4971.
320 (*a*) D. P. Dubal, B. Ballesteros, A. A. Mohite and P. Gomez-Romero, *ChemSusChem*, 2017, **10**, 731–737; (*b*) D. P. Dubal, N. R. Chodankar, A. Vinu, D. H. Kim and P. Gomez-Romero, *ChemSusChem*, 2017, **10**, 2742–2750; (*c*) V. Ruiz, J. Suarez-Guevara and P. Gomez-Romero, *Electrochem. Commun.*, 2012, **24**, 35–38.
321 (*a*) M. Genovese and K. Lian, *J. Mater. Chem. A*, 2017, **5**, 3939–3947; (*b*) M. Genovese and K. Lian, *Curr. Opin. Solid State Mater. Sci.*, 2015, **19**, 126–137; (*c*) H. Y. Chen, R. Al-Oweini, J. Friedl, C. Y. Lee, L. Li, U. Kortz, U. Stimming and M. Srinivasan, *Nanoscale*, 2015, **7**, 7934–7941.
322 Y. Chen, M. Han, Y. Tang, J. Bao, S. Li, Y. Lan and Z. Dai, *Chem. Commun.*, 2015, **51**, 12377–12380.
323 V. Prabhakaran, B. L. Mehdi, J. J. Ditto, M. H. Engelhard, B. Wang, K. Don, D. Gunaratne, D. C. Johnson, N. D. Browning, G. E. Johnson and J. Laskin, *Nat. Commun.*, 2016, **7**, 11399.
324 (*a*) R. R. Salunkhe, Y. V. Kaneti, J. Kim, J. H. Kim and Y. Yamauchi, *Acc. Chem. Res.*, 2016, **49**, 2796–2806; (*b*) R. R. Salunkhe, Y. V. Kaneti and Y. Yamauchi, *ACS Nano*, 2017, **11**, 5293–5308; (*c*) W. Xuan, C. Zhu, Y. Liu and Y. Cui, *Chem. Soc. Rev.*, 2012, **41**, 1677–1695.
325 (*a*) O. M. Yaghi and H. Li, *J. Am. Chem. Soc.*, 1995, **117**, 10401–10402; (*b*) C. K. Brozeka and M. Dinca, *Chem. Soc. Rev.*, 2014, **43**, 5456–5467; (*c*) N. Campagnol, T. R. C. Van Assche, M. Li, L. Stappers, M. Dinca, J. F. M. Denayer, K. Binnemans, D. E. DeVose and J. Fransaer, *J. Mater. Chem. A*, 2016, **4**, 3914–3925.
326 A. Mahmood, W. Guo, H. Tabassum and R. Zou, *Adv. Energy Mater.*, 2016, **6**, 1600423.
327 (*a*) D. Y. Lee, S. J. Yoon, N. K. Shresth, S. H. Lee, H. Ahn and S. H. Han, *Microporous Mesoporous Mater.*, 2012, **153**, 163–165; (*b*) R. Dıaz, M. G. Orcajo, J. A. Botas, G. Calleja and J. Palma, *Mater. Lett.*, 2012, **68**, 126–128.
328 A. Basu, K. Roy, N. Sharma, S. Nandi, R. Vaidhyanathan, S. Rane, C. Rode and S. Ogale, *ACS Appl. Mater. Interfaces*, 2016, **8**, 31841–31848.
329 F. Yu, T. Wang, Z. Wen and H. Wang, *J. Power Sources*, 2017, **364**, 9–15.
330 D. Fu, H. Zhou, X. M. Zhang, G. Han, Y. Chang and H. Li, *ChemistrySelect*, 2016, **2**, 285–289.
331 L. Wang, X. Feng, L. Ren, Q. Piao, J. Zhong, Y. Wang, H. Li, Y. Chen and B. Wang, *J. Am. Chem. Soc.*, 2015, **137**, 4920–4923.
332 Y. Zhang, B. Lin, Y. Sun, P. Han, J. Wang, X. Ding, X. Zhang and H. Yang, *Electrochim. Acta*, 2016, **188**, 490–498.
333 L. Sun, M. G. Campbell and M. Dinca, *Angew. Chem., Int. Ed.*, 2016, **55**, 3566–3579.
334 D. Sheberla, J. C. Bachman, J. S. Elias, C. J. Sun, Y. Shao-Horn and M. Dinca, *Nat. Mater.*, 2017, **16**, 220–224.
335 W. H. Li, K. Ding, H. R. Tian, M. S. Yao, B. Nath, W. H. Deng, Y. Wang and G. Xu, *Adv. Funct. Mater.*, 2017, **27**, 1702067.
336 L. Li, Y. Yu, G. J. Ye, Q. Ge, X. Ou, H. Wu, D. Feng, X. H. Chen and Y. Zhang, *Nat. Nanotechnol.*, 2014, **9**, 372–377.
337 M. Köpf, N. Eckstein, D. Pfister, C. Grotz, I. Krüger, M. Greiwe, T. Hansen, H. Kohlmann and T. Nilges, *J. Cryst. Growth*, 2014, **405**, 6–10.
338 C. Hao, B. Yang, F. Wen, J. Xiang, L. Li, W. Wang, Z. Zeng, B. Xu, Z. Zhao, Z. Liu and Y. Tian, *Adv. Mater.*, 2016, **28**, 3194–3201.
339 (*a*) T. Lu, S. Dong, C. Zhang, L. Zhang and G. Cui, *Coord. Chem. Rev.*, 2017, **332**, 75–99; (*b*) S. S. Karade and B. R. Sankapal, *J. Electroanal. Chem.*, 2017, **802**, 131–138; (*c*) Y. Qiu, X. Li, M. Bai, H. Wang, D. Xue, W. Wang and J. Cheng, *Inorg. Chem. Front.*, 2017, **4**, 675–682; (*d*) P. Xu, W. Zeng, S. Luo, C. Ling, J. Xiao, A. Zhou, Y. Sun and K. Liao, *Electrochim. Acta*, 2017, **241**, 41–49.
340 C. Zhang, H. Yin, M. Han, Z. Dai, H. Pang, Y. Zheng, Y. Q. Lan, J. Bao and J. Zhu, *ACS Nano*, 2014, **8**, 3761–3770.
341 P. Yu, W. Fu, Q. Zeng, J. Lin, C. Yan, Z. Lai, B. Tang, K. Suenag, H. Zhang and Z. Liu, *Adv. Mater.*, 2017, **29**, 1701909.
342 H. Wang, J. Deng, C. Xu, Y. Chen, F. Xu, J. Wang and Y. Wang, *Energy Storage Mater.*, 2017, **7**, 216–221.
343 A. Ramadoss., K. Yoon, M. Kwak, S. Kim, S. Ryu and J. Jang, *J. Power Sources*, 2017, **337**, 159–165.
344 H. Li, J. Song, L. Wang, X. Feng, R. Liu, W. Zeng, Z. Huang, Y. Ma and L. Wang, *Nanoscale*, 2017, **9**, 193–200.
345 H. Zhang, C. Lu, C. Chen, L. Xie, P. Zhou and Q. Kong, *ChemElectroChem*, 2017, **4**, 1–8.
346 X. Jian, H. Yang, J. Li, E. Zhang, L. Cao and Z. Liang, *Electrochim. Acta*, 2017, **228**, 483–493.

347 Z. Li, Y. Li, L. Wang, L. Cao, X. Liu, Z. Chen, D. Pan and M. Wu, *Electrochim. Acta*, 2017, **235**, 561–569.

348 L. Liu, D. Ye, Y. Yu, L. Liu and Y. Wu, *Carbon*, 2017, **111**, 121–127.

349 L. Song, X. Cao, L. Li, Q. Wang, H. Ye, L. Gu, C. Mao, J. Song, S. Zhang and H. Niu, *Adv. Funct. Mater.*, 2017, **27**, 1700474.

350 Y. Zheng, Z. Lin, W. Chen, B. Liang, H. Du, R. Yang, X. He, Z. Tang and X. Gui, *J. Mater. Chem. A*, 2017, **5**, 5886–5894.

351 Y. Li, X. Wang, Q. Yang, M. Javed, Q. Liu, Weina Xu, C. Hu and D. Wei, *Electrochim. Acta*, 2017, **234**, 63–70.

352 H. Li, Y. Yu, L. Liu, L. Liu and Y. Wu, *Electrochim. Acta*, 2017, **228**, 553–561.

353 J. Zhu, S. Tang, J. Wu, X. Shi, B. Zhu and X. Meng, *Adv. Energy Mater.*, 2017, **7**, 1601234.

354 H. Li, Y. Hou, F. Wang, M. Lohe, X. Zhuang, L. Niu and X. Feng, *Adv. Energy Mater.*, 2017, **7**, 1601847.

355 R. Soni, A. Raveendrana and S. Kurungot, *Nanoscale*, 2017, **9**, 3593–3600.

356 K. Li, J. Liu, Y. Huang, F. Bu and Y. Xu, *J. Mater. Chem. A*, 2017, **5**, 5466–5474.

357 Y. Fan, W. Song, X. Li and L. Fan, *Carbon*, 2017, **111**, 658–666.

358 N. Li, X. Huang, H. Zhang, Y. Li and C. Wang, *ACS Appl. Mater. Interfaces*, 2017, **9**, 9763–9771.

359 P. Li, J. Li, Z. Zhao, Z. Fang, M. Yang, Z. Yuan, Y. Zhang, Q. Zhang, W. Hong, X. Chen and D. Yu, *Adv. Sci.*, 2017, **4**, 1700003.

360 S. Akbulut, M. Yilmaz, S. Raina, S. Hsu and W. Kang, *Diamond Relat. Mater.*, 2017, **74**, 222–228.

361 A. Liu, H. Lv, H. Liu, Q. Li and H. Zhao, *J. Mater. Sci.: Mater. Electron.*, 2017, **28**, 8452–8459.

362 Y. Qiu, X. Li, M. Bai, H. Wang, D. Xue, W. Wang and J. Cheng, *Inorg. Chem. Front.*, 2017, **4**, 675–682.

363 D. Zhao, Q. Zhang, W. Chen, X. Yi, S. Liu, Q. Wang, Y. Liu, J. Li, X. Li and H. Yu, *ACS Appl. Mater. Interfaces*, 2017, **9**, 13213–13222.

364 J. Cao, T. Huang, R. Liu, X. Xi and D. Wu, *Electrochim. Acta*, 2017, **230**, 265–270.

365 B. Yao, H. Wang, Q. Zhou, M. Wu, M. Zhang, C. Li and G. Shi, *Adv. Mater.*, 2017, **29**, 1700974.

366 F. Chen, P. Wan, H. Xu and X. Sun, *ACS Appl. Mater. Interfaces*, 2017, **9**, 17865–17871.

367 X. Hou, T. Peng, J. Cheng, Q. Yu, R. Luo, Y. Lu, X. Liu, J. Kim, J. He and Y. Luo, *Nano Res.*, 2017, **10**, 2570–2583.

368 I. Moon, S. Yoon and J. Oh, *Chem. – Eur. J.*, 2017, **23**, 597–604.

369 Y. Wu, Q. Wang, T. Li, D. Zhang and M. Miao, *Electrochim. Acta*, 2017, **245**, 69–78.

370 H. Su, P. Zhu, L. Zhang, F. Zhou, G. Li, T. Li, Q. Wang, R. Sun and C. Wong, *J. Electroanal. Chem.*, 2017, **786**, 28–34.

371 X. Li, K. Liu, Z. Liu, Z. Wang, B. Lia and D. Zhang, *Electrochim. Acta*, 2017, **240**, 43–52.

372 C. Chen, J. Cao, Q. Lu, X. Wang, L. Song, Z. Niu and J. Chen, *Adv. Funct. Mater.*, 2017, **27**, 1604639.

373 C. Liu, S. Zhao, Y. Lu, Y. Chang, D. Xu, Q. Wang, Z. Dai, J. Bao and M. Han, *Small*, 2017, **13**, 1603494.

374 S. Chen, L. Wang, M. Huang, L. Kang, Z. Lei, H. Xu, F. Shi and Z. Liu, *Electrochim. Acta*, 2017, **242**, 10–18.

375 C. Wan, Y. Jiao and J. Li, *J. Mater. Chem. A*, 2017, **5**, 3819–3831.

376 (*a*) S. Xu, G. Wei, J. Li, W. Han and Y. Gogotsi, *J. Mater. Chem. A*, 2017, **5**, 17442–17451; (*b*) Z. Yang, J. Deng, X. Sun, H. Li and H. Peng, *Adv. Mater.*, 2014, **26**, 2643–2647.

377 (*a*) X. Xiao, T. Ding, L. Yuan, Y. Shen, Q. Zhong, X. Zhang, Y. Cao, B. Hu, T. Zhai, L. Gong, J. Chen, Y. Tong, J. Zhou and Z. L. Wang, *Adv. Energy Mater.*, 2012, **2**, 1328–1332; (*b*) J. i. Sun, Y. Huang, Y. N. S. Sea, Q. Xue, Z. Wang, M. Zhu, H. Li, X. Tao, C. Zhi and H. Hu, *Mater. Today Energy*, 2017, **5**, 1–14; (*c*) S. C. Lee, U. M. Patil, S. J. Kim, S. Ahn, S. W. Kang and S. C. Jun, *RSC Adv.*, 2016, **6**, 43844–43854.

378 (*a*) W. Tang, Y. Zhu, Y. Hou, L. Liu, Y. Wu, K. P. Loh, H. Zhang and K. Zhu, *Energy Environ. Sci.*, 2013, **6**, 2093–2104; (*b*) J. Yan, Z. Fan, W. Sun, G. Ning, T. Wei, Q. Zhang, R. Zhang, L. Zhi and F. Wei, *Adv. Funct. Mater.*, 2012, **22**, 2632–2641.

379 F. Luan, G. Wang, Y. Ling, X. Lu, H. Wang, Y. Tong, X. X. Liu and Y. Li, *Nanoscale*, 2013, **5**, 7984–7990.

380 (*a*) L. Wu, R. Li, J. Guo, C. Zhou, W. Zhang, C. Wang, Y. Huang, Y. Li and J. Liu, *AIP Adv.*, 2013, **3**, 082129; (*b*) Y. Zhang, M. Zheng, M. Qu, M. Sun and H. Pang, *J. Alloys Compd.*, 2015, **651**, 214–221.

381 H. Pang, X. Li, Q. Zhao, H. Xue, W. Y. Lai, Z. Hu and W. Huang, *Nano Energy*, 2017, **35**, 138–145.

382 (*a*) Z. Gao, W. Yang, J. Wang, N. Song and X. Li, *Nano Energy*, 2015, **13**, 306–317; (*b*) J. Zhao, S. Wang, Z. Run, G. Zhang, W. Du and H. Pang, *Part. Part. Syst. Charact.*, 2015, **32**, 880–885; (*c*) J. Zhao, J. Chen, S. Xu, M. Shao, Q. Zhang, F. Wei, J. Ma, M. Wei, D. G. Evans and X. Duan, *Adv. Funct. Mater.*, 2014, **24**, 2938–2946.

383 Z. Pan, Y. Qiu, J. Yang, F. Ye, Y. Xu, X. Zhang, M. Liu and Y. Zhang, *Nano Energy*, 2016, **26**, 610–619.

384 J. Zhao, M. Zheng, Z. Run, J. Xia, M. Sun and H. Pang, *J. Power Sources*, 2015, **285**, 385–392.

385 S. Zhu, Z. Wang, F. Huang, H. Zhang and S. Li, *J. Mater. Chem. A*, 2017, **5**, 9960–9969.

386 J. Sun, P. Zan, L. Ye, X. Yang and L. Zhao, *J. Mater. Chem. A*, 2017, **5**, 9815–9823.

387 Y. Shao, H. Wang, Q. Zhang and Y. Li, *J. Mater. Chem. C*, 2013, **1**, 1245–1251.

388 J. Yang, G. Li, Z. Pan, M. Liu, Y. Hou, Y. Xu, H. Deng, L. Sheng, X. Zhao, Y. Qiu and Y. Zhang, *ACS Appl. Mater. Interfaces*, 2015, **7**, 22172–22180.

389 (*a*) X. Wang, B. Liu, R. Liu, Q. Wang, X. Hou, D. Chen, R. Wang and G. Shen, *Angew. Chem., Int. Ed.*, 2014, **53**, 1849–1853; (*b*) D. Ghosh, M. Mandal and C. K. Das, *Langmuir*, 2015, **31**, 7835–7843.

390 D. Kong, W. Ren, C. Cheng, Y. Wang, Z. Huang and H. Y. Yang, *ACS Appl. Mater. Interfaces*, 2015, **7**, 21334–21346.

391 J. Tao, N. Liu, L. Li, J. Su and Y. Gao, *Nanoscale*, 2014, **6**, 2922–2928.

392 H. Yang, H. Xu, M. Li, L. Zhang, Y. Huang and X. Hu, *ACS Appl. Mater. Interfaces*, 2016, **8**, 1774–1779.

393 C. Guan, W. Zhao, Y. Hu, Z. Lai, X. Li, S. Sun, H. Zhang, A. K. Cheetham and J. Wang, *Nanoscale Horiz.*, 2017, **2**, 99–105.

394 (*a*) N. R. Chodankar, D. P. Dubal, A. C. Lokhande, A. M. Patil, J. H. Kim and C. D. Lokhande, *Sci. Rep.*, 2016, **6**, 39205; (*b*) G. S. Gund, D. P. Dubal, N. R. Chodankar, J. Y. Cho, P. Gomez-Romero, C. Park and C. D. Lokhande, *Sci. Rep.*, 2015, **5**, 12454.

395 (*a*) S. Trasatti, *Pure Appl. Chem.*, 1986, **58**, 955–966; (*b*) P. V. Rysselberghe, *Appl. Phys. Lett.*, 1953, **21**, 1550–1551; (*c*) J. Cheng and M. Sprik, *Phys. Chem. Chem. Phys.*, 2012, **14**, 11245–11267.

396 (*a*) M. T. Greiner, M. G. Helander, W. M. Tang, Z. B. Wang, J. Qiu and Z. H. Lu, *Nat. Mater.*, 2012, **11**, 76–81; (*b*) C. A. Pan and T. B. Ma, *Appl. Phys. Lett.*, 1980, **37**, 714; (*c*) Z. Viskadourakis, M. L. Parames, O. Conde, M. Zervos and J. Giapintzakis, *Appl. Phys. Lett.*, 2012, **101**, 033505; (*d*) F. Chen, R. Schafranek, W. Wu and A. Klein, *J. Phys. D: Appl. Phys.*, 2011, **44**, 1; (*e*) M. N. Islam and M. O. Hakim, *J. Mater. Sci. Lett.*, 1986, **5**, 63.

397 (*a*) G. R. Li, Z. L. Wang, F. L. Zheng, Y. N. Ou and Y. X. Tong, *J. Mater. Chem.*, 2011, **21**, 4217; (*b*) J. Chang, M. Jin, F. Yao, T. H. Kim, V. T. Le, H. Yue, F. Gunes, B. Li, A. Ghosh, S. Xie and Y. H. Lee, *Adv. Funct. Mater.*, 2013, **23**, 5074–5083.

398 (*a*) Q. T. Qu, S. B. Yang and X. L. Feng, *Adv. Mater.*, 2011, **23**, 5574; (*b*) X. Lu, Y. Zeng, M. Yu, T. Zhai, C. Liang, S. Xie, M. S. Balogun and Y. Tong, *Adv. Mater.*, 2014, **26**, 3148–3155; (*c*) Q. Tang, W. Wang and G. Wang, *J. Mater. Chem. A*, 2015, **3**, 6662–6670.

399 P. Yang, Y. Ding, Z. Lin, Z. Chen, Y. Li, P. Qiang, M. Ebrahimi, W. Mai, C. P. Wong and Z. L. Wang, *Nano Lett.*, 2014, **14**, 731–736.

400 W. Ma, H. Nan, Z. Gu, B. Geng and X. Zhang, *J. Mater. Chem. A*, 2015, **3**, 5442–5448.

401 J. Xu, Q. Wang, X. Wang, Q. Xiang, B. Liang, D. Chen and G. Shen, *ACS Nano*, 2013, **7**, 5453–5462.

402 X. Lu, T. Zhai, X. Zhang, Y. Shen, L. Yuan, B. Hu, L. Gong, J. Chen, Y. Gao, J. Zhou, Y. Tong and Z. L. Wang, *Adv. Mater.*, 2012, **24**, 938–944.

403 Z. Yu, J. Moore, J. Calderon, L. Zhai and J. Thomas, *Small*, 2015, **11**(39), 5289–5295.

404 T. Gu and B. Wei, *J. Mater. Chem. A*, 2016, **4**, 12289–12295.

405 X. Lu, M. Yu, G. Wang, T. Zhai, S. Xie, Y. Ling, Y. Tong and Y. Li, *Adv. Mater.*, 2013, **25**, 267–272.

406 (*a*) S. Murugesan, P. Kuppusami, N. Parvathavarthini and E. Mohandas, *Surf. Coat. Technol.*, 2007, **201**, 7713–7719; (*b*) G. M. Wang, H. Y. Wang, Y. C. Ling, Y. C. Tang, X. Y. Yang, R. C. Fitzmorris, C. C. Wang, J. Z. Zhang and Y. Li, *Nano Lett.*, 2011, **11**, 3026–3033.

407 (*a*) L. Y. Yuan, X. H. Lu, X. Xiao, T. Zhai, J. J. Dai, F. C. Zhang, B. Hu, X. Wang, L. Gong, J. Chen, C. G. Hu, Y. X. Tong, J. Zhou and Z. L. Wang, *ACS Nano*, 2012, **6**, 656–661; (*b*) X. H. Lu, D. Z. Zheng, T. Zhai, Z. Q. Liu, Y. Y. Huang, S. L. Xie and Y. X. Tong, *Energy Environ. Sci.*, 2011, **4**, 2915–2921.

408 J. X. Feng, S. H. Ye, X. F. Lu, Y. X. Tong and G. R. Li, *ACS Appl. Mater. Interfaces*, 2015, **7**, 11444–11451.

409 H. Gao, F. Xiao, C. B. Ching and H. Duan, *ACS Appl. Mater. Interfaces*, 2012, **4**, 7020–7026.

410 (*a*) B. Avasarala and P. Haldar, *Electrochim. Acta*, 2010, **55**, 9024–9034; (*b*) I. Milošv, H. H. Strehblow, B. Navinšek and M. Metikoš-Hukovic, *Surf. Interface Anal.*, 1995, **23**, 529–539.

411 X. Lu, M. H. Yu, T. Zhai, G. Wang, S. Xie, T. Lu, C. Liang, Y. X. Tong and Y. Li, *Nano Lett.*, 2013, **13**, 2628–2633.

412 (*a*) A. Achour, J. B. Ducros, R. L. Porto, M. Boujtita, E. Gautron, L. Le Brizoual, M. A. Djouadi and T. Brousse, *Nano Energy*, 2014, **7**, 104–113; (*b*) Z. L. Wang, *Nano Today*, 2010, **5**, 540–552.

413 (*a*) Y. Yue, P. Han, X. He, K. Zhang, Z. Liu, C. Zhang, S. Dong, L. Gu and G. Cui, *J. Mater. Chem.*, 2012, **22**, 4938–4943; (*b*) Y. Qiu, K. Yan, S. Yang, L. Jin, H. Deng and W. Li, *ACS Nano*, 2010, **4**, 6515–6526; (*c*) F. Tian, Y. Xie, H. Du, Y. Zhou, C. Xia and W. Wang, *RSC Adv.*, 2014, **4**, 41856–41863.

414 C. Zhu, P. Yang, D. Chao, X. Wang, X. Zhang, S. Chen, B. K. Tay, H. Huang, H. Zhang, W. Mai and H. J. Fan, *Adv. Mater.*, 2015, **27**, 4566–4571.

415 X. F. Lu, X. Y. Chen, W. Zhou, Y. X. Tong and G. R. Li, *ACS Appl. Mater. Interfaces*, 2015, **7**, 14843–14850.

416 Y. Jin, H. Chen, M. Chen, N. Liu and Q. Li, *ACS Appl. Mater. Interfaces*, 2013, **5**, 3408–3416.

417 N. Kurra, R. Wang and H. N. Alshareef, *J. Mater. Chem. A*, 2015, **3**, 7368–7374.

418 Z. Zheng, M. Retana, X. Hu, R. Luna, Y. Ikuhara and W. Zhou, *ACS Appl. Mater. Interfaces*, 2017, **9**, 16986–16994.

419 C. Ji, F. Liu, L. Xu and S. Yang, *J. Mater. Chem. A*, 2017, **5**, 5568–5576.

420 P. Li, Z. Jin and D. Xiao, *J. Mater. Chem. A*, 2017, **5**, 3274–3283.

421 J. Zhao, M. Zheng, Z. Run, J. Xia, M. Sun and H. Pang, *J. Power Sources*, 2015, **285**, 385–392.

422 Z. Zhang, K. Chi, F. Xiao and S. Wang, *J. Mater. Chem. A*, 2015, **3**, 12828–12835.

423 H. Yang, H. Xu, M. Li, L. Zhang, Y. Huang and X. Hu, *ACS Appl. Mater. Interfaces*, 2016, **8**, 1774–1779.

424 J. X. Feng, S. H. Ye, X. F. Lu, Y. X. Tong and G. R. Li, *ACS Appl. Mater. Interfaces*, 2015, **7**, 11444–11451.

425 J. Zhao, S. Wang, Z. Run, G. Zhang, W. Du and H. Pang, *Part. Part. Syst. Charact.*, 2015, **32**, 880–885.

426 C. Wei, C. Cheng, B. Zhou, X. Yuan, T. Cui, S. Wang, M. Zheng and H. Pang, *Part. Part. Syst. Charact.*, 2015, **32**, 831–839.

427 D. Kong, W. Ren, C. Cheng, Y. Wang, Z. Huang and H. Y. Yang, *ACS Appl. Mater. Interfaces*, 2015, **7**, 21334–21346.

428 D. Kong, C. Cheng, Y. Wang, J. I. Wong, Y. Yang and H. Y. Yang, *J. Mater. Chem. A*, 2015, **3**, 16150–16161.

429 G. Sun, X. Zhang, R. Lin, J. Yang, H. Zhang and P. Chen, *Angew. Chem., Int. Ed.*, 2015, **54**, 4651–4656.
430 D. Ghosh, M. Mandal and C. K. Das, *Langmuir*, 2015, **31**, 7835–7843.
431 H. Pang, Y. Zhang, W. Y. Laib, Z. Huc and W. Huang, *Nano Energy*, 2015, **15**, 303–312.
432 Z. Zhang, F. Xiao and S. Wang, *J. Mater. Chem. A*, 2015, **3**, 11215–11223.
433 Z. Zhang, F. Xiao, J. Xiao and S. Wang, *J. Mater. Chem. A*, 2015, **3**, 11817–11823.
434 N. Yu, M. Q. Zhu and D. Chen, *J. Mater. Chem. A*, 2015, **3**, 7910–7918.
435 Z. Gao, W. Yang, J. Wang, N. Song and X. Li, *Nano Energy*, 2015, **13**, 306–317.
436 Y. Zhang, M. Zheng, M. Qu, M. Sun and H. Pang, *J. Alloys Compd.*, 2015, **651**, 214–221.
437 Y. Chen, B. Liu, Q. Liu, J. Wang, Z. Li, X. Jing and L. Liu, *Nanoscale*, 2015, **7**, 15159–15167.
438 N. R. Chodankar, D. P. Dubal, G. S. Gund and C. D. Lokhande, *Energy Technol.*, 2015, **3**, 625–631.
439 A. V. Shinde, N. R. Chodankar, V. C. Lokhande, A. C. Lokhande, T. Ji, J. H. Kim and C. D. Lokhande, *RSC Adv.*, 2016, **6**, 58839–58843.
440 H. Xie, S. Tang, J. Zhu, S. Vongehr and X. Meng, *J. Mater. Chem. A*, 2015, **3**, 18505–18513.
441 T. Chen, Y. Tang, Y. Qiao, Z. Liu, W. Guo, J. Song, S. Mu, S. Yu, Y. Zhao and F. Gao, *Sci. Rep.*, 2016, **6**, 23289.
442 Q. Wang, Y. Ma, Y. Wu, D. Zhang and M. Miao, *ChemSusChem*, 2017, **10**, 1427–1435.
443 K. Subramani, N. Sudhan, R. Divya and M. Sathish, *RSC Adv.*, 2017, **7**, 6648–6659.
444 W. Liu, K. Feng, Y. Zhang, T. Yu, L. Han, G. Lui, M. Li, G. Chiu, P. Fung and A. Yu, *Nano Energy*, 2017, **34**, 491–499.
445 J. Noh, C. Yoon, Y. Kim and J. Jang, *Carbon*, 2017, **116**, 470–478.
446 H. Pang, X. Li, Q. Zhao, H. Xue, W. Lai, Z. Hu and W. Huang, *Nano Energy*, 2017, **35**, 138–145.
447 Z. Zheng, M. Retana, X. Hu, R. Luna, Y. Ikuhara and W. Zhou, *ACS Appl. Mater. Interfaces*, 2017, **9**, 16986–16994.
448 K. Chi, Z. Zhang, Q. Lv, C. Xie, J. Xiao, F. Xiao and S. Wang, *ACS Appl. Mater. Interfaces*, 2017, **9**, 6044–6053.
449 J. Wang, L. Zhang, X. Liu, X. Zhang, Y. Tian, X. Liu, J. Zhao and Y. Li, *Sci. Rep.*, 2017, **7**, 41088.
450 Z. Tian, H. Dou, B. Zhang, W. Fan and X. Wang, *Electrochim. Acta*, 2017, **237**, 109–118.
451 M. Zheng, L. Li, P. Gu, Z. Lin, W. Du, H. Xue and H. Pang, *Energy Technol.*, 2017, **5**, 544–548.
452 H. Wang, C. Xu, Y. Chen and Y. Wang, *Energy Storage Mater.*, 2017, **8**, 127–133.
453 Z. Pan, M. Liu, J. Yang, Y. Qiu, W. Li, Y. Xu, X. Zhang and Y. Zhang, *Adv. Funct. Mater.*, 2017, **27**, 1701122.
454 K. Ghosh, C. Yue, M. Sk and R. Jena, *ACS Appl. Mater. Interfaces*, 2017, **9**, 15350–15363.
455 H. Xie, S. Tang, D. Li, S. Vongehr and X. Meng, *ChemSusChem*, 2017, **10**, 2301–2308.
456 L. Gao, J. Surjadi, K. Cao, H. Zhang, P. Li, S. Xu, C. Jiang, J. Song, D. Sun and Y. Lu, *ACS Appl. Mater. Interfaces*, 2017, **9**, 5409–5418.
457 Y. Liu, N. Fu, G. Zhang, M. Xu, W. Lu, L. Zhou and H. Huang, *Adv. Funct. Mater.*, 2017, **27**, 1605307.
458 H. Pang, X. Li, Q. Zhao, H. Xue, W.-Y. Lai, Z. Hu and W. Huang, *Nano Energy*, 2017, **35**, 138–145.
459 S. Cheng, T. Shi, Y. Huang, X. Tao, J. Li, C. Cheng, G. Liao and Z. Tang, *Ceram. Int.*, 2017, **43**, 2155–2164.
460 X. He, Q. Liu, J. Liu, R. Li, H. Zhang, R. Chen and J. Wang, *Chem. Eng. J.*, 2017, **325**, 134–143.
461 T. Wang, S. Zhang, X. Yan, M. Lyu, L. Wang, J. Bell and H. Wang, *ACS Appl. Mater. Interfaces*, 2017, **9**, 15510–15524.
462 Y. Zhong, T. Shi, Z. Liu, Y. Huang, S. Cheng, C. Cheng, X. Li, G. Liao and Z. Tang, *Energy Technol.*, 2017, **5**, 656–664.
463 W. Ma, S. Chen, S. Yang, W. Chen, W. Weng, Y. Cheng and M. Zhu, *Carbon*, 2017, **113**, 151–158.
464 K. Lu, J. Zhang, Y. Wang, J. Ma, B. Song and H. Ma, *ACS Sustainable Chem. Eng.*, 2017, **5**, 821–827.
465 J. Zhao, C. Li, Q. Zhang, J. Zhang, X. Wang, Z. Lin, J. Wang, W. Lv, C. Lu, C. Wong and Y. Yao, *J. Mater. Chem. A*, 2017, **5**, 6928–6936.
466 Z. Li, M. Shaon, L. Zhou, R. Zhang, C. Zhang, J. Han, M. Wein, D. G. Evans and X. Duan, *Nano Energy*, 2016, **20**, 294–304.
467 R. Zhang, H. An, Z. Li, M. Shao, J. Han and M. Wei, *Chem. Eng. J.*, 2016, **289**, 85–92.
468 Q. Yang, Z. Li, R. Zhang, L. Zhou, M. Shao and M. Wei, *Nano Energy*, 2017, **41**, 408–416.
469 (*a*) D. Qi, Y. Liu, Z. Liu, L. Zhang and X. Chen, *Adv. Mater.*, 2017, **29**, 1602802; (*b*) Y. Fu, X. Cai, H. Wu, Z. Lv, S. Hou, M. Peng, X. Yu and D. Zou, *Adv. Mater.*, 2012, **24**, 5713–5718.
470 (*a*) F. R. Fan, W. Tang and Z. L. Wang, *Adv. Mater.*, 2016, **28**, 4283–4305; (*b*) T. Q. Trung and N. E. Lee, *Adv. Mater.*, 2016, **28**, 4338–4372; (*c*) Y. Huang, M. S. Zhu, Y. Huang, Z. X. Pei, H. F. Li, Z. F. Wang, Q. Xue and C. Y. Zhi, *Adv. Mater.*, 2016, **28**, 8344–8364.
471 Z. Wang and J. Song, *Science*, 2006, **312**, 242–246.
472 (*a*) Z. L. Wang, T. Jiang and L. Xu, *Nano Energy*, 2017, **39**, 9–23; (*b*) J. Ma, Y. Jie, J. Bian, T. Li, X. Cao and N. Wang, *Nano Energy*, 2017, **39**, 192–199; (*c*) M. Zhu, Y. Huang, Y. Huang, H. Li, Z. Wang, Z. Pei, Q. Xue, H. Geng and C. Zhi, *Adv. Mater.*, 2017, **29**, 1605137.
473 (*a*) Z. Tian, J. He, X. Chen, Z. Zhang, T. Wen, C. Zhai, J. Han, J. Mu, X. Hou, X. Chou and C. Xue, *Nano Energy*, 2017, **39**, 562–570; (*b*) W. Gong, C. Hou, Y. Guo, J. Zhou, J. Mu, Y. Li, Q. Zhang and H. Wang, *Nano Energy*, 2017, **39**, 673–683.
474 (*a*) X. Wang, Y. Yin, F. Yi, K. Dai, S. Niu, Y. Han, Y. Zhang and Z. You, *Nano Energy*, 2017, **39**, 429–436; (*b*) X. He, Y. Zia, H. Yu, S. L. Zhang, J. Wang, W. Ding, H. Zou, W. Zhang, C. Lu and Z. L. Wang, *Nano Energy*, 2017, **39**, 328–336; (*c*) A. Maitra, S. K. Karan, S. Paria, A. K. Das, R. Bera, L. Halder, S. K. Si, A. Bera and B. B. Khatua, *Nano Energy*, 2017, **40**, 633–645.

475 R. Song, H. Jin, X. Li, L. Fei, Y. Zhao, H. Huang, H. L. Chan, Y. Wang and Y. Chai, *J. Mater. Chem. A*, 2015, **3**, 14963–14970.

476 A. Ramadoss, B. Saravanakumar, S. W. Lee, Y. S. Kim, S. J. Kim and Z. L. Wang, *ACS Nano*, 2015, **9**, 4337–4345.

477 J. Luo, F. R. Fan, T. Jiang, Z. Wang, W. Tang, C. Zhang, M. Liu, G. Cao and Z. L. Wang, *Nano Res.*, 2015, **8**, 3934–3943.

478 (*a*) A. Scalia, F. Bella, A. Lamberti, S. Bianco, C. Gerbaldi, E. Tresso and C. F. Pirri, *J. Power Sources*, 2017, **359**, 311–321; (*b*) P. Yang, X. Xiao, Y. Li, Y. Ding, P. Qiang, X. Tan, W. Mai, Z. Lin, W. Wu, T. Li, H. Jin, P. Liu, J. Zhou, C. P. Wong and Z. L. Wang, *ACS Nano*, 2013, **7**, 2617–2626.

479 X. Chen, H. Sun, Z. Yang, G. Guan, Z. Zhang, L. Qiu and H. Peng, *J. Mater. Chem. A*, 2014, **2**, 1897–1902.

480 Z. Zhang, X. Chen, P. Chen, G. Guan, L. Qiu, H. Lin, Z. Yang, W. Bai, Y. Luo and H. Peng, *Adv. Mater.*, 2014, **26**, 466–470.

481 (*a*) C. Li, M. Islam, J. Moore, J. Sleppy, C. Morrison and K. Konstantinov, *Nat. Publ. Gr*, 2016, **7**, 1–10; (*b*) T. Chen, L. Qiu, Z. Yang, Z. Cai, J. Ren, H. Li, H. Lin, X. Sun and H. Peng, *Angew. Chem., Int. Ed.*, 2012, **51**, 11977–11980.

482 L. Liu, B. Shen, D. Jiang, R. Guo, L. Kong and X. Yan, *Adv. Energy Mater.*, 2016, **6**, 1600763.

483 Y. Huang, M. Zhu, Z. Pei, Q. Xue, Y. Huang and C. Zhi, *J. Mater. Chem. A*, 2016, **4**, 1290–1297.

484 J. Deng, Y. Zhang, Y. Zhao, P. Chen, X. Cheng and H. Peng, *Angew. Chem., Int. Ed.*, 2015, **54**, 15419–15423.

485 J. Zhong, J. Meng, Z. Yang, P. Poulind and N. Koratkar, *Nano Energy*, 2015, **17**, 330–338.

486 (*a*) B. E. Logan and K. Rabaey, *Science*, 2012, **337**, 686–690; (*b*) R. D. Cusick, Y. Kim and B. E. Logan, *Science*, 2012, **335**, 1474–1477; (*c*) B. E. Logan, *Nat. Rev. Microbiol.*, 2009, **7**, 375–381.

487 (*a*) N. Uría, X. Muñoz Berbel, O. Sánchez, F. X. Muñoz and J. Mas, *Environ. Sci. Technol.*, 2011, **45**, 10250–10256; (*b*) A. Deeke, T. H. Sleutels, H. V. Hamelers and C. J. Buisman, *Environ. Sci. Technol.*, 2012, **46**, 3554–3560; (*c*) E. J. Gardel, M. E. Nielsen, P. T. Grisdela Jr and P. R. Girguis, *Environ. Sci. Technol.*, 2012, **46**, 5222–5229.

488 N. S. Malvankar, T. Mester, M. T. Tuominen and D. R. Lovley, *ChemPhysChem*, 2012, **13**, 463–468.

489 H. Ren, H. Tian, H. S. Lee, T. Park, F. C. Leung, T. L. Ren and J. Chae, *Nano Energy*, 2015, **15**, 697–708.

490 R. S. Jayashree, M. Mitchell, D. Natarajan, L. J. Markoski and P. J. Kenis, *Langmuir*, 2007, **23**, 6871–6874.

491 P. Yang, P. Sun and W. Mai, *Mater. Today*, 2016, **19**, 394–402.

492 T. Xu, E. C. Walter, A. Agrawal, C. Bohn, J. Velmurugan, W. Zhu, H. J. Lezec and A. A. Talin, *Nat. Commun.*, 2015, **7**, 10479–10484.

493 R. T. Wen, C. G. Granqvist and G. A. Niklasson, *Nat. Mater.*, 2015, **14**, 996–1001.

494 (*a*) G. Cai, X. Wang, M. Cui, P. Darmawan, J. Wang, A. Eh and P. Lee, *Nano Energy*, 2015, **12**, 258–267; (*b*) M. Zhu, W. Meng, Y. Huang, Y. Huang and C. Zhi, *ACS Appl. Mater. Interfaces*, 2014, **6**, 18901–18910; (*c*) D. DeLongchamp and P. T. Hammond, *Adv. Mater.*, 2001, **13**, 1455–1459; (*d*) B. P. Jelle and G. Hagen, *Sol. Energy Mater. Sol. Cells*, 1999, **58**, 277–286.

495 (*a*) P. Yang, P. Sun, L. Du, Z. Liang, W. Xie, X. Cai, L. Huang, S. Tan and W. Mai, *J. Phys. Chem. C*, 2015, **119**, 16483–16489; (*b*) G. Cai, P. Darmawan, M. Cui, J. Wang, J. Chen, S. Magdassi and P. S. Lee, *Adv. Energy Mater.*, 2016, **6**, 1501882.

496 P. Yang, P. Sun, Z. Chai, L. Huang, X. Cai, S. Tan, J. Song and W. Mai, *Angew. Chem., Int. Ed.*, 2014, **53**, 11935–11939.

497 Y. Chen, Y. Wang, P. Sun, P. Yang, L. Du and W. Mai, *J. Mater. Chem. A*, 2015, **3**, 20614–20618.

498 Y. Tian, S. Cong, W. Su, H. Chen, Q. Li, F. Geng and Z. Zhao, *Nano Lett.*, 2014, **14**, 2150–2156.

499 D. Wei, M. R. J. Scherer, C. Bower, P. Andrew, T. Ryhanen and U. Steiner, *Nano Lett.*, 2012, **12**, 1857–1862.

500 X. Chen, H. Lin, J. Deng, Y. Zhang, X. Sun, P. Chen, X. Fang, Z. Zhang, G. Guan and H. Peng, *Adv. Mater.*, 2014, **26**, 8126–8132.

501 (*a*) P. Yao, S. Xie, M. Ye, R. Yu, Q. Liu, D. Yan, W. Cai, W. Guo and X. Y. Liu, *RSC Adv.*, 2017, **7**, 29088–29095; (*b*) P. Zhang, F. Zhu, F. Wang, J. Wang, R. Dong, X. Zhuang, O. G. Schmidt and X. Feng, *Adv. Mater.*, 2017, **29**, 1604491.

502 (*a*) C. K. Chan, H. Peng, G. Liu, K. McIlwrath, X. Zhang, A. R. Huggins and Y. Cui, *Nat. Nanotechnol.*, 2008, **3**, 31–35; (*b*) Y. Chen, Y. Hsu, Y. Lin, Y. Lin, Y. Horng, L. Chen and K. Chen, *Electrochim. Acta*, 2011, **56**, 7124–7130.

503 Y. Huang, Y. Huang, M. Zhu, W. Meng, Z. Pei, C. Liu, H. Hu and C. Zhi, *ACS Nano*, 2015, **9**, 6242–6251.

504 H. Wang, B. Zhu, W. Jiang, Y. Yang, W. Leow, H. Wang and X. Chen, *Adv. Mater.*, 2014, **26**, 3638–3643.

505 H. Sun, X. You, Y. Jiang, G. Guan, X. Fang, J. Deng, P. Chen, Y. Luo and H. Peng, *Angew. Chem., Int. Ed.*, 2014, **53**, 9526–9531.

506 Y. Huang, M. Zhong, Y. Huang, M. Zhu, Z. Pei, Z. Wang, Q. Xue, X. Xie and C. Zhi, *Nat. Commun.*, 2015, **6**, 10310–10317.

507 (*a*) Y. Huang, S. Kershaw, Z. Wang, Z. Pei, J. Liu, Y. Huang, H. Li, M. Zhu, A. Rogach and C. Zhi, *Small*, 2016, **12**, 3393–3399; (*b*) D. Kim, D. Kim, H. Lee, Y. R. Jeong, S. J. Lee, G. Yang, H. Kim, G. Lee, S. Jeon, G. Zi, J. Kim and J. S. Ha, *Adv. Mater.*, 2016, **28**, 748–756; (*c*) J. Yun, Y. Lim, H. Lee, G. Lee, H. Park, S. Y. Hong, S. W. Jin, Y. H. Lee, S. S. Lee and J. S. Ha, *Adv. Funct. Mater.*, 2017, **27**, 1700135; (*d*) D. Kim, K. Keum, G. Lee, D. Kim, S. S. Lee and J. S. Ha, *Nano Energy*, 2017, **35**, 199–206.

508 X. Wang, S. Yao, X. Wu, Z. Shi, H. Sun and R. Que, *RSC Adv.*, 2015, **5**, 17938–17944.

509 Y. Qi and M. C. McAlpine, *Energy Environ. Sci.*, 2010, **3**, 1275–1285.